

NOVEL TECHNIQUES FOR INVESTIGATING THE PERMEATION PROPERTIES OF ENVIRONMENTALLY-FRIENDLY PAPER COATINGS:

The influence of structural anisotropy on fluid permeation in porous media

By

PAUL BODURTHA

A thesis submitted to the University of Plymouth
in partial fulfilment for the degree of

2.854 T
820012460x

DOCTOR OF PHILOSOPHY

Department of Chemistry, School of Environmental Science
Faculty of Science

In collaboration with SCA Graphic Research AB, Sundsvall, Sweden

MAY 2003

LIBRARY STORE

REFERENCE ONLY

UNIVERSITY OF PLYMOUTH	
Item No.	Q00548069X
Date	- 2 SEP 2003S
Class No.	THESIS 532.51 BOD
Cont. No.	X704619988
FLYMOO BRARY	

ABSTRACT

By: Paul Bodurtha

TITLE: NOVEL TECHNIQUES FOR INVESTIGATING THE PERMEATION PROPERTIES OF ENVIRONMENTALLY-FRIENDLY PAPER COATINGS

Sub-Title: The influence of structural anisotropy on fluid permeation in porous media

In this study, we have investigated the effects of structural anisotropy of porous media on the permeation of fluids. The motivation for the work was an increased understanding of the permeation of inks into paper coatings, which often contain platey or needle-like particles, which have been aligned during the coating process. However, the findings are also relevant to other systems, such as the sub-terranean migration of fluids, including pollutants, within shale that contains particles of high aspect ratio. Mineral pigments, comprising mainly of calcium carbonate or clay, are often applied to the surface of paper to improve optical and printing properties. For a high quality image to be achieved, the coating should have sufficient capillarity to allow the ink film to set within the time-scale of a modern printing press.

The permeation of fluids into a range of different coating formulations has been investigated, with its main focus on the following samples: Speswhite and Amazon90 SD, which belong to the Kaolin (clay) mineral group, and OpacarbA40 and Albaglos, which belong to the Precipitated Calcium Carbonate (PCC) mineral group. The permeation was measured by five different techniques, including a novel use of the Ink Surface Interaction Tester.

The results were modelled using a modified version of the software package 'Pore-Cor', which simulated both permeability and capillary absorption of a wetting liquid into porous media containing anisotropic voids, and allowed the effects of anisotropy to be isolated from other closely related pore properties. The model generated a simplified three-dimensional void network having pores with a rectangular cross-section and throats with an elliptic cross-section.

From visual inspection of the modelled structures, the effect of anisotropy revealed advance wetting in the narrow features of Speswhite-CL and OpacarbA40-CL. Overall, to gain a clear understanding of the permeation of anisotropic structures both inertia and surface throat density is needed to be included in the Pore-Cor model. Once these factors were applied to the model, it was able to predict the permeation of fluids more successfully than those predicted by the Kozeny and aligned cylinders models. The insights gained from this study have allowed conclusions to be drawn about the nature of fluid permeation; they have therefore opened the way to more sophisticated modelling and the engineering of high performance coating structures.

LIST OF CONTENTS

COPYRIGHT STATEMENT	I
TITLE PAGE	II
ABSTRACT	III
LIST OF CONTENTS	IV
LIST OF FIGURES	XI
Chapter 1.....	xi
Chapter 2.....	xi
Chapter 3.....	xiii
Chapter 4.....	xiii
Chapter 5.....	xiv
Chapter 6.....	xvi
Chapter 7.....	xvii
Chapter 8.....	xx
Chapter 9.....	xxiii
LIST OF TABLES	XXIV
Chapter 2.....	xxiv
Chapter 5.....	xxiv
Chapter 6.....	xxiv
Chapter 7.....	xxv
Chapter 9.....	xxvi
APPENDIX	XXVI
LIST OF EQUATIONS	XXVII
Chapter 2.....	xxvii
Chapter 3.....	xxviii
Chapter 6.....	xxviii
Chapter 7.....	xxix
ACKNOWLEDGEMENTS	XXX
AUTHOR'S DECLARATION	XXXI
PUBLICATIONS, CONFERENCES AND TRAINING	XXXII
PRESENTATIONS AND CONFERENCES ATTENDED	XXXII
PUBLICATIONS	XXXIII
TRAINING	XXXIII
PREVIOUS ACADEMIC ACCOLADES	XXXIII

1. INTRODUCTION.....	1
1.1. Structure of thesis.....	1
1.2. Background of project.....	2
1.3. Rationale and aim of project.....	2
1.3.1. Thesis Hypotheses.....	2
1.3.2. Thesis Objectives.....	4
1.4. Scientific terms and definitions.....	5
1.4.1. Porous medium.....	5
1.4.2. Permeation and Permeability.....	7
1.4.3. Anisotropy.....	8
1.5. Why is paper coated?	10
1.6. Composition and structure of paper and paper coatings.....	11
1.7. Mineral Pigments.....	12
1.7.1. Kaolin mineral group.....	12
1.7.2. Calcium Carbonate mineral group.....	14
1.7.2.1. Ground calcium carbonate (GCC) mineral group.....	16
1.7.2.2. Precipitated Calcium Carbonate (PCC) mineral group.....	16
1.8. History of paper making.....	17
1.9. Environmental Implications.....	24
2. LITERATURE REVIEW.....	26
2.1 Darcy's experiment.....	26
2.2 The permeability concept.....	28
2.2.1 Saturated permeability.....	29
2.3 The Measurement of Permeability.....	30
2.3.1 Anisotropic permeability measurements.....	31
2.3.2 Permeation measurements in paper coatings.....	32
2.3.2.1 Gurley permeameter.....	32
2.3.2.2 Ink tack test.....	32
2.3.2.3 Dynamic Absorption Tester (DAT).....	33
2.3.2.4 Ink stain density test.....	33
2.4 Continuous matter theory.....	34
2.4.1 Turbulence and Reynolds number.....	36
2.5 Permeability Models.....	37

2.5.1 Empirical correlations.....	37
2.5.2 Theoretical Correlation.....	37
2.5.3 Capillary Models.....	38
2.5.3.1 Aligned cylinders model (Straight capillary model)	38
2.5.3.2 Parallel type models.....	40
2.5.4 Hydraulic radius theories.....	42
2.5.5 The Kozeny theory.....	42
2.5.5.1 Criticism of the Kozeny theory.....	44
2.6 Fluid pressure in porous structures.....	45
2.6.1 Fluid movement and contact angle in non-cylindrical tubes.....	46
2.6.2 Dynamic fluid motion.....	51
2.7 The Characterization of particles.....	52
2.7.1 The packing of particles.....	52
2.7.2 Particle size determination.....	54
2.7.3 The aspect ratio.....	54
2.8 Different approaches to the modelling of porous materials.....	56
2.8.1 Continuum model.....	56
2.8.2 One dimensional approximation.....	56
2.8.3 Extended one-dimensional approximation.....	59
2.8.4 Three-dimensional structures.....	59
2.8.5 Fibre networks.....	66
2.9 Modelling paper coatings with 'Pore-Cor'.....	69
2.9.1 Cross-correlation of percolation and permeability characteristics....	69
2.9.2 Pore and throat shapes.....	72
2.9.2.1 Conical throats.....	72
2.9.2.2 Capillary element aspect ratio.....	75
2.10 Representative elementary volume.....	76
2.11 The property 'inversion' problem.....	77
2.12 Difficulties in proving the hypothesis.. ..	78
2.12.1 Approximation framework.....	79
3. MATERIALS AND EXISTING METHODS AND APPROACHES.....	83
3.1. Types of paper coatings investigated.....	83
3.1.1. Mineral pigments.....	83
3.1.2. Binders.....	86
3.1.3. Coating preparation.....	87
3.1.4. Sample Selection.....	88

3.2. Existing techniques for characterising particle and void size distributions..	89
3.3. Existing techniques for measuring permeation.....	91
3.3.1. Ink stain density (ISD) procedure.....	92
3.3.2. DAT procedure.....	95
3.4. The 'Gurley' Air Resistance Method (Gurley method)	98
3.5. Use of existing models for measuring permeation.....	100
3.5.1. Application of the Aligned Cylinders model.....	100
3.5.2. Application of the Kozeny models.....	101
3.5.3. Application of the Effective hydraulic radius (EHR) model.....	102
4. DEVELOPMENT OF NOVEL EXPERIMENTAL METHODS.....	103
4.1 Prufbau Printability Absorption Method (PPAM).....	103
4.1.1 Experimental procedure.....	103
4.1.2 Theory.....	105
4.1.3 Disadvantages.....	105
4.2 Ink Surface Absorption Method (ISAM)	106
4.2.1 Experimental procedure for the ISAM.....	106
4.2.2 Fluids.....	108
4.2.2.1 Fluid used in modelling ISAM results.....	109
5. RESULTS FROM EXISTING AND NOVEL EXPERIMENTAL METHODS AND APPROACHES.....	111
5.1. Characterisation of the particle and void structures of the primary samples.....	111
5.1.1. Characterisation of the particles.....	111
5.1.2. Characterisation of the void structure.....	112
5.1.3. Scanning electron micrographs.....	115
5.1.4. Packing-structure trends for the primary samples.....	121
5.2. Experimental permeation results for the primary samples.....	123
5.2.1. Permeation results from Prufbau Printability Absorption Method (PPAM).....	124
5.2.2. Permeation results from the Ink Stain Density (ISD) test.....	126
5.2.3. Permeation results from the Dynamic Absorption Test (DAT).....	126
5.2.4. Permeation results from the Ink Surface Absorption Method (ISAM).....	128
5.2.5. Permeation results from Gurley Air Resistance Method (Gurley method).....	130
5.2.6. Comparison of permeation results from the primary samples.....	131

5.3. Experimental results from the addition of complementary samples.....	134
5.3.1. Characterisation of void structures.....	134
5.3.2. ISD Permeation results.....	138
5.3.3. DAT Permeation results.....	140
5.3.4. ISAM Permeation results.....	142
5.3.5. Permeation results from the Gurley method.....	143
5.4. Summary of results from primary samples.....	144
5.4.1. Characterisation of the particle and void structures.....	144
5.4.2. Experimental permeation results.....	145
5.5. Summary of results from the addition of complementary samples.....	146
5.5.1. Characterisation of the particle and void structures.....	146
5.5.2. Experimental permeation results.....	146
6. DEVELOPMENT OF THE PORE-COR MODEL.....	148
6.1. Basic Theory.....	148
6.2. New developments in Pore-Cor.....	150
6.3. Porosity algorithm in Pore-Cor.....	160
6.4. Percolation algorithm in Pore-Cor.....	161
6.5. Wetting algorithm in Pore-Cor.....	162
6.6. Absolute permeability algorithm in Pore-Cor.....	165
6.6.1. Capacity term.....	167
6.6.2. Slip correction.....	171
6.7. Matching of the model to the experimental characteristics.....	174
6.7.1. Fit of the simulated to the experimentally measured void properties.....	176
6.8. Comparing the Pore-Cor model to much simpler approaches.....	178
6.9. Summary.....	179
7. COMPUTER MODELLING OF PERMEABILITY.....	181
7.1. Modelling the flow capacity of a non-isometric structure.....	181
7.2. Modelled flow capacity trends.....	189
7.3. Modelling the permeabilities of isotropic and anisotropic structures.....	191
7.4. Permeability results from Pore-Cor and other existing models.....	201
7.5. Comparison of ISD permeation rates with the modelled permeabilities...	202
7.5.1. Ranking of modelled permeabilities to ISD permeation rates.....	205
7.5.2. Comparison of experimental ISD permeation rates with samples of similar surface throat number densities.....	207
7.6. Comparison of DAT permeation rates with the modelled permeabilities..	210

7.6.1. Ranking of modelled permeabilities to DAT permeation rates.....	213
7.6.2. Comparison of experimental DAT permeation rates with samples of similar surface throat number densities.....	214
7.7. Comparison of the Gurley permeability results with the modelled.....	
permeabilities.....	216
7.7.1. Ranking of modelled permeabilities to Experimental Gurley.....	
permeabilities.....	218
7.7.2. Comparison of experimental Gurley permeability with samples of.....	
similar surface throat number densities.....	220
7.8. Summary.....	221
8. COMPUTER MODELLING OF THE WETTING OF COATING STRUCTURES	
.....	224
8.1. Introduction.....	224
8.2. Volume-averaged extent of wetting.....	224
8.2.1. Visual examination of structure.....	228
8.3. The effects of anisotropy on the wetting profile of a structure.....	234
8.3.1. Effects of anisotropy for a slit-like pore structure ($\alpha < 1$)	235
8.3.1.1. The effects of Inertia ignored in the wetting simulation (Lucas-Washburn equation)	237
8.3.1.2. The Effects of inertia included in the wetting simulation (Bosanquet Equation)....	239
8.3.2. Effects of anisotropy for rod-like pore structure ($\alpha > 1$)	246
8.3.2.1. The effects of inertia ignored in the wetting simulations (Lucas-Washburn equation)	249
8.3.2.2. The effects of inertia included in the wetting simulations (Bosanquet equation)	253
8.4. Summary.....	255
9. DISCUSSION OF SIMULATED WETTING AND EXPERIMENTAL TRENDS.....	257
9.1. Comparison of the permeation rates from the Ink Surface Absorption Method (ISAM) with the modelled wetting results.....	257
9.1.1. Comparison of Volume-averaged Pore-Cor distance and the Effective Hydraulic Radius (EHR) model.....	
9.2. Summary.....	264
10. OVERVIEW.....	266
10.1. Hypotheses.....	266

10.2. Experimental methods.....	267
10.3. Samples.....	269
10.4. Results.....	269
10.5. Modelling.....	270
10.6. Results in the context of modelling.....	273
10.7. Implications for design of paper coatings.....	275
10.8. Implications for future work.....	278
APPENDIX.....	280
A. LIST OF SYMBOLS.....	280
A.1. List of abbreviations.....	284
B. TABLES.....	286
B.1. Number density calculations.....	286
B.2. Calculated network permeabilities and optimised Pore-Cor parameters for complementary samples.....	287
C. PORE-COR PROGRAMMING.....	289
C.1. Calculation for the flow capacity of an arc.....	289
C.2. Modelling the permeation of a wetting fluid.....	292
END NOTES.....	308
REFERENCES.....	310

LIST OF FIGURES

Chapter 1

Fig. 1. 1. Example of a porous medium.	7
Fig. 1. 2. The crystallographic axes for an isometric structure (left-hand side) and an example of the different isometric shapes.	9
Fig. 1. 3. An example of the different non-isometric forms.....	10
Fig. 1. 4. Structural formula for Kaolinite mineral.....	13
Fig. 1. 5. Picture of a secondary Kaolin deposit from Georgia, USA (left-hand side) and a scanning electron micrograph image of Kaolin minerals.....	14
Fig. 1. 6. Different types of Calcium Carbonate crystallographic habits.....	15
Fig. 1. 7. Different types of Calcium Carbonate crystallographic habits. Both pictures show an Aragonitic structure with a needle form habit.....	15
Fig. 1. 8. Paper mill from Louisiana, www.ajmeek.com	17
Fig. 1. 9. The impact of new technology on coated paper volume (O'Shea, 1997).	18
Fig. 1. 10. SCA Graphic Sundsvall AB- Ortviken Paper mill, located in Sundsvall, Sweden.	19
Fig. 1. 11. Diagram of the paper production process of SCA Graphic Sundsvall AB- Ortviken Mill, located in Sundsvall, Sweden.	20
Fig. 1. 12. Example of an Off-machine coater (www.repap.com).	22
Fig. 1. 13. Example of a Supercalender machine (www.repap.com).	23

Chapter 2

Fig. 2. 1. Darcy's filtration experiment (Scheidegger, 1974).....	26
Fig. 2. 2. Parabolic velocity flow profile for laminar flow in a cylindrical tube. V_{max} represents the point of maximum velocity, while the walls of the cylinder show a velocity of zero.....	35
Fig. 2. 3. Example of the porous medium represented by the straight capillarc model (Scheidegger, 1974).....	39
Fig. 2. 4. Example of a non-wetting fluid entering a cylindrical tube, presenting some of variables of the Laplace equation.....	46
Fig. 2. 5. Effect of contact angle on imbibition capillary pressure curves for square tubes. The minimum of the pinned arc menisci occurs at a contact angle of	

135°. At this angle the cross-section of the arc menisci becomes semi-circular (Ma <i>et al.</i> , 1996).....	49
Fig. 2. 6. Fraction of tube emptied at constant curvature, C_d , and filled at the minimum imbibition curvature C_i , vs shape factor (Mason <i>et al.</i> , 1991).....	50
Fig. 2. 7. Overview of influences on imbibition from a reservoir (left) into an evacuated capillary tube (Schoelkopf <i>et al.</i> , 2000).....	52
Fig. 2. 8. The one-dimensional approximation.....	57
Fig. 2. 9. A percolation curve, its first derivative, and the corresponding size distribution.....	57
Fig. 2. 10. Network representation of a porous coating (Pan <i>et al.</i> , 1995).....	60
Fig. 2. 11. Erosion of void space – each successive erosion shown darker. b) Identification of pore centres as maxima of erosion contours (false maxima shown grey). c) Partitioned pore space (Toivakka <i>et al.</i> , 2000).....	61
Fig. 2. 12. (a) Computer generated random sphere packing, (b) cross-section through pore space, (c) pore and throat map (Toivakka <i>et al.</i> , 2000).....	62
Fig. 2. 13. Segmented pore structure. Capillary pressure is calculated from the contact angle and radius at the liquid front. The resistance to flow is the sum of the hydraulic radii of the filled pores (Bousfield <i>et al.</i> , 2000).....	63
Fig. 2. 14. Fractal dimensions of (a) 2.49 for mono-disperse and (b) 2.19 for polydisperse packings. Dotted lines show Euclidean behaviour, which was not observed (Kent, 1991).....	64
Fig. 2. 15. Volume uptake as a function of time for the plastic pigment coatings at three latex concentrations (Preston <i>et al.</i> , 2002).....	65
Fig. 2. 16. Computer-generated fibre network structures (Knackstedt <i>et al.</i> , 2000).....	66
Fig. 2. 17. Computer generated fibrous network (Niskanen <i>et al.</i> , 1999).....	67
Fig. 2. 18. Contours of the flow velocity field within a computer-generated fibrous network (Niskanen <i>et al.</i> , 1999).....	68
Fig. 2. 19. Water, shown dark, entering the Pore-Cor unit cell of a compressed ground calcium carbonate (Schoelkopf <i>et al.</i> , 2000).....	71
Fig. 2. 20. Pore-Cor unit cell incorporating double-conical throats (Ridgway <i>et al.</i> , 2001).	72
Fig. 2. 21. Cross-sectional view of a nonwetting fluid entering a double-conical throat (Ridgway <i>et al.</i> , 2001).....	73

Fig. 2. 22. Change in velocity of water (contact angles 0° and 10°) and 1,3-propanediol with distance through a double-conical throat where r , h , and r_{\max} are 0.609, 0.604, and 0.76 μm , respectively (Ridgway <i>et al.</i> , 2001).....	75
--	----

Chapter 3

Fig. 3. 1. Slurry sample of Speswhite: scanning electron micrographs of surface (image on left-hand side) and resin-embedded cross-sectional scan (image on right-hand side). Scale bars: 5 μm for left-hand size image and 2 μm for right hand size image.	84
Fig. 3. 2. Slurry sample of Amazon: scanning electron micrograph of surface scan. Scale bar: 2 μm	85
Fig. 3. 3. Slurry samples of Hydrocarb60 (image on left-hand side) and Hydrocarb90 (image on right-hand side): scanning electron micrographs of surface scan. Scale bar: 2 μm for left-hand side image and 2 μm for right-hand side image.	85
Fig. 3. 4. Slurry samples of OpacarbA40 (image on left-hand side) and OpacarbA60 (image on right-hand side): scanning electron micrographs of surface scan. Scale bar: 2 μm for left-hand side image and 2 μm for right-hand side image.	86
Fig. 3. 5. Slurry sample of Albaglos: scanning electron micrographs of surface scan. Scale bar: 2 μm	86
Fig. 3. 6. Application of the ISIT with the ISD experiments.....	92
Fig. 3. 7. Example of the ink stain obtained from the Speswhite (A) and Amazon (B) coating strips at various elapsed times (shown in minutes).	93
Fig. 3. 8. Comparison of the Setting Rates for coating samples, containing CMC and latex, from ink stain density experiments.	95
Fig. 3. 9. Dynamic Absorption Tester (DAT) showing the instrument (pictured on the left hand side) and the video camera monitor (pictured on the right hand side).....	95
Fig. 3. 10. A number of images at different time intervals of a fluid droplet applied to an Amazon clay coating surface.....	96
Fig. 3. 11. DAT permeation curves for the primary samples, showing the surface angle of the droplet with time.....	97

Chapter 4

Fig. 4. 1. Picture of the Prufbau Printability tester (PPT).	104
Fig. 4. 2. Use of the ISIT in a novel way.	106
Fig. 4. 3. Amount of oil transferred from gravure roller to Amazon coating for a range of contact pressures, at a contact speed of 0.5 m/s.	108

Chapter 5

Fig. 5. 1. The median particle diameter and the width of the particle size distribution of the four samples, analysed by sedimentation.....	112
Fig. 5. 2. Uncorrected, corrected and fully-corrected mercury intrusion curves for Amazon.	113
Fig. 5. 3. Fully-corrected mercury intrusion curves of the four samples, and conversion of the applied pressure to an effective throat entry diameter.....	114
Fig. 5. 4 The median throat size diameter and the width of the void size distribution of the four samples.	114
Fig. 5. 5. The porosity and surface area of the four samples.....	115
Fig. 5. 6. Speswhite-CL: scanning electron micrographs of surface scan. Scale bar: 2 μ m.	116
Fig. 5. 7. Speswhite-CL: scanning electron micrographs of resin-embedded cross-sectional scan. Scale bar: 5 μ m.....	116
Fig. 5. 8. Amazon-CL: scanning electron micrographs of surface scan. Scale bar: 2 μ m.	117
Fig. 5. 9. Amazon-CL: scanning electron micrographs of resin-embedded cross-sectional scan. Scale bar: 5 μ m.....	117
Fig. 5. 10. OpacarbA40-CL: scanning electron micrographs of surface scan. Scale bar: 2 μ m.	118
Fig. 5. 11. OpacarbA40-CL: scanning electron micrographs of resin-embedded cross-sectional scan. Scale bar: 5 μ m.	118
Fig. 5. 12. Albaglos-CL: scanning electron micrographs of (a) surface scan. Scale bar: 2 μ m.	119
Fig. 5. 13. Albaglos-CL: scanning electron micrographs of resin-embedded cross-sectional scan. Scale bar: 5 μ m.....	120
Fig. 5. 14. Packing structure trends for the primary samples.....	122

Fig. 5. 15. Results from the PPAM showing the percent volume uptake of oil and the percent saturation for the samples from the printing strips.	125
Fig. 5. 16. Saturation rate for all four coating samples, measured from the Ink stain density curves. The results are also termed as the ISD permeation rate. ...	126
Fig. 5. 17. DAT permeation curves for the primary samples, showing the change in height of the droplet normalized to surface area over an elapsed wetting time.	127
Fig. 5. 18. Change in normalized height for the droplet of oil at 0.4s for all four coating samples. The result is measured from the use of the DAT instrument, and is termed as the DAT permeation rate.	127
Fig. 5. 19. Amount of oil transferred from gravure roller to coating samples at 100N contact pressure.	128
Fig. 5. 20. Results of Figure 5.20 corrected for film transfer and with respect to absolute contact time.	129
Fig. 5. 21. ISAM permeation rate of the primary samples at 0.002s contact time.	129
Fig. 5. 22. Gurley permeability measurements varying with coat weight. The % standard error was calculated to be between 1 to 5% for the Gurley permeability measurements of each sample (refer to Table 5.6). Error bars were therefore not shown on the curves as they would be too small in size to be clearly visible.	130
Fig. 5. 23. Gurley permeability measurements at a coat weight of 11 g/m ²	131
Fig. 5. 24. Comparison of the permeation results from the ISD and DAT methods with the Experimental number density of each sample.	132
Fig. 5. 25. Comparison of the permeation results from the ISAM and the Gurley methods with the Experimental number density of each sample.	133
Fig. 5. 26. Fully corrected mercury intrusion curves of coating samples, comprising of a mineral pigment with CMC and latex.	134
Fig. 5. 27. Fully corrected mercury intrusion curves of coating samples, comprising of a mineral pigment with starch and latex.	135
Fig. 5. 28. Median throat size diameter, d ₅₀ , for the CMC and latex and the starch and latex samples.	136
Fig. 5. 29. Width of throat size distribution for the CMC and latex and the starch and latex samples.	136
Fig. 5. 30. Porosity measurements for the CMC and latex and the starch and latex samples.	137

Fig. 5. 31. Comparison of the Setting Rates for coating samples, containing CMC and latex, from ink stain density experiments.....	138
Fig. 5. 32. Comparison of the Setting Rates for coating samples, containing starch and latex, from ink stain density experiments.....	139
Fig. 5. 33. Saturation rate for pigment coating colours containing CMC and latex and starch and latex. The rate, measured from the Ink stain density curves, is also termed the ISD permeation rate.....	140
Fig. 5. 34. DAT permeation curves for the Kaolin and PCC coating samples, showing the change in height of the droplet normalized to surface area over an elapsed wetting time.....	141
Fig. 5. 35. Change in normalized height for the droplet of oil at 0.4s for all Kaolin and PCC coatings containing CMC and latex.....	141
Fig. 5. 36. ISAM permeation results for the primary and complementary samples. The results were corrected for film transfer and were performed at 100N contact pressure.....	142
Fig. 5. 37. ISAM permeation rate of the primary and complementary samples at 0.002s contact time.	143
Fig. 5. 38. Gurley permeability measurements at a coat weight of 11 g/m ²	144

Chapter 6

Fig. 6. 1. Example of a pore and throat size distribution for a pore skew value of 2 and a throat skew value of 0.8. The throat size distribution shows a minimum and maximum throat diameter of 0.0036µm and 2.4µm, respectively.	149
Fig. 6. 2. Example of Anisotropic Structure showing throats with elliptic cross-sections and plate-like pores with rectangular cross-sections. Aspect factor equals 0.4.....	151
Fig. 6. 3. Example of Anisotropic Structure showing throats with elliptic cross-sections and rod-like pores with rectangular cross-sections. Aspect factor equals 2.1.....	152
Fig. 6. 4. Horizontally-banded structure #1. The brown squares represent the pores, while the blue cylinders represent the throats.....	153
Fig. 6. 5. Horizontally-banded structure #2. The brown squares represent the pores, while the blue cylinders represent the throats.....	154
Fig. 6. 6. Horizontally-banded structure #3. The brown squares represent the pores, while the blue cylinders represent the throats.....	155

Fig. 6. 7. Simulated mercury intrusion curves for the three horizontally-banded structures shown in Fig. 6.4, 6.5 and 6.6. The parameters for the simulated structures are for a connectivity of 2.4, throat skew of 1, correlation level of 1, porosity of 7.5%, and a minimum and maximum throat diameter of approximately 2.3 μm and 0.0036 μm , respectively.	156
Fig. 6. 8. Same as Fig. 6.7, except the x-axis is represented by the equivalent throat diameter.	156
Fig. 6. 9. Horizontally-banded structure #1. A simulated partial fill of mercury at an applied pressure of about 14 MPa (equivalent throat diameter of approximately 0.1 μm). The grey colour represents the intrusion of mercury into the top surface of the void structure; the blue represents the throats and the brown the pores.	157
Fig. 6. 10. Horizontally-banded structure #2. A simulated partial fill of mercury at an applied pressure of about 145 MPa (equivalent throat diameter of approximately 0.01 μm). The grey colour represents the intrusion of mercury into the top surface of the void structure; the blue represents the throats and the brown the pores.	158
Fig. 6. 11. Horizontally-banded structure #2. A simulation for an applied mercury pressure of about 296 MPa (equivalent throat diameter of approximately 0.005 μm). The grey colour represents the intrusion of mercury into the void structure.	159
Fig. 6. 12. Schematic diagram of an arc. Representation of an isotropic structure showing cylindrical throats and cubic pores.	168
Fig. 6. 13. Schematic diagram of an arc. Representation of an anisotropic structure showing elliptical throats and a rectangular pores (slit-like or rod-like pores).	170
Fig. 6. 14. Experimental and simulated mercury intrusion curves for the clay coating samples.	177
Fig. 6. 15. Experimental and simulated mercury intrusion curves for the PCC coating samples.	178

Chapter 7

Fig. 7. 1. The volumetric flow rate of a pore (Q_{pore}) and throat (Q_{throat}) in the x-y direction.	182
---	-----

Fig. 7. 2. Volumetric flow rate (Q) in the x or y direction, showing the typical size dimensions for the pore and throat, when $\alpha=10$.	183
Fig. 7. 3. The volumetric flow rate (Q) in the x and y direction when L_a and L_b are held constant with respect to L_c .	184
Fig. 7. 4. The volumetric flow rate, Q , of a pore and throat in the $-z$ direction.	185
Fig. 7. 5. Volumetric flow rate (Q) in the $-z$ direction, showing the typical size dimensions for the pore and throat, when $\alpha=10$.	186
Fig. 7. 6. The flow capacity of an Arc (F_{arc}) in the $\pm x$, $\pm y$ or $-z$ direction.	187
Fig. 7. 7. Simulated liquid permeabilities at various aspect factors for two stochastic generations. All other parameters are held constant and are as follows: Random structure, Connectivity=5, pore-skew=2, throat skew=1, minimum throat diameter=3.6e-3 μ m, maximum throat diameter 2.4 μ m.	188
Fig. 7. 8. Flow capacity modelling trends in $\pm x$ and $\pm y$ direction. The abbreviations in the legend are deciphered as follows: 'eff diam' refers to effective diameter, 'thr ht' refers to throat height, p-t ratio refers to pore-throat ratio.	189
Fig. 7. 9. Flow capacity modelling trends in the $-z$ direction. The abbreviations in the legend are deciphered as follows: 'eff diam' refers to effective diameter, 'thr ht' refers to throat height, p-t ratio refers to pore-throat ratio.	190
Fig. 7. 10. OpacarabA40-CL. Permeability changes with stochastic generation number at aspect factors 1.5 and 1.0.	195
Fig. 7. 11. Albaglos-CL. Permeability changes with stochastic generation number at aspect factor of 1.0.	195
Fig. 7. 12. Speswhite-CL. Permeability changes with stochastic generation number at aspect factors 1.0 and 0.6.	196
Fig. 7. 13. Speswhite-CL. Permeability changes with stochastic generation number at aspect factors 1.0 and 0.1.	196
Fig. 7. 14. Amazon-CL. Permeability changes with stochastic generation number at aspect factors 1.0 and 0.8.	197
Fig. 7. 15. Calculated geometric means of the network permeabilities for each sample, at their chosen and isotropic aspect factors.	197
Fig. 7. 16. Speswhite-CL. Network permeabilities of liquid, methane and nitrogen gas with stochastic generation number, at $\alpha=1.0$.	199
Fig. 7. 17. Speswhite-CL. Network permeabilities of liquid, methane and nitrogen gas with stochastic generation number, at $\alpha=0.6$.	199
Fig. 7. 18. The mean connectivity and throat skew of the four samples.	201

Fig. 7. 19. Comparison of the simulated permeabilities of the four samples from the three Pore-Cor models. The experimental ISD permeation rates of the four samples were graphed on the secondary y axis.....	203
Fig. 7. 20. Comparison of the simulated permeabilities of the four samples from the Kozeny and Aligned cylinders models. The experimental ISD permeation rates of the four samples were graphed on the secondary y axis.....	204
Fig. 7. 21. The ranking scheme between samples for the ISD permeation rates and the permeability models.....	206
Fig. 7. 22. Modelling trend error on the calculated permeabilities for the ISD permeation rates.....	207
Fig. 7. 23. Amazon-SL: scanning electron micrographs of surface scan. Scale bar: 2µm. The number density of surface throats was calculated to be 3.16 µm ⁻¹	209
Fig. 7. 24. Comparison of the calculated liquid permeability and the experimental ISD permeation rate for Amazon-CL and Amazon-SL, using an aspect factor of 0.6 for both samples.	210
Fig. 7. 25. Comparison of the simulated permeabilities of the four samples from the three Pore-Cor models. The DAT permeation rates of the four samples were graphed on the secondary y axis.....	211
Fig. 7. 26 Comparison of the simulated permeabilities of the four samples from the Kozeny, Kozeny-Carman and the Aligned cylinders models. The experimental DAT permeation rates of the four samples were graphed on the secondary y axis.....	212
Fig. 7. 27. The ranking scheme between samples for the experimental DAT permeation rates and the permeability models. The anisotropic Pore-Cor model with correction factor is shown to give a better qualitative prediction than any other model.....	213
Fig. 7. 28. The modelling trend errors for the DAT permeation rates. The anisotropic Pore-Cor model with correction factor has a zero modelling trend error – i.e. it is shown to give a perfect prediction.....	214
Fig. 7. 29. OpacarbA60-CL: scanning electron micrographs of surface scan. Scale bar: 2µm. The number density of surface throats was calculated to be 2.87 µm ⁻¹	215
Fig. 7. 30. Comparison of the calculated liquid permeability and the experimental DAT permeation rate for OpacarbA40-CL and OpacarbA60-CL, using an aspect factor of 1.5 and 2.0, respectively.	216

Fig. 7. 31. Comparison of the simulated nitrogen gas permeabilities from the three Pore-Cor models for three of the four samples. The experimental Gurley permeability of the three samples were graphed on the secondary y axis...	217
Fig. 7. 32. Comparison of the simulated permeabilities for three of the four samples from the Kozeny, Kozeny-Carman and the Aligned cylinders models. The experimental Gurley permeability of the three samples was graphed on the secondary y axis.....	217
Fig. 7. 33. The ranking scheme between samples for the experimental Gurley permeabilities and the permeability models. The anisotropic Pore-Cor model with correction factor is shown to give a better qualitative prediction than any other model.....	219
Fig. 7. 34. The modelling trend error for the experimental Gurley permeabilities. The anisotropic Pore-Cor model with correction factor has a zero modelling trend error – i.e. it is shown to give a perfect prediction.....	219
Fig. 7. 35. Comparison of the calculated nitrogen gas permeabilities from the Anisotropic Pore-Cor model and the experimental Gurley permeabilities for OpacarbA40-CL and OpacarbA60-CL, using an aspect factor of 1.5 and 2.0, respectively.....	220

Chapter 8

Fig. 8. 1. Simulated absorption of oil per unit area ($\mu\text{m}^3/\mu\text{m}^2$) for aspect factors from 0.01 to 2.0 for the Speswhite-CL sample, up to an elapsed wetting time of 1 millisecond.....	225
Fig. 8. 2. Simulated absorption of oil per unit area ($\mu\text{m}^3/\mu\text{m}^2$) for aspect factors of 0.01, 0.6 and 1.0 for the Speswhite-CL sample, up to an elapsed wetting time of 1 millisecond, showing steps due to filling of successive layers.	226
Fig. 8. 3. Simulated absorption of oil per unit area ($\mu\text{m}^3/\mu\text{m}^2$) for the clay coating samples, Speswhite-CL and Amazon-CL, at their estimated ($\alpha=0.6$ and 0.8 , respectively) and isotropic ($\alpha=1$) aspect factors, and up to an elapsed wetting time of 0.1 seconds.....	227
Fig. 8. 4. The amount of oil absorbed for the PCC samples, OpacarbA40-CL and Albaglos-CL, at their estimated ($\alpha=1.5$ and 1.0 , respectively) and isotropic ($\alpha=1$) aspect factors.....	228
Fig. 8. 5. Simulation of the absorption of oil into Speswhite-CL at 0.1 seconds, and at an aspect factor=0.6. Red voids are empty of wetting fluid, dark blue voids	

are full, and intermediate colours are allocated on a logarithmic scale, as shown on the colour bar.	229
Fig. 8. 6. Detail of Fig. 8.5, showing permeation into Speswhite-CL at 0.1 seconds.	230
Fig. 8. 7. The permeation of Amazon-CL sample at 0.1 seconds.	231
Fig. 8. 8. Simulation of the absorption of oil into OpacarbA40-CL at 0.1 seconds, and at an aspect factor=1.5. Colours as fig. 8.17.	232
Fig. 8. 9. The permeation of Albaglos-CL sample at 0.1 seconds.	233
Fig. 8. 10. Detail of Fig. 8.8, showing permeation into OpacarbA40-CL at 0.1 seconds.	234
Fig. 8. 11. Simulated permeation curves for Speswhite-CL at its estimated ($\alpha=0.6$) and isotropic ($\alpha=1.0$) aspect factor, and also shows the results when applying the Lucas-Washburn or the Bosanquet equation.	235
Fig. 8. 12. Simulated Darcy length curves for Speswhite-CL at its estimated ($\alpha=0.6$) and isotropic ($\alpha=1.0$) aspect factor, and also shows the results when applying the Lucas-Washburn or the Bosanquet equation.	236
Fig. 8. 13. Simulated absorption of oil into Speswhite-CL control (isotropic aspect factor) at 0.1 seconds, but ignoring inertial effects (Lucas-Washburn equation).	238
Fig. 8. 14. Simulated absorption of oil into Speswhite-CL at its estimated aspect factor ($\alpha=0.6$) at 0.1 seconds, but ignoring inertial effects (Lucas-Washburn equation).	239
Fig. 8. 15. Simulated absorption of oil into Speswhite-CL control ($\alpha=1$) at 0.1 seconds, including inertial effects (Bosanquet equation).	240
Fig. 8. 16. Simulated absorption of oil into Speswhite-CL at its estimated aspect factor ($\alpha=0.6$) at 0.1 seconds, including inertial effects (Bosanquet equation).	241
Fig. 8. 17. Detail of Fig. 8.14.	242
Fig. 8. 18. Simulated absorption of oil into Speswhite-CL at its estimated aspect factor ($\alpha=0.6$) at 1 millisecond, including inertial effects (Bosanquet equation).	243
Fig. 8. 19. Simulated absorption of oil into Speswhite-CL at its isotropic aspect factor ($\alpha=1.0$) at 1 millisecond, including inertial effects (Bosanquet equation).	244

Fig. 8. 20. Simulated absorption of oil into Speswhite-CL at its estimated aspect factor ($\alpha=0.6$) at 1 millisecond, including inertial effects (Bosanquet equation). The back of the structure is shown in the figure, and it is brightened by a 'headlamp' for better visibility.....	245
Fig. 8. 21. Simulated absorption of oil into Speswhite-CL at its estimated aspect factor ($\alpha=0.6$) at 1 millisecond, including inertial effects (Bosanquet equation). The back of the structure is shown in the figure, and it is brightened by a 'headlamp' for better visibility.....	246
Fig. 8. 22. Simulated permeation curves for OpacarbA40-CL at its estimated ($\alpha=1.5$) and isotropic ($\alpha=1.0$) aspect factor, and also shows the results when applying the Lucas-Washburn or the Bosanquet equation.	247
Fig. 8. 23. Simulated Darcy length curves for OpacarbA40-CL at its estimated ($\alpha=1.5$) and isotropic ($\alpha=1.0$) aspect factor, and also shows the results when applying the Lucas-Washburn or the Bosanquet equation.	248
Fig. 8. 24. Simulated absorption of oil into OpacarbA40-CL using the isotropic aspect factor ($\alpha=1.0$) at 0.1 seconds, but ignoring inertial effects (Lucas-Washburn equation).	249
Fig. 8. 25. Simulated absorption of oil into OpacarbA40-CL using the estimated aspect factor ($\alpha=1.5$) at 0.1 seconds, but ignoring inertial effects (Lucas-Washburn equation).	250
Fig. 8. 26. Simulated absorption of oil into OpacarbA40-CL applying the isotropic aspect factor ($\alpha=1.0$) at 0.1 seconds, but ignoring inertial effects (Lucas-Washburn equation). The structure is rendered into a wire frame in which the voids containing any amount of fluid are outlined with a blue colour, while voids containing no fluid are outlined with a red colour.	251
Fig. 8. 27. Simulated absorption of oil into OpacarbA40-CL applying the estimated aspect factor ($\alpha=1.5$) at 0.1 seconds, but ignoring inertial effects (Lucas-Washburn equation). The structure is rendered into a wire frame in which the voids containing any amount of fluid are outlined with a blue colour, while voids containing no fluid are outlined with a red colour.	252
Fig. 8. 28. Simulated absorption of oil into OpacarbA40-CL showing an isotropic structure ($\alpha=1.0$) at 0.1 seconds, including inertial effects (Bosanquet equation).....	253

Fig. 8. 29. Simulated absorption of oil into OpacarbA40-CL using the estimated aspect factor ($\alpha=1.5$) at 0.1 seconds, including inertial effects (Bosanquet equation).....	254
Chapter 9	
Fig. 9. 1. The modelled absorption rates of the four coatings, before applying the correction factor, compared to the experimental absorption rates at a time, t , of approximately 0.002s. The modelled absorption rate is measured in $\mu\text{m}^3/\mu\text{m}^2/\text{s}$ at the respective estimated aspect factors, while the experimental absorption rate is measured in g/s.....	258
Fig. 9. 2. The modelled absorption rates of the four coatings, after applying the correction factor, compared to the experimental absorption rates at a time, t , of approximately 0.002s. The modelled absorption rate is measured in $\mu\text{m}^3/\mu\text{m}^2/\text{s}$ and at their respective estimated aspect factors, while the experimental absorption rate is measured in g/s.	259
Fig. 9. 3. Ranking of ISAM and modelled absorption rates between samples	260
Fig. 9. 4. Modelling trend error for each of the absorption models.....	261
Fig. 9. 5. Distance travelled by a wetting front, from the absorption of oil after 0.002 s. The modelled Darcy length calculated from the Effective hydraulic radius (EHR) model has been scaled down by one order of magnitude, and the ISAM absorption rate has been graphed on the secondary y-axis.	262
Fig. 9. 6. Ranking of ISAM absorption rates and the modelled Darcy lengths between samples.....	263
Fig. 9. 7. Modelling trend error of the calculated Darcy distances on the ISAM absorption rates.....	264

LIST OF TABLES

Chapter 2

Table 2. 1. Representative values of permeability for various substances (Scheidegger, 1974).....	31
---	----

Chapter 5

Table 5. 1. Characteristics of particles and voids in coating samples. * represents the value estimated visually. See Section 3.2 for definitions of parameters.	111
Table 5. 2. Characteristics of void structure in coating samples. See Section 3.2 for definitions of parameters.	113
Table 5. 3. Estimates of number density of surface throats and the correction factor, F , used for each sample.	121
Table 5. 4. Experimental permeation results from the three experiments.....	124
Table 5. 5. Characteristics of void structure for the coating samples containing CMC and latex and starch and latex. See Section 3.2 for definitions of parameters.	135
Table 5. 6. Permeation results from Gurley method.	143

Chapter 6

Table 6. 1. The resulting values of aspect factor, f , used for each sample, and the estimates of number density of surface throats and the correction factor, f , used for each sample.	175
Table 6. 2. The Pore-Cor fitting parameters used to generate the simulated structures for each sample.	177

Chapter 7

Table 7. 1. The optimised Pore-Cor parameters for Speswhite-CL, for an isotropic aspect factor ($\alpha=1$), at each stochastic generation. The Calculated liquid permeabilities and its mean, median and geometric mean are also calculated.	192
--	-----

Table 7. 2. The optimised Pore-Cor parameters for Speswhite-CL, for a chosen aspect factor of $\alpha=0.6$, at each stochastic generation. The Calculated network permeabilities and its mean, median and geometric mean are also calculated.	192
Table 7. 3. The optimised Pore-Cor parameters for Speswhite-CL, for a lower aspect factor of $\alpha=0.1$, at each stochastic generation. The Calculated network permeabilities and its mean, median and geometric mean are also calculated.	192
Table 7. 4. The optimised Pore-Cor parameters for Amazon-CL, for an isotropic aspect factor ($\alpha=1$), at each stochastic generation. The Calculated network permeabilities and its mean, median and geometric mean are also calculated.	193
Table 7. 5. The optimised Pore-Cor parameters for Amazon-CL, for a chosen aspect factor of $\alpha=0.8$, at each stochastic generation. The Calculated network permeabilities and its mean, median and geometric mean are also calculated.	193
Table 7. 6. The optimised Pore-Cor parameters for OpacarbA40-CL, for an isotropic aspect factor ($\alpha=1$), at each stochastic generation. The Calculated network permeabilities and its mean, median and geometric mean are also calculated.	193
Table 7. 7. The optimised Pore-Cor parameters for OpacarbA40-CL, for a chosen aspect factor of $\alpha=1.5$, at each stochastic generation. The Calculated network permeabilities and its mean, median and geometric mean are also calculated.	194
Table 7. 8. The optimised Pore-Cor parameters for Albaglos-CL, for an isotropic aspect factor ($\alpha=1$), at each stochastic generation. The Calculated network permeabilities and its mean, median and geometric mean are also calculated.	194
Table 7. 9. Statistical paired t-test and the mean liquid permeability results for the four samples at their chosen and isotropic aspect factors. A significant difference between the mean permeabilities is observed within 95% confidence level, if the absolute value of t is greater than the value of t critical two-tail.	198
Table 7. 10 Calculated permeabilities for the primary samples, from using the Pore-Cor models and other existing models.	202

Chapter 9

Table 9. 1. Wetting measurements from the different versions of the Pore-Cor model and the Effective Hydraulic Radius (EHR) model, comparing the absorption rates and the Darcy lengths of the primary samples.....	258
---	-----

Appendix

Table B. 1. The total number of surface throats in each of the samples.....	286
Table B. 2. The number density calculations for each of the samples.....	286
Table B. 3. The optimised Pore-Cor parameters for OpacarbA60-CL, for a chosen aspect factor of $\alpha=2.0$, at each stochastic generation. The Calculated liquid permeabilities and its mean, median and geometric mean are also calculated.	287
Table B. 4. The optimised Pore-Cor parameters for Amazon-SL, for a chosen aspect factor of $\alpha=0.80$, at each stochastic generation. The Calculated liquid permeabilities and its mean, median and geometric mean are also calculated.	287

LIST OF EQUATIONS

Chapter 2

Eq. 2. 1	27
Eq. 2. 2	27
Eq. 2. 3	27
Eq. 2. 4	27
Eq. 2. 5	28
Eq. 2. 6	28
Eq. 2. 7	29
Eq. 2. 8	29
Eq. 2. 9	34
Eq. 2. 10	35
Eq. 2. 11	36
Eq. 2. 12	39
Eq. 2.13	39
Eq. 2. 14	40
Eq. 2. 15	40
Eq. 2. 16	40
Eq. 2. 17	40
Eq. 2. 18	41
Eq. 2. 19	41
Eq. 2. 20	42
Eq. 2. 21	43
Eq. 2. 22	43
Eq. 2. 23	43
Eq. 2. 24	44
Eq. 2. 25	45
Eq. 2. 26	48
Eq. 2. 27	48
Eq. 2. 28	51
Eq. 2. 29	59
Eq. 2. 30	63
Eq. 2. 31	63
Eq. 2. 32	64

Eq. 2. 33	68
Eq. 2. 34	69
Eq. 2. 35	70

Chapter 3

Eq. 3. 1	91
Eq. 3. 2	94
Eq. 3. 3	97
Eq. 3. 4	98
Eq. 3. 5	99
Eq. 3. 6	100
Eq. 3. 7	100
Eq. 3. 8	101
Eq. 3. 9	101
Eq. 3. 10	101
Eq. 3. 11	102
Eq. 3. 12	102
Eq. 3. 13	102

Chapter 6

Eq. 6. 1	160
Eq. 6. 2	160
Eq. 6. 3	161
Eq. 6. 4	161
Eq. 6. 5	162
Eq. 6. 6	163
Eq. 6. 7	163
Eq. 6. 8	163
Eq. 6. 9	163
Eq. 6. 10	163
Eq. 6. 11	164
Eq. 6. 12	165
Eq. 6. 13	165
Eq. 6. 14	166

Eq. 6. 15	166
Eq. 6. 16	166
Eq. 6. 17	167
Eq. 6. 18	168
Eq. 6. 19	168
Eq. 6. 20	169
Eq. 6. 21	169
Eq. 6. 22	169
Eq. 6. 23	170
Eq. 6. 24	170
Eq. 6. 25	171
Eq. 6. 26	171
Eq. 6. 27	172
Eq. 6. 28	172
Eq. 6. 29	172
Eq. 6. 30	173
Eq. 6. 31	173
Eq. 6. 32	173
Eq. 6. 33	173
Eq. 6. 34	176

Chapter 7

Eq. 7. 1	206
----------------	-----

ACKNOWLEDGEMENTS

I wish to express my sincere gratitude to my supervisor, Dr. Peter Matthews, and Dr. John Kettle, of SCA Graphic Research AB, for their continuous support, encouragement and friendship throughout the course of this work.

I wish to thank Sven Lohmander, of STFi, for his academic support and assistance throughout the project. I would like to give special thanks to Dr. Pat Gane, of Omya AG, for all his advice and enthusiasm towards the project. Many thanks are given for the advice and assistance provided by Edward Seyler of SeGan Ltd, for the development of the ISIT oil absorption procedures. I wish to express my gratitude to Mikael Bouveng, of STFi, for his assistance in my research, and for his friendship during my visit to Stockholm. I would like to thank the researchers at SCA Graphic Research AB for all their assistance throughout my project, and making my stay in Sundsvall a pleasure. I thank Dr. Joachim Schoelkopf and Dr. Cathy Ridgway, of Omya AG, for their support, for many helpful discussions, for the confocal microscopy and for the wetting contact angle measurements. I would also like to give my appreciation to Alexander Matthews for creating the virtual reality world of Pore-Cor, used to generate the graphics.

I would like to give special thanks to my research colleagues, Anthony Johnson, Maurizio Laudone, Debbie Holtham and Dr. Ian Roy, for all the support and assistance at the University of Plymouth, and I will value the friendships that I have gained throughout my work. They all contributed in some manner in making my time in Plymouth most enjoyable.

I wish to express my sincere thanks to Ruth Adams and her family for all their support, love and encouragement. I wish to thank my brother and my sister for always being there for me. Last, but certainly not least, I would like to express my sincere thanks to my parents without whom none of this would have been possible. I am forever indebted to them, and I wish to thank them for always believing in me.

AUTHOR'S DECLARATION

At no time during the registration for the degree of Doctor of Philosophy has the Author been registered for any other University award.

This project was funded by the University of Plymouth Science Faculty from its block research grant, with additional support from SCA Graphic Research AB, Sundsvall, Sweden. Assistance in this project was also given by STFi, Sundsvall, Sweden.

Relevant scientific seminars and conferences were regularly attended at which work was often presented; external research centers and institutions were visited for consultation purposes and several papers prepared for publication.

Signed..... *Paul Babiak*

Date..... *June 26, 2003*

PUBLICATIONS, CONFERENCES AND TRAINING

Presentations and conferences attended

Tappi Advanced Coating Fundamentals Symposium, April 30-May 1, 1999
Toronto, Canada. Attended.

"Cleaner Paper-Coating Technology: Novel Experimental and Computational Techniques for the Optimisation of the Permeation Properties of Environmentally-Friendly Pigment Coatings", School of Environmental Science, University of Plymouth; April 2000. Oral presentation.

"Optimising Binders and Pigments for the Permeation Properties of Paper Coatings", *Paper and Coating Chemistry Symposium 2000*, Stockholm, Sweden, June 2000. Oral presentation.

"Optimising binders and pigments for the permeation properties of paper coatings", *10th International Conference On Colloid and Interface Science*, Bristol, UK; July 24, 2000. Oral presentation.

"Fluid Permeation into Porous Coatings", IMERYS Minerals Ltd, St. Austell, UK. December 5, 2000. Oral presentation.

"The influence of structural anisotropy on fluid permeation in porous media", *2001 Advanced Coating Fundamentals Symposium*. May 4, 2001; Tappi, San Diego, USA. Oral presentation.

"Particle Coatings in Paper Making: The Effects of Structural Anisotropy on the Permeation of Fluids". *Royal Society of Chemistry Annual Conference 2001*. Birmingham, UK, July 2001. Oral presentation

"Modelling Flow In Oil Reservoirs". *The institute of Mathematics and its Applications (IMA) Conference*, University of Cambridge, Cambridge, UK, 2002. Attended.

"Investigation and manipulation of Soil structure". *British Soil Water Physics Group conference 2003*. University of Plymouth, Plymouth, UK, May 2003. Attended.

Publications

Bodurtha, P., Matthews, G. P., Kettle, J. P., Lohmander, S., and James, P. W., "The influence of structural anisotropy on fluid permeation in porous media". *Proceedings of the Advanced Coating Fundamentals Symposium*. San Diego, USA: Tappi Press. 2001, p. 393-438.

Bodurtha, P.A., Matthews, G.P., Kettle, J.P and Roy, I., "Influence of anisotropy on the dynamic wetting and permeation of paper coatings". *Journal of Colloid and Interface Science*. Submitted. 2003.

Bodurtha, P.A., Matthews, G.P., Kettle, J.P and Roy, I., *Transport in porous media*. *In prep.*, 2003

Training

External training on numerous analytical instruments relevant to the printing and graphics paper industry was performed at STFi (Stockholm, Sweden), SCA Graphic Research AB (Sundsvall, Sweden), and at SeGan Ltd. (Lostwithiel, Cornwall, UK). All other training was performed at the Environmental and Fluid Modelling Group, University of Plymouth.

Previous academic accolades

Degrees:

B.Sc. (Honours) - Environmental Geology
Queen's University (Kingston, Canada)

M.Sc. (Geology) - Specializing in Environmental and aqueous geochemistry
McMaster University (Hamilton, Canada)

Publications

Bodurtha, P., Brassard, P., "neutralization of acid by steel-making slags".
Environmental Technology, 2000, **21**, p. 1271-1281.

Brassard, P., Bodurtha, P., "A feasible set for chemical speciation problems".
Computers & Geosciences, 2000, **26**, p. 277-291.

1. INTRODUCTION

1.1. Structure of thesis

The structure of this thesis is divided into three main components; experimental, modelling, and comparison of experimental and modelling trends. Each main component is divided into two sections. The experimental component is divided into the results from both the existing and the novel experimental methods, and the modelling component is divided into the development of a new computer model and the application of the new model. The third component is divided into a comparison of experimental trends with simulated permeability trends and simulated wetting trends.

The Introduction chapter will describe the background of the project, its hypotheses, scientific terms and definitions, crystallography, the industrial background and the environmental implications of the project. The fundamental scientific background and the review of relevant scientific literature are presented after the Introduction (Chapter 2). A section on the difficulties and problems arising from attempting to prove the thesis hypotheses are presented at the end of this chapter. The literature review should enable the reader to gain a general understanding on the theoretical and practical difficulties in attempting to prove these hypotheses. A summary of the key points from the results and discussion chapters (Chapter 5, 7-9), and from the 'Development of the new Pore-Cor model' chapter (Chapter 6), is presented at the end of each of these chapters. An overview of the work is presented at the end of the thesis (Chapter 10), and includes a section on the implications for the design of paper coatings and for future work. Appendix A provides a list of symbols and abbreviations. Appendix B

lists additional tables, and Appendix C provides some of the FORTRAN code written for this project.

1.2. Background of project

In this study, we have investigated the effects of the structural anisotropy of porous media on the permeation of fluids. The motivation for the work was an increased understanding of the permeation of printing ink into paper coatings, which often contain platey particles which have usually been aligned during the coating process. However, the findings are also relevant to other systems, such as the subterranean migration of fluids, including pollutants within substances such as shale which contain particles of high aspect ratio (Sherwood, 1994).

The research was driven by a number of major advances in the graphic printing and paper industry, namely:

- The development of high performance paper coatings for high-speed, high quality offset and ink-jet printing.
- The development of advanced computational methods for the modelling of paper coatings and the permeation of ink into paper coatings.
- The development of a novel technique for measuring permeation from the use of an ink-tack testing apparatus (Gane *et al.*, 1994).

1.3. Rationale and aim of project

1.3.1. Thesis Hypotheses

A General set of hypotheses for this project has been formulated for testing:

1. That highly controlled application of fluid, using an experimental technique with minimal unknown parameters, can provide useful insights into the effect of void structure on printability.
2. That computer modelling of the behaviour of fluids in porous media can shed new light on the complicated relationship between permeation, void structure and properties.
3. That computer modelling can allow anisotropy to be isolated from other characteristics of void structure, and hence explain effects which are otherwise intractable.

Sub-hypotheses have also been formulated, namely that the permeation of a fluid into anisotropic void structures can be modelled:

1. Successfully, as judged by
 - a. A close fit to experimental percolation characteristics and porosity.
 - b. Better explanation of trends in permeation experiments than using either a straight aligned-tubes model or an isotropic three-dimensional network.

2. Usefully, as judged by
 - a. Explanatory and predictive capabilities.

1.3.2. Thesis Objectives

The objectives of the study, derived directly from the hypotheses and sub-hypotheses listed above, have been pursued by experimentation and modelling of the paper coating samples.

From the experimental side, five methods were used for measuring liquid permeation properties:

1. Ink stain density (ISD) test, involving the use of an Ink Surface Interaction Tester (ISIT)¹. This test indirectly measures rate of ink absorption from an optical measure of a change in reflectance factor of the ink stain on the coating surface (Bristow *et al.*, 1982).
2. Dynamic Absorption Tester (DAT)². The absorption of the test liquid is indirectly measured as the rate of change of the contact angle with the paper substrate as a function of time (Technical Association of the Pulp and Paper Industry, 2002).
3. Gurley permeameter³. This instrument measures the air permeability of a paper structure (Institute of Paper Science & Technology, 1940).
4. Development of a new test protocol, involving the use of the Prufbau Printability tester (PPT)⁴ and referred to as the 'Prufbau Printability Absorption Method (PPAM)'.

5. Development of a new test protocol, also involving the use of an ISIT and referred to as the 'Ink Surface Absorption Method (ISAM)'.

From the modelling side, the observed effects were simulated using a modified version of the software package 'Pore-Cor' (Pore-Level Properties Correlator)⁵. It was enhanced to model anisotropic void structures, by re-scaling the *z*-axis relative to the *x* and *y*-axes. This produced a more realistic model for coating structures that contain pigment particles with high aspect ratios (i.e. Speswhite clay). The equations for laminar flow include those of Laplace and Poiseuille, and were used to determine network permeability. The equation for dynamic wetting was an expanded version of the Lucas/Washburn equation developed by Bosanquet. It included viscous, inertial, and capillary force effects, and was used to determine the rate of permeation of a wetting fluid into the simulated coating structures (Bosanquet, 1923).

Pore-Cor was also modified to demonstrate the effect of anisotropy in terms of spatial distribution of differently sized void spaces, rather than in the anisotropy of individual voids, specifically the effect of horizontally layering or laminating the structure.

1.4. Scientific terms and definitions

1.4.1. Porous medium

One may loosely define 'porous media' as solid bodies that contain 'pores'. Intuitively, 'pores' are void spaces which must be distributed more or less throughout the material if it is to be called 'porous'. Extremely small voids in a

solid are called 'molecular interstices', and very large ones are called 'caverns'. 'Pores' are void spaces intermediate in size between caverns and molecular interstices. The pores in a porous system may be *interconnected* or *non-interconnected*, as shown in Fig. 1.1. Flow of interstitial fluid is possible only if at least part of the pore space is interconnected. Effective porosity refers to the interconnected pore volume in a porous medium that contributes to fluid flow; it excludes isolated pores. Total porosity is the total void space in the rock whether or not it contributes to fluid flow. Thus, effective porosity is typically less than total porosity.

Pore spaces can be divided into *voids*, *capillaries* and *force spaces* (Scheidegger, 1974). *Voids* are characterized by the fact that their walls have only an insignificant effect upon hydrodynamic phenomena in their interior; in *capillaries*, the walls do have a significant effect upon hydrodynamic phenomena in their interior, but do not bring the molecular structure of the fluid into evidence; in *force spaces* the molecular structure of the fluid is brought into evidence. In natural porous media, many larger voids are constrained by smaller apertures. The large voids have traditionally been called pores and the smaller constraining voids, throats (see Fig. 1.1).

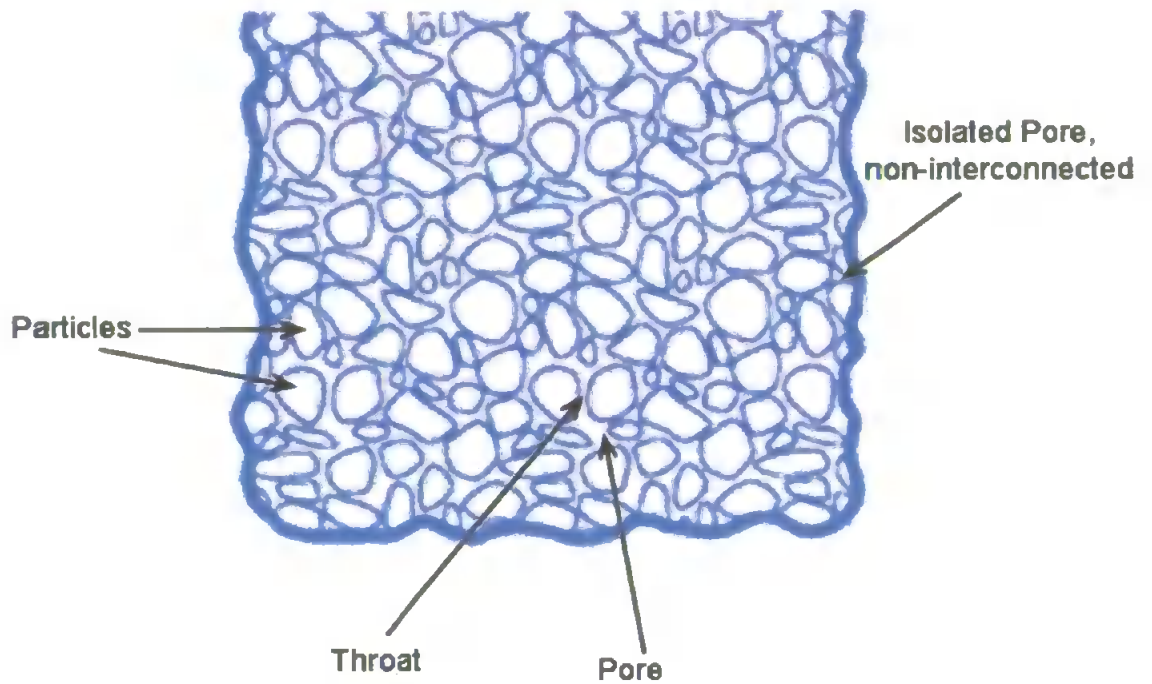


Fig. 1. 1. Example of a porous medium.⁹

An alternative definition of a throat would be the small pore space at the point where two grains meet, which connects two larger pore volumes. The number, size and distribution of the throats control many of the resistivity, flow and capillary-pressure characteristics of the medium.

1.4.2. Permeation and Permeability

We use the term 'permeation' as the measure of the overall extent of entry of a fluid into porous samples, while 'permeability' is defined quantitatively as the extent to which a porous material allows a fluid to pass through under a given pressure differential. The extent of entry into individual features is referred to as 'filling', and the localised processes which cause a wetting fluid to fill individual features and permeate through the structure are termed 'wetting'.

Wetting and consequent permeation starts at the contact point or surface between the fluid reservoir or droplet and the porous solid. The way the fluid subsequently permeates through the structure is determined by the size and geometry of the voids (Ma *et al.*, 1996), the way they are connected into a network (Adler *et al.*, 1990, Jerauld *et al.*, 1990; Liu *et al.*, 1992, Portsmouth *et al.*, 1991; Portsmouth *et al.*, 1992), the surface energy between the fluid and the solid phase (Starov *et al.*, 1994; Lundqvist, 1997), and the density, viscosity and applied pressure of the fluid (Bear, 1988; Choi *et al.*, 1988; Coulliette *et al.*, 1998; Dullien, 1992; Gane *et al.*, 1999; Gane *et al.*, 2000; Ginzbourg *et al.*, 1995). If a porous solid is made up from a homogeneous packing of unsorted spherical particles bound together, the resulting void structure will normally be structurally isotropic – i.e. it will have the same structural characteristics in any direction, and hence the same permeation characteristics (Bryant *et al.*, 1993; Patwardhan *et al.*, 1985). However, a sample made up from non-isometric particles such as clay platelets, packed in an aligned manner, would be structurally anisotropic (Patwardhan, *et al.*, 1986). Consequently, the permeation characteristics of such a sample would also be anisotropic. The measurements of structural characteristics in these comparisons must involve meaningful averaged quantities, which could be measured by auto-correlation functions of size and geometry measured over lengths corresponding to several average void sizes. In geostatistics, these lengths are referred to as lag distances (Ioannidis, *et al.*, 1993; Mathews *et al.*, 1997).

1.4.3. Anisotropy

Directional properties of a crystal are measured along *specific directions* in a crystal (Bloss, 1994). If their value changes with direction of measurement, the crystal is *anisotropic* in respect to this directional property; if not, the crystal is *isotropic* in respect to it. A crystal that is isotropic for some properties may be

anisotropic for others. In this study, we have investigated anisotropic pore structures, by first modelling and comparing the pore structure of an isometric and non-isometric system.

Isometric pore structures have a cubic form, represented by three axes of equal length that make right angles with each other (Klein *et al.*, 1985). The cube is composed of six square faces that make 90° angles with each other. Each face intersects one of the crystallographic axes and is parallel to the other two. Because the axes are identical, they are interchangeable. The crystallographic axes for an isometric structure and an example of the different isometric forms are shown in Fig. 1.2.

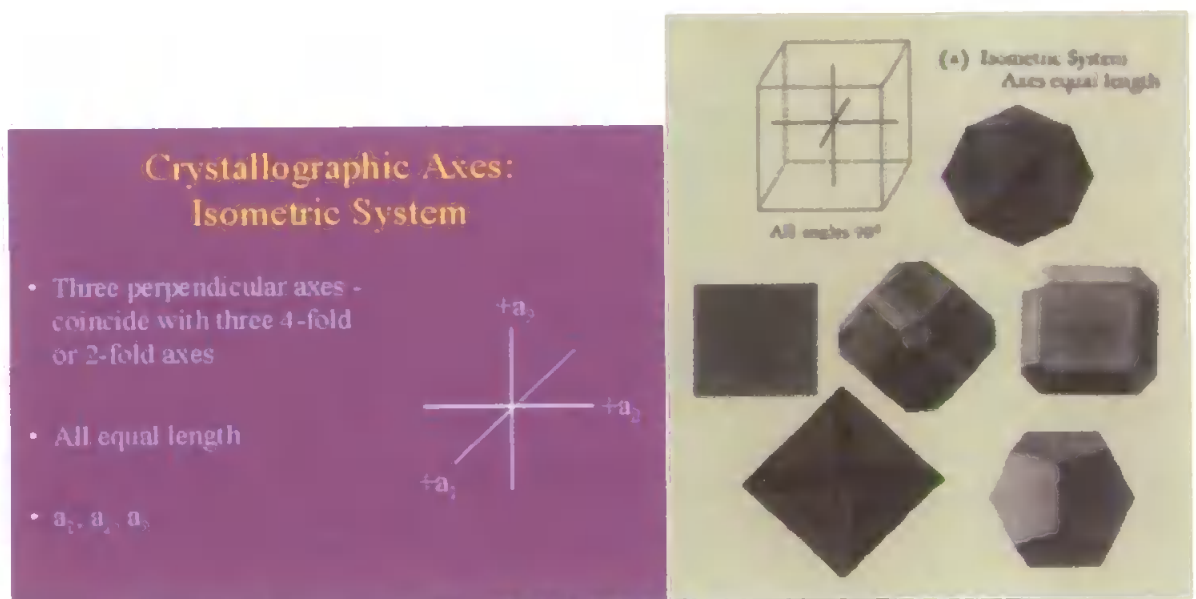


Fig. 1. 2. The crystallographic axes for an isometric structure (left-hand side) and an example of the different isometric shapes.⁷

A non-isometric pore structure would belong to a tetragonal system, and have a prismatic form. The three crystallographic axis would make right angles with each other, the two horizontal axis, x and y, are equal in length and interchangeable. The vertical axis, z, however, is of a different length (Klein *et al.*, 1985). An example of the different non-isometric forms are shown in Fig. 1.3.

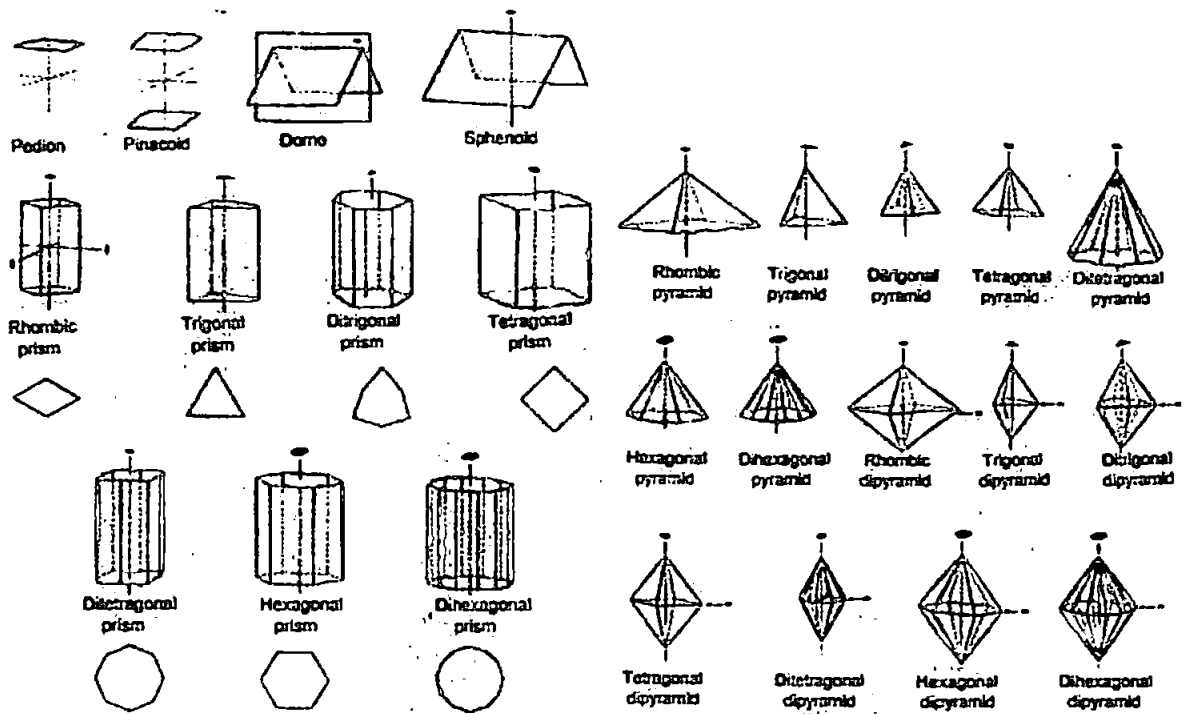


Fig. 1. 3. An example of the different non-isometric forms.⁸

In this thesis, we have also investigated anisotropism caused by correlated positions of voids of a particular size.

1.5. Why is paper coated?

In modern life, paper has many uses and one of the most important uses is as a medium for information transfer. To transfer information successfully, paper has to be printed with an image of the required information and the print has to be distinct from its background and sufficiently durable to prevent loss of quality by handling. The principal reasons for applying a pigment coating to paper and paperboard are to improve printability and appearance.

Amongst the most important properties of the coated paper are a smooth surface to allow good ink transference, a high opacity and high brightness, sufficient

mechanical strength to withstand the stresses during printing and a pore structure that interacts beneficially with the printing ink. The paper should also have sufficient capillarity to allow the ink film to set within the timescale of modern printing press.

These important parameters of paper quality are key issues within the paper and printing industries. The coating provides a surface that is more uniform in appearance and more receptive to printing ink than are the uncoated paper fibers. This in turn both facilitates the printing process and enhances the graphic reproduction.

Designing coatings for the requirements of controlled absorption on a modern printing press, or in the environment of the rapidly developing field of so-called ink jet and digital printing, is a demanding area of research. The high level of coated grades in use today reflects the desire on the part of the advertiser and printer to have a uniform surface structure for enhanced printability.

1.6. Composition and structure of paper and paper coatings

The term "coating" or "coating colour" within the paper industry refers to an aqueous pigment/binder suspension applied to the surface of the base-paper by drying. The main constituent of a coating is the pigment, usually kaolin clay and/or calcium carbonate, which is dispersed in water at high solids content. A latex binder (such as a styrene-butadiene copolymer) and a co-binder (such as starch or carboxymethyl cellulose, CMC) are added in order to ensure the required mechanical strength of the coating layer and to control the water retention of the coating colour during the coating process. The solid in the water dispersion is

usually between 58 and 70% by weight. A typical composition of a coating colour foundation is usually 80-90% (dry) mineral pigment and 10-20% binder by weight. Dispersants are used in the formulation of the coating colour in lower weight percentages to act as stabilizing agents and to make the components compatible in water suspensions. Other components, such as optical brighteners, preservatives and lubricating agents may also be included in the coating colour.

The term base-paper refers to paper that has been made on a paper machine using an aqueous suspension of cellulose fibres, fine mineral pigment and sufficient chemicals to keep the whole matrix together. Finished or coated paper usually contains at least one coating layer on the base paper. The void structure of the coating layer is determined by the particle packing of the coating pigment and the interactions of pigment particles with binders, and with the paper substrate, whilst the coating is dried and consolidated. The pore structure of a pigmented coating is generally on a different size scale compared with uncoated paper, with a size distribution close to, but somewhat broader than, the pigment particle size distribution.

1.7. Mineral Pigments

The characteristics of two different types of mineral pigments used in paper coatings are shown below:

1.7.1. Kaolin mineral group

Kaolin is a type of clay mineral, and it is the most widely used pigment in the paper coating industry. It has for many years been the major pigment form used in acid papermaking to add smoothness and opacity to paper. The

morphology of the two clay minerals shows a platy or foliated mineral structure. It has an idealised structural formula of $Al_2SiO_5(OH)_2$, and forms a 1:1 planar silicate layer, Fig. 1.4.

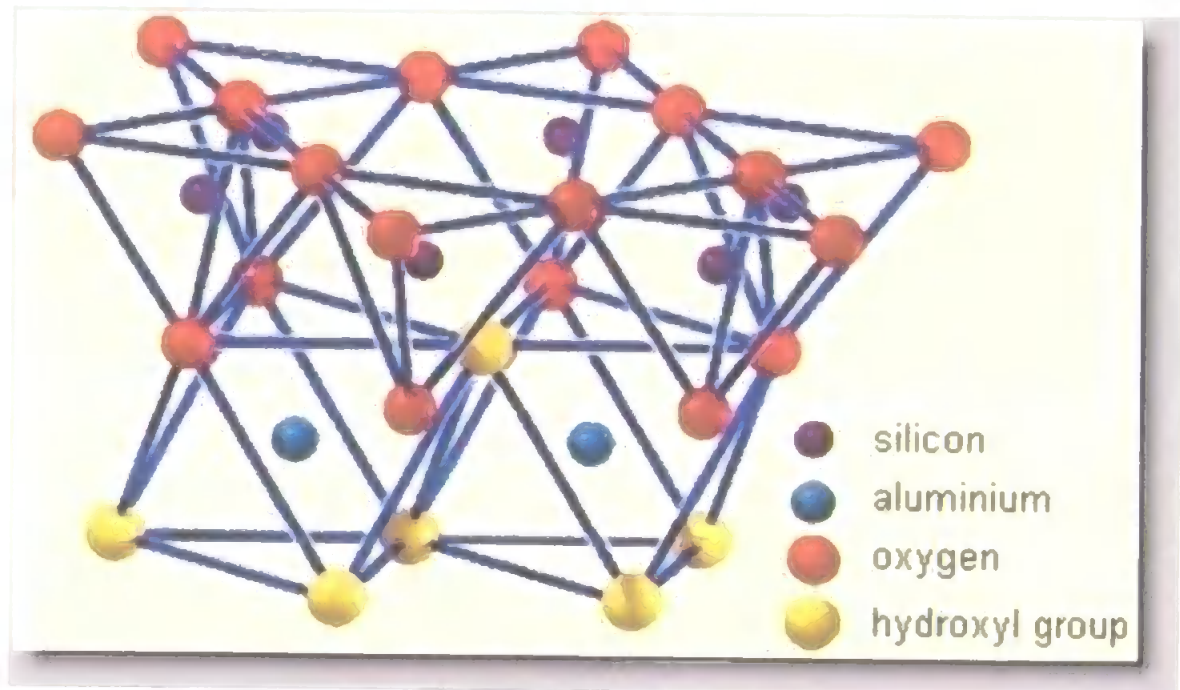


Fig. 1. 4. Structural formula for Kaolinite mineral.^v

The morphology of kaolin can differ greatly from source to source, and the deposits for Kaolin are mined as being either primary or secondary minerals. Primary kaolins are formed by the alteration of crystalline rocks such as granite and remain in situ, where they are formed. These minerals would accommodate 10-30% of the primary deposit. Such deposits occur in Cornwall, in Southwest England. The crystal form is well-defined with high aspect ratio platelets occurring throughout the size distribution of particles (Gane, 2001).

Secondary kaolins refer to a clay mineral that have been transported from their place of origin, and concentrated in deposits which may be some distance away, Fig. 1.5.

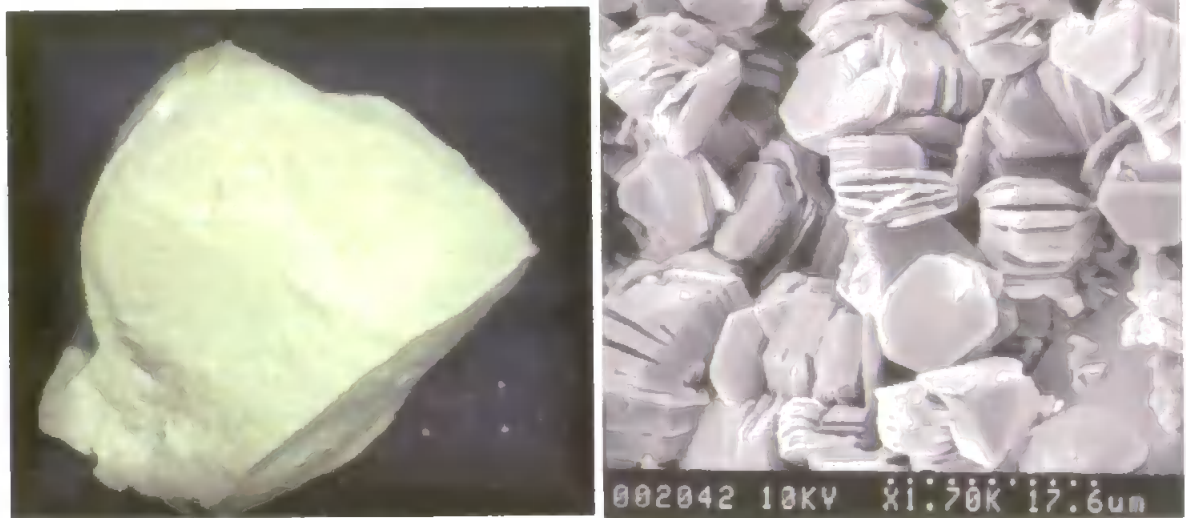


Fig. 1. 5. Picture of a secondary Kaolin deposit from Georgia, USA (left-hand side) and a scanning electron micrograph image of Kaolin minerals.¹⁰

The sedimentary beds form together with organic, humic deposits leading to reduced aspect ratios, and particles of finer size. Secondary kaolins contain much lower mine-waste, as the rock comprise of 85-95% of the secondary deposit.

1.7.2. Calcium Carbonate mineral group

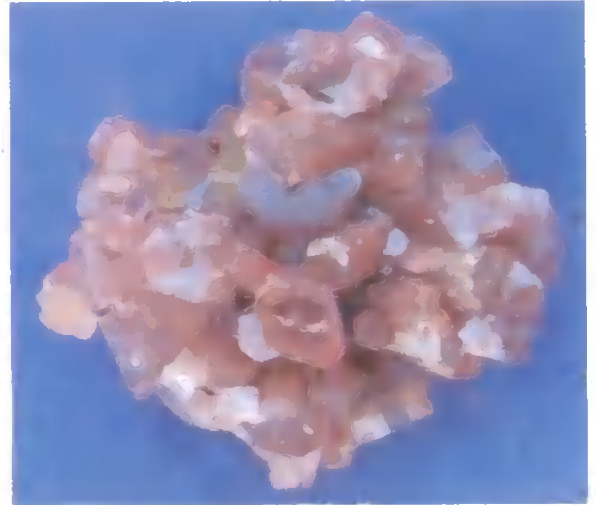
Calcium carbonate can be found in nature or synthetically produced in a myriad of types and forms. Calcium carbonate belongs to the mineral type calcite- CaCO_3 , and forms a number of useful crystal habits such as a rhombohedral calcite (as found in marble), prismatic, spherically agglomerated, scalenohedral ("cigar"-shaped crystals occurring frequently in a clustered form), and aragonitic (needle form) habit. A number of different crystal habits for Calcium carbonate are shown in Fig. 1.6 and 1.7.



a. Prismatic habit

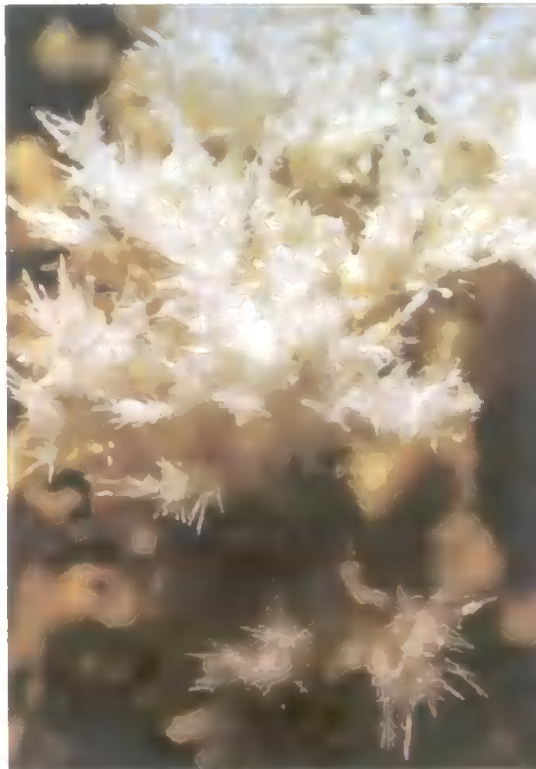


b. Rhombohedral habit



c. Scalenohedral habit

Fig. 1. 6. Different types of Calcium Carbonate crystallographic habits.¹¹



Aragonitic- Needle form habit

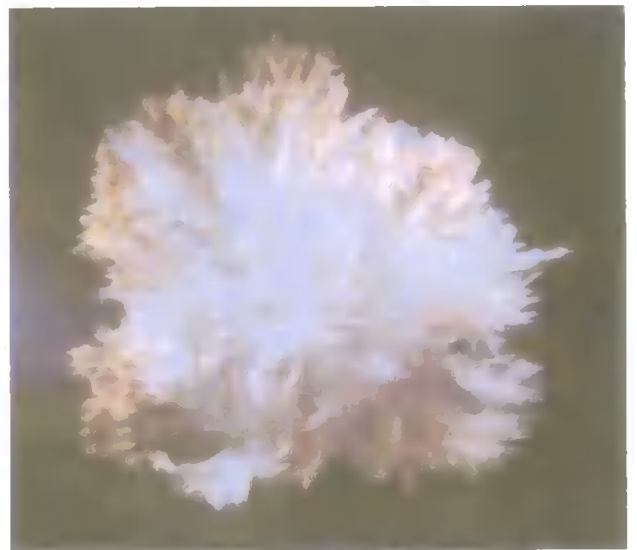


Fig. 1. 7. Different types of Calcium Carbonate crystallographic habits. Both pictures show an Aragonitic structure with a needle form habit.¹²

1.7.2.1. Ground Calcium Carbonate (GCC) Mineral Group

Calcium carbonate is a structural component of most skeletal creatures which have lived on earth. It is part of an unbroken cycle and so, in principle, is inexhaustible. The majority of deposits were formed by the capture of CO₂ from the atmosphere by microorganisms which combined the dissolved gas with calcium ions to form their exo-skeleton providing protection and structural support (Gane, 2001). Deposits of calcium carbonate (e.g. Coccoliths) formed chalk beds at the sea bottom which later became transformed under pressure to form limestone and in some cases combining high pressure and temperature to promote re-crystallisation into marble, the hardest and brightest form of calcite, CaCO₃. The most common sources of GCC are mined from chalk, limestone or marble quarries.

1.7.2.2. Precipitated Calcium Carbonate (PCC) mineral group

The PCC group is chemically synthesised crystalline material having a similar structure to that found in a calcium carbonate mineral, belonging to either a calcitic or an aragonitic crystalline polymorph. The crystalline material is manufactured by a series of stages:

- i. Limestone is first mined and then calcined in a kiln, producing carbon dioxide and calcium oxide (quicklime).
- ii. The CO₂ gas is then cooled, scrubbed if necessary to remove other gaseous impurities, and stored for use in preparation of the PCC.

- iii. The calcium oxide is slaked with water to produce calcium hydroxide slurry, which in turn is screened to remove any unreacted lime or other impurities.
- iv. The carbon dioxide gas is then bubbled through the lime slurry, to produce a calcium carbonate precipitate.
- v. The commercial PCC pigments are typically 97%CaCO₃ with the remainder being MgCO₃ (1-2%) and other minor impurities.

1.8. History of paper making

Paper making first began in China in the first century AD, and has continued world-wide ever since. Fig 1.8 depicts an example of a pulp and paper mill in Louisiana, in the 1800's.



Fig. 1. 8. Paper mill from Louisiana, www.ajmeek.com

Efforts to coat paper with pigment particles were made as long as several hundred years ago. In the latter half of the nineteenth century, the situation changed

markedly when substantial technical effort resulted in the development of mechanical methods for coating paper on a commercial scale.

During the 1930's a number of developments combined to produce a marked increase in the demand for pigment-coated paper. The application of coating on the paper machine, rather than as a separate operation, greatly reduced the cost of producing pigment-coated paper. The invention of high-speed heat-set letterpresses made high volume, low cost printing a reality. Together these developments made possible the high-volume graphic periodicals such as *Life* and *Fortune*. A graphical illustration of the general relationship between the introduction of new technology and the increase in coated paper volume appears in Fig. 1.9.

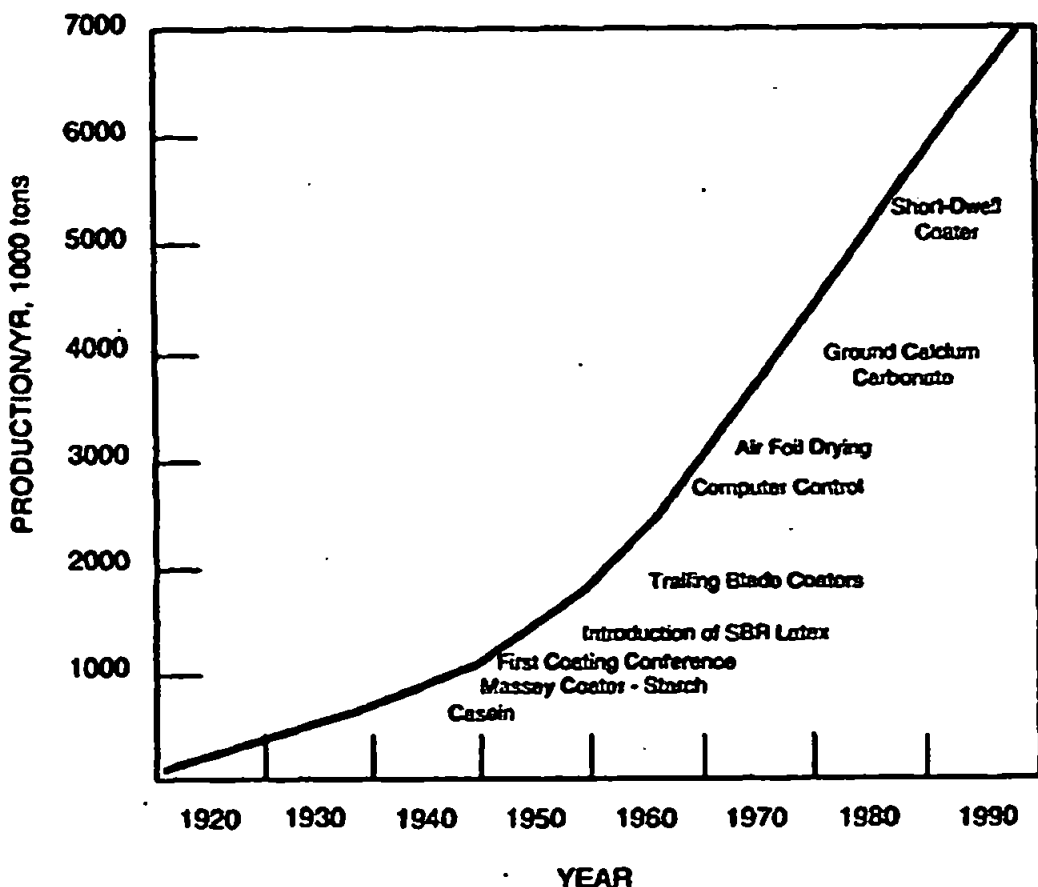


Fig. 1. 9. The impact of new technology on coated paper volume (O'Shea, 1997).

Development of mechanical methods for coating paper on a commercial scale began in the later half of the 19th century. In the 1930's, the invention of high-speed heat-set letter presses made high volume, low cost printing a reality.

An example of a modern paper mill is shown in Fig. 1.10, which shows the SCA Graphic Sundsvall AB- Ortviken paper mill, located in Sundsvall, Sweden.



Fig. 1. 10. SCA Graphic Sundsvall AB- Ortviken Paper mill, located in Sundsvall, Sweden.

The steps involved in the production process of the paper are numbered in Fig. 1.11.

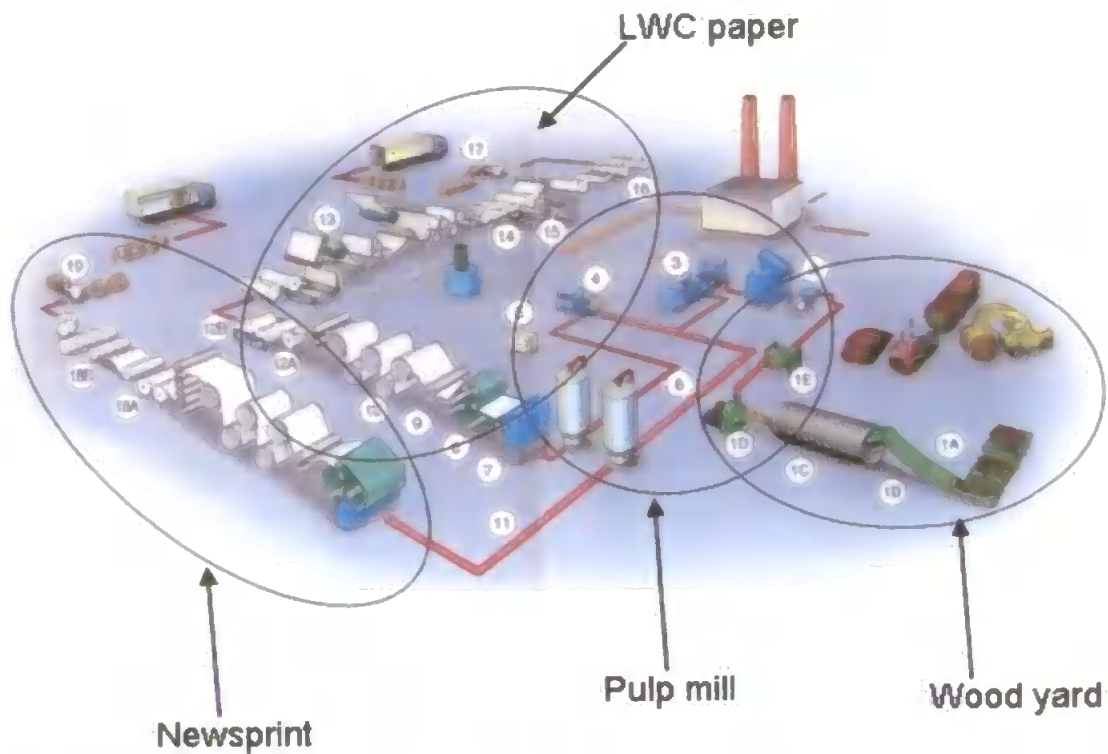


Fig. 1. 11. Diagram of the paper production process of SCA Graphic Sundsvall AB- Ortviken Mill, located in Sundsvall, Sweden.

The production process is shown as four stages; Wood yard, Pulp mill, production of Light Weight Coated (LWC) paper, and the production of newsprint. The numbers of interest are labelled as the following:

Wood yard:

1- Fresh spruce logs are slashed (1A), de-iced (1B), debarked (1C), chipped (1D) and screened (1-E).

Pulp mill:

2- The chips are transported to the mill for thermomechanical pulp production.

4- Pulp for LWC paper is processed further in a second refiner stage and bleached.

6- The pulp is screened and pumped to storage towers.

LWC paper:

7,8- The fully processed pulp mixture, called stock, which consists of approximately 1 percent fibre and 99 percent water, is pumped onto a fine-meshed plastic fabric, a so-called wire. The paper sheet begins to form as the pulp drains and the fibres bind together.

9,10- In the press section, the paper's dryness and strength are increased by pressing out the water and determining the thickness of paper. The paper is dried further by passing between the drying section's steam-heated cylinders.

13- The paper is first coated on one side and then the other. After each coating station the paper is dried using infrared heat, warm air and steam.

15- The paper surface is smoothed in calendars.

An example of an off-machine coater and of a supercalender machine is shown in Fig. 1.12 and 1.13, respectively. The function of the off-machine coater is to apply the coating colour to the basepaper, while the purpose of the supercalender machine is to apply thermal and physical compression to the paper to smoothen and densify it.



Fig. 1. 12. Example of an Off-machine coater (www.repap.com).



Fig. 1. 13. Example of a Supercalender machine (www.repap.com).

The rate of growth in demand for pigment-coated paper far exceeds the rate of growth for total paper demand. This has provided a strong stimulus for the continuing development of new and improved materials that are both environmentally friendly, and quality and cost effective. Numerous factors are cited for the above-average growth, with the more significant including a rising level of education, increased leisure time, and growing affluence in the developed economies. A rapid rise in literacy will add to the demand in developing countries. There is some concern that the growth of electronic communication systems will have an adverse impact on coated paper volume. Most individuals knowledgeable in the area foresee an eventual possibility for some substitution, but it is generally agreed that any major incursion into the present system is many years off. The

convenience, cost effectiveness, and portability of hard copy afforded by coated paper will be very difficult, if not impossible, to match.

1.9. Environmental Implications

The mining of different mineral pigments used in paper coating production (see Section 1.7) have substantially different environmental effects. There are several different generic species of pigments and a number of variations within each category. The dominant material is kaolin, also referred to as clay. Other compositions include calcium carbonate, titanium dioxide, talc and plastic pigments. Ground calcium carbonate (GCC) is essentially a low-waste mining venture, as almost all of the mined rock is processed for use as a pigment in the paper industry. Amazon and Speswhite clay are medium and high-waste mining ventures, respectively, as only a small percentage of the rock contains the mineral of concern. Due to Amazon clay being a secondary mineral, there will be a higher percentage of clay in the ore deposit. This will produce less mine-waste than the primary mineral, Speswhite clay. Also, the production of Precipitated Calcium Carbonate (PCC) requires a high use of energy compared to the other pigments, due to calcination of limestone and subsequent recarbonation.

The use of different additives in the coating process will also have different environmental implications. Binders are usually divided in two types: natural and synthetic. Starch is a naturally produced binder (i.e. potato starch), and will thus be a more environmentally friendly product and a renewable resource. Meanwhile, latex (such as styrene-butadiene or styrene-acrylic latex) is a synthetically produced binder and is therefore a non-renewable resource.

Carboxymethyl cellulose is also used as an ingredient in a coating colour, and can be considered a cross between a natural and synthetic co-binder.

2. LITERATURE REVIEW

2.1 Darcy's experiment

The theory of laminar flow through homogeneous porous media is based on a classical experiment originally performed by Henry Darcy in 1856, and is shown in Fig. 2.1 (Scheidegger, 1974).

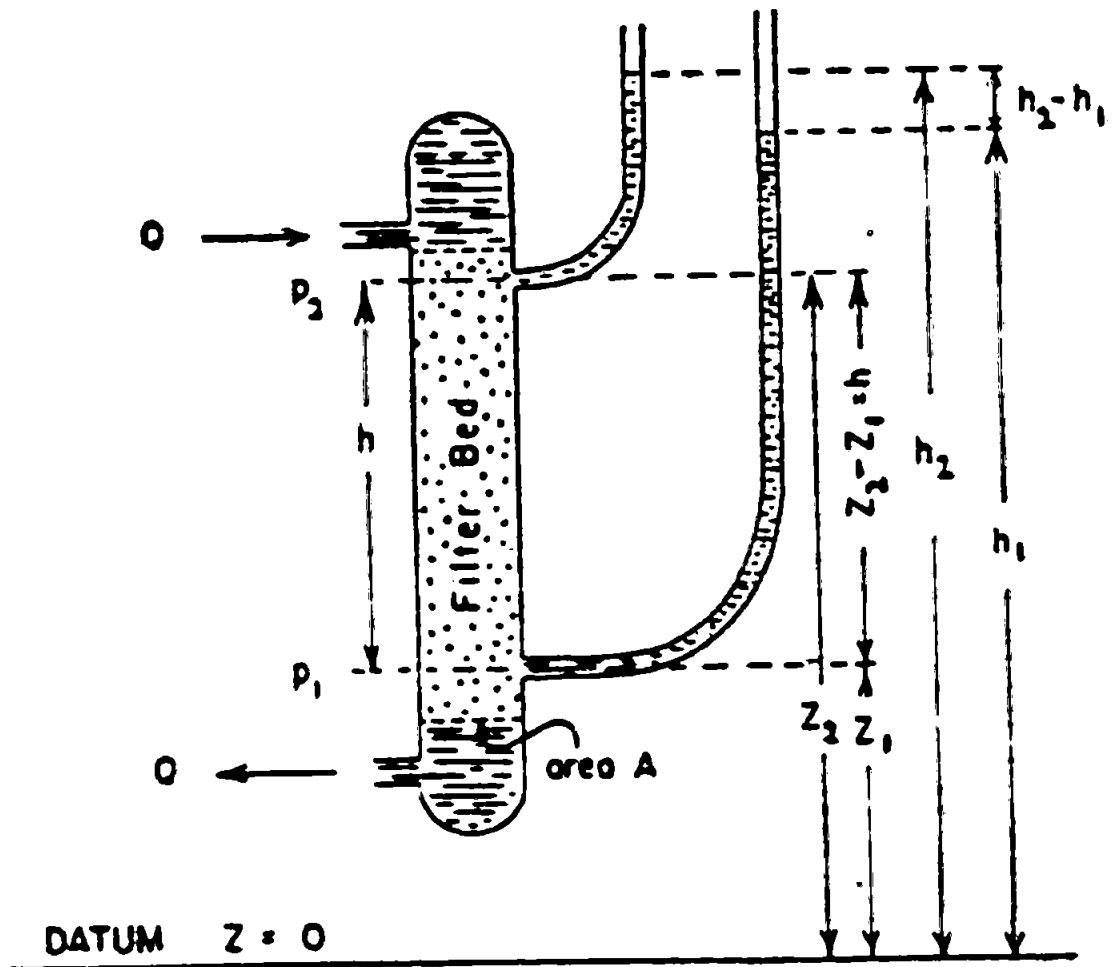


Fig. 2. 1. Darcy's filtration experiment (Scheidegger, 1974)

A homogeneous filter bed of height h is bounded by horizontal plane areas of equal size A . These areas are congruent so that corresponding points could be connected by vertical straight lines. The filter bed is percolated by an incompressible liquid. If open manometer tubes are attached at the upper and

lower boundaries of the filter bed, the liquid rises to the heights h_2 and h_1 , respectively above an arbitrary datum level. By varying the various quantifiers involved, one can deduce the following relationship:

$$Q = -KA(h_2 - h_1) / h, \quad \text{Eq. 2. 1}$$

where Q is the total volume of fluid percolating in unit time and K is a constant depending on the properties of the fluid and of the porous medium. The relationship is known as *Darcy's law*. The minus sign in the expression for Q indicates that the flow is in the opposite direction of increasing h .

Darcy's law can be restated in terms of the hydrostatic pressure difference, Δp , across the specimen of porous material of length L , and is expressed as

$$Q = KA\Delta p / L \quad \text{Eq. 2. 2}$$

Referring to Fig. 2.1, the upper boundary of the bed (elevation above the datum level denoted by z_2) has a pressure $p_2 = \rho g(h_2 - z_2)$, where ρ refers to the density of the liquid. The lower boundary (denoted by z_1) of the bed is shown to have a pressure $p_1 = \rho g(h_1 - z_1)$. Inserting this statement into Eq. 2.1, one obtains (as $z_2 - z_1 = h$)

$$Q = -KA[(p_2 - p_1) / (\rho gh) + 1]; \quad \text{Eq. 2. 3}$$

or, upon introduction of a new constant K' , assuming ρ and g to be constants,

$$Q = -K' A(p_2 - p_1 + \rho gh) / h \quad \text{Eq. 2. 4}$$

All the above equations are equivalent statements of Darcy's law. The quantity Q/A has dimensions LT^{-1} and is the flow rate, flux or Darcy velocity q , so that Darcy's law is more commonly written as

$$q = K\Delta p / L$$

Eq. 2. 5

Darcy's law is a simple transport law and has exactly the same form as Ohm's law, Fick's law and the heat conduction equation. Each of these laws defines a transport property, a *conductivity* that relates to the flow process that each describes. Darcy's law has been shown to be valid for a wide domain of flows. However, for liquids at high velocities and for gases at very low and at very high velocities, Darcy's law becomes invalid, as will be discussed later in section 2.4.1.

It is important to note that Darcy's law is phenomenological. The Darcy permeability is defined such that the overall equation is obeyed, and therefore individual results can never deviate from the law, which is based purely on an observed phenomenon.

2.2 The Permeability concept

The constant K is obviously indicative of the permeability of a certain medium to a particular fluid. It depends on the properties of both the medium and the fluid. For permeation flows which are geometrically similar the permeability K varies inversely as the fluid viscosity, μ . We can therefore define an intrinsic (specific) permeability as

$$k = K\mu ,$$

Eq. 2. 6

where k is a material property independent of the fluid used to measure it. The relationship has been verified by numerous experiments.

The dimension of (specific) permeability is a length squared, which suggests that the natural permeability unit in the c.g.s system should be cm^2 . In some branches of applied science, (i.e. the oil industry), the 'Darcy' has been adopted as the unit, with

$$1 \text{ Darcy} = 9.87 \times 10^{-9} \text{ cm}^2$$

2.2.1 Saturated permeability

For a porous medium fully saturated with liquid, Darcy's law may be expressed locally as

$$\mathbf{q} = -K_s \Delta P,$$

Eq. 2. 7

where \mathbf{q} is known as the vector flow velocity. The quantity K_s is the conventional saturated permeability of the material, with dimensions LT^{-1} , while P has the dimension L , and is the pressure potential equivalent to the hydrostatic head such that

$$P = p / \rho g.$$

Eq. 2. 8

Once the permeability concept has been defined, one has to determine the dependence of the permeability on external conditions of the porous medium. The permeability would be expected to depend on external stresses on the porous medium if the latter is compressible. There is also the possibility that a directional variation of permeability occurs. Thus, if a cube is cut out of a macroscopically

faces. This effect has been observed by Johnson and Breston (Johnson *et al.*, 1951).

2.3 The Measurement of Permeability

To determine the permeability of a particular system, one needs to measure the pressure drop and flow rate, and then use of the forms of Darcy's law. Measurements of permeability can be performed using any of the forms of Darcy's law. Thus experiments are performed in which, in a certain system, a pressure drop and a flow rate are measured. Physically, permeability measurements are very simple, involving chiefly questions of experimental technique. Methods have been discussed in general terms, for example by Eastman and Carlson (Eastman, 1940). Permeabilities in various substances may have a wide range. In table 2.1, we give a compilation of some representative values. The 'range' does not signify that the indicated values are the extreme limits of permeability which may be found in the substances; rather it signifies the range in which one is likely to find the permeability.

Substance	Permeability Range / cm ²
Sand (loose beds)	2.0×10^{-7} to 1.8×10^{-6}
Soils	2.9×10^{-9} to 1.4×10^{-7}
Sandstone ('oil sand')	5.0×10^{-12} to 3.0×10^{-8}
Limestone, dolomite	2.0×10^{-11} to 4.5×10^{-10}
Brick	4.8×10^{-11} to 2.2×10^{-9}
Bituminous concrete	1.0×10^{-9} to 2.3×10^{-7}
Cigarette	1.1×10^{-5}
Fibreglass	2.4×10^{-7} to 5.1×10^{-7}

Table 2. 1. Representative values of permeability for various substances (Scheidegger, 1974).

2.3.1 Anisotropic permeability measurements

Most equipment for measuring directional permeability described in the literature uses a block of porous material, where the inlet and outlet for the percolating fluid are restricted to a small part of the surface (usually a cubic sample is used, with inlet and outlet on different faces). Equipment of this type has been described by Maasland and Kirkham (Maasland *et al.*, 1955) in connection with the analysis of soils and by Dutta and Griffiths (Dutta *et al.*, 1955) in connection with the analysis of oil well cores.

Li *et al.* (Li *et al.*, 1999) investigated the porous structure of paper coating layers with various amounts of kaolin and precipitated calcium carbonate (PCC) pigments by studying the diffusion behaviour of water absorbed in the coatings, using a pulsed field gradient NMR technique. It was shown that water diffusion in the coating layers was significantly anisotropic. The interpretation of the diffusion measurements showed Kaolin to give a denser, less porous coating structure, which presented more restrictions to the diffusion of absorbed water, especially in the direction perpendicular to the plane of the paper. Their research also showed diffusion anisotropy to directly reflect the anisotropy of the porous structure. The porous structure of the Kaolin layers was revealed to be highly anisotropic in comparison to the PCC coating layer, an effect associated with the disc-like structure of the kaolinite particles.

2.3.2 Permeation measurements in paper coatings

2.3.2.1 Gurley permeameter

In the paper industry, the air permeability of a paper structure is usually measured with a Gurley permeameter (Institute of Paper Science & Technology, 1940). The air pressure is supplied by an inverted piston floating freely in a cylinder partly filled with oil. The cylinder is clamped between two plates and air is forced through the sheet. The Gurley air permeability is reported as the time (in seconds) for 100 ml of air to pass through the sheet (Physical Committee of the Process and Product Quality Division, 1946).

2.3.2.2 Ink tack test

This technique was used to investigate the ink setting behaviour of paper coatings from following the development of the ink tack force using the Ink Surface Interaction Tester (ISIT). A full description of this method has been given by Gane and Seyler (Gane *et al.*, 1994). The instrument measures the force required to separate a trilayer consisting of the paper surface, the ink layer, and the rubber printing blanket. The force required to attain separation is a measure of the adhesion at the ink-blanket interfaces or the cohesion within the ink layer itself which is related to the state of drying (Preston *et al.*, 2002). The time taken for the initial increase in tack force to reach a plateau was taken as indicative of the rate at which ink solvent is lost into the coating.

It has been established that the mean coating pore diameter has a strong influence on ink setting rate, and empirical work has shown that coatings with smaller pores accelerate ink setting rates (Donigian *et al.*, 1997). However, further

work by Preston *et al.* (Preston *et al.*, 2001) showed that this is due to the fact that these coatings have a higher pore density (number of pores per unit area).

2.3.2.3 Dynamic Absorption Tester (DAT)

This instrument measures the contact angle of a test liquid in contact with a film or paper substrate under specified test conditions (Technical Association of the Pulp and Paper Industry, 2002). The absorption of the test liquid is represented as the rate of change of the contact angle as a function of time. A drop of a specified volume is automatically applied to a test specimen surface using a liquid delivery system and specified deposition parameters. Images of the drop in contact with the substrate are captured by a video camera at specified time intervals following deposition. The contact angle between the drop and substrate at various time intervals are determined by image analysis techniques on the captured images. Other test variables are also analyzed, such as the changes in droplet height and diameter.

2.3.2.4 Ink stain density test

The ink stain tests are used to study printability properties of paper coatings and for quality control purposes in the production of coated papers. The ISD tests can also be used to give an indirect measure of the rate of permeation of a fluid into the paper coatings (Bristow *et al.*, 1982). The general routine for an ink-stain test involves the following stages:

1. An excess of ink is applied to the surface of the paper coating
2. The ink is allowed to remain on the surface of the paper for a given contact time.

3. The excess of ink is removed from the surface of the paper by wiping.
4. The intensity and appearance of the resulting stain are assessed.

Although the ink stain value may be considered to be a measure of ink absorption it should be observed that the value is an optical measure of a change in reflectance factor of the coating surface, and that the ink stain value is not linearly related to the quantity of ink absorbed.

2.4 Continuous matter theory

The subject of hydromechanics in porous media is concerned with the pore space of a porous medium as filled with various fluids. It is therefore also necessary to investigate the mechanics of fluids that may fill the pore spaces. There are two possible aspects of the mechanics of fluids: macroscopic and microscopic. The macroscopic aspect is manifested in what one might call the 'continuous matter theory', meaning that the fluid is treated as a continuous medium. The microscopic aspect is obtained if the molecular structure of the fluid is taken into account.

The motion of a fluid, if the fluid is regarded as a continuum, is described geometrically if the position of every material point of the fluid is known at every time-instant. The Navier and Stokes (Borhan *et al.*, 1993; Moshinskii, 1997) is applicable to incompressible viscous fluids and is stated as:

$$\nu \text{grad} \nabla v + \partial v / \partial t = F - (1/\rho) \text{grad} p - (\mu/\rho) \text{curl} \text{curl} v$$

Eq. 2. 9

Here v is the local velocity-vector of a point of the fluid, t the time, F the volume-force per unit mass, and p , μ , and ρ are respectively the pressure, viscosity, and density of the fluid (Scheidegger, 1974). The boundary conditions prescribed that $v = 0$ at the walls of the container. Laminar viscous flow of an incompressible fluid in a tube takes up a parabolic velocity profile distributed about the axis of the capillary tube, with the maximum flow rate down the centre of the tube, fig 2.2.

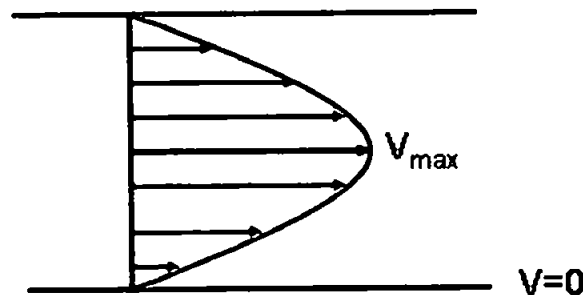


Fig. 2. 2. Parabolic velocity flow profile for laminar flow in a cylindrical tube. V_{max} represents the point of maximum velocity, while the walls of the cylinder show a velocity of zero.

The Navier-Stokes equation can be solved exactly for a straight, circular tube. Consider the total volume throughput Q through a circular tube of radius r and length h , with the pressure drop from end to end being Δp . The solution to the Navier-Stokes equation, which is called the 'Hagen-Poiseuille equation', becomes (Borhan *et al.*, 1993; Moshinskii, 1997).

$$Q = \frac{\pi \Delta p r^4}{-8 h \mu}$$

Eq. 2. 10

The Hagen-Poiseuille equation was deduced under the assumption that the term $v \text{ grad } v$ is zero. This equation is only true for straight tubes. In curved tubes, the above equation is no longer true, and one has the conditions of non-linear laminar flow.

2.4.1 Turbulence and Reynolds number

Theory and experiment show that for high flow velocities the flow pattern becomes transient although the boundary conditions remain steady; eddies are formed which proceed into the fluid at intervals (Wang *et al.*, 1994). For any one system, there seems to be a 'transition point' below which steady flow is stable. Above the 'transition point' the steady flow is more and more likely to become unsteady and to form eddies upon the slightest disturbance. The steady flow is often termed *laminar*, and the flow containing eddies *turbulent*. In turbulent flow, the law of Hagen-Poiseuille is no longer valid. It has been shown by Reynolds that circular straight tubes are dynamically similar, as far as the Hagen-Poiseuille equation is concerned, if the following 'Reynolds number' (denoted by Re) is the same:

$$Re = 2\rho r v / \mu,$$

Eq. 2.11

where all the constants have the same meaning as before, and v is now the average flow velocity in the tube. It must be expected therefore, that turbulence will occur in any straight tube if a certain Reynolds number is reached. This critical Reynolds number has been determined to be in the neighbourhood of 2200 (Scheidegger, 1974).

2.5 Permeability Models

2.5.1 Empirical correlations

The concept of permeability permits a phenomenological description of the flow through porous media in a certain velocity domain. An understanding of the phenomena can be obtained only if the concept of permeability can be reduced to more fundamental physical principles.

A direct approach to finding relationships between the various properties of porous media is by an attempt to establish empirical correlations. A most obviously sought after correlation was that between *porosity* and *permeability*. A simple consideration of theoretical possibilities of the structures of porous media, however, makes one realise that a general correlation between porosity and permeability cannot exist. It is obviously quite possible for two porous media of the same porosity to have entirely different permeabilities (Cloud, 1941).

The next more involved correlation that might be looked for is between *structure* and *permeability*. One may interpret 'pore structure' as meaning the 'pore size distribution' as obtained from capillary pressure curves. The correlations between capillary pressure and permeability are mainly based upon theoretical considerations which will be discussed later.

2.5.2 Theoretical Correlation

The simplest way to try to establish correlations theoretically is to represent the porous media by theoretical models which can be treated mathematically. Only trial and error can show which models exhibit the characteristic phenomena

taking place in the porous medium and which do not. If a proper model is found it can be substituted for an actual porous medium and then one can predict by calculation how the medium will behave under yet untried conditions. Relationships deduced from such models would have some degree of general validity.

2.5.3 Capillarc Models

The simplest models that can be constructed are those consisting of capillaries. Scheidegger (Scheidegger, 1953b) gave a review of such models. The models aim at correlating the permeability with either an 'average' pore size or with the pore size distribution (i.e. capillary pressure) curve.

2.5.3.1 Aligned cylinders model (Straight capillarc model)

The simplest capillarc model of the linear case is one representing a porous medium by a bundle of straight, parallel capillaries (Scheidegger, 1953a) of uniform diameter, d , as shown in Fig. 2.3.

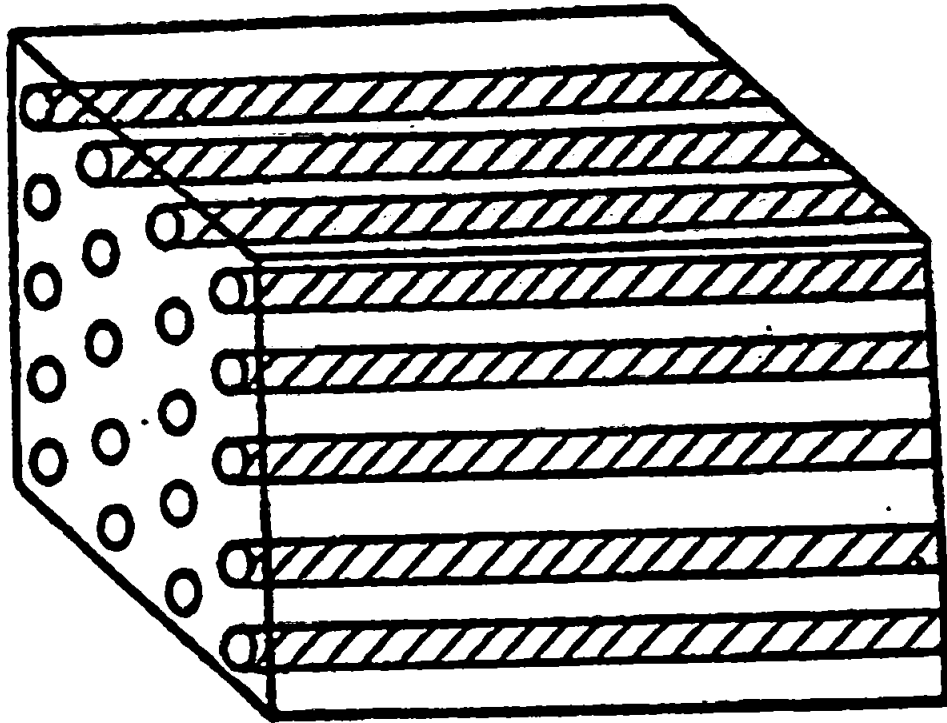


Fig. 2. 3. Example of the porous medium represented by the straight capillary model (Scheidegger, 1974).

The total volume-flow Q through a capillary is then given by the law of Hagen-Poiseuille (see Eq. 2.10). If there are n such capillaries per unit area of cross-section of the model, the flow per unit area q (or the macroscopic or 'filter' velocity) will be

$$q = \frac{n\pi d^4}{128\mu} \frac{dp}{dx}$$

Eq. 2. 12

where dp/dx is the pressure gradient along the capillary. As the flow can also be expressed by Darcy's law

$$q = -\frac{k}{\mu} \frac{dp}{dx},$$

Eq. 2.13

it follows that

$$k = -n\pi d^4 / 128$$

Eq. 2. 14

A relationship with porosity, ϕ , can be introduced with Eq. 2.14 as

$$k = \phi d^2 / 32$$

Eq. 2. 15

If these equations are applied to actual porous medium, d is assumed to be an 'average' pore diameter, δ . Since the equation does not correctly represent the relationship between permeability and porosity in porous media, as it is actually observed, the factor 32 is commonly replaced by some arbitrary factor T^2 , where T is called the 'tortuosity'. Similarly, instead of δ^2 the 'average specific surface area' S can be introduced. A relationship with these factors can also be introduced, taking the form as:

$$k = \phi^3 / (T^2 S^2)$$

Eq. 2. 16

A theoretical justification for the equation was given by Kozeny (Kozeny, 1927).

2.5.3.2 Parallel type models

Since all the capillaries in the Aligned cylinders model are parallel, there can be no flow orthogonal to the capillaries. The first modification of the relationship between porosity and permeability was to have one-third of the capillaries put in each of the three spatial dimensions. The permeability is thus lowered by a factor 3 and Eq. 2.14 will read

$$k = \phi \delta^2 / 96$$

Eq. 2. 17

The average diameter δ was then reduced to some value calculated from the 'pore size distribution', $f(d)$ or from the 'differential pore size distribution' $g(d)$. This method aimed at a connection between capillary pressure and permeability since the pore size distribution is usually measured by the capillary pressure method. A model was constructed where all the capillaries permitting flow in a given direction are parallel to that direction, but vary in pore-diameter, leading from one face of the porous medium through to the other. The pore size distribution of the model and an actual porous medium was made identical, and the result referred to as a 'parallel type model'. A model of this type was first devised by Purcell (Purcell, 1949) in a somewhat different fashion. The following explanation is taken from Scheidegger (Scheidegger, 1953a), showing the permeability being related to the following formula:

$$k = \frac{\phi}{96} \int_0^{\infty} d^2 g(d) d(d)$$

Eq. 2. 18

We obtain the same expression as Eq. 2.17 except that the average pore diameter δ has now a more exactly defined meaning. It is given by the equation

$$\delta^2 = \int_0^{\infty} d^2 g(d) d(d)$$

Eq. 2. 19

No fundamental deviation from Eq. 2.15 and 2.17 are therefore obtained. Specific surface area and tortuosity can again be introduced, and would thus result in a 'Kozeny' equation of the type of Eq. 2.16. It would seem that the parallel type models have not much advantage over the simple model of parallel capillaries.

2.5.4 Hydraulic radius theories

The previous theories all make use of the fundamental observation that the permeability, in absolute units, has the dimension of an area or of a length squared. It may be argued that the length should be characteristic for the permeability of a porous medium. Such a length may be called the 'effective hydraulic radius (EHR)' of the porous medium, and is linked to the hypothetical channels to which the porous medium is thought to be equivalent. A possible measure of a hydraulic radius would, for instance, be the ratio of the volume to the surface of the pore space. The hydraulic radius theories assume the following basic expression for the permeability:

$$k = c R_H^2 / F(\phi),$$

Eq. 2. 20

where R_H is the 'hydraulic radius', $F(\phi)$ is the 'porosity factor', and c is some dimensionless constant which could be incorporated into the porosity factor. The assumptions basic to the hydraulic theories have been discussed by Carman (Carman, 1941).

2.5.5 The Kozeny theory

The Kozeny theory is today a widely accepted explanation for permeability, although rather severe objections against it will be pointed out later (Kozeny, 1927). The Kozeny theory represents the porous medium by an assemblage of channels of various cross-sections, but of a definite length. The Navier-Stokes equations are solved simultaneously for all channels passing through a cross-section normal to the flow in the porous medium. The permeability is expressed in terms of the specific surface of the porous medium, which is a measure of a

properly defined (reciprocal) hydraulic radius. The Kozeny equation was developed independently by Fair and Hatch (Fair *et al.*, 1933), and is expressed as follows:

$$q = -\frac{c\phi^3}{\mu S^2} \text{grad } p$$

Eq. 2. 21

Comparing this with Darcy's law we obtain for the permeability

$$k = c\phi^3 / S^2$$

Eq. 2. 22

This relation shows that the filter velocity q is inversely proportional to the square of the surface area per unit volume, S . The number c fluctuates, theoretically only very little, as for particles with a circular cross-section $c=0.50$; for a square $c=0.5619$; for an equilateral triangle $c=0.5974$; and for a strip $c=2/3$. The number c is known as the 'Kozeny constant'.

One can extend the Kozeny equation by introducing a 'tortuosity' T as an undetermined factor, in accordance with what was done for capillary models, and will indicate that the actual flow path is T times longer than the 'apparent' path straight across the porous medium; T is then called the 'tortuosity'. This changes the expression for permeability to read:

$$k = c\phi^3 / (TS^2)$$

Eq. 2. 23

It should be noted that the concept of tortuosity is quite alien to the Kozeny theory, as it does not come into play during the actual deduction of the Kozeny equation

and can therefore be justified only by the desire to have another arbitrary parameter.

A much used modification to the Kozeny equation was postulated by Carman (Carman, 1939). The Kozeny-Carman equation is

$$k = \phi^3 / [5S_o^2(1-\phi)^2]$$

Eq. 2. 24

where S_o is Carman's 'specific' surface exposed to the fluid, e.g. the surface exposed to the fluid per unit volume of *solid* (not porous) material.

2.5.5.1 Criticism of the Kozeny theory

Coulson (Coulson, 1949) made an extensive investigation of the data of previous authors, and on the basis of information obtained from flow through systems of packed spheres, prisms, cubes, cylinders, and plates, he concluded that more general formulations still must be developed to describe adequately flow phenomena in non-spherical systems. Childs and Collis-George (Childs *et al.*, 1950) put forward severe criticisms of the Kozeny theory from the theoretical reasoning that the hydraulic radius theories utterly fail to describe structured bodies such as, for example, 'stiff-fissured' clays. The structural fissures contribute negligibly both to porosity and to specific surface, and yet they dominate the permeability. Again, neither the porosity nor the internal surface is a directed quantity, and therefore the Kozeny formula cannot indicate anisotropic permeability, which nevertheless seems to be the rule rather than the exception in nature.

Macey (Macey, 1940) found enormous changes in permeability with porosity which is not explainable by the Kozeny equation. Brooks and Purcell (Brooks *et al.*, 1952) found a large discrepancy when areas are measured by the gas-adsorption method and with the aid of the Kozeny equation.

In the light of these criticisms, the success and popularity of the Kozeny-Carmen equation may seem strange. However, its success is based on its partly phenomenological character arising from the parameters c , T , and S_o , Eq 2.23 and 2.24. So although not entirely phenomenological like the Darcy equation, nevertheless its partly phenomenological character grants it a success perhaps beyond its merits.

2.6 Fluid pressure in porous structures

The theory of fluid movement in porous structures continues to be based on the original equation of Laplace. He approximated the forces in a meniscus to those acting on the surface skin. Having done so, it followed that the capillarity force acted along the line of contact, and the component of that force in the axial direction was $\gamma \cos \theta$, where γ is the interfacial tension between liquid and vapour and θ the contact angle of the meniscus surface with the solid surface, fig. 2.4:

$$P = h\rho g \frac{2\gamma \cos \theta}{r} \quad \text{(Laplace Equation)}$$

Eq. 2. 25

where P is the pressure difference generated across the fluid meniscus, h is the height to which the liquid rises in the tube in the equilibrium stationary state, ρ is the liquid density, g is the acceleration due to gravity, γ is the interfacial tension

and θ is the contact angle of the fluid meniscus with the wall of the tube. For a fluid which is entirely wetting, $\theta = 0^\circ$, and for an entirely non-wetting fluid, $\theta = 180^\circ$.

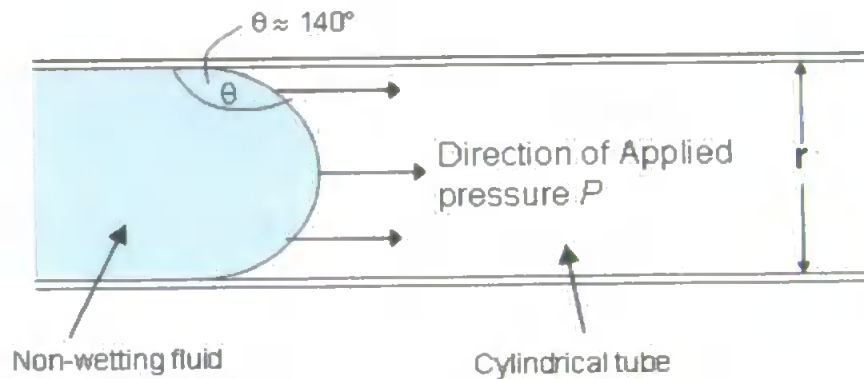


Fig. 2. 4. Example of a non-wetting fluid entering a cylindrical tube, presenting some of variables of the Laplace equation.

The use of these equations has many well known shortcomings, discussed by van Brakel (van Brakel *et al.*, 1981), such as:

- Uncertainties in the values of γ and θ .
- The porous solid is considered to be a bundle of non-interconnecting capillary tubes.
- The voids are all considered to be cylindrical.
- The voids must be of constant diameter along their length.

2.6.1 Fluid movement and contact angle in non-cylindrical tubes

To model the absorption of fluid into a large array of voids within a porous sample, it is necessary to make major simplifying approximations. Pore structure is often characterised quantitatively by interpreting mercury injection measurements in terms of a parallel bundle of cylindrical tubes. This is the most popular model of porous media, but it does not show features such as residual

saturation and capillary hysteresis. The unrealistic nature of such an approximation can be readily demonstrated by the microscopy of a Woods metal cast of void structure (Wardlaw *et al.*, 1987), or the image analysis of tomographs of nuclear magnetic resonance signals (Melrose, 1988). Therefore modelling pores as uniform cylinders can be improved upon by considering the pores to be angular tubes.

The geometry of the interface between the liquid and solid is a crucial factor, much studied in the literature (Borhan *et al.*, 1993; Dong *et al.*, 1995; Ma *et al.*, 1996). However, Ransohoff and Radke (Ransohoff *et al.*, 1988) emphasise that irregular shapes require specific calculations, and that large errors occur if the flow is assumed to occur down a single tube with an effective radius, as in the effective hydraulic radius (EHR) approximation. The case of a non-wetting fluid passing from a cylindrical throat into a spherical pore, or into a pore with a sinusoidal entry, has been calculated by Tsakiroglou and Payatakes (Tsakiroglou *et al.*, 1990). With regards to other geometries, Borhan and Rungta (Borhan *et al.*, 1993) have investigated the wetting of periodically corrugated plates, and there have been many studies of menisci in other non-cylindrical tubes (Dong *et al.*, 1995; Ma *et al.*, 1996; Mason *et al.*, 1991; Ransohoff *et al.*, 1988; Weislogel *et al.*, 1998).

Ma and Mason *et al.* (Ma *et al.*, 1996; Mason *et al.*, 1991) showed the displacement of fluid from tubes of, for example, equilateral triangular or square cross-section can be calculated using the Mayer and Stowe-Princen (MS-P) theory (Ma *et al.*, 1996). This theory can be used to calculate the capillary behaviour of complex pore geometries. If one was to consider a single corner in an m -sided tube with an angle of 2α , with the corner being just one of the m corners in an m -sided tube, the number of sides, m , is related to the half angle of the corner, α_c , by

$$\alpha_c = 90 \left(\frac{m-2}{m} \right)$$

Eq. 2. 26

Each corner of the tube can contain an arc meniscus. The fraction of the tube area occupied by the arc menisci gives the wetting phase saturation:

$$S_w = \frac{\tan \alpha_c}{C_n^2} \left[\frac{\cos \theta}{\sin \alpha_c} \cos(\alpha_c + \theta) - \frac{\pi}{2} \left(1 - \frac{\alpha_c + \theta}{90} \right) \right]$$

Eq. 2. 27

It indicates that the water saturation is reciprocally proportional to the curvature, C , (or the capillary pressure) squared. The equation relates saturation to meniscus curvature at a general contact angle. Ma *et al.* (Ma *et al.*, 1996) showed drainage and imbibition saturations as a function of curvature for square tubes (Fig. 2.5). In general the behaviour is similar to that of triangular tubes, except that the saturations for comparable conditions are all lower.

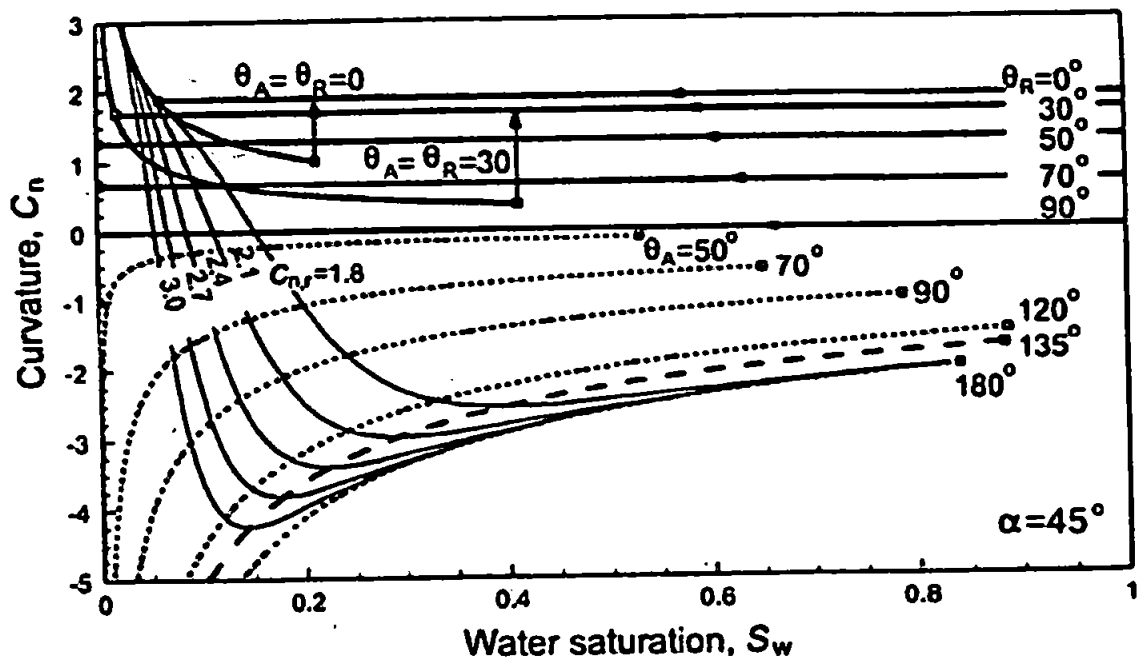


Fig. 2. 5. Effect of contact angle on imbibition capillary pressure curves for square tubes. The minimum of the pinned arc menisci occurs at a contact angle of 135° . At this angle the cross-section of the arc menisci becomes semi-circular (Ma *et al.*, 1996).

Mason and Morrow (Mason *et al.*, 1991) calculated the drainage penetration curvature C_d for all possible shapes of triangular tubes. The amount of wetting phase that drains at the penetration curvature is shown to decrease as aspect ratio of base to height increases, and the remaining liquid is retained in the corners of the triangular pore. The imbibition is also shown to increase by the progressive filling of corners. The corner filling is shown to continue even when the meniscus curvature falls below the drainage penetration curvature, thus giving hysteresis. As the curvature decreases, the filled volume increases until an imbibition threshold curvature is reached at which the menisci in the tube corners overlap. This causes a capillary instability, and the liquid spontaneously redistributes. A portion of the tube length refills and the meniscus curvature jumps to the drainage penetration curvature (Fig. 2.6).

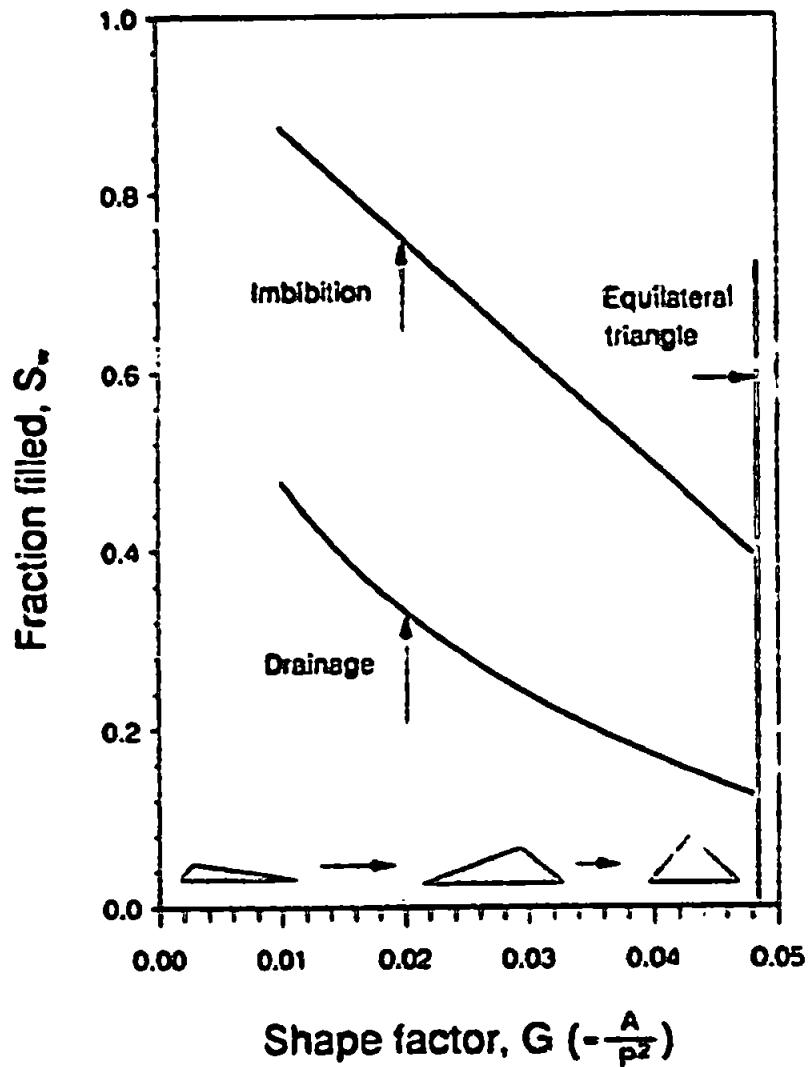


Fig. 2. 6. Fraction of tube emptied at constant curvature, C_d , and filled at the minimum imbibition curvature C_i , vs shape factor (Mason *et al.*, 1991).

Spontaneous redistribution is an example of “snap-off” and may give rise to the entrapment of non-wetting phase. By suitable manipulation of size and shape, pores that drain at the same capillary pressure, but leave behind different volumes of liquid wedges, can be constructed. The natural normalizing shape factor, G , is shown to be A/P^2 (where A is the triangular area and P its perimeter). Tubes with the same shape factor are shown to have the same capillary behaviour even though they are geometrically different (Mason *et al.*, 1991). (Note that there are several different uses and definitions of the term ‘shape factor’ used by different authors cited in this literature review.)

2.6.2 Dynamic fluid motion

To obtain an equation of laminar flow of liquid down a cylindrical capillary tube, the Laplace relation was incorporated into Poiseuille's equation of laminar flow. This approach was introduced by Lucas (Lucas, 1918) and Washburn (Washburn, 1921) and they obtained the well-known relation of

$$x^2 = \left(\frac{r t}{2\mu} \right) \gamma \cos \theta$$

Eq. 2. 28

where x is the distance travelled by the liquid front in time t in a horizontal capillary tube, and μ is the viscosity of the liquid.

There are numerous approximations in this approach. As schematically depicted by the numbers in Fig. 2.7 to which the following numbers in italic parentheses refer, there is much uncertainty about the dynamic contact angle (12), and the exact meniscus shape (8). These easily observable characteristics are related to more subtle factors such as the condition of the tube's inner surface, in terms of microroughness (10,11) and cleanliness. Wetting is also greatly affected by the development of a pre-cursive wetting film (9) which can be anything from a monolayer to a bulk mass of fluid. There are also meniscus distortions due to "fountain" flow close to the wetting front (7) and dynamic effects at the entrance region (1-5) are complicated. There is also an inconsistency between the implicitly assumed flow profiles within different parts of the equations, as the Poiseuille flow velocity profile is incompatible with the concave meniscus shape caused by the force along the contact line (6).

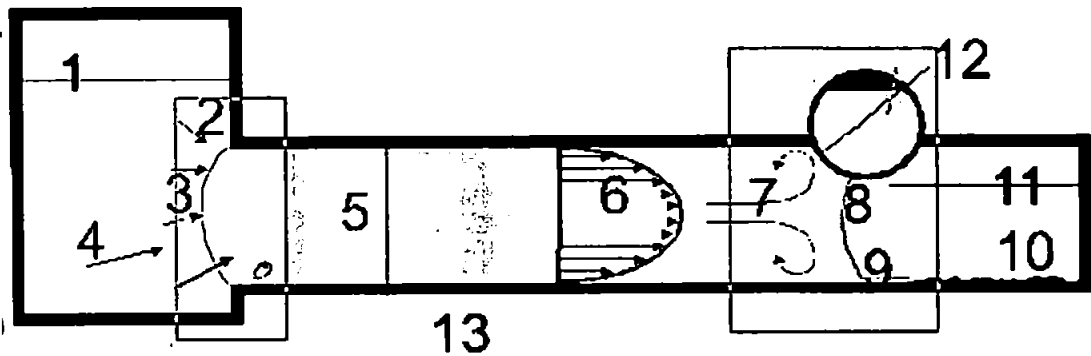


Fig. 2. 7. Overview of influences on imbibition from a reservoir (left) into an evacuated capillary tube (Schoelkopf *et al.*, 2000).

These complexities are rarely addressed in the literature, as there is no point in refining the mathematics of permeation into a void if the gross dimensions of the feature are wrong. Once the gross dimensions approach reality, it becomes worthwhile to revisit the most important complexities of the flow process, as is discussed in section 2.9.

2.7 The Characterization of particles

2.7.1 The packing of particles

The packing ability of monodisperse spheres, which is the simplest system obtained, has been thoroughly investigated by Graton and Fraser (Graton *et al.*, 1935). In addition to the frequently occurring random systems (such as dense random packing with a density 64%), there are six orderly arranged packing systems, ranging from the cubic systems with a solidity of 52% to the rhombohedral system with a solidity of 74%. This latter system is of interest in practice, as a maximum degree of compressibility will yield this structure. The rhombohedral system in turn consists of two different systems, the face-centred cubic and the hexagonal close-packing. Despite the fact that the two systems are

identical with respect to solidity, particle size, void size and number of voids per sphere, fluid flow through these packing systems will differ greatly, and thus have a great impact on permeability (Cumberland *et al.*, 1987).

The introduction of polydisperse size distributions and other particle shapes greatly increases the complexity of the packing problem. Such variables affecting the packing ability are particle shape, size and shape distribution, methods of deposition, surface properties and elasticity (Cumberland *et al.*, 1987). Computer simulation as a tool to study particle packing has received increasing attention in recent years. Most of these studies have been limited to the packing of spheres of different size distributions (Powell, 1980; Reyes *et al.*, 1991; Soppe, 1990; Suzuki *et al.*, 1985). However, Hwang *et al.* (Hwang, *et al.*, 1997) studied the two-dimensional packing of spheroids with various types of size distributions, but of fixed aspect ratio ($=2$) in cake filtrations. An interesting result of the study showed that for all types of size distributions, the porosity was higher for spheroids than for spheres.

The packing of particles depends to a large extent on the particle size. For large particles, the ratio of the surface area to the volume is small and gravitational forces are large compared to colloidal forces (Tiller *et al.*, 1987); beds containing such particles are in general incompressible. For small particles roughly below 10 μm , both repulsive and attractive colloidal forces are large in comparison to gravitational effects, and such beds tend to be compressible. Typical coating pigments with most of the particles below 2 μm can therefore be expected to form compressible beds (Lohmander, 2000c).

2.7.2 Particle size determination

Image analysis is the most appropriate way to estimate particle sizes and shapes. However, it is time-consuming, tedious and expensive and more rapid methods are required for routine analyses. In particle size analysis, it is common to interpret data in terms of the theory applicable to spherical particles. The dimension obtained is the "equivalent spherical diameter" (ESD), which is the diameter of a sphere that would have the same behaviour as that recorded for the sample by the method in question (Lohmander, 2000c). Two such size-determining methods are sedimentation, based on Stokes' law (weight) and light scattering, based mainly on laser diffraction.

For light scattering method, the minimum detectable particle size depends on the size and location of the detector, but a common value is 0.1 μm . Cadle (Cadle, 1965) also discusses some serious problems with the particle size measurements using light scattering: such as the refractive index of the particles is often not available and has to be chosen quite arbitrarily and the scattering pattern is circular only in the case of spherical particles, but for anisometric particles it is irregular and broadened. For the sedimentation method, the particle size must not be too small, as Brownian motion will start to play a significant role (Allen, 1981). The displacement due to Brownian motion will start to predominate greatly at a particle size of about 0.2 μm , and the analysis cannot be considered appropriate below this size for coating pigments dispersed in water (Allen, 1981).

2.7.3 The aspect ratio

The aspect ratio of platey particles like kaolin or talc is commonly defined as the ratio of the diameter across the face of the particle surface to the thickness. Thus,

a higher aspect ratio means a more platey particle. The aspect ratio of acicular (needle-shaped) pigment particles, like aragonite, is commonly defined as the ratio of the length to the diameter. The aspect ratio of these particles is usually determined by image analysis which yields a number-based value (Morris *et al.*, 1965). This method is however time-consuming, expensive and somewhat subjective. More simple and rapid methods are required. Such methods can be based on conductivity measurements, light scattering analysis, etc (Baudet *et al.*, 1993). However, none of these methods are satisfying, as most evaluate only the average aspect ratio and the aspect ratio distribution is neglected.

Lohmander *et al.* (Lohmander, 2000a) discusses the principle method which can be used for platey (kaolin, talc) and acicular (aragonite, PCC) particle shapes, namely Kaolin and aragonite particles. The method is very rapid and easy to handle compared to image analysis, and it is based on a comparison between the results obtained by two different sizing instruments, such as the Sedigraph (based on sedimentation) and instruments using light scattering (Jennings *et al.*, 1988; Slepetyts *et al.*, 1993). Mathematical models of an oblate spheroid representing the platey particles (kaolin) and of a prolate spheroid representing the acicular particle (aragonite), respectively, are applied (Lohmander, 2000a; Slepetyts *et al.*, 1993). A mass (volume)-based shape factor and a shape factor distribution are determined from the principle method as a function of the ESD for pigment particles.

Although the shape factor is closely related to the aspect ratio, it is not proportional to the aspect ratio and should be used to rank the samples, rather than as an absolute value. Although the principal method has lower accuracy than achieved by image analysis, it was found to yield a result that was clearly related to the

result derived from image analysis (Lohmander, 2000c). The shape factor can be a valuable tool for comparison purposes, in regards to the rheological properties of the coating colour and the packing ability of pigment particles in the coating layer (Lohmander, 2000b; Lohmander *et al.*, 2000).

2.8 Different approaches to the modelling of porous materials

2.8.1 Continuum model

There is a different approach in modelling porous structures, which is to bear the complexities in mind, but instead approach the problem from a continuum point of view. Formally the explicit features of the structure that is being permeated disappear, and one deals with bulk parameters such as permeability and diffusion coefficients. If they are merely the result of phenomenological equations, which can never be disobeyed, then their predictive power and general usefulness are very limited. One can present a whole range of Darcy permeabilities of paper coatings, for example, but it is difficult to imagine being able to extrapolate outside the measured sample parameter range to gain predictive insights.

2.8.2 One dimensional approximation

The one-dimensional approximation springs from the implicit assumption that all voids act independently, which in turn usually springs from the basing of a pore size distribution on the first derivative of a percolation intrusion curve. Fig. 2.8 illustrates an example.

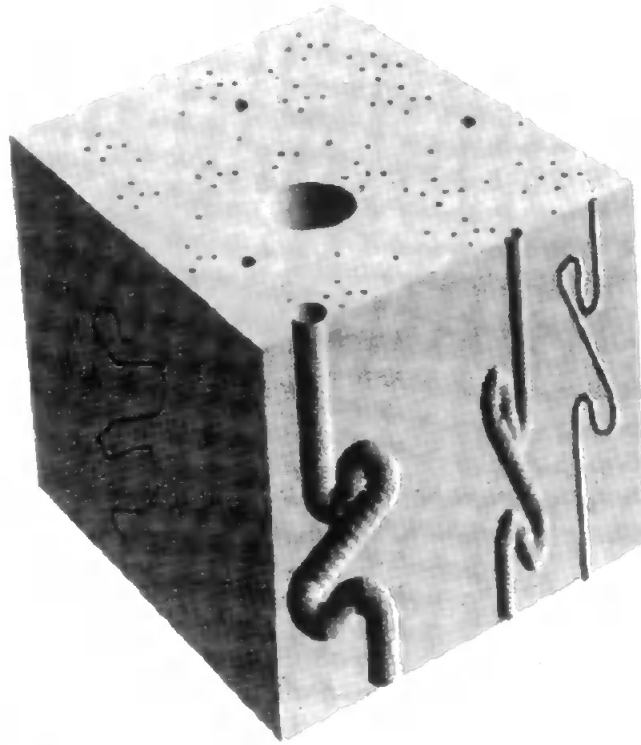


Fig. 2. 8. The one-dimensional approximation.

A percolation intrusion curve, derived from mercury porosimetry, has been converted to a diameter scale by application of Eq. 2.25, and is displayed in Fig. 2.9.

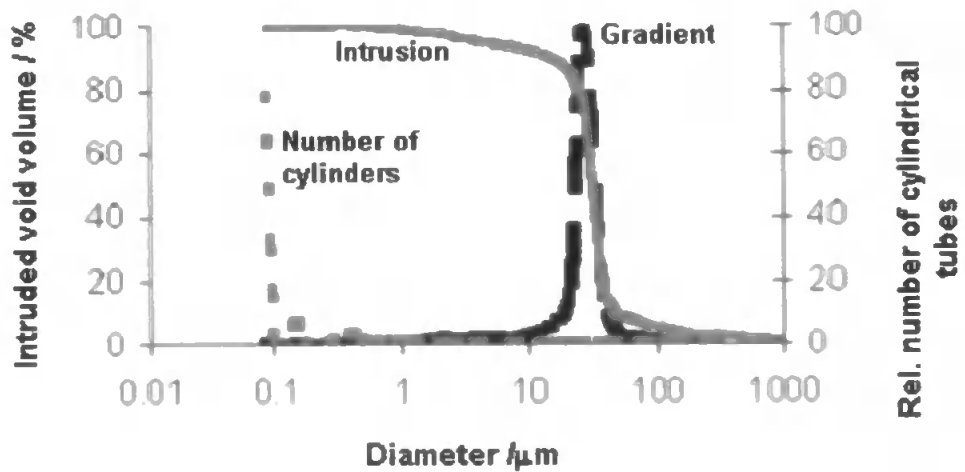


Fig. 2. 9. A percolation curve, its first derivative, and the corresponding size distribution.

The first derivative, shown dashed, has then been converted to a throat size distribution. The distribution is shown as the left-hand dotted line, which refers to the right-hand axis. To achieve the correct volume contribution, it can be seen that the distribution is heavily, and indeed unrealistically, skewed to smaller sizes. The reason for the unrealism is the well-known effect of shielding or shadowing of larger voids by smaller voids during the percolation process.

The resulting one-dimensional approximation can be pictured as shown in Fig 2.8. The void size distribution is that shown on the top surface, exposed to the intruding non-wetting fluid. No information is gained about the rest of the structure – although the diagram shows a typical tortuosity.

One frequent appearance of the 1-dimensional approximation is in the guise of a hydraulic stream tube or effective hydraulic radius (EHR) approximation (Chibowski *et al.*, 1997). Many wicking experiments use this approximation, as briefly reviewed by Schoelkopf *et al.* (Schoelkopf *et al.*, 2001). A typical approach is to apply the Washburn equation to describe the permeation of wetting fluid into the wicking sample. The equation predicts a $\sqrt{\text{time}}$ dependence, which is often observed experimentally, at least to a first approximation. The approach is therefore popular. Again, however, it is difficult to gain predictive power, since effective hydraulic radius is a phenomenological parameter and the surface interaction parameters change unrealistically as the dimensions of the structures change.

2.8.3 Extended one-dimensional approximation

If the tubes are implicitly assumed to be unconnected then one can at least allow for the fact that they behave differently. In particular, if certain tubes fill with a wetting fluid, then they cease to be part of the array being permeated. Yamazaki *et al.* have developed such a model, to simulate the uptake of ethanol into a paper measured by a Bristow wheel (Yamazaki *et al.*, 1993). The model may be expressed mathematically as:

$$V(t) = A_s + \sum_{i=1}^n V_i + \frac{1}{T t_p} \left(\frac{\gamma t}{2 \eta} \right)^{1/2} \sum_{i=n+1}^{end} V_i r_i^{1/2} .$$

Eq. 2. 29

$V(t)$ is the volume uptake at time t , A_s the surface absorption, V_i the total volume of pores of the i^{th} radius, T the tortuosity, and t_p the effective thickness of the paper. The capillary tubes are numbered in decreasing order of radius, and the largest are assumed to fill first. The main limitation is that a '1-dimensional' array similar to that shown in Fig. 2.8 is explicitly assumed. Therefore the phenomenological nature of the radii of the filled tubes again limits predictive power, and there is an incentive to move towards explicitly three-dimensional structures.

2.8.4 Three-dimensional structures

The most obvious approach to generating explicitly three-dimensional structures is to create a network of voids. A prime example of this approach is the work of Scriven (Pan *et al.*, 1995), Fig. 2.10.

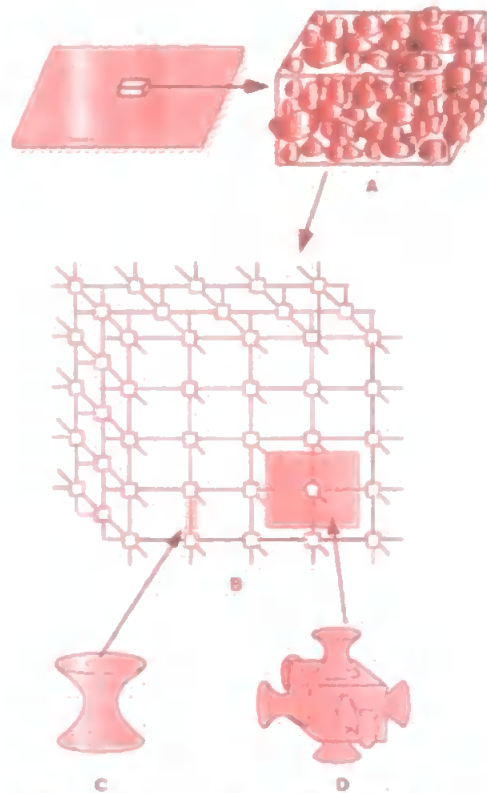


Fig. 2. 10. Network representation of a porous coating (Pan *et al.*, 1995).

We now seem to be considerably closer to reality. However, there are still limitations. The connectivity is fixed at a high value of 6 (Fig 2.10 D) and the size distribution is arbitrary, following a Rayleigh distribution. Also, the shapes of the doughnut-hole throats are arbitrary (Fig. 2.10 C), although of a shape likely to be encountered in reality.

Other workers, notably Toivakka *et al.* (Toivakka *et al.*, 2000), have attempted to overcome the arbitrariness in pore shape. The direct approach to this is via image analysis of thin sections, which have been treated to show clearly what was originally void and what was solid phase. Having done this, one is left with the problem of identifying pores and throats. This can be achieved by eroding the void space as shown in Fig 2.11(a), where each successive erosion is shown as a darker colour. Then the darkest points in the void space must be the centre of pores or throats. However, false centres appear, Fig. 2.11(b), which it is

necessary to eliminate before getting a void structure map comprising individual features such as that shown in Figure 2.11(c).



Fig. 2. 11. Erosion of void space – each successive erosion shown darker. b) Identification of pore centres as maxima of erosion contours (false maxima shown grey). c) Partitioned pore space (Toivakka *et al.*, 2000).

Ideally, one would perform this process on each successive slice of a closely thin-sectioned sample. However, there are two almost insuperable problems. The first is that due to experimental limitations, thin-section slices are a minimum of 5 μm apart, and the second is that it is impossible to calculate the vertical connectivity without the use of some arbitrary rule to connect one slice with another.

To circumvent this problem, Toivakka *et al.* (Toivakka *et al.*, 2000) generated the void structures by computer, having either a cubic, hexagonal, or random packing of spheres. Fig 2.12(a) shows a computer generated random packing of 0.5 μm diameter spheres. Fig 2.12(b) shows the mapping of the void structures achieved by the erosion process, and Fig 2.12(c) the pore and throat map.

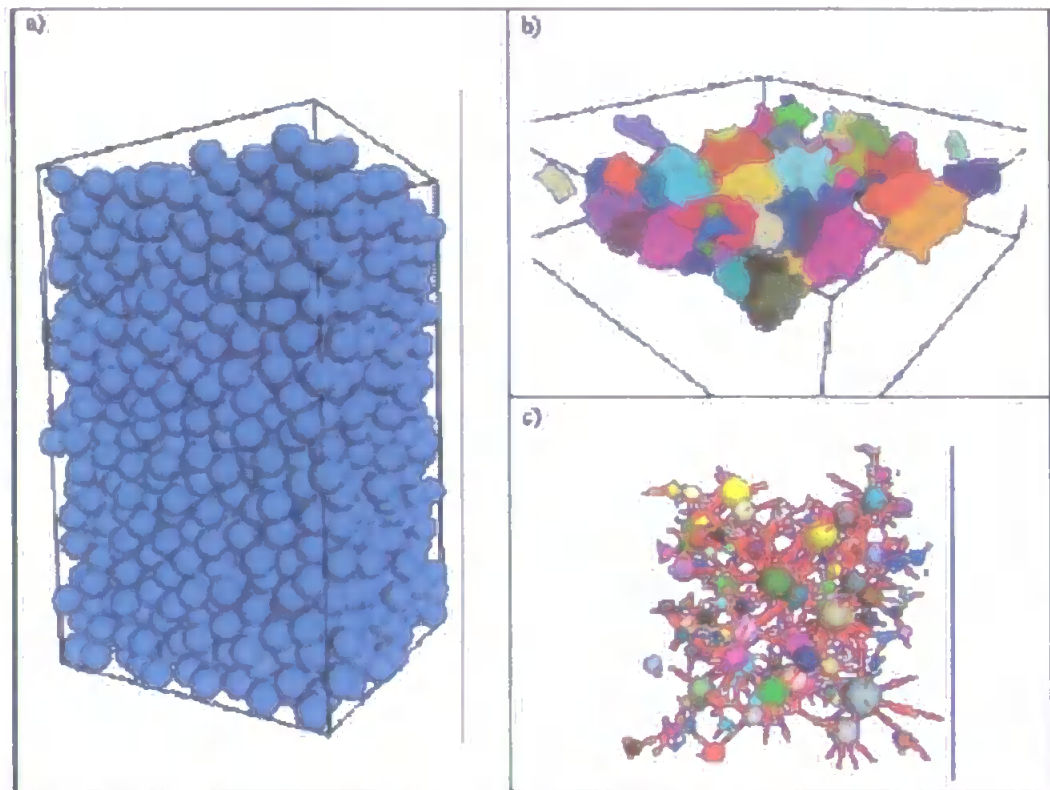


Fig. 2. 12. (a) Computer generated random sphere packing, (b) cross-section through pore space, (c) pore and throat map (Toivakka *et al.*, 2000).

Bousfield (Bousfield *et al.*, 2000) then calculated the flow characteristics of these features by firstly segmenting them, Fig. 2.13.

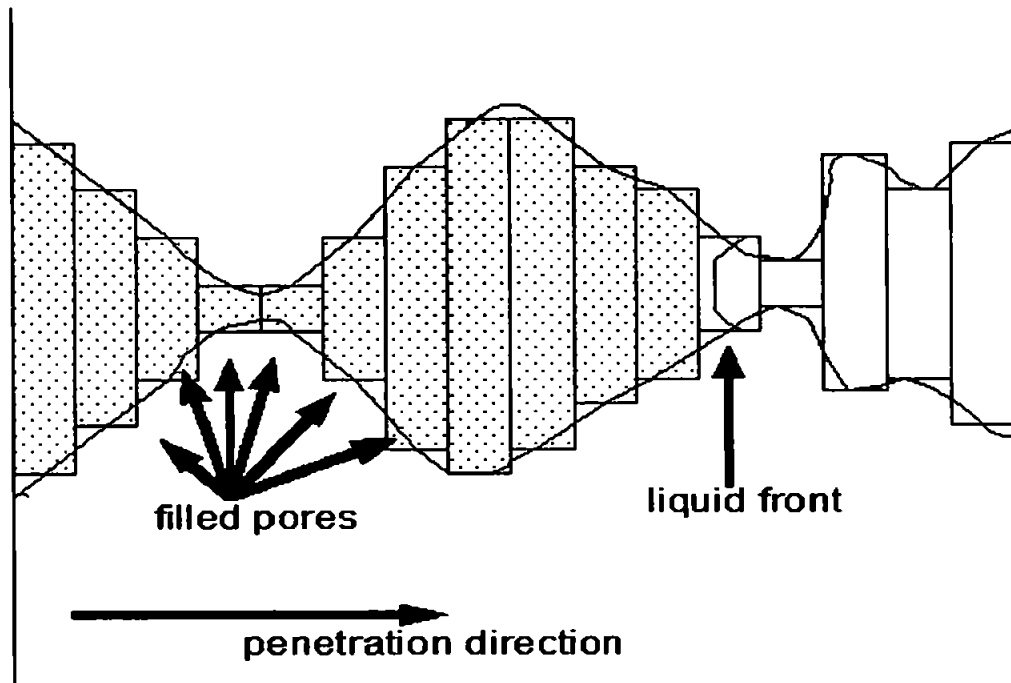


Fig. 2. 13. Segmented pore structure. Capillary pressure is calculated from the contact angle and radius at the liquid front. The resistance to flow is the sum of the hydraulic radii of the filled pores (Bousfield *et al.*, 2000).

Assuming laminar flow, as described by the Poiseuille equation, the resistance to flow, Ω , in a segment i or channel of length dj is

$$\Omega_i = \frac{8 \eta d j}{\pi R^4}$$

Eq. 2. 30

where dj is the length of the segment, and R is the radius. The volumetric flow rate Q through a series of sections is then assumed to be analogous to a series-resistor type of term, namely

$$Q = \frac{\Delta P}{\Sigma \Omega_i}$$

Eq. 2. 31

where ΔP is the difference between the capillary pressure and the externally applied pressure.

Having to computer-generate the void space is clearly a disadvantage with respect to applicability. However, the structures do have the attraction of being fractal. Fractal dimensions calculated for a pore space can be used to investigate e.g. whether a scaling relationship to the pore size distribution exists. The relationship exists if surface areas of pores S_i and corresponding volumes V_i scale as to some characteristic length L_i (Kent, 1991):

$$S_i \propto L_i^D \propto V_i^{D/3} \tag{Eq. 2.32}$$

where D is the fractal dimension. For an Euclidean space $D=2$, and for fractal structures $2 < D \leq 3$. If surface area of pores is plotted against cube root of corresponding pore volumes on a log-log scale, the possible fractal nature of a structure can be assessed. Fig. 2.14 shows the fractal dimensions for mono- and poly-dispersed packings.

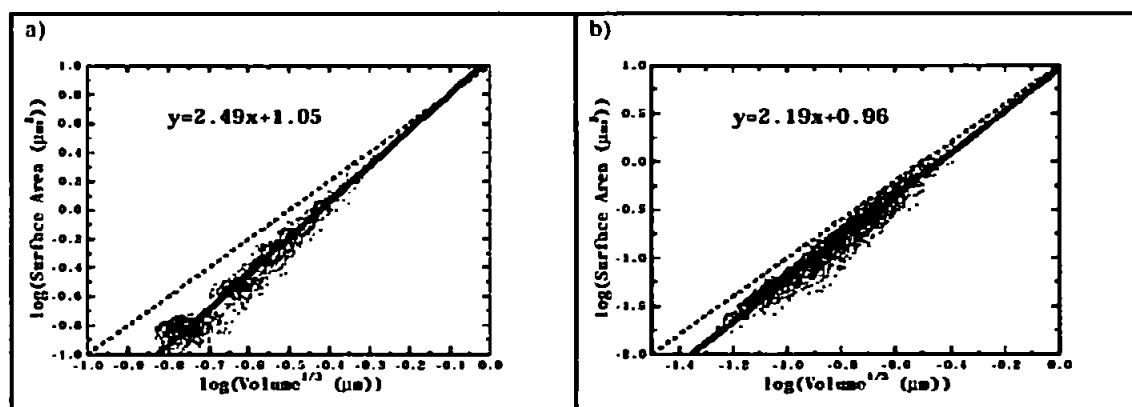


Fig. 2.14. Fractal dimensions of (a) 2.49 for mono-disperse and (b) 2.19 for polydisperse packings. Dotted lines show Euclidean behaviour, which was not observed (Kent, 1991).

There is a mantra that all natural systems must be fractal, whereas of course they do not need to be. Indeed, even the most obvious examples of fractals in nature only exhibit this property over a relatively narrow scale range. Nevertheless, as

we shall see later, one can be equally suspicious of structures at the other extreme, i.e., those that are grossly Euclidean with no fractal nature at all.

At this stage we hit another major problem of computer modelling. We have a void structure which is entirely realistic for packed mono- and poly-disperse spheres. However, the void structure is obviously a gross over-simplification of void structure relative to real coatings structures. Even if it were fully realistic, the complexities of the void structure are such that arbitrary routes have to be chosen through it for fluids to travel. Obviously the widest routes are chosen, but much of the subtlety of the flow patterns is lost. Also, particular packing has to be chosen (Preston, *et al.*, 2002). For example, the structures can be generated to compare with plastic pigment coatings at various latex concentrations, and the uptake compared, Fig. 2.15.

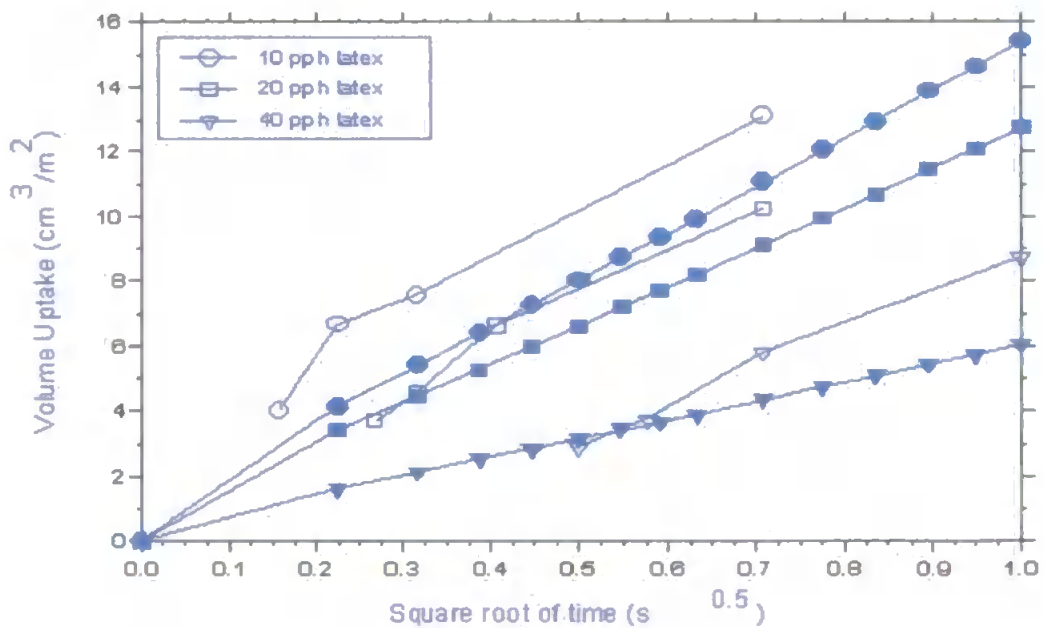


Fig. 2. 15. Volume uptake as a function of time for the plastic pigment coatings at three latex concentrations (Preston *et al.*, 2002).

The open symbols are the experimental results and the filled symbols are the model prediction using an average pore generated by random packing of spheres. This model begins to look like a powerful simulation of observed fluid uptake. The problem, however, is that to achieve correlation with experiment, the fluid contact angle and surface energy have to become fitting parameters rather than absolute physical characteristics. Additionally, the digitized structure gives a series of steps, rather than a smoothly changing geometry, and if one were to take these steps literally, fluid acceleration and inertia would need to be taken into account.

2.8.5 Fibre networks

The next stage along the route to reality is therefore to generate structures more akin to real paper and paper coatings. Typical of this approach are these anisotropic fibre networks generated by Knackstedt *et al.*, Fig. 2.16 (Knackstedt *et al.*, 2000).

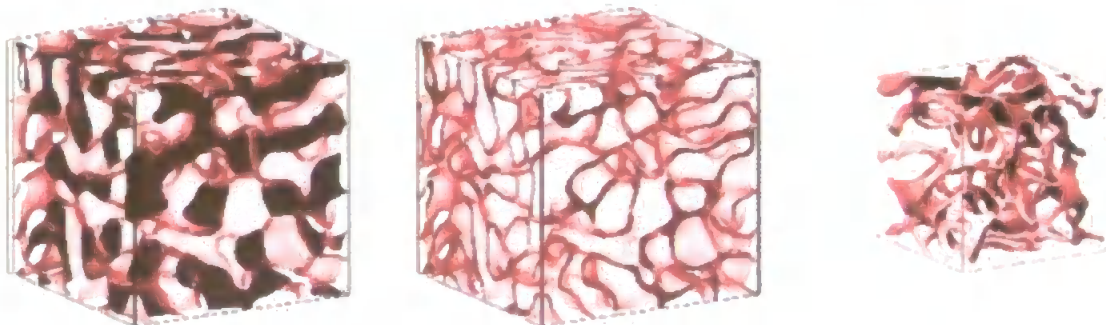


Fig. 2. 16. Computer-generated fibre network structures (Knackstedt *et al.*, 2000).

Other fibre networks have been generated by Niskanen *et al.* (Niskanen *et al.*, 1999). Fig. 2.17 shows a typical example of an isotropic structure, generated by a growth algorithm.

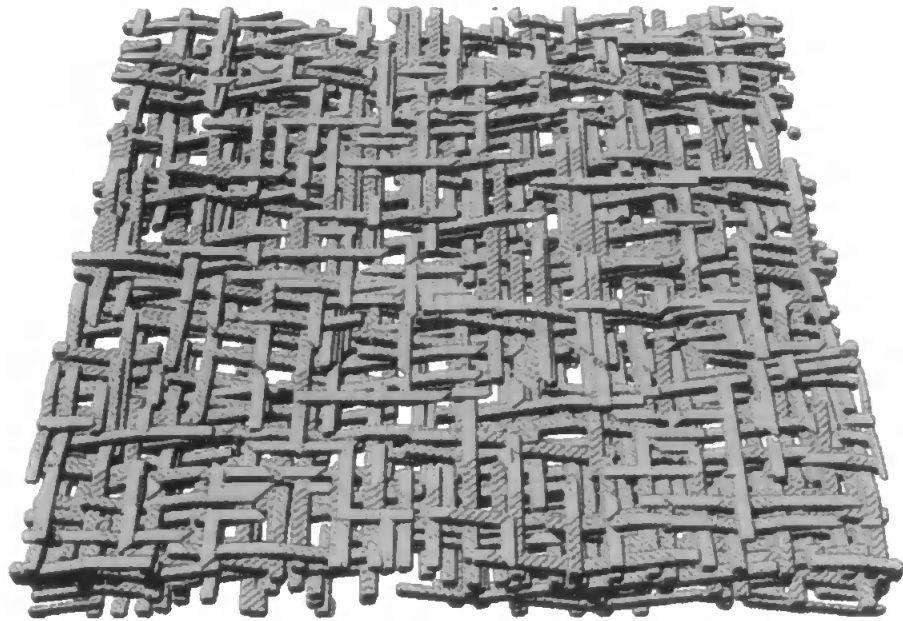


Fig. 2. 17. Computer generated fibrous network (Niskanen *et al.*, 1999).

Both Knackstedt *et al.* (Knackstedt *et al.*, 2000) and Niskanen *et al.* (Niskanen *et al.*, 1999) calculate the flow-through properties using a lattice-Boltzmann method, which is a development of the lattice-gas model. Fluid flow is modelled in terms of distributions of particles moving on a regular lattice. In Fig. 2.18, the fluid velocity field is indicated by contours rather difficult to see in black and white. However, it can be seen that there is high velocity flow in a region towards the top left of the structure.

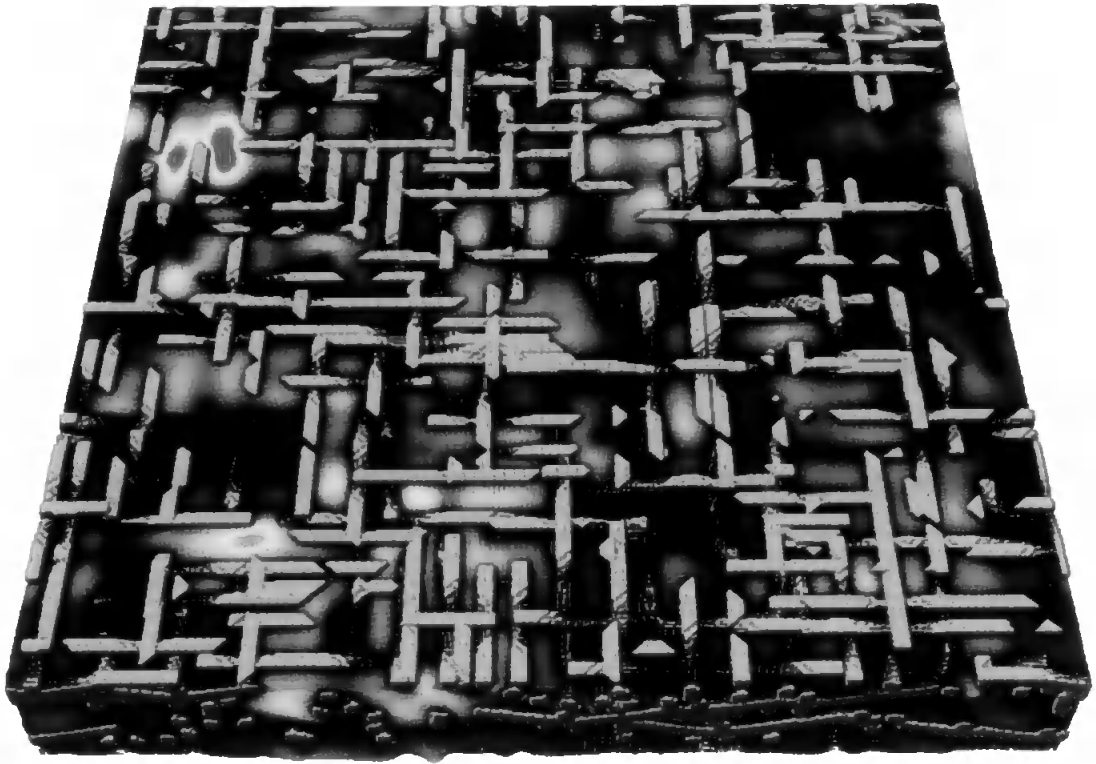


Fig. 2. 18. Contours of the flow velocity field within a computer-generated fibrous network (Niskanen et al., 1999).

The lattice-Boltzmann approach is microscopic rather than macroscopic in nature. It is therefore necessary to jump into the macroscopic realm if the modelling is to be compared with other approaches and experimental data. Niskanen and co-workers do this firstly by fitting experimental porosity / permeability data to an empirically fitted Kozeny-Carmen equation:

$$c = 3.5 \varphi^3 [1 + 57(1 - \varphi^3)] / (1 - \varphi)^{1/2}$$

Eq. 2. 33

where c is the permeability coefficient, and φ the porosity. They then obtain similar trends for simulated and experimental fibrous media.

2.9 Modelling paper coatings with 'Pore-Cor'

2.9.1 Cross-correlation of percolation and permeability characteristics

Despite all the sophistication of computer-generated three-dimensional structures, we are still a long way from reality. Most of the structures have arbitrary connectivities and sizes, or are based on arbitrary spheres computer-packed.

An alternative method to get around this problem is to use 'Pore-Cor'. This network model has already been used to simulate the structures of a wide range of porous materials including sandstones (Matthews *et al.*, 1993), medicinal tablets, (Ridgway *et al.*, 1997) and soil (Peat *et al.*, 2000). However, in using Pore-Cor, we lose the visible degree of reality of the structures such as those shown in Figures 2.18 and 2.19, but we gain a structure which has the same percolation characteristics as an experimental one. The sizes, at least, become believable, because account is taken of shadowing and shielding effects. The void shapes, though, are not at all believable - the Pore-Cor structure is a 10x10x10 cubic lattice of cubic pores, connected by cylindrical throats.

Pore-Cor has been used by Schoelkopf *et al.* (Schoelkopf *et al.*, 2000) to model how a wetting fluid permeates through a void structure. Bosanquet (Bosanquet, 1923) derived an equation describing the inertia of an accelerating fluid entering a capillary tube, Fig. 2.4. The force balance is:

$$\frac{d}{dt} \left(\pi r^2 \rho x \frac{dx}{dt} \right) + 8 \pi \mu x \frac{dx}{dt} = P_e \pi r^2 + 2 \pi r \gamma \cos \theta$$

Eq. 2. 34

where P_e is the external pressure, if applied, at the entrance of the capillary tube (label 1 in Fig. 2.7). If there is no applied external pressure P_e , then it can be shown that

$$x^2 = \frac{2\gamma \cos\theta}{r\rho} t^2 \quad (at \ll 1, P_e = 0)$$

Eq. 2.35

where $a = \frac{8\mu}{r^2\rho}$

The above approximation (Eq. 2.35) is shown to be only valid at very short times ($at \ll 1$) and describes what we refer to as 'inertial flow'. The distance travelled, x , is directly proportional to time t , in contrast to the Laplace-Poiseuille flow regime described by the Lucas-Washburn Equation (Schoelkopf *et al.*, 2000) for which $x \propto \sqrt{t}$. Also in contrast, the distance travelled by inertial flow is independent of viscosity, but inversely related to the radius of the tube r and the fluid density ρ .

Under the conditions of inertial uptake, the regime of Eq. 2.35 describes a monolithic block of fluid entering a tube, driven by the wetting force of the liquid contacting the initial sidewalls of the tube. The fluid is assumed to have a flat meniscus front, except in practice at the actual wall contact, and all parts of the fluid within the tube move at the same rate – hence the independence from viscosity. The flow is retarded more for a high density fluid entering a large tube because the mass of fluid, and hence its inertia, is higher. Also, the higher the viscosity of the fluid, the faster the effect of viscous drag becomes apparent. This effect of inertial retardation and subsequent introduction of viscous drag is discussed quantitatively in by Shoelkopf *et al.* (Schoelkopf *et al.*, 2000).

Two of the parameters which characterise the Pore-Cor unit cell are its pore row spacing W , and its porosity ϕ . Fig 2.19 shows a unit cell, which when repeated infinitely in the horizontal (x and y) directions, has the same porosity and almost identical percolation characteristics to that of an experimental sample of compressed ground calcium carbonate – of a formulation which is a key component of many paper coatings. The details are given by Schoelkopf *et al.* (Schoelkopf *et al.*, 2000). The arrow highlights the extreme heterogeneity of the wetting front, and how the wetting of some pores further into the structure occurs before those nearer to the fluid-exposed top surface. The overall behaviour of the simulation is shown to have good correlation between simulation and experiment, once differing boundary conditions are allowed for.

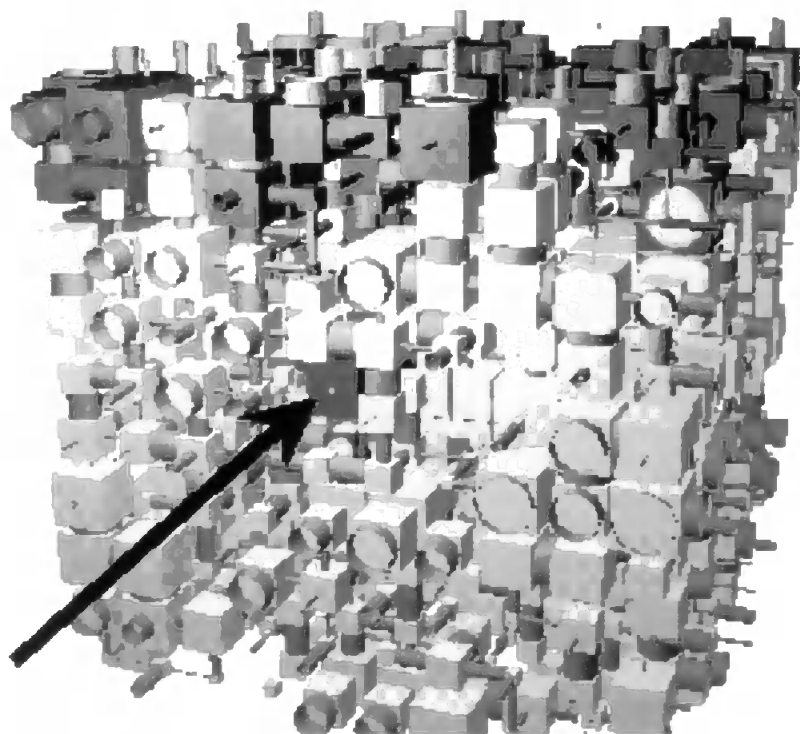


Fig. 2. 19. Water, shown dark, entering the Pore-Cor unit cell of a compressed ground calcium carbonate (Schoelkopf *et al.*, 2000).

2.9.2 Pore and throat shapes

2.9.2.1 Conical throats

Ridgway *et al.* (Ridgway *et al.*, 2001) have worked on Pore-Cor structures including double-conical throats, as shown in the detail of Fig. 2.20. The importance of these structures is that they make an attempt to model the hold-up of non-wetting fluids, and the velocity changes for wetting fluids, caused by geometry changes within void structures. Another benefit is that structures of correct porosity may be generated, without arbitrarily bulking up the pores using a 'pore skew' parameter as in previous works.

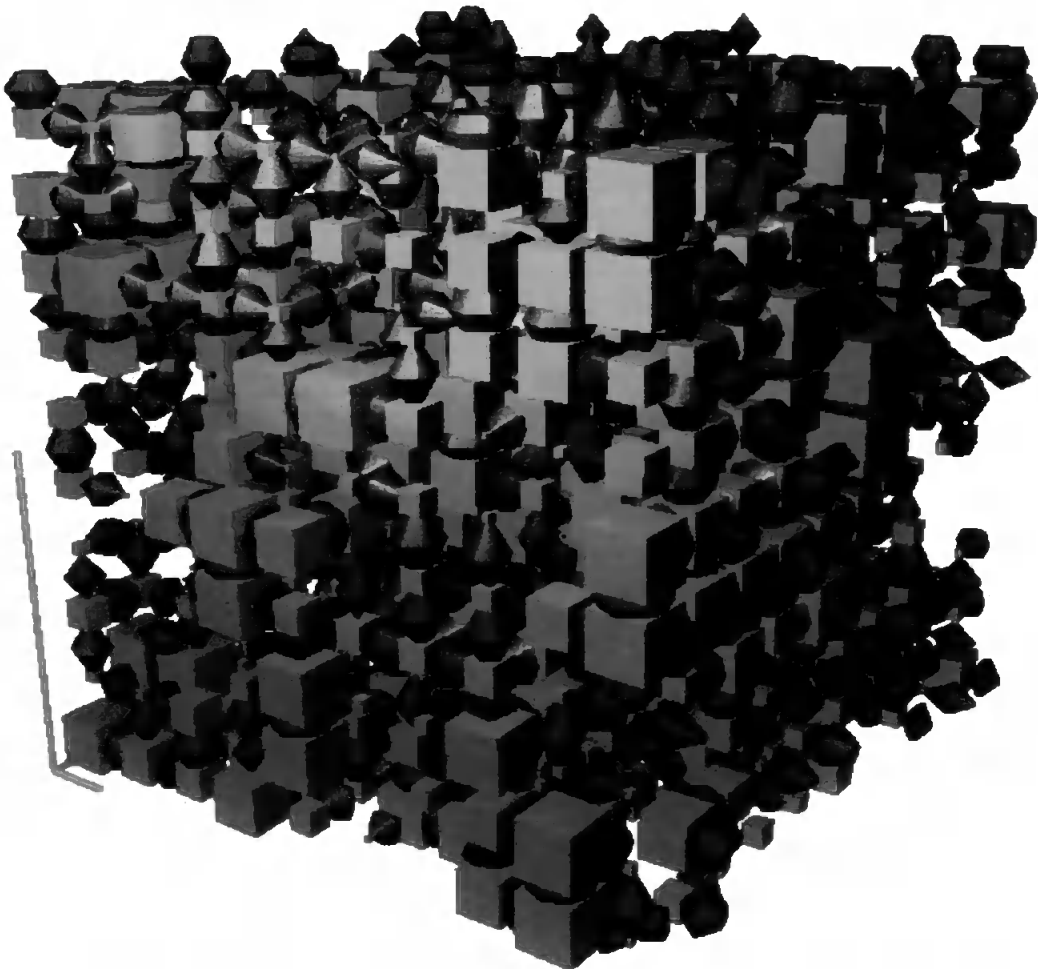


Fig. 2. 20. Pore-Cor unit cell incorporating double-conical throats (Ridgway *et al.*, 2001).

The double cones are shown to be strictly double frustums as the cones are truncated, and their geometry in cross section is shown in Fig. 2.21.

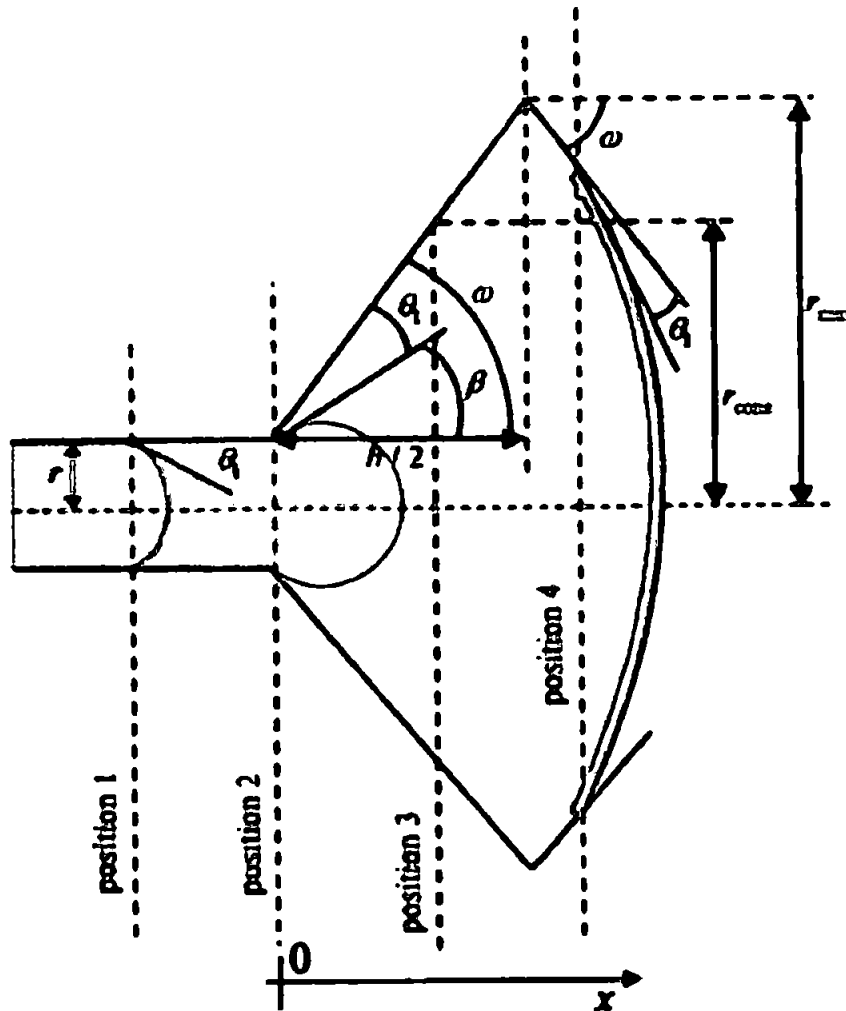


Fig. 2. 21. Cross-sectional view of a nonwetting fluid entering a double-conical throat (Ridgway *et al.*, 2001).

The fluid is initially contained in a cylinder of radius r (In the Pore-Cor network, the double cones are joined directly onto the cubic pores, so these cylinders are of negligible length). Position 1 on the diagram is a typical position of the fluid in the cylinder, in which the fluid would be moving in a piston-like fashion toward the double cone. At position 2 ($x=0$), the fluid begins to enter the diverging part of the double cone, and the meniscus bulges as shown. As the fluid moves to position 3,

the feature radius r_{cone} increases as $(r+x\tan\omega)$, where the maximum radius of the double cone is r_{max} . The hold-up pressure is a function of r_{cone} , and is calculated by balancing the forces on the fluid in the axial direction:

It is shown by Ridgway *et al.* (Ridgway *et al.*, 2001) that as the intrusion of the fluid proceed both into the diverging and converging part of the cone, the hold-up pressure decreases. Therefore, once the applied pressure has been increased sufficiently to overcome the initial hold-up, the intrusion continues spontaneously until the whole divergent double cone is full. The intrusion of the double cone is, therefore, piston-like as for a cylinder. The intrusion in terms of the effective radius r_{eff} was measured and showed on average r_{eff} to be less than r . In this case, the pores within the structure will be more shielded by conical throats than by cylindrical throats of the same entry size. Thus it will take more pressure to intrude the structure with mercury, and the voids will appear smaller when investigated by porosimetry.

The Bosanquet equation was modified by Ridgway *et al.* (Ridgway *et al.*, 2001) for double-conical throats and Fig. 2.22 shows the change in velocity of water and 1,3-propanediol with distance through a double-cone geometry, using a time step of 1 ns .

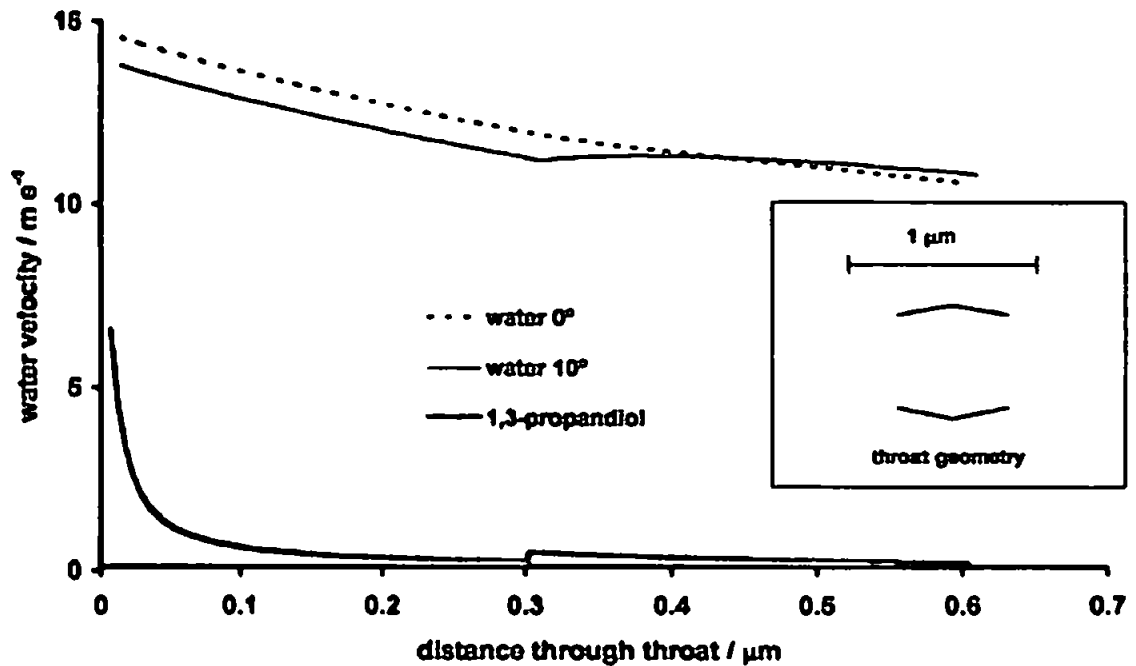


Fig. 2. 22. Change in velocity of water (contact angles 0° and 10°) and 1,3-propanediol with distance through a double-conical throat where r , h , and r_{max} are 0.609 , 0.604 , and $0.76 \mu\text{m}$, respectively (Ridgway *et al.*, 2001).

It can be seen that the velocity of the wetting front of water decreases after the initial entry until it reaches the maximum diameter of the double cone. For the larger contact angle the fluid accelerates before decelerating after the maximum diameter. The velocity for the 1,3-propanediol decreases much more rapidly than that of the water in the diverging part of the double cone. At the start of the second half of the double cone the velocity undergoes a slight increase and then decreases again slowly through to the exit.

2.9.2.2 Capillary element aspect ratio

Ridgway *et al.* (Ridgway *et al.*, 2002) used the Pore-Cor model to show that the aspect ratio of a capillary (defined as its length divided by its radius) plays an important role, in combination with the capillary radii themselves, in determining the filling rate of individual elements. The Pore-Cor model was also used to investigate the distribution of this ratio associated with the capillary throat

elements. The result showed that a preferred pathway of permeation under supersource imbibition conditions was observed when a broad size distribution of capillary elements occurred within a network structure.

2.10 Representative elementary volume

All the models so far described do not represent the heterogeneity in structure of a real sample. This is because the size of the unit cell or representative element of all the computer models which have been discussed is much smaller than the representative elementary volume (REV) of the experimental sample. All the models have implicit or explicit repeating periodic boundary conditions, but the repetition is of the same unit cell, not a different one.

There are two approaches to the overall problem; the first is use of massively parallel computing. Knackstedt and co-workers have shown that such techniques can be applied to lattice Boltzmann techniques. If they could be scaled up several orders of magnitude further, then simulated sample sizes comparable to experimental sample sizes might be achievable.

Another approach, used by Pore-Cor, is to generate different stochastic realisations of the unit cells using a different seed for the pseudo-random number generator. The model is designed so that different structural parameters in conjunction with the same seed of the pseudo-random number generator produce a family or 'generation' of unit cells that are similar to each other – for example, all may have a group of large pores in the same region. Therefore subtle trends can be studied within a family of unit cells isolated from the vagaries of the random generation.

This aspect of the modelling is discussed in detail in a recent publication by Peat *et al.* (Peat *et al.*, 2000). Different stochastic generations can either use the original Pore-Cor optimisation parameters or can be re-optimised to the experimental data. The parameters and procedure are described in more detail elsewhere, (Matthews *et al.*, 1995; Peat *et al.*, 2000; Ridgway *et al.*, 1997). It was shown by Schoelkopf *et al.* (Schoelkopf *et al.*, 2000) that for modelling pigment samples the properties of the two stochastic generations are fairly similar, and one can have confidence that the small size of the unit cell is not producing meaningless results when compared to experiment.

However, with samples that contain a very wide range of voids sizes, covering more than two orders of magnitude, individual permeabilities of unit cells of different stochastic generations can vary widely (Peat *et al.*, 2000). Under these circumstances one must apply the 'Principle of Parsimony' – which is to say that the minimum common information between the results for different stochastic generations is that which is valid. All structures, for example, may possess connectivity, in terms of the simplified Pore-Cor geometry, of between 3 and 3.2 – whereupon it would be a correct inference that the modelled connectivity would genuinely lie within this range, and would be a valid mapping of the actual connectivity of the experimental sample. The Principle of Parsimony, is, in effect, an alternative but useful way of expressing the results of a sensitivity analysis.

2.11 The property 'inversion' problem

In porous structures, one is in fact dealing with a property 'inversion' problem, requiring analogous but much more complicated efforts than those of

Smith and his co-workers studying gas viscosities (Maitland *et al.*, 1981). The property 'inversion' problem arises from the fact that any single porous structure will give rise to a single mercury intrusion curve, and a single permeability. However, the reverse is not true – there are an infinite number of unit cells that correspond to a single permeability or single percolation curve. The temptation is to dodge this problem by applying arbitrary restrictions to the void structure – the 1-D approximations are an extreme example of this. The greater the freedom one allows for the permissible void structure, the wider the range of resulting possible structures, and the greater the necessity of applying the Principle of Parsimony.

For samples with large REV's compared to the unit cell, one could generate an array of stochastic generations assembled together to give an overall unit cell of sufficient size and complexity. Such an approach could be applied to all the different models produced by the growth algorithms of e.g. Knackstedt (Knackstedt *et al.*, 2000) or Niskanen (Niskanen *et al.*, 1999). However, between one stochastic generation and its different neighbour is a boundary condition problem – because one structure no longer joins up with the next. However, with the advent of hugely powerful and highly accessible computers, we should be in a position to obtain modelled structures that are closer to realism.

2.12 Difficulties in proving the hypothesis

Despite all these actual and potential advances in the study of fluids in porous media, all the structures which have been considered are isotropic, and this is obviously an unsatisfactory approximation for a paper coating mainly comprising clay platelets. It is this approximation which will be addressed in this thesis.

The difficulty in considering the effect of anisotropy is that one cannot perform a 'control' experiment. Specifically, it is not possible to compare the permeation into a control sample with permeation into a different sample, which has all characteristics the same except for a changed anisotropy. Thus to date, most discussion of the effects of anisotropy has been based on qualitative inferences from experimental trends. In this work, we will use a computer model to elucidate the effects of anisotropy which are otherwise hidden within the experimental trends. Pore-Cor can accommodate changes in void sizes and connectivity between samples, such that additional changes caused by anisotropy can be revealed and studied.

2.12.1 Approximation framework

The isolation of anisotropy from the many other effects governing the flow of fluids through porous media requires an appropriate level of approximation.

One approach is to stand back from the minutiae of the wetting processes, and consider the overall phenomena in terms of the time-dependent thermodynamics of the processes. Such considerations suggest that the wetting is dependent on the thickness of the sample layer (Marmur, 1992), and the size of the droplet (Marmur, 1988).

An approach which is slightly more mechanistic is to use a hydraulic stream tube or effective hydraulic radius approximation (Chibowski *et al.*, 1997). The surface free energies of powders have been determined in this way by Surface Tension Component theory or the Equation of State approach (Lee, 1993). However, investigations using networks between packed glass capillary tubes have revealed

movements of the liquid front which are totally different to those in an unconnected bundle of capillary tubes (Lu *et al.*, 1995).

So we need an approach which reflects at least some of the complexities of flow in real pore networks. However in doing so, we have to make a series of approximations. These are necessary to make tractable the computation of the wetting process within a porous network. (A tractable solution, for our purposes, is one that takes less than 30 hours to solve on a 1 GHz computer.) However, such approximations must not lose the link between the simulated and experimental porous network, and must not mask the subtleties of fluid flow which stem directly from anisotropy.

We therefore chose to use the simplest possible network which could closely match the experimental porosity and percolation properties, while being capable of being adjusted to different levels of anisotropy. The unit cell of such a network comprised an array of 1000 rectangular cross-section pores, connected by cylindrical or elliptical cross-section throats. All features were equally spaced in each Cartesian direction. Periodic boundary conditions were applied, with each unit cell connected to a replicate in each direction. The void size distributions, spacing between features, connectivity, and local size auto-correlation could be optimised such that the porosity and percolation characteristics were a very close match to those of the chosen experimental samples. The anisotropy could be also adjusted, although structures of nearly any anisotropy could be made to match the percolation characteristics. An independent measure of anisotropy was therefore made and used to adjust the networks, as described in Section 6.7.

Wetting and consequent permeation starts at the contact point or surface between the fluid reservoir or droplet and the porous solid. The first problem is that there is an almost instantaneous wetting jump when a wetting fluid contacts a wettable porous sample (Schoelkopf *et al.*, 2000). We take this into account in the present study, although we approximate it as simply the extent of the jump which occurs too quickly to be measured by our apparatus. Next, the fluid has to accelerate from rest into the various pore features. Both the Bosanquet equation (Bosanquet, 1923) used to describe this process, and the Lucas Washburn equation to which it is related, suffer from two major problems. The first is that there is an inconsistency between the implicitly assumed flow profiles within different parts of the equations. Poiseuillian flow adopts a parabolic flow profile across the tube, with the fastest flow being at the centre of the tube. The capillary force which is assumed to induce it, however, acts along the line of contact of the fluid with the wall of the cylinder, and therefore fluid near the edge of the feature travels fastest. In response, many workers have improved Bosanquet's description of initial, inertial, and continuity influences (Marmur, 1992), and have included a kinetic energy term (Ichikawa *et al.*, 1994). Some recent approaches use the full Navier Stokes equations (Borhan *et al.*, 1993; Moshinskii, 1997).

The second problem is that the Bosanquet equation is essentially a second order differential equation which does not have a simple analytical solution, and can only be solved numerically if the velocity and acceleration are non-zero at time zero when the fluid is at the entrance to the tube. Improvements have been suggested by Szekely *et al.* (Szekely *et al.*, 1971), who conclude that the improvements are important for times of the order of $\rho r^2 / 8 \mu \eta$. Here ρ is the fluid density, r is the feature radius and μ is the fluid viscosity. In the present work, we are primarily interested in the total time it takes a fluid to penetrate a pore, which is typically

much larger than this time threshold, and so the Bosanquet model should be adequate. Because the equation is applied to several thousand features at a time, which are being intruded at different moments, it is essential not to miss the transient effect of inertia as the fluid enters each feature in turn. Hence the time-step for the calculation must be set at no more than 1 nanosecond. This causes all more detailed approaches to the problem, as cited above, to be beyond our limits of tractability when applied to the several thousand features in a unit cell.

The way the fluid subsequently permeates through the structure is then determined by a further series of factors, all of which we have to approximate. Firstly, the sizes and shapes of the voids matter (Ma *et al.*, 1996). Clearly the actual pores and throat geometries are more complicated than our simple simulated shapes. The next factor is that way in which the voids are connected into the network (Adler *et al.*, 1990; Jerauld *et al.*, 1990; Portsmouth *et al.*, 1992). It is known that wetting fluid tends to jump at feature junctions, like those represented in the Pore-Cor model by multiple connected cubic pores (Haines *et al.*, 1996). At the present time, however, there is too little quantitative information about these jumps for them to be included within our model. The surface energy between the fluid and the solid phase is a major factor (Starov *et al.*, 1994), and its dependence on surface history in the present study is discussed in Section 4.2.2.

Finally the density, viscosity and applied pressure of the fluid need to be taken into account (Coulliette *et al.*, 1998; Gane *et al.*, 1999; Ginzbourg *et al.*, 1995). In the present work, the applied pressure is taken as zero, and experimental evidence given for this assumption is described in Section 4.2.1. There is also a workable match between the properties of the test fluid and the simulated fluid, and is discussed in Section 4.2.2.

3. MATERIALS AND EXISTING METHODS AND APPROACHES

3.1. *Types of paper coatings investigated*

In its simplest form a paper coating consists of mineral pigments, binders and air voids. The main constituent of the coating colour (the water-based suspension applied to the printing surface) is the pigment, usually kaolin clay and/or calcium carbonate, and hence this is the most important factor affecting the properties of the coating. Typically, the volume fraction of the pigment is about 70% of the solid material of the coating, a corresponding weight fraction of between 80 and 95% (Lepoutre, 1989). This estimation is based upon a pigment density of 2.6 g cm^{-3} and a density for the rest of the solid material of 1.0 g cm^{-3} .

A latex binder (such as a styrene-butadiene copolymer) and a co-binder (such as starch or carboxymethyl cellulose) are added for the following reasons:

- In order to ensure the required mechanical strength of the coating layer
- To control the water retention of the coating colour during the coating process.
- To act as an adhesive to bind the pigment particles together and to the substrate (O'Shea, 1997).

3.1.1. Mineral pigments

The experiments and modelling were carried out on seven different mineral pigments: Speswhite clay (Speswhite), Amazon 90 SD (Amazon), OpacarbA40, OpacarbA60, Albaglos, Hydrocarb90 and Hydrocarb60¹³.

The pigment slurries can be grouped into three categories; Speswhite and Amazon belong to the Kaolin (clay) mineral group, OpacarbA40, OpacarbA60 and Albaglos belong to the Precipitated Calcium Carbonate (PCC) mineral group, and Hydrocarb90 and Hydrocarb60 belong to the Ground Calcium Carbonate (GCC) mineral group.

Speswhite is a primary coarse-grained kaolin mineral supplied from Imerys, UK, Fig. 3.1; while Amazon is a secondary fine-grained kaolin supplied from Caulim da Amazônia S.A., Brazil, fig. 3.2 (Details of the electron microscopy technique are given in Section 3.2).

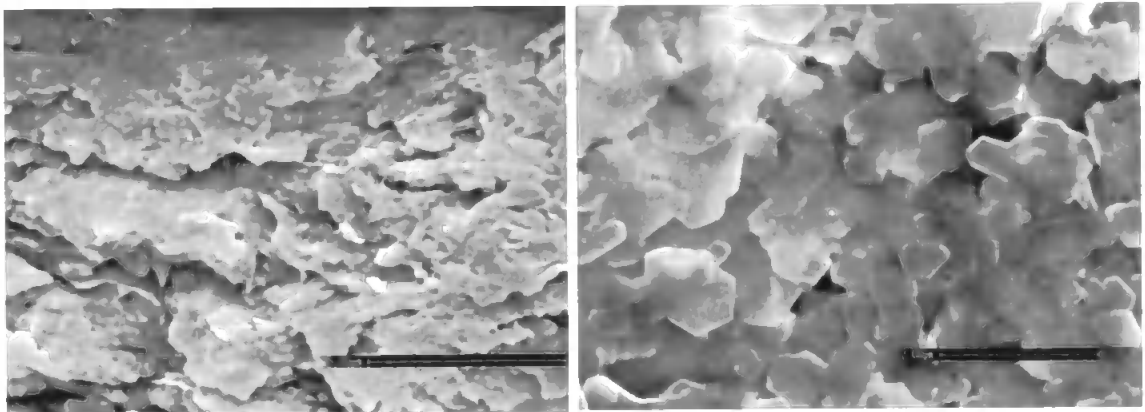


Fig. 3. 1. Slurry sample of Speswhite: scanning electron micrographs of surface (image on left-hand side) and resin-embedded cross-sectional scan (image on right-hand side). Scale bars: 5 μ m for left-hand size image and 2 μ m for right hand size image.

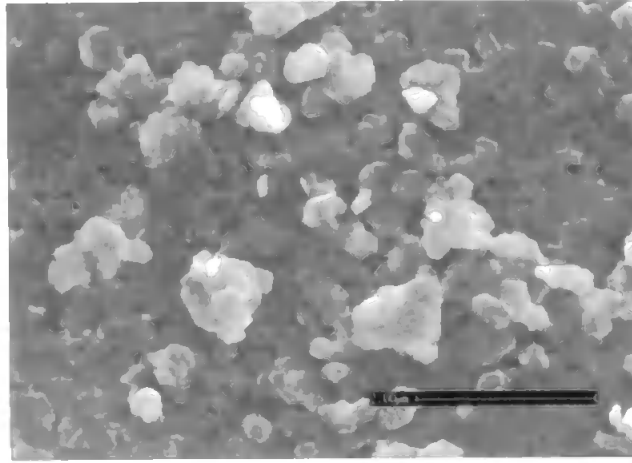


Fig. 3. 2. Slurry sample of Amazon: scanning electron micrograph of surface scan. Scale bar: 2 μ m

Hydrocarb60 and Hydrocarb90 both have a calcitic chemical structure with a rhombohedral morphology and were supplied from Omya Plüss-Staufer AG, Switzerland. Hydrocarb60 is more coarse-grained than Hydrocarb90, as the latter contains 90% of grains less than 2 μ m in diameter, while Hydrocarb60 contains only 60%, Fig. 3.3.

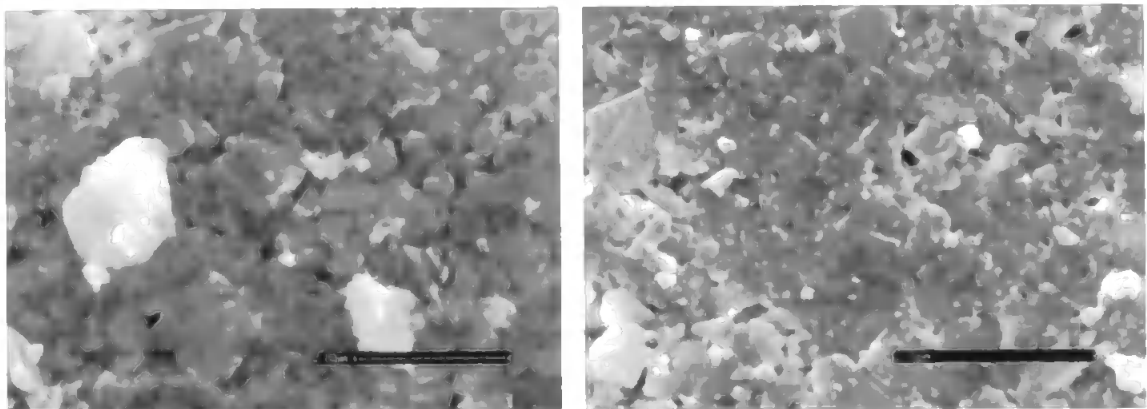


Fig. 3. 3. Slurry samples of Hydrocarb60 (image on left-hand side) and Hydrocarb90 (image on right-hand side): scanning electron micrographs of surface scan. Scale bar: 2 μ m for left-hand side image and 2 μ m for right-hand side image.

Both OpacarbA60 and OpacarbA40 are aragonitic in structure, with an acicular (or needle-like) crystal habit. OpacarbA60 has a median grain size of around 0.60 μ m; while OpacarbA40 has a median grain size of around 0.40 μ m, Fig. 3.4.

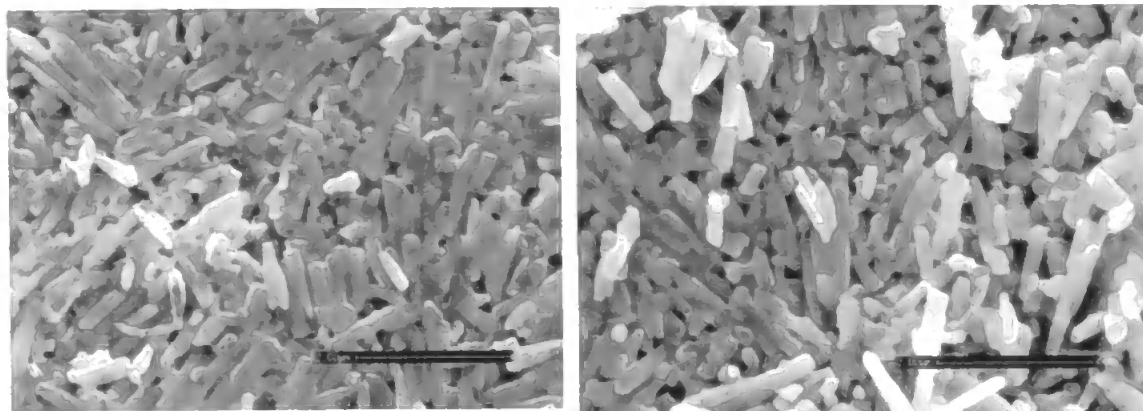


Fig. 3. 4. Slurry samples of OpacarbA40 (image on left-hand side) and OpacarbA60 (image on right-hand side): scanning electron micrographs of surface scan. Scale bar: 2 μ m for left-hand side image and 2 μ m for right-hand side image.

Meanwhile, Albaglos is calcitic in structure, with a rhombohedral crystal habit, Fig. 3.5.

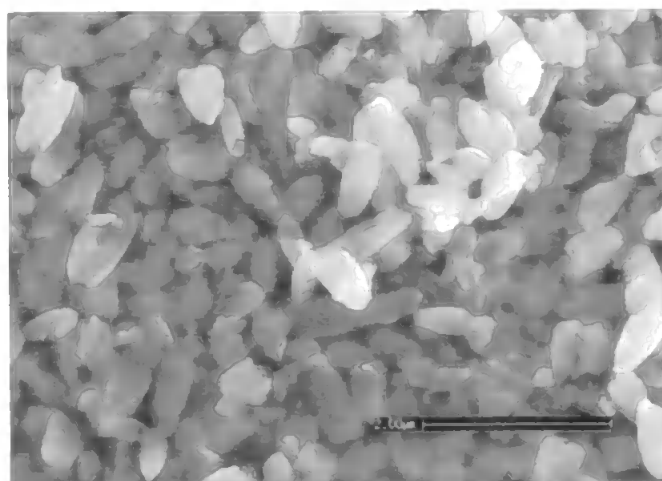


Fig. 3. 5. Slurry sample of Albaglos: scanning electron micrographs of surface scan. Scale bar: 2 μ m.

The aragonite and Albaglos pigments were supplied by Specialty Minerals Nordic Oy, Finland.

3.1.2. Binders

The pigment coating suspensions or 'coating colours' were prepared with two different groups of binders. The first group contained a carboxylated styrene-

butadiene (SB) latex binder and carboxymethyl cellulose (CMC) co-binder; while the second group contained SB latex binder and starch co-binder¹⁴. The coating colours in the first group contained one part CMC per hundred parts of pigment coating (1pph) and 10 pph latex; while the second group contained 6 pph SB latex and 6 pph starch. The SB latex binder (trade name: DPL 935) has a particle diameter of 0.15 μm and a glass transition temperature T_g of 8 °C, and CMC co-binder had an average molecular weight of 45000 and was used as water retention aid.

3.1.3. Coating preparation

All suspensions were prepared in a conventional manner to 60 % solids content by weight and a pH-value of 8.5. The kaolin pigments were received in a dry form and were dispersed in water under conditions suggested by the manufacturers. For Speswhite, 0.3 parts of dispersant per 100 parts of clay by weight (pph) and 0.15 pph NaOH were used; while for Amazon, 0.1 pph dispersant and 0.06 pph NaOH were used. Sodium polyacrylate was used as the dispersant¹⁵. OpacarA40, OpacarbA60, Albaglos, Hydrocarb60 and Hydrocarb90 were all received as slurries.

It was necessary to use three different substrates for the samples. The pigment slurry samples were coated onto an impermeable plastic backing known as Synteape¹⁶, having a coat weight of about 18 g/m². It was used in all permeation experiments except the Gurley method (refer to Section 3.4). The substrate has a slightly rough hooked surface on which the coating can adhere, producing the flexible but stable surface necessary for the ISIT experiments (refer to Section 3.3.1 and 4.2). The pigment slurry samples were also coated onto a base paper

for use in the Gurley method. The coating layer thus obtained was dried using hot-air and infra-red dryers, having a coat weight of approximately 10 g/m².

In mercury porosimetry, Syntepe undergoes mercury intrusion from the sides, which it is awkward to correct for. While for coated base paper, the mercury intrusion shows a bi-modal distribution of the base paper and coating layer, respectively, and is also awkward to correct for. Thus for mercury porosimetry, the pigment coating colours were drawn down on impermeable aluminium backing foils using a wire-wound rod in a bench coater¹⁷. They could flake off from this substrate, but such removal made no difference to the mercury intrusion curves. The drawdown coatings were all produced and dried at room temperature. However, the Albaglos pigment coating colour containing starch and latex was not able to adhere to the surface of the aluminium substrate during the drying process. It was therefore not included in the mercury porosimetry runs.

3.1.4. Sample Selection

The General set of hypotheses for this project (refer to the Section 1.3.1) did not need to be tested on the entire range of samples, but only on a chosen selection of samples, which are referred to as the primary samples. The selected samples were of the four mineral pigments; Speswhite, Amazon, OpacarbA40 and Albaglos, with each one containing the first group of binders, CMC and SB latex (referred to as 'latex' throughout the thesis). These samples exhibited a wide difference in shape, aspect ratio and particle size distribution and created void structures that provided sufficient evidence to validate the hypothesis.

Some of the experimental methods were also performed on some of the additional samples, and are included in the thesis and are referred to as the complementary

samples. However, no full modelling analysis was performed on the complementary samples. To differentiate in the text between the samples containing either starch and latex or CMC and latex, the former will be labelled '-SL' at the end of each pigment name (i.e. Amazon-SL), while the samples containing the latter will be labelled '-CL' at the end of each pigment name (i.e. OpacarbA40-CL).

3.2. Existing techniques for characterising particle and void size distributions

Sedimentation rates were measured by use of a Micromeritics Sedigraph¹⁸, which measures the sedimentation rate of particles in a water column by scanning the column with X-rays (Lohmander, 2000). Median equivalent-spherical diameters based on weight fraction were estimated from Stokes' Law, and also the width of the size distribution. The width, expressed as a number of orders of magnitude, was defined as $\log_{10}(d_{75}) - \log_{10}(d_{25})$, where d_{75} and d_{25} are the diameters of the first and third quartiles of the size distribution.

The aspect ratio was estimated from image analysis of atomic force micrographs (Lohmander, 2000). Aspect ratio is defined for plate-like structures as the ratio of the maximum dimension of the particle, divided by the thickness of the particle; the more platey a particle, the higher its aspect ratio. For acicular (rod-like) structures, aspect ratio is defined as the length of the particle divided by the axial diameter.

A scanning electron microscope (SEM)¹⁹ was used to obtain two types of view of the void structure of the samples, namely that manifest at the surface of the sample and that visible in a cross-section, at magnifications around 40,000 X. For the surface views, the samples were gold plated, whereas for the cross-sections,

the samples were embedded in epoxy resin and viewed in back-scatter mode (McCoy, 1998). The micrographs were used to gain semi-quantitative estimates of appropriate aspect factors, and to estimate the number density of surface throats.

The number density of surface throats (or surface capillaries) was calculated from the electron micrographs of the coating surfaces, covering areas of around 40 μm^2 . Each micrograph was split into four equal areas, and a count made in each area of the number of throats at the surface, which appeared to lead into the bulk of the material (refer to Appendix B for detail of results on experimental method). This was done visually rather than by image analysis, because image analysis algorithms find it difficult to identify throats rather than surface pores in a surface electron micrograph.

The specific surface area of the samples was measured by use of a Micromeritics BET surface analyzer²⁰. The internal surface area of a solid material was analyzed by the instrument from using a nitrogen gas adsorption technique, and measured by use of the BET isotherm method (Webb *et al.*, 1997).

The percolation characteristics of the samples were measured by removal of the coatings from the aluminium foil backing and using a Micromeritics Autopore III Mercury Porosimeter²¹. The maximum applied pressure of mercury was 414MPa (60 000 psia), equivalent to a Laplace throat diameter of 0.004 μm , and the equilibration time at each of the increasing applied pressures of mercury was set to 60s. The mercury intrusion measurements were corrected for the compression of mercury, expansion of the glass sample chamber or 'penetrometer' and compressibility of the solid phase of the sample by use of the following equation from Gane *et al.* (Gane *et al.*, 1995):

$$V_{\text{int}} = V_{\text{obs}} - \delta V_{\text{blank}} + \left[0.175(V_{\text{bulk}}^1) \log_{10} \left(1 + \frac{P}{1820} \right) \right] - V_{\text{bulk}}^1 (1 - \Phi^1) \left(1 - \exp \left[\frac{(P^1 - P)}{M_{\text{ss}}} \right] \right)$$

Eq. 3. 1

V_{int} is the volume of intrusion into the sample, V_{obs} the intruded mercury volume reading, δV_{blank} the change in the blank run volume reading, V_{bulk}^1 the sample bulk volume at atmospheric pressure, P the applied pressure, Φ^1 the porosity at atmospheric pressure, P^1 the atmospheric pressure and M_{ss} the bulk modulus of the solid sample. The volume of mercury intruded at the maximum pressure, once corrected for sample compression effects, was used to calculate the porosity of the sample. The width of the throat size distribution was also expressed as a number of orders of magnitude, and was defined as $\log_{10}(d_{90}) - \log_{10}(d_{10})$, where d_{90} and d_{10} are the diameters at 10% and 90% of the size distribution.

3.3. Existing techniques for measuring permeation

Three existing techniques were used for measuring liquid permeation properties; ink stain density (ISD) tests, involving the use of an Ink Surface Interaction Tester (ISIT) the Dynamic Absorption Tester (DAT) and the Gurley Air Resistance Method (Gurley method). The ISD tests gave an indirect measure of the rate of permeation of a fluid into the paper coatings over time periods greater than 60 seconds (Bristow *et al.*, 1982), while the DAT gave an indirect measure of the rate of permeation over much shorter time periods of less than one second. The 'Gurley' permeameter is used in the Gurley method as an indirect indicator of fluid permeance and obtains an absolute permeability value for a coated paper sample (Institute of Paper Science & Technology, 1940).

3.3.1. Ink stain density (ISD) procedure

As discussed in Section 2.3.2, the ink stain test is considered to be a measure of ink absorption by an optical measure of a change in the reflectance factor of the paper surface. Croda-Red ink was used for the experiment as the ink is essentially non-volatile, and contains magenta particles within an oil fluid phase known as the 'ink vehicle'. The ink has a higher viscosity and hence slower permeation than the more commonly used 'K&N' ink. The ISIT provided a rotating rubber roller in non-sliding contact with a coating on Syntape backing mounted on a delivery carrier, with adjustable roller rotation speed, and adjustable pressure between the roller and the sample. (The instrument also featured a horizontally moving contact roller with pressure sensor, normally used to measure ink tack, which was not used.) The sample was in the form of a rectangular strip of coating measuring 40 mm x 250 mm. The contact speed was set at 1.0 m/s, with a contact force of 500 N. The instrument is shown in Fig. 3.6, below.

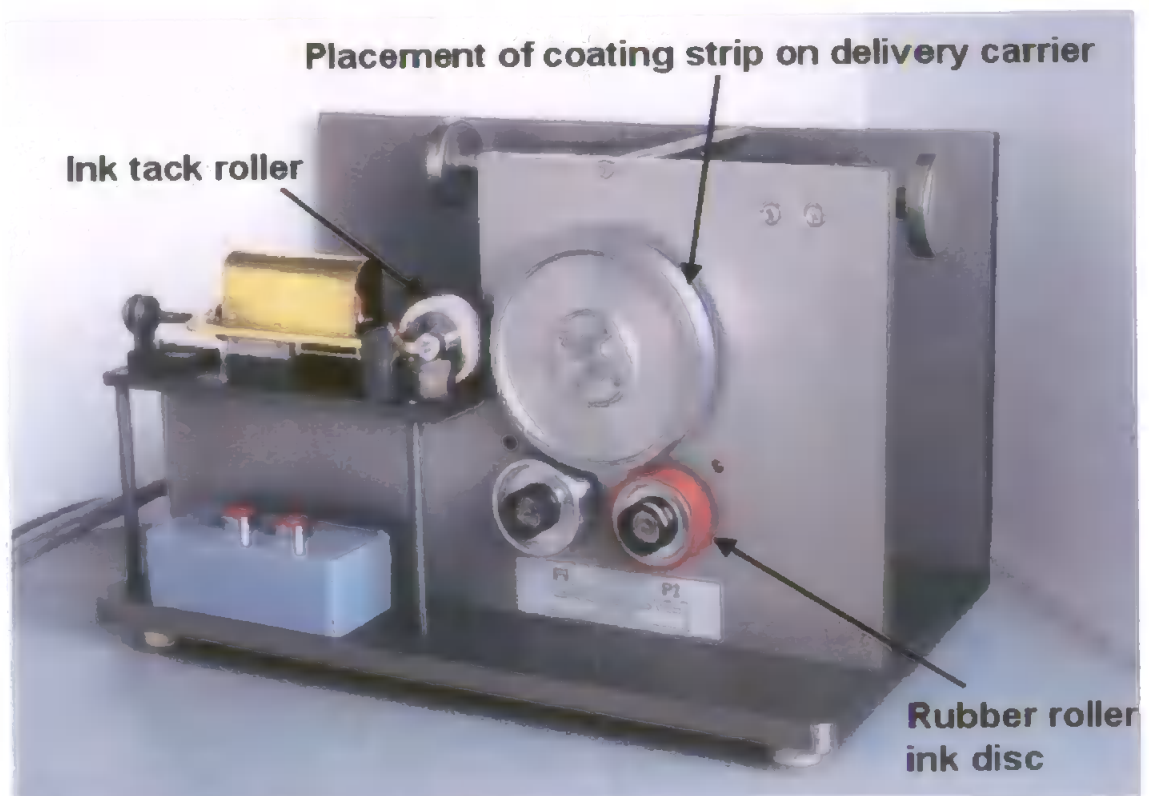


Fig. 3. 6. Application of the ISIT with the ISD experiments.

After transfer from the roller, the ink vehicle permeated into the void structure of the coating. The volume of fluid contained in the pigment particles decreased and the coloured particles began to coalesce on the surface. The coating strips were divided into sections, with any free liquid and un-coalesced particles being wiped from the coating surface after various elapsed times. The colour intensities of the remaining ink stains were measured in calibrated arbitrary units with a Gretag densitometer²². The intensity of the colour is inversely related to the remaining unfilled porosity (background) of the sample. An example is shown in Fig. 3.7, below.



Fig. 3. 7. Example of the ink stain obtained from the Speswhite (A) and Amazon (B) coating strips at various elapsed times (shown in minutes).

There are a number of uncertainties when measuring the change in colour intensity that may affect the reliability of comparing the ink stain density results from the primary samples, collectively. A major concern is the difference in brightness between the two coating categories; the PCC and clay samples. The solid phase of each coating has a defined, but different, brightness depending on light scattering and the absorption coefficient. It therefore follows that for the same relative volume of ink in the pores, the PCC samples and clay samples may have different colour densities, because of the differences in optical properties, and differences in geometry which cause different patterns of filling, and different fluid/solid interactions.

These uncertainties can be overcome by only using the time taken for the colour density of each coating to reach a time-infinity asymptote. At this time, it is assumed that the entire void structure is full of fluid. Differences in the optical properties may alter the shape of the curve to reach this asymptote, and the absolute colour intensity at the asymptote. However, to a first approximation the uncertainties should not alter the time at which the colour density reaches its asymptotic value. Therefore, it is reasonable to compare these times to reach an asymptote with the simulated permeability of the systems.

Hence, the ISD permeation rate for the samples was indirectly calculated as the inverse of the amount of time elapsed to reach the maximum colour density or ink saturation point (T_s), and was given the term 'saturation rate' (R_s):

$$\text{where } R_s = \frac{1}{T_s}$$

Eq. 3. 2

The curve for Speswhite was extrapolated to an asymptote, as there was an insufficient amount of time for the curve to reach its maximum colour density, as shown in figure 3.8.

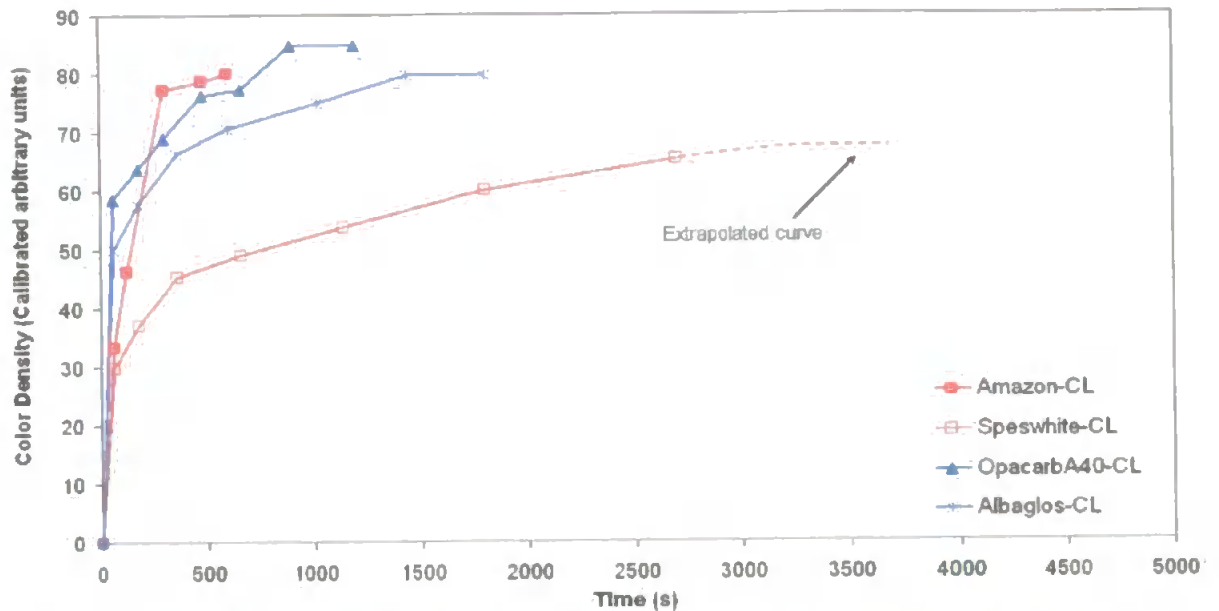


Fig. 3. 8. Comparison of the Setting Rates for coating samples, containing CMC and latex, from ink stain density experiments.

3.3.2. DAT procedure

As discussed in Section 2.3.2, the DAT was used to measure the absorption of a droplet of fluid on the coating samples with Synteape backing, Fig. 3.9 (Technical Association of the Pulp and Paper Industry, 2002).

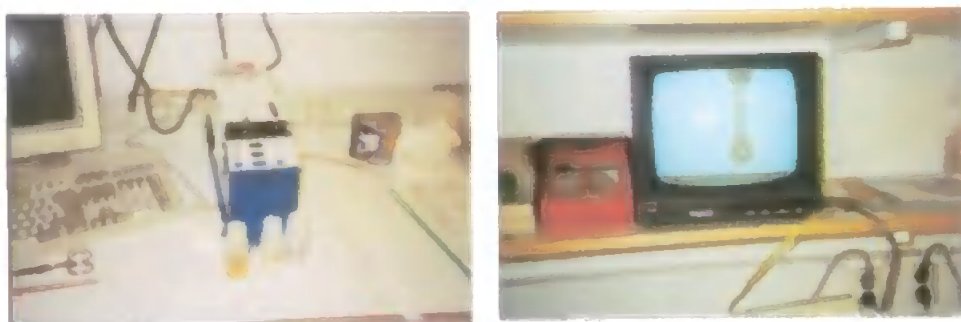


Fig. 3. 9. Dynamic Absorption Tester (DAT) showing the instrument (pictured on the left hand side) and the video camera monitor (pictured on the right hand side).

A cold set oil having a viscosity of 22 centipoises (mPas) was used in these experiments. A fluid drop of a pre-selected volume (approximately 4 μ l) was automatically applied to the flat upper surface of the sample and a number of

images at different time intervals were captured by a video camera. As the droplet absorbed into the coating, it spread over the surface decreasing in height, volume and surface angle. An example of the absorption of a droplet is shown in fig. 3.10.

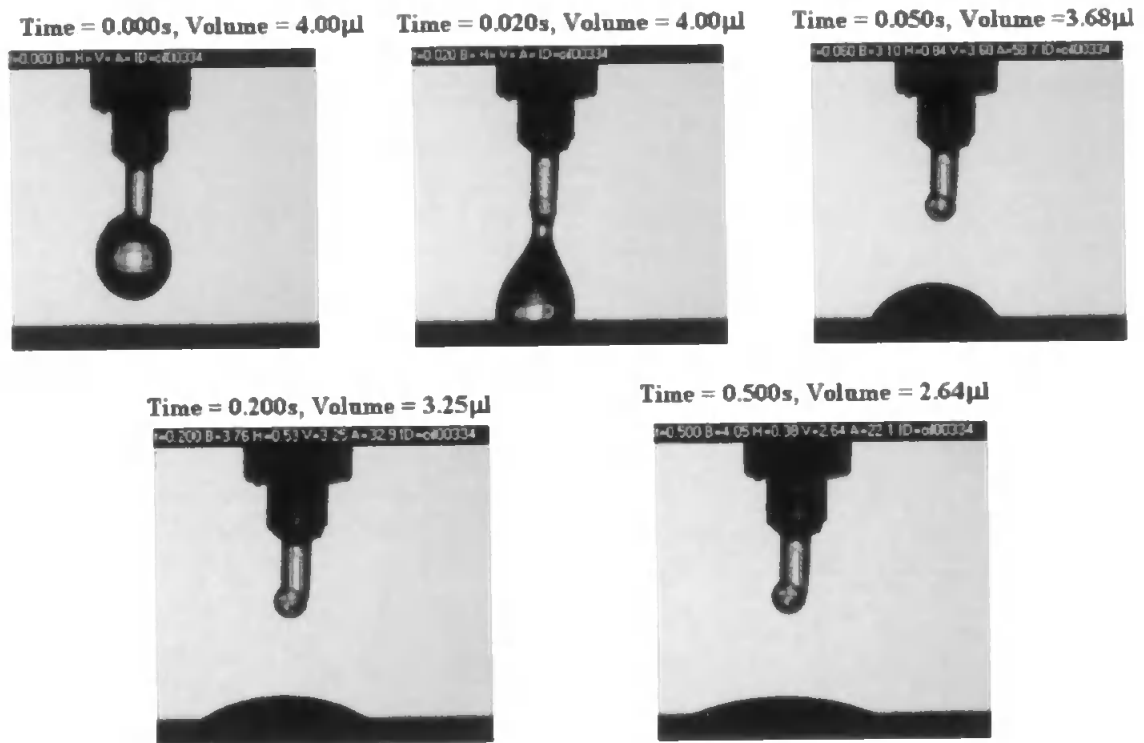


Fig. 3. 10. A number of images at different time intervals of a fluid droplet applied to an Amazon clay coating surface.

The surface angle is the angle between the droplet and coated surface, and is sometimes referred to as the contact angle, although the term surface angle emphasises that the contact is with a relatively large area of surface. The DAT is limited to calculating surface angles no lower than around 17°, as lower angles would have a high degree of uncertainty due to the pixel limitations of the DAT instrument. The DAT also assumes that the droplet spreads on the surface at an equal distance in every direction, and forms a half-sphere with an equal radius in every direction. The measurements were therefore taken near the beginning of absorption to ensure more consistent measurements, as at longer time periods the droplet begins to spread unevenly, and alters from a half-spherical shape. The

unreliability of the DAT measurements at longer time scales can be seen in Fig. 3.11, as the measurements on the graphs follow an uneven trend at the long times.

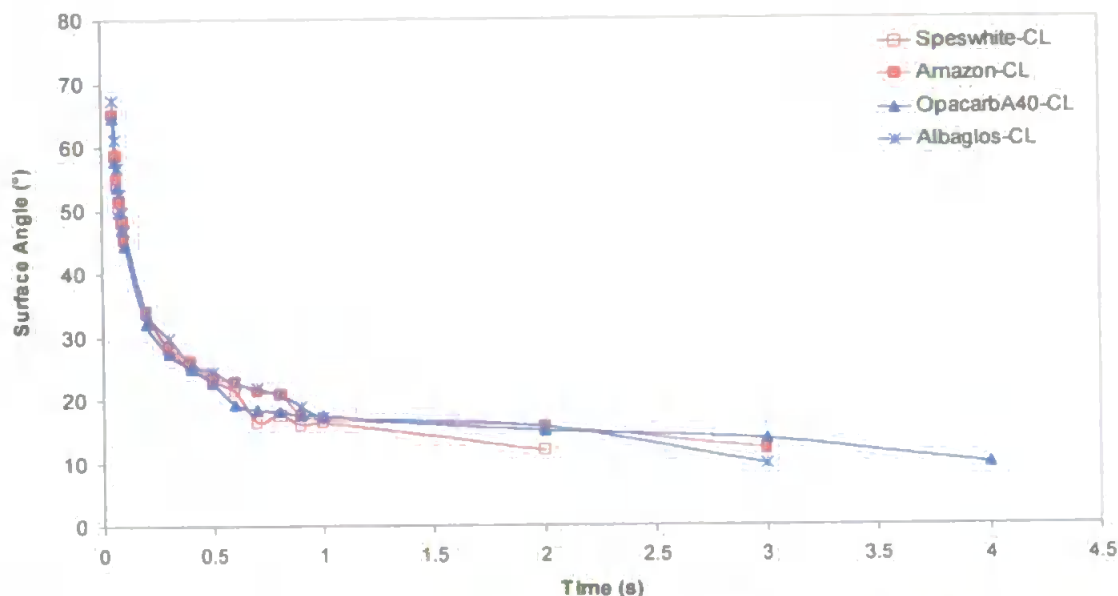


Fig. 3. 11. DAT permeation curves for the primary samples, showing the surface angle of the droplet with time.

The height of the droplet (h), diameter of the base (d_{base}) and the contact angle of the droplet was measured by the DAT at a series of time intervals (t_i). Each measurement of height was normalized (h_n) with respect to the contact surface area (S_d) of the droplet at time, t_i . An indirect measurement of the absorption (A_s) was calculated from subtracting the normalized height of the droplet (h_n) at each time interval from the normalized height of the droplet at the initial time of contact (h_0), as shown below:

$$A_s = h_{ni} - h_{n0}, \text{ where } h_n = \frac{h}{S_d}, \text{ and } S_d = \pi \left(\frac{d_{base}}{2} \right)^2$$

Eq. 3. 3

An absorption rate (R_A) was also calculated for each sample from the initial contact time (t_0) to a time (t_1) of 0.4 seconds, and was used as an indirect measure for the DAT permeation rate:

$$R_A = \frac{A}{t_1 - t_0} \rightarrow R_A = \frac{A}{0.4}$$

Where $t_1 = 0.4 \text{ s}$ and $t_0 = 0 \text{ s}$

Eq. 3. 4

The availability of the DAT instrument was limited during the project due to travel restrictions, and as a result, only the Kaolin and PCC coating samples, with CMC and latex, were tested with the instrument.

3.4. The 'Gurley' Air Resistance Method (Gurley method)

As discussed in Section 2.3.2, the Gurley method measures the amount of time required for a certain volume of air to pass through a test specimen (Physical Committee of the Process and Product Quality Division, 1946; Institute of Paper Science & Technology, 1940). The air pressure is generated by a gravity-load cylinder that captures an air volume within a chamber using a liquid seal. The pressurized volume of air is directed to the clamping gasket ring, which holds the test specimen. Air resistance is the resistance to the passage of air, offered by the coated paper structure, when a pressure differential exists across the boundaries of the specimen. It is quantified by obtaining the time for a given volume of air to flow through a specimen of given dimensions, under a specified pressure, pressure difference, temperature, and relative humidity.

The Gurley method measured the air resistance of approximately 6.4 cm² circular area of a coated paper using a pressure differential of 1.22 kPa. Due to limited availability of the apparatus, coated paper samples of only four different mineral

pigments were prepared, ranging in coat weight from about 10 to 13 g/m². The coated paper samples were as follows: Speswhite-CL (coat weight- 10.8 and 13.2 g/m²), Amazon-CL (coat weight- 9.2, 9.7 and 12.6 g/m²), OpacarbA40-CL (coat weight- 10.1 and 12.6 g/m²) and OpacarbA60-CL (coat weight- 9.5 and 11.4 g/m²). The results of the test are reported as seconds per 100 ml cylinder displacement per 6.4 cm², and are commonly referred to as Gurley seconds. The actual volume of air that passes through the coated paper is 106 ml at 1.22 kPa, or 107 ml at atmospheric pressure.

Five tests were run for each coated paper sample with the average time being used. A relationship between time in Gurley seconds, t , and air permeance (AP), measured in micrometers per Pascal second, is shown below (referenced to the density at 1.22 kPa):

$$AP = \frac{135.5}{t}$$

Eq. 3. 5

where t is equal to seconds per 100ml cylinder displacement.

An impervious metal plate with a tiny hole, having a diameter of 42.5 μm and a thickness of 300 μm, was used to calibrate the Gurley instrument. The flow of air through the calibration plate was verified from Reynolds Equation (Eq. 2.11) to be approximately 0.002, so the flow was well into the laminar region.

An absolute permeability for the calibration plate was calculated by combining Darcy's law (Eq. 2.2 and Eq. 2.6) with the 'Hagen-Poiseuille' equation (Eq. 2.10) to obtain the following equation:

$$k = \frac{\pi r^4}{8A},$$

Eq. 3. 6

where k refers to the absolute permeability of the material, r refers to radius of the hole and A refers to the cross-sectional area of the plate.

The permeability of the calibration plate was calculated to be equal to approximately $1.25 \times 10^{-16} \text{ m}^2$, having a flow time through the hole of 23.8 Gurley seconds. The absolute permeability of the sample runs (k_{samp}) was calculated from multiplying the permeability of the calibration plate (k_{cal}) by the ratio of the air permeance of the sample (AP_{samp}) and calibration plate (AP_{cal}) :

$$k_{\text{samp}} = k_{\text{cal}} \times \frac{AP_{\text{samp}}}{AP_{\text{cal}}}$$

Eq. 3. 7

3.5. Use of existing models for measuring permeation

3.5.1. Application of the Aligned Cylinders model

The aligned cylinders model (also known as the straight capillarie model) is the simplest capillarie model representing a porous medium by a bundle of straight, parallel capillaries (Scheidegger, 1974), and it is discussed in more detail in Section 2.5.3. Permeability calculations were carried out on the primary samples using this model.

The aligned tubes are assumed to stem from the observed surface throats, and to extend indefinitely normal to the surface, without lateral inter-connections. The total volume-flow Q through a capillary would be then given by Poiseuille, as shown in Eq. 2.10. If there are n such capillaries per unit area of cross-section of

the model an 'average' radius (r_m) of the capillaries is used, and the flow per unit area q (or macroscopic velocity) will be

$$q = -\frac{n \pi r_m^4 \delta P}{8 \mu l} \quad , \quad \text{Eq. 3. 8}$$

As the flow can also be expressed by Darcy's law

$$Q = -\frac{k \delta P}{\mu l} \quad , \quad \text{Eq. 3. 9}$$

The combination of Eq. 3.8 and 3.9 results in an expression for permeability:

$$k = \frac{-n \pi r_m^4}{8} \quad \text{Eq. 3. 10}$$

This model is implicit in the traditional interpretation of mercury porosimetry curves, in which the first derivative of the intrusion curve is used to determine the void size distribution. However, no inertial effects are taken into account (Schoelkopf *et al.*, 2000), nor the network interconnectivity, which becomes important when the fluids have travelled through the surface throats. The number density of surface throats for each sample and the radius of the median void size (d_{50}), which was measured by mercury porosimetry, were used as a measure for n and r_m , respectively.

3.5.2. Application of the Kozeny models

The Kozeny models (see Section 2.5) were used to calculate the permeability, k , of the coating samples by the following equations:

$$k = c\phi^3 / S^2$$

Kozeny

Eq. 3. 11

$$k = \phi^3 / [5S_o^2(1-\phi)^2]$$

Kozeny-Carman

Eq. 3. 12

In the Kozeny equation, S refers to specific surface area per unit bulk volume, while in the Kozeny-Carman equation, S_o refers to the specific surface area exposed to the fluid per unit volume of solid material. ϕ refers to the fractional void volume in the bulk samples (porosity), and c is a constant and shown for particles with a circular cross-section to have a value of 0.50. The specific surface area of the samples, S , was measured by BET surface analysis (see Section 3.2), while the porosity, ϕ , was measured from mercury porosimetry.

3.5.3. Application of the Effective hydraulic radius (EHR) model

The simplest model of wetting is to equate the capillary wetting force to the force required for laminar flow as described by the Poiseuille equation. This results in the Lucas-Washburn equation (Lucas, 1918). The distance travelled, x , by a liquid front in time, t , is then:

$$x = \sqrt{\frac{r_e \gamma t \cos \theta}{2\mu}}$$

Eq. 3. 13

The radius of the median void size (d_{50}), which was measured by mercury porosimetry, was used as an approximate value for the effective hydraulic radius, r_e .

4. DEVELOPMENT OF NOVEL EXPERIMENTAL METHODS

Both the Prufbau Printability tester (PPT) and the Ink Surface Interaction Tester (ISIT) were tested for its effectiveness in measuring and comparing the absorption rate of various paper coatings at short contact times (less than 1s). These two absorption test methods are referred to as the Prufbau Printability Absorption Method (PPAM) and the Ink Surface Absorption Method (ISAM), respectively. The difference between the two instruments pertains to the operation and arrangement of the delivery carrier.

4.1 Prufbau Printability Absorption Method (PPAM)

4.1.1 Experimental procedure

The Prufbau Printability Tester (PPT) was first tested for use as a potential absorption technique on a range of different coating samples. Coating colours with no binder additives (slurry) or with just CMC were found to not have enough adhesive strength to remain on its Synteape backing during experimental runs. These coating samples were therefore not tested with the instrument.

With the PPT, the delivery carrier is a rectangular-shaped metal platen that travels on a flat moving conveyer belt, with the printing and ink disc on each end, as shown in Fig. 4.1.

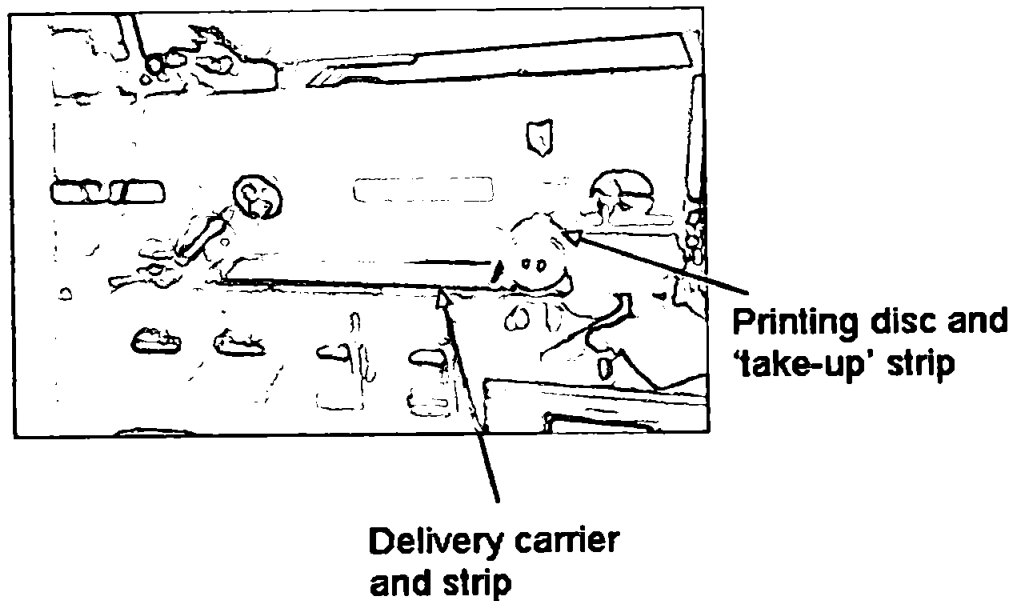


Fig. 4. 1. Picture of the Prufbau Printability tester (PPT).

A coating strip is placed on a platen, and enough oil was distributed on and delivered from an ink disc to the coating such that its void structure was close to saturation (80 to 100% saturated). A metal rather than a rubber ink disc was used as it gave much better oil distribution on the coating strip. A cold set oil of 110 centipoises was used as the delivered fluid since they were non-setting and contained no solid particles.

A 'dry' coating strip (2cm width x 20cm in length) of the same type was wrapped around the printing disc, and came into contact with the saturated coating strip on the platen. The saturated and 'dry' coating strips had approximately a 1mm contact delivery length and the Prufbau Printability Tester was run at controlled contact speeds of 0.5 and 1.0 m/s, which is equated to a contact time of 0.002s and 0.001s, respectively. The contact pressure between the saturated coating strip and the 'dry' strip was set at a pressure of 1200 N (equivalent to a line load of 30 kN m⁻¹). This caused the oil to be delivered from the saturated carrier strip and to

be absorbed by the printing or 'take-up' strip. The amount of fluid uptake could be measured gravimetrically.

4.1.2 Theory

The 'saturated coating sample was used to deliver a quantity of fluid to the 'dry' coating sample in a manner such that flooding of surface pores did not occur. Delivery from the saturated coating strip to the 'dry' strip was by direct contact. The strength of the capillary suction and the amount of capillaries on the coating surface played a dominant role in determining the amount of oil absorbed. The two strips were of the same coating colours and therefore enabled the delivery/uptake system to be symmetrical. There would therefore be no need for mathematical assumptions and operations (like the 'Bristow Wheel' experiment) to solve the fluid delivery equations. However, there was a need to extrapolate out the effects of contact pressure by running a series of experiments at different contact pressures.

4.1.3 Disadvantages

The disadvantages of the PPAM were discovered after performing experimental trial runs of some of the coating samples, and they are as follows:

Disadvantage 1:

The faster printing speed of 1.0 m/s created considerable difficulty in obtaining accurate gravimetric readings, as the contact time was insufficient for this type of delivery/uptake system.

Disadvantage 2:

There were a number of uncertainties, in regards to the mode of transfer of the fluid onto the sample. The amount of fluid delivered to the coating strip may be inaccurate and not uniformly distributed. There was also the possibility that the 'saturated' coating strip could become flooded due to excess oil on its surface. This caused oil to be transferred from the surface rather than from the void structure of the coating.

4.2 Ink Surface Absorption Method (ISAM)

4.2.1 Experimental procedure for the ISAM

The disadvantages found from using the PPT as an absorption test method, could be removed by the use of the ISIT in a novel way, as shown in fig. 4.2.

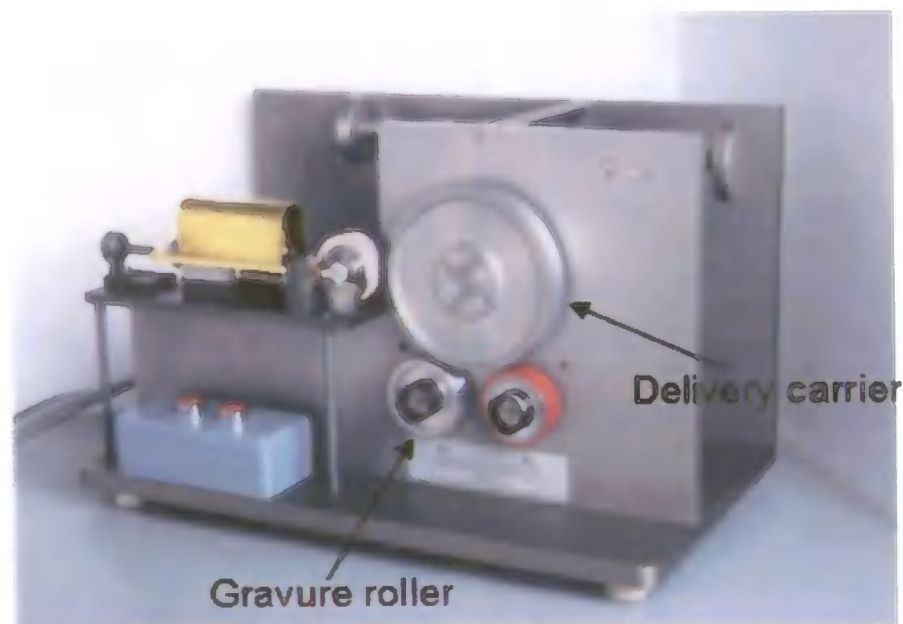


Fig. 4. 2. Use of the ISIT in a novel way.

Similar to the PPT, only the coating strips containing latex or starch had enough adhesive strength to remain on its Syntape backing during experimental runs.

A rectangular coating strip on Syntape backing was attached to a sample roller. Mineral oil was then delivered from a gravure roller to the strip on the sample roller, with both rollers moving at a speed of 1.0 m s^{-1} . A jig and scalpel was then used to cut out an exactly reproducible rectangular area of the saturated sample, while avoiding compressing the sample and keeping away from edges or partially saturated areas. The weight of the cut rectangle was then weighed, and the amount of fluid uptake calculated by comparison with an equal area of dry sample.

The gravure roller²³ comprised an array of small pits in a polished surface, with sizes and spacings such that complete transfer of the fluid onto a substrate of the same surface area would produce a film of thickness $1.5 \text{ }\mu\text{m}$. The footprint of the gravure roller in contact with the mounted coating strip was measured by the use of carbon paper, and found to be approximately 1 mm in the direction of rotation. The use of a gravure roller had the benefit that flooding of the sample was avoided, and that there was minimal uncertainty in the mode of transfer of the fluid onto the sample. Since the fluid was recessed in the gravure pattern, the fluid itself had a delivery pressure of zero when in contact with the sample.

The fluid was delivered from the gravure roller to the sample in the order of 0.01 seconds (t_*), as the results below show. So the fluid velocity $v = s / t_*$ was of the order of 1 mm per second . On the basis of the dimensions of the gravure roller pits and the fluid properties described above, the Reynolds Number ($2 \rho r v / \mu$) was of the order of 0.01 , i.e. five orders of magnitude lower than the turbulence threshold of around 2000 .

The compressing action of the roller on the coating structure was accounted for by a series of experiments using Amazon coating as a test sample. The amount of

fluid transferred to the coating was measured at a range of contact pressures from 100-600 N at a slower contact speed of 0.5 m s^{-1} to emphasise any pressure-induced effects. At lower pressures (100-300 N) there was no significant change in oil uptake, but at higher pressures (400-600 N), there was a significant increase, Fig. 4.3.

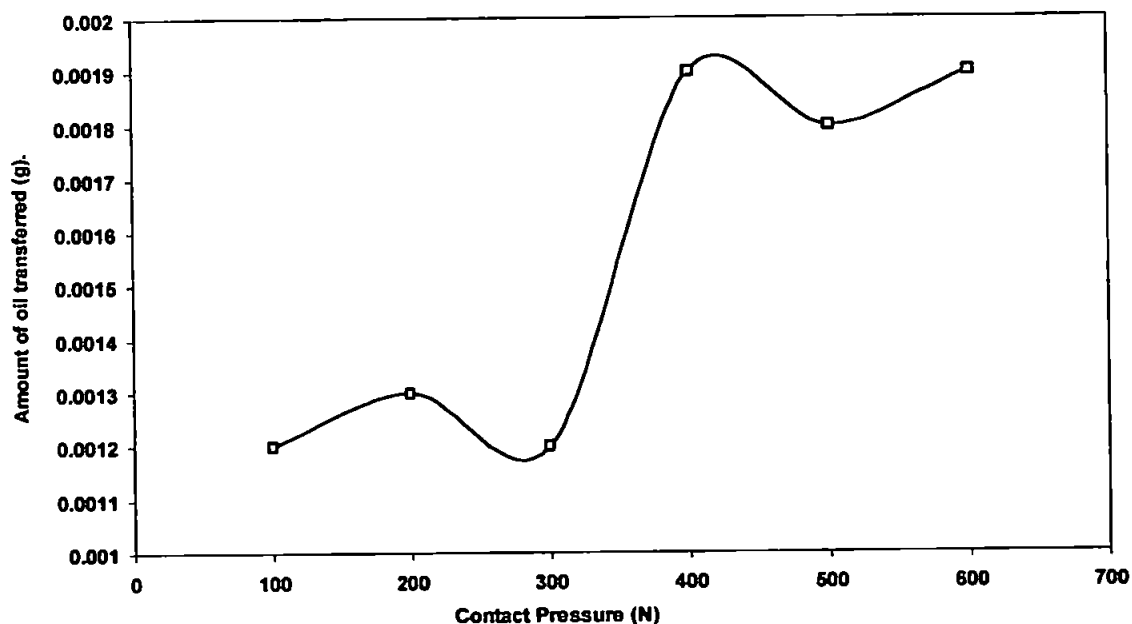


Fig. 4. 3. Amount of oil transferred from gravure roller to Amazon coating for a range of contact pressures, at a contact speed of 0.5 m/s.

This was attributed to a 'sponge' effect, with enhanced uptake being caused by the compression and subsequent relaxation of the coating structure. Although such an effect may well occur during a commercial printing process, it is also dependent on the sample elasticity, which brings in another experimental variable. Therefore all the other experiments reported in this work were carried out at a contact pressure of 100 N to avoid this effect.

4.2.2 Fluids

With the interests of the printing industry in mind, the oil used with the ISAM was a non-setting test oil designed for use as the solvent or 'vehicle' for offset

printing inks²⁴. It contained a mixture of paraffinic, naphthenic and aromatic hydrocarbons (mainly C₁₆-C₁₈ chains). Its density was measured gravimetrically to be approximately 1025.3 kg m⁻³, and its viscosity was measured by a Control Stress Rheometer²⁵ to be about 0.0074 N s m⁻². This suggested mainly paraffinic components, although its exact formulation was confidential.

4.2.2.1 Fluid used in modelling ISAM results

The use of such oil gave experimental results which were in themselves of interest to the paper coating and printing industries. However, even if the formulation of the ink vehicle were known, its mixture of fluids was too complicated to model. Therefore it was decided to model a fluid which was a close analogue to it. Hexadecane (C₁₆H₃₄) was chosen, as being representative paraffinic oil, which would have similar physical properties. It had a surface tension γ of 0.0246 N m⁻¹, a density ρ of 773.31 kg m⁻³, and a viscosity μ of 0.00334 N s m⁻² at 20°C (Weast, 1979). The contact angle θ was 40°, estimated from comparing contact angles of similar mineral oils (Ishigami *et al.*, 1994; Woodward *et al.*, 1996).

As a check, the properties of both the test oil and hexadecane were tested on a freshly ground calcite crystal surface, using wet grinding with tap water to prevent oxidation and 1200 grit paper. Both the test oil and hexadecane were fully wetting, in that no fluid contact angle was visible. On aged surfaces, which have adsorbed atmospheric aerosols, smoke or vapours including water, the contact angle of both fluids increases to around 40° as published (Ishigami *et al.*, 1994; Woodward *et al.*, 1996). This behaviour on aged surfaces was taken to be that which was most representative of actual paper coatings.

It will be seen that the comparison between experiment and simulation involved a comparison of trends, and a close inspection of the exact nature of wetting, rather than an attempt at a precise quantitative match between theory and experiment. The match between the experimental and simulated liquids was therefore sufficient to allow appropriate comparison of trends to be made.

5. RESULTS FROM EXISTING AND NOVEL EXPERIMENTAL METHODS AND APPROACHES

5.1. Characterisation of the particle and void structures of the primary samples

5.1.1. Characterisation of the particles

The characteristics of the particles for the primary samples, as measured by sedimentation and light scattering, are shown in columns 3 to 6 of Table 5.1. The aspect ratios, estimated from atomic force microscopy, are shown in column 7. Note that these aspect ratios are a more direct and therefore more robust measure than shape factors that arise as correction factors for sedimentation and light scattering experiments (refer to Section 2.7.3).

Mineral group	Sample name	Sedimentation		Light Scattering		Atomic Force Microscopy
		Median particle diameter, d_{50} (μm)	Width of particle size distribution (μm)	Median particle diameter, d_{50} (μm)	Width of Particle distribution (μm)	Aspect Ratio (particles)
PCC	Albaglos-CL	0.8	0.22	-	-	1*
	OpacarbA40-CL	0.39	0.37	0.49	0.36	2
Kaolin (clay)	Amazon-CL	0.23	0.38	0.48	0.44	8
	Speswhite-CL	0.6	0.85	3.28	0.57	16

Table 5. 1. Characteristics of particles and voids in coating samples. * represents the value estimated visually. See Section 3.2 for definitions of parameters.

The median particle diameter and the width of the particle size distribution of the four samples, analysed by sedimentation, are shown in Fig. 5.1.

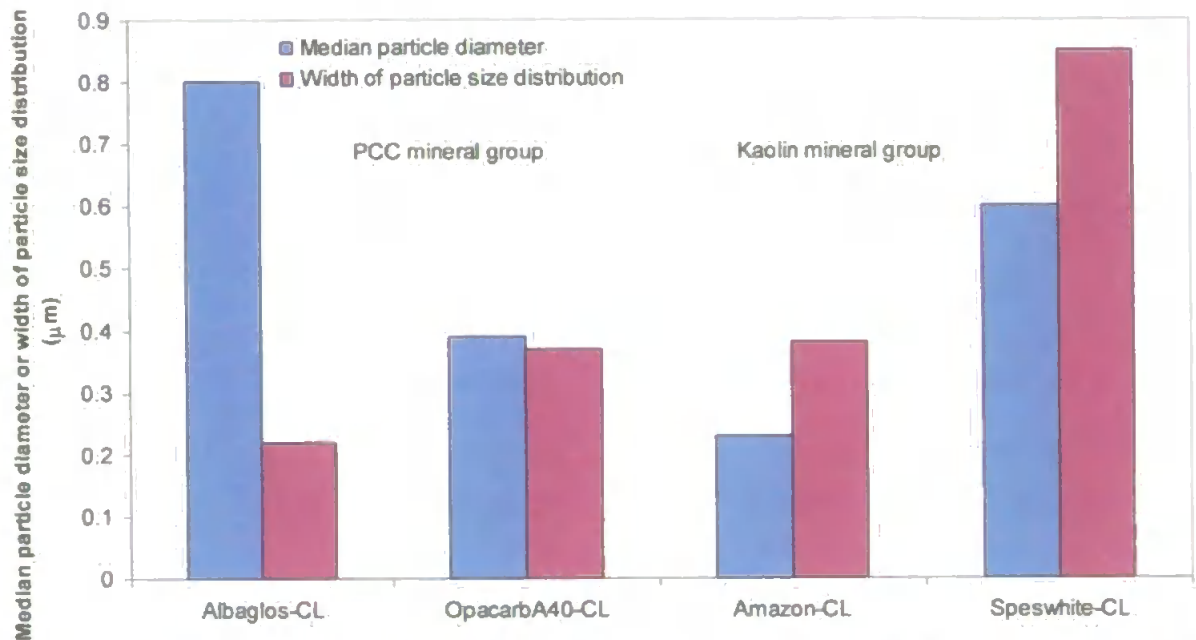


Fig. 5. 1. The median particle diameter and the width of the particle size distribution of the four samples, analysed by sedimentation.

The samples belonging to the Kaolin mineral group (clay samples) showed a larger width of particle size distribution than the samples belonging to the PCC mineral group, with Speswhite-CL having the largest distribution. Albaglos is shown to have the largest median particle size but also the smallest width of particle size distribution, while Amazon is shown to have the smallest median particle size.

5.1.2. Characterisation of the void structure

The characteristics of the void structures for the primary samples, as measured by mercury porosimetry and BET surface area analysis, are shown in Table 5.2.

Sample Type	Sample name	Mercury Porosimetry			BET surface area analysis
		Median throat diameter, d_{50} (μm)	Width of throat size distribution (orders of magnitude)	Porosity (%)	Surface area (m^2/g)
PCC	Albaglos-CL	0.198	0.25	37.6	4.4056
	OpacarbA40-CL	0.192	0.5	38.3	3.9384
Kaolin	Amazon-CL	0.064	0.24	30.0	7.3557
	Speswhite-CL	0.119	0.37	25.8	3.3475

Table 5. 2. Characteristics of void structure in coating samples. See Section 3.2 for definitions of parameters.

An example of the difference in the experimental mercury intrusion curves when first corrected for chamber expansion and mercury compressibility, and then fully corrected for sample compressibility, is shown for Amazon in Fig. 5.2. The fully-corrected intrusion curve is shown to decrease in porosity as the compressibility of the sample is taken into account, Eq. 3.1.

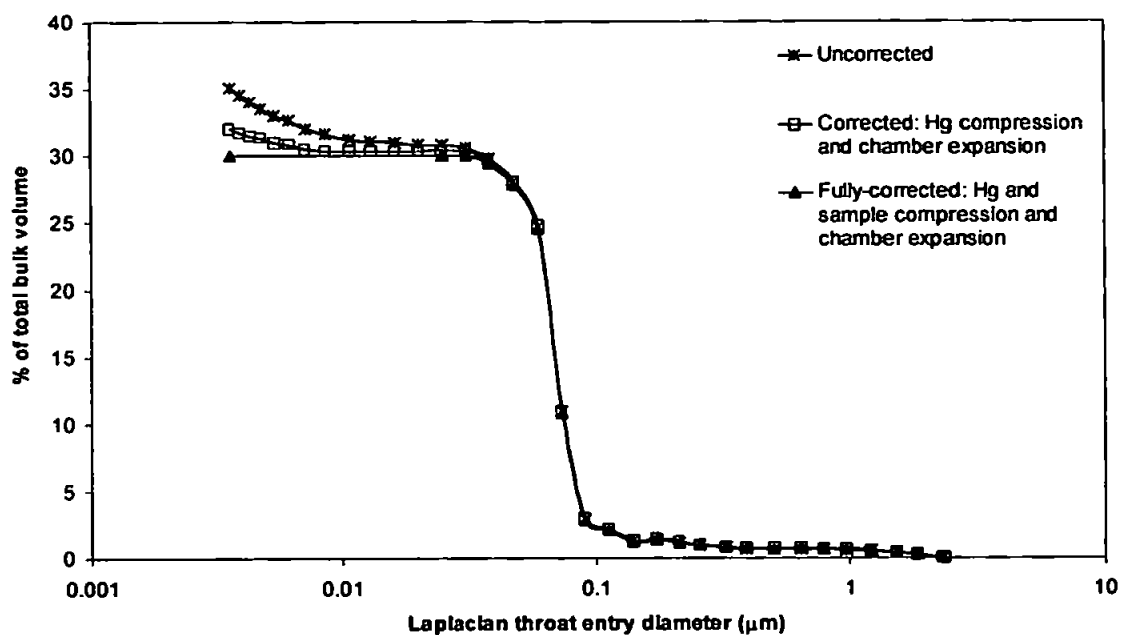


Fig. 5. 2. Uncorrected, corrected and fully-corrected mercury intrusion curves for Amazon.

The fully-corrected mercury intrusion curves for all four samples, and conversion of the applied pressure to an effective throat entry diameter, Eq. 2.25, are shown in Fig. 5.3.

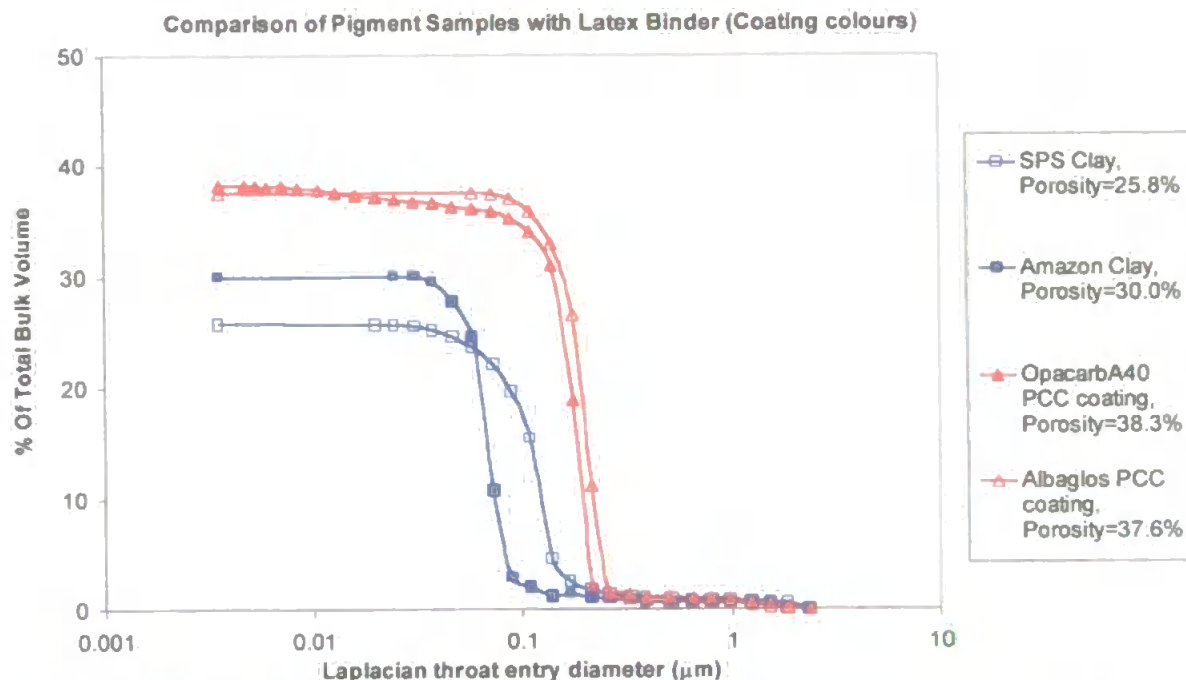


Fig. 5. 3. Fully-corrected mercury intrusion curves of the four samples, and conversion of the applied pressure to an effective throat entry diameter.

It can be seen that the clay samples had markedly different intrusion curves. The median throat size diameter and the width of the void size distribution of the four samples are shown in Fig. 5.4, while the porosity and the surface area of the four samples are shown in Fig. 5.5.

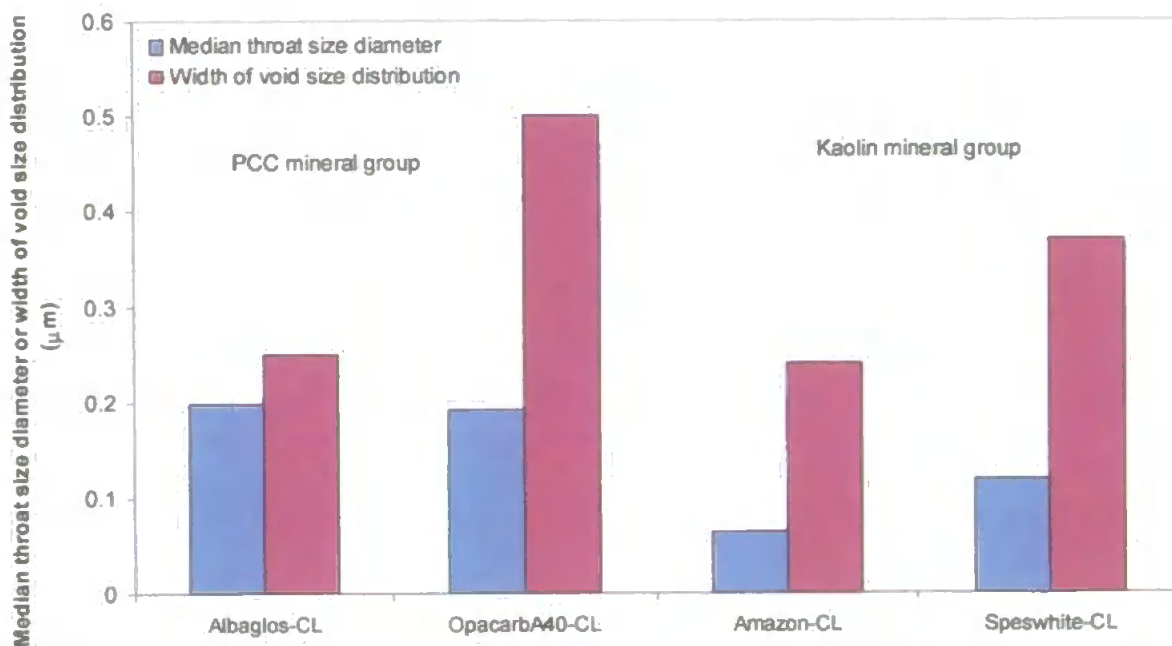


Fig. 5. 4 The median throat size diameter and the width of the void size distribution of the four samples.

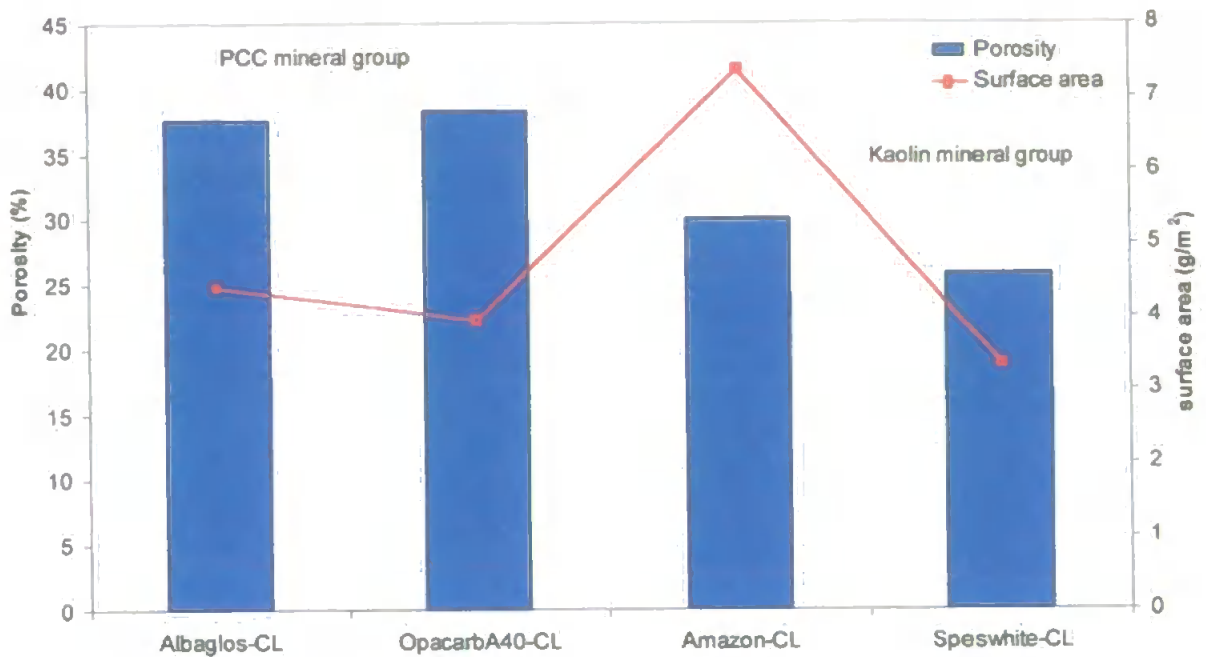


Fig. 5. 5. The porosity and surface area of the four samples

The PCC samples are shown to have a larger median throat size diameter and porosity than the clay samples. Of the two mineral coating groups, OpacarbA40-CL and Speswhite-CL are shown to have the largest void size distribution. Although Amazon-CL is shown to have the smallest throat size diameter of the four samples, it was shown to have the largest surface area.

5.1.3. Scanning electron micrographs

The surface and cross-sectional void structures of the coating samples are displayed in Figs 5.6 to 5.13. The particles in the Speswhite-CL have the highest aspect ratio, and the coating process favours a horizontal orientation during packing, resulting in slit-like pores (Figs 5.6 and 5.7).

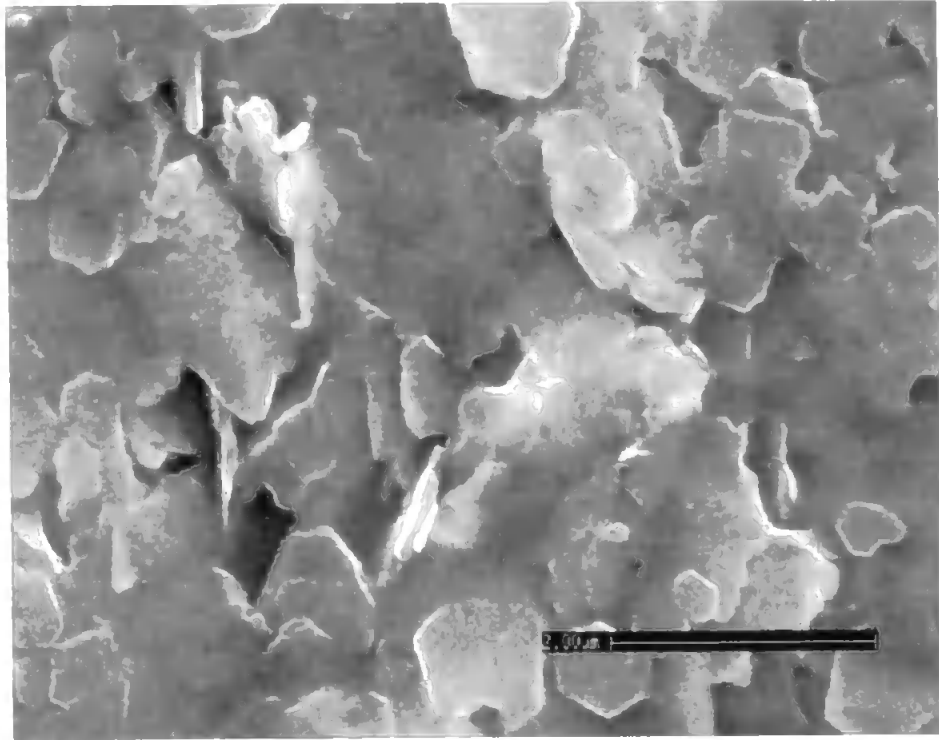


Fig. 5. 6. Speswhite-CL: scanning electron micrographs of surface scan. Scale bar: 2μm.

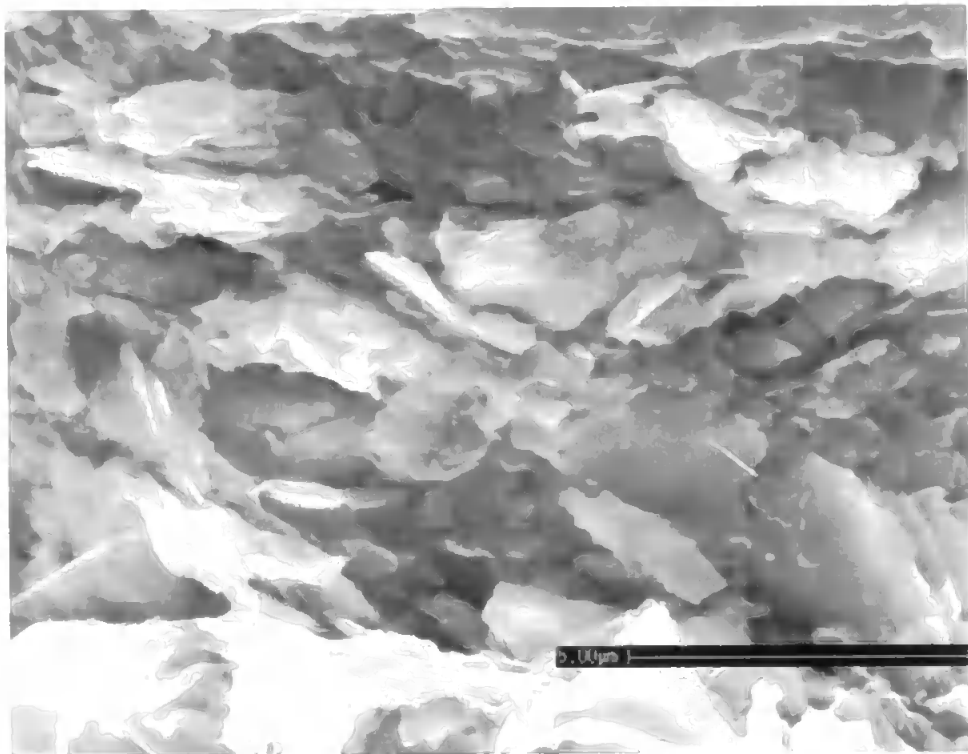


Fig. 5. 7. Speswhite-CL: scanning electron micrographs of resin-embedded cross-sectional scan. Scale bar: 5μm.

The Amazon particles have a lower aspect ratio, resulting in voids, which are less slit-like than for Speswhite (Figs 5.8 and 5.9).

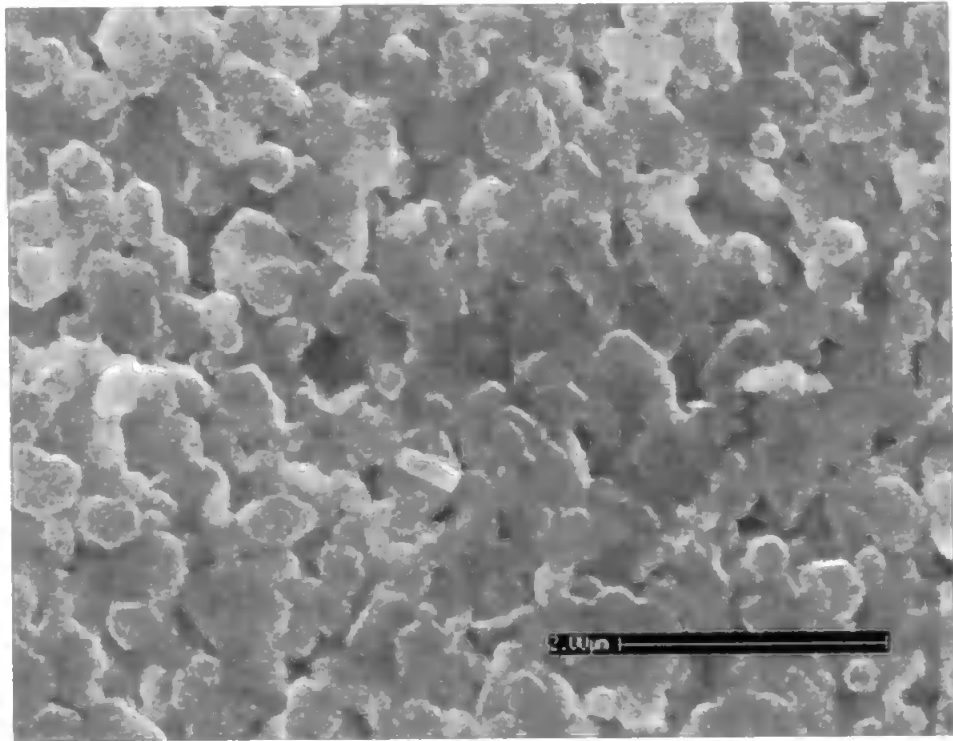


Fig. 5. 8. Amazon-CL: scanning electron micrographs of surface scan. Scale bar: 2μm.

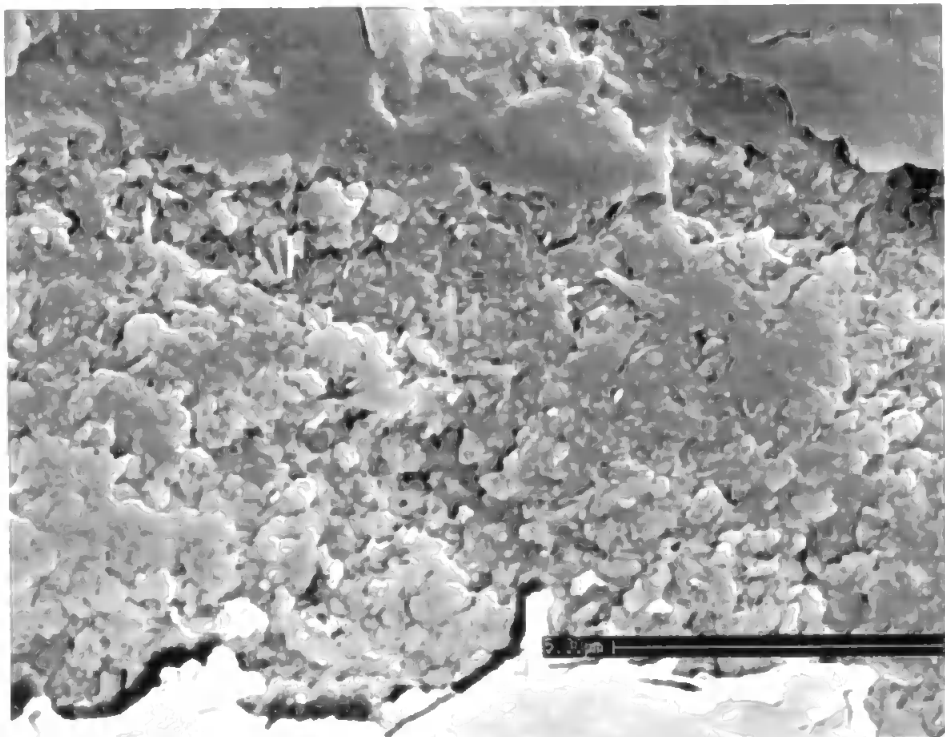


Fig. 5. 9. Amazon-CL: scanning electron micrographs of resin-embedded cross-sectional scan. Scale bar: 5μm.

The particles in the OpA40 coating samples have an elongated prismatic shape, which pack together to give pores, which may also have a rod-like structure (Fig. 5.10 and 5.11).

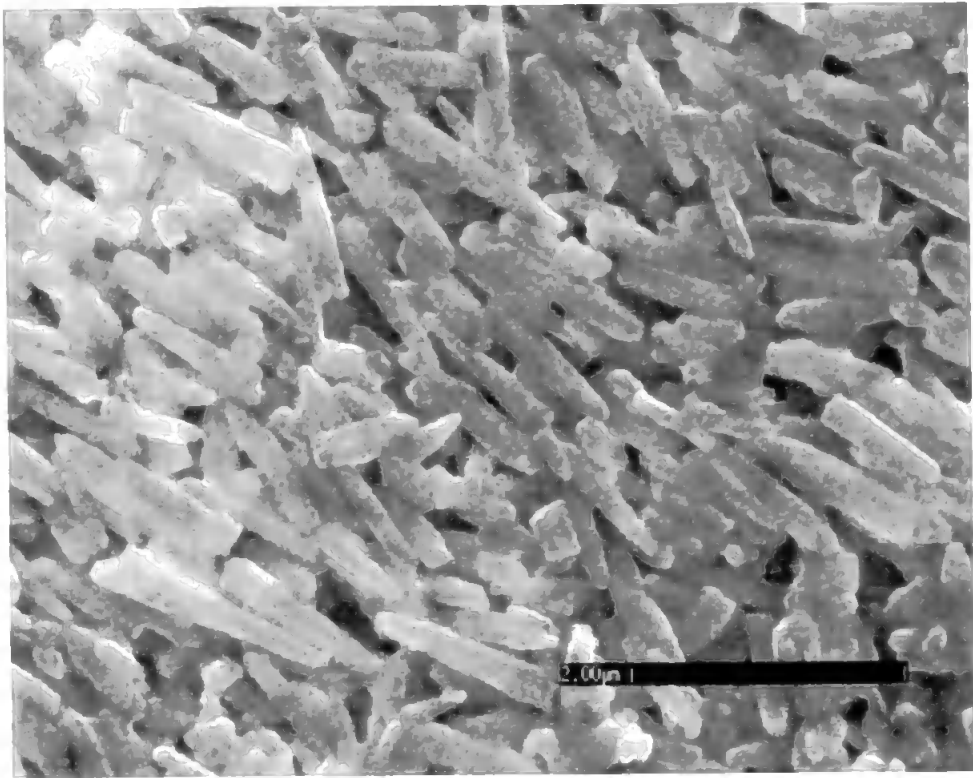


Fig. 5. 10. OpacarbA40-CL: scanning electron micrographs of surface scan. Scale bar: 2 μ m.



Fig. 5. 11. OpacarbA40-CL: scanning electron micrographs of resin-embedded cross-sectional scan. Scale bar: 5 μ m.

The Albaglos particles, due to their calcitic morphology and rhombohedral shape, create almost spherical particles, which in turn form an isotropic porous network structure (Figs 5.12 and 5.13).

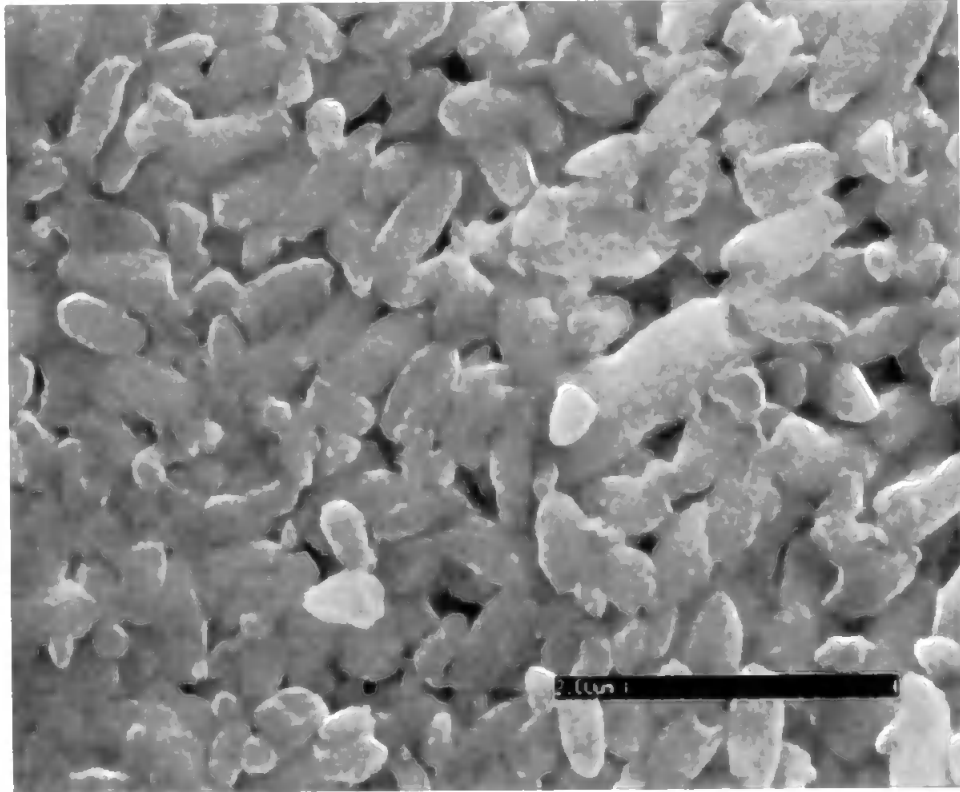


Fig. 5. 12. Albaglos-CL: scanning electron micrographs of (a) surface scan. Scale bar: 2 μ m.

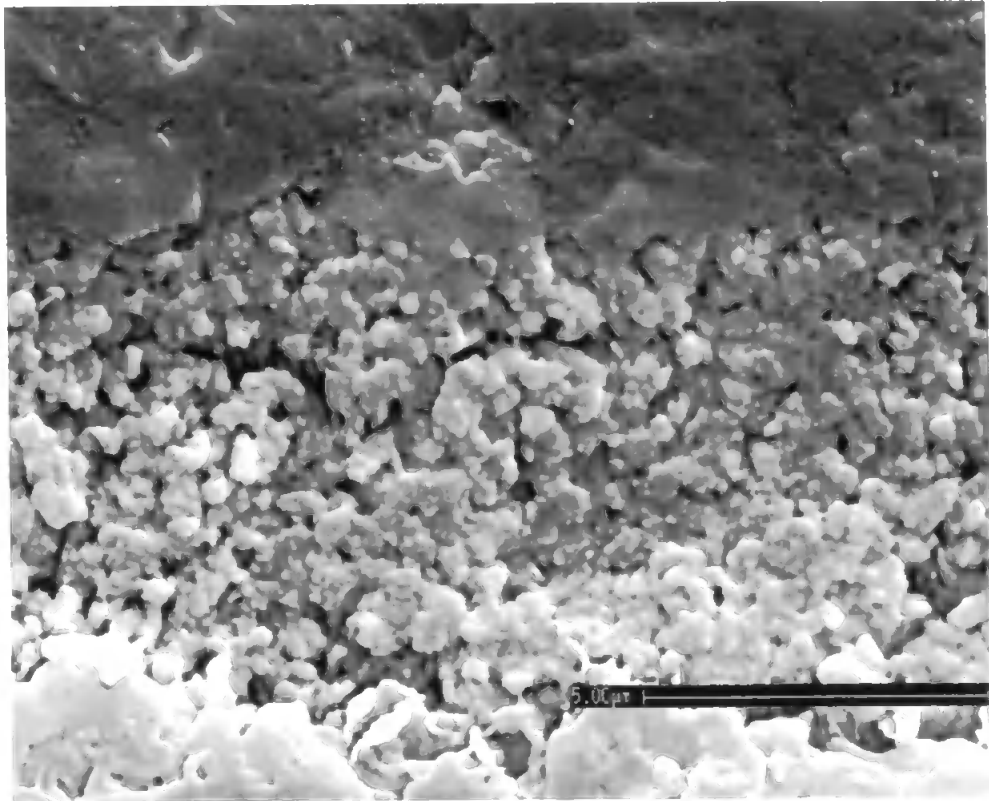


Fig. 5. 13. Albaglos-CL: scanning electron micrographs of resin-embedded cross-sectional scan. Scale bar: 5μm.

These and other electron micrographs of the surfaces were examined, covering areas of surface of around $40 \mu\text{m}^2$. Each micrograph was split into four equal areas, and a count made in each area of the number of throats at the surface, which appeared to lead into the bulk of the material. This was done visually rather than by image analysis, because image analysis algorithms find it difficult to identify throats rather than surface pores in a surface electron micrograph. The results are shown in Table 5.3, together with the % standard errors of the means, which arose chiefly from the heterogeneity of the surface structures rather than the inevitable subjectivity in the visual count. Clearly the standard error increases with the number of areas into which the image is split. The lower limit when the image is a standard error of a throat size, in which case it becomes an almost binary only problem (throat or no throat) with a standard error of $\pm 100\%$. Only if the sample was a self-similar fractal would the observation be independent of image area.

There is no way of avoiding this arbitrariness of this standard error, but splitting the image into four gives some feel for the surface heterogeneity.

It can be seen that the number density of surface throats (or surface capillaries) is lower for Speswhite-CL than for Amazon-CL, while a smaller number density is observed for Albaglos-CL than for OpacarbA40-CL.

Primary samples	Aspect factor (α)	Number density of surface throats (μm^{-2})			Surface throat number density correction factor, f
		Experimental	Experimental standard error	Model	
Albaglos-CL	1	1.4	0.22	12.13	0.12
OpacarbA40-CL	1.5	3.02	0.12	13.54	0.22
Amazon-CL	0.8	4.09	0.15	10.66	0.38
Speswhite-CL	0.6	0.66	0.07	7.89	0.084

Table 5. 3. Estimates of number density of surface throats and the correction factor, F , used for each sample.

5.1.4. Packing-structure trends for the primary samples

In the context of the hypotheses of this thesis, it is important to consider which features of the experimental data are due to anisotropy and which are not. One must also make a distinction between trends in this figure which arise mainly from the manufacturing processes, and those which arise from the more subtle trends arising from the structures of the particles both separately and in the coating. We are interested in the latter category, which we shall call 'packing-structure trends'.

The characteristics of the particles, which were summarised in Table 5.1, are plotted against aspect ratio in Figure 5.14. None of the experimental methods give direct measurements of the required properties, so any conclusions must be made with great caution. In particular: (i) light scattering is highly sensitive to particle anisotropy, (ii) sedimentation is also very sensitive to particle anisotropy and (iii)

the void size distribution from mercury intrusion implicitly assumes a parallel-tube model.

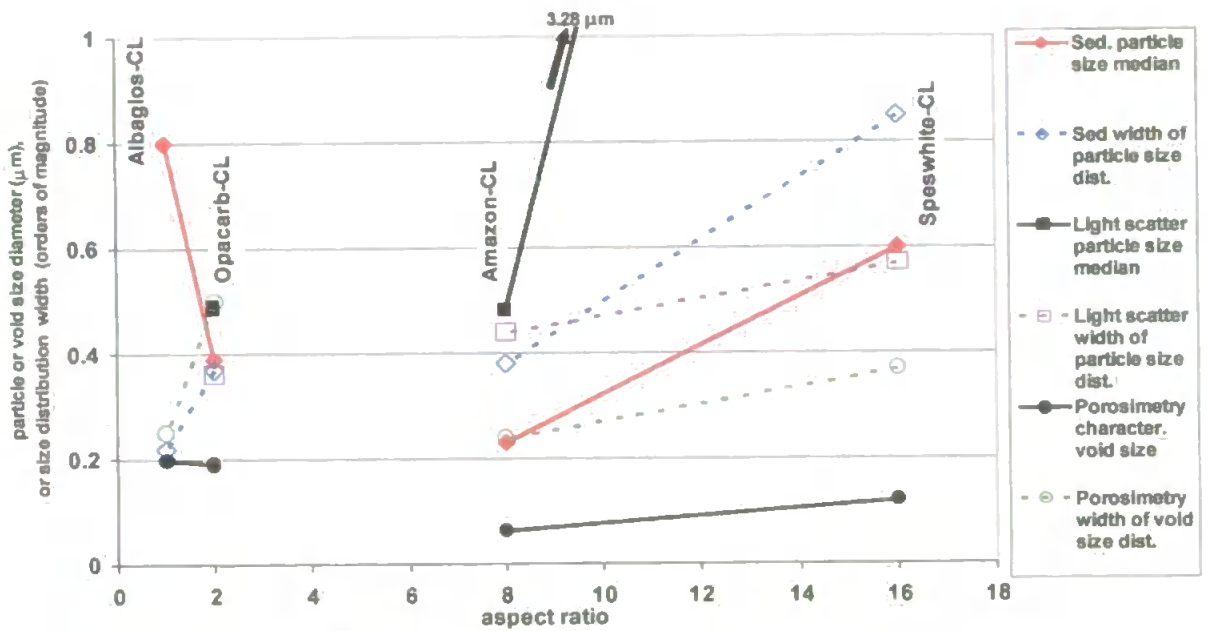


Fig. 5. 14. Packing structure trends for the primary samples.

Over all the samples, the median sizes of the particles, as measured by sedimentation, which takes a spherical average value, are in the range 0.23 to 0.8 μm - but these sizes are largely determined by the manufacturing process. As expected, light scattering, which is sensitive to aspect ratio, highlights the large face dimensions of the Speswhite particles. The widths of the particle size distributions depend both on the innate mineralogical characteristics, and the way that the particles are sorted during manufacture. Thus, the increases of these distribution widths with aspect ratio within the PCC and kaolin mineral groups are not packing-structure trends.

Importantly, various packing-structure trends are also evident in Figure 5.14. Within the two coating groups (the PCC and the Kaolin mineral group), the width of the void size distribution in the coatings (\circ) increased with the width of the particle size distributions (\diamond and \square). However, the void size distributions are shown to vary

rather less markedly than the particle size distributions, which can be interpreted as the greater efficiency of the particle packing for the wider size distributions (Lohmander, 2000). For the low aspect ratio PCCs, the width of the void size distribution is higher than the width of the particle size distribution, whereas for the higher aspect-ratio clays, the converse is true. An interpretation for this is that for the higher aspect ratio clay particles, structures containing aligned particles pack more efficiently than those with lower aspect ratios. This interpretation is substantiated by inspection of fig. 5.6 and 5.7.

However, such increase in packing efficiency could be either because of the increase of the width of the particles size distributions, giving a wider range of sizes of building blocks to fit together, or it could be because of the increase in aspect ratio causing particles to become more aligned and therefore pack more efficiently. The particle packing causes a much lower number density of voids on the Speswhite surface compared to the Amazon surface. Although the median particle and void sizes are larger for Albaglos-CL than OpacarbA40-CL, they both have similar porosities (Fig. 5.5). The particle packing, therefore, created a structure for Albaglos-CL with a lower number density than OpacarbA40-CL, as larger but fewer voids were created. However, all these conclusions are tentative, in the context of the approximations mentioned above.

5.2. *Experimental permeation results for the primary samples*

The permeation results from the Ink Stain Density (ISD), Dynamic Absorption Test (DAT), Gurley Air Resistance Method (Gurley Method), Prufbau Printability absorption method (PPAM) and the Ink Surface Absorption Method (ISAM) are shown in Table 5.4, and discussed further in the sections below.

Experimental permeation experiments	Speswhite-CL	Amazon-CL	Albaglos-CL	OpacarbA40-CL
DAT permeation rate x 10 ³ (μm μm ⁻²)	104.58	109.83	119.15	121.80
ISD permeation rate x 10 ⁵ (s ⁻¹)	27.40	166.67	69.44	111.11
ISAM permeation rate (g s ⁻¹)	0.05	0.70	0.10	0.55
PPAM volume uptake (at 0.5 m/s)	7.59	10.53	4.46	5.19
Gurley Permeability at 11 g m ⁻² coat weight (mDarcy)	6.00E-03	7.50E-03	-	1.43E-02

Table 5. 4. Experimental permeation results from the three experiments.

5.2.1. Permeation results from Prufbau Printability Absorption Method (PPAM)

Experimental trial runs using the Prufbau Printability Absorption Method (PPAM) on the four coating samples are shown in Fig. 5.15 for a printing speed of 0.5 m/s and 1.0 m/s. The figure displayed two results; the percent volume of oil transferred from the carrier strip to the printing strip, and the percent saturation for the printing strip. The results for the percent saturation were calculated by using the measured porosity from mercury porosimetry for each coating sample.

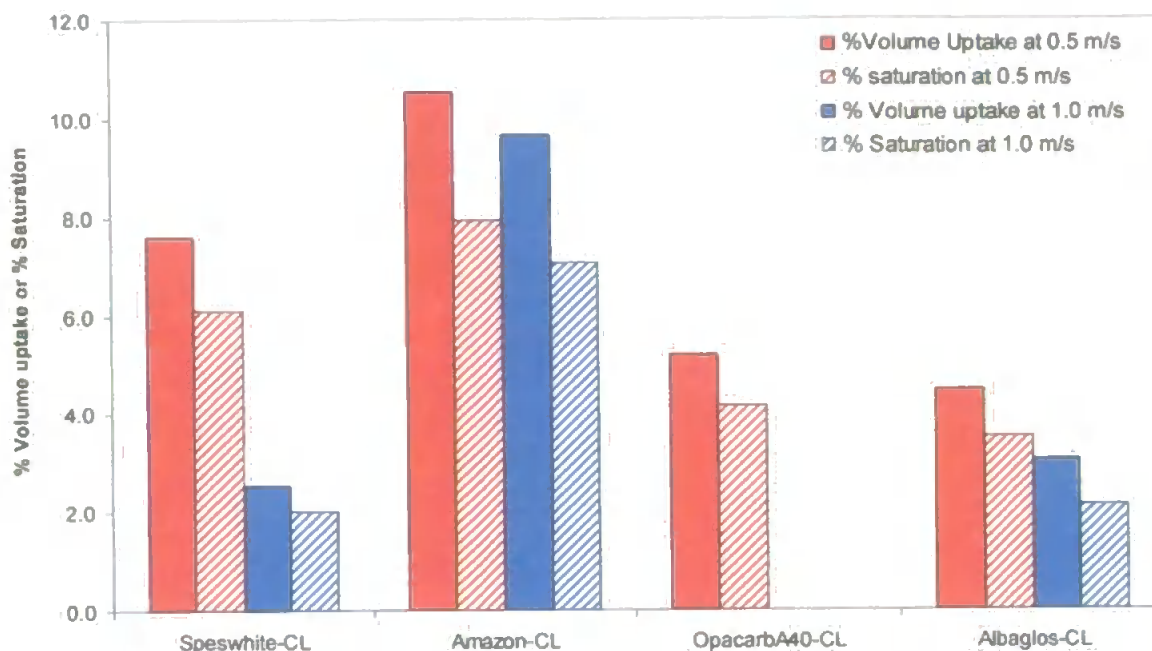


Fig. 5. 15. Results from the PPAM showing the percent volume uptake of oil and the percent saturation for the samples from the printing strips.

The results showed the Kaolin samples (Speswhite-CL and Amazon-CL) to have a higher uptake of oil than the PCC samples. An increase in delivery speed from 0.5 to 1.0 m/s caused a significant drop in the amount of oil absorbed for all the samples, with OpacarbA40-CL having no absorption, as shown. Of the four samples, Amazon had the highest uptake of oil. The results of the percent saturation showed that none of the samples from the printing strips were close to reaching saturation. The saturation results, for both printing speeds, also followed a similar trend with the percent volume uptake.

There are a number of uncertainties in these experimental results due to the disadvantages in its experimental method, as discussed in Section 4.1.3. Due to the unreliability of this method, the PPAM results will not be discussed again until the Overview chapter.

5.2.2. Permeation results from the Ink Stain Density (ISD) test

The saturation rates for the samples were calculated from the ink stain colour density curves (Fig. 3.7) and are shown in Fig. 5.16.

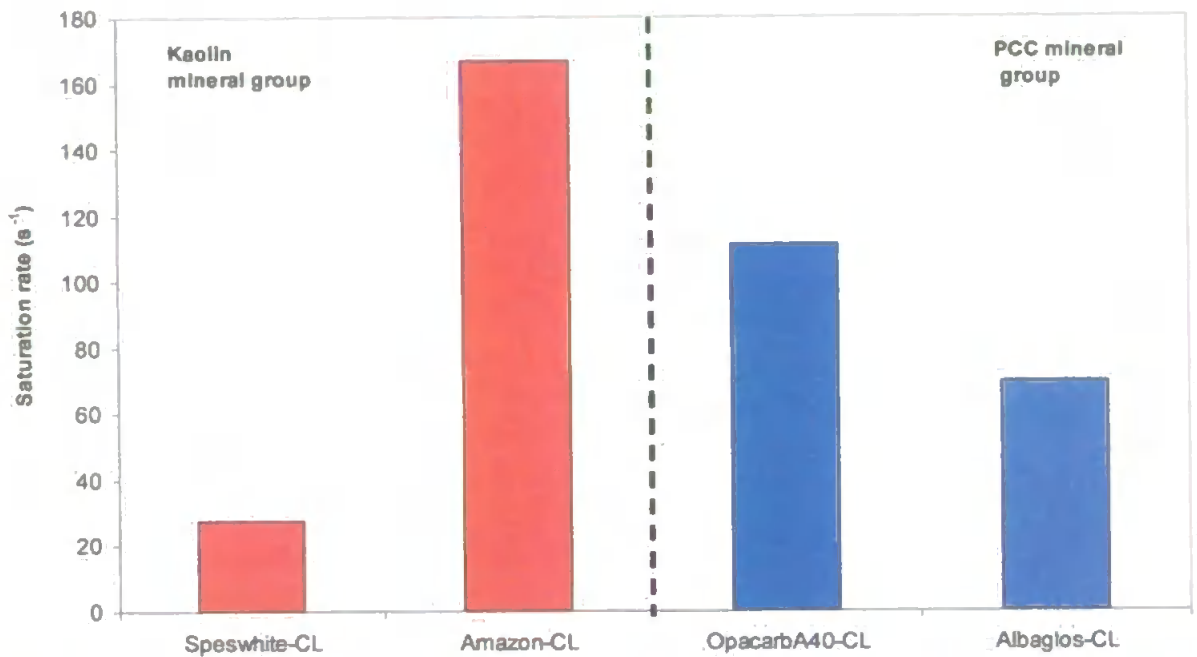


Fig. 5. 16. Saturation rate for all four coating samples, measured from the Ink stain density curves. The results are also termed as the ISD permeation rate.

The saturation rates of the samples are termed as the ISD permeation rate. Amazon-CL and Speswhite-CL are shown to have the highest and lowest ISD permeation rates, respectively.

5.2.3. Permeation results from the Dynamic Absorption Test (DAT)

The change in normalized height for the droplet is calculated from the DAT experiments at 0.4s and the results are shown in Fig. 5.17 and Fig. 5.18.

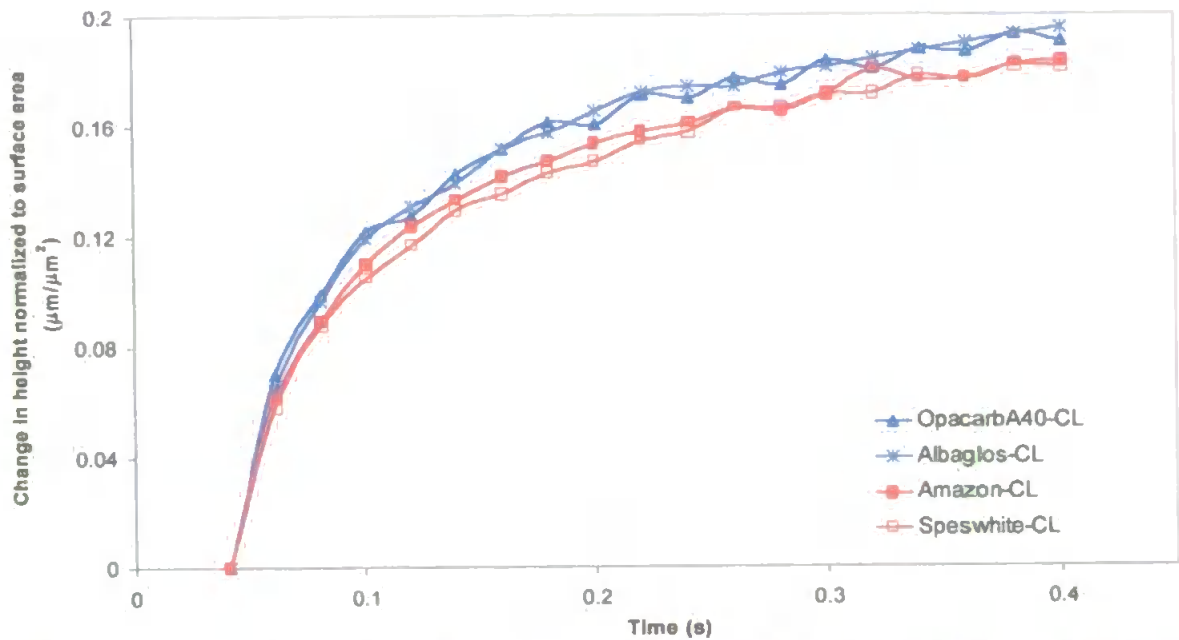


Fig. 5. 17. DAT permeation curves for the primary samples, showing the change in height of the droplet normalized to surface area over an elapsed wetting time.

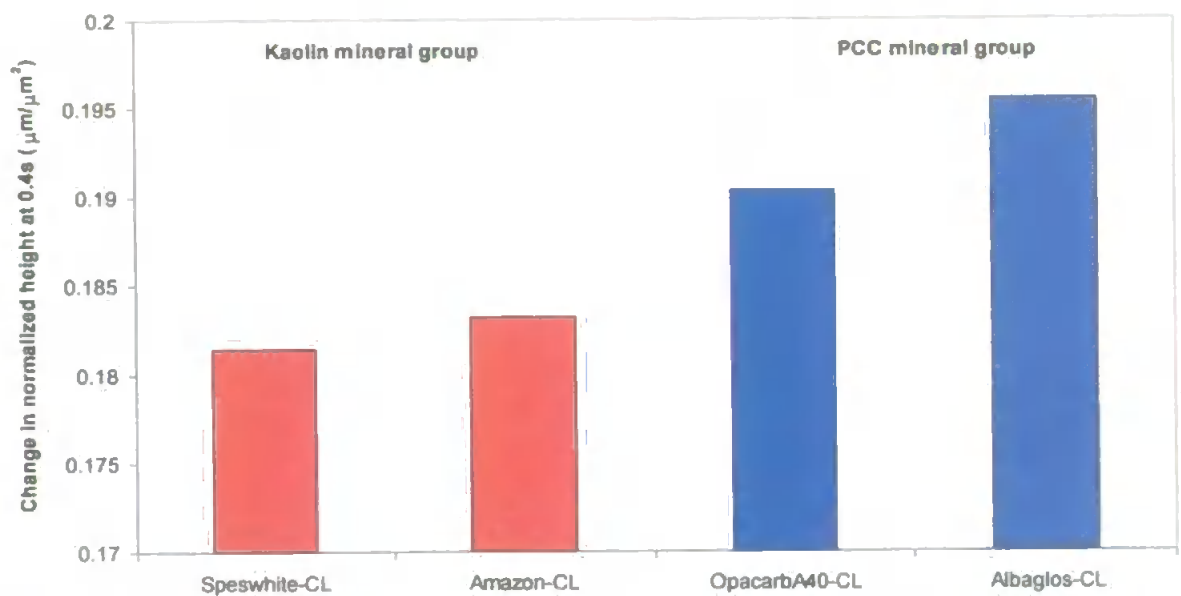


Fig. 5. 18. Change in normalized height for the droplet of oil at 0.4s for all four coating samples. The result is measured from the use of the DAT instrument, and is termed as the DAT permeation rate.

The measured change in normalized height is termed as the DAT permeation rate. The PCC mineral group is shown to have greater DAT permeation rates than the Kaolin mineral group, as Albaglos and Speswhite are shown to have the highest and lowest DAT permeation rates, respectively.

5.2.4. Permeation results from the Ink Surface Absorption Method

(ISAM)

Fig. 5.19 showed the results of the ISAM for the primary samples.

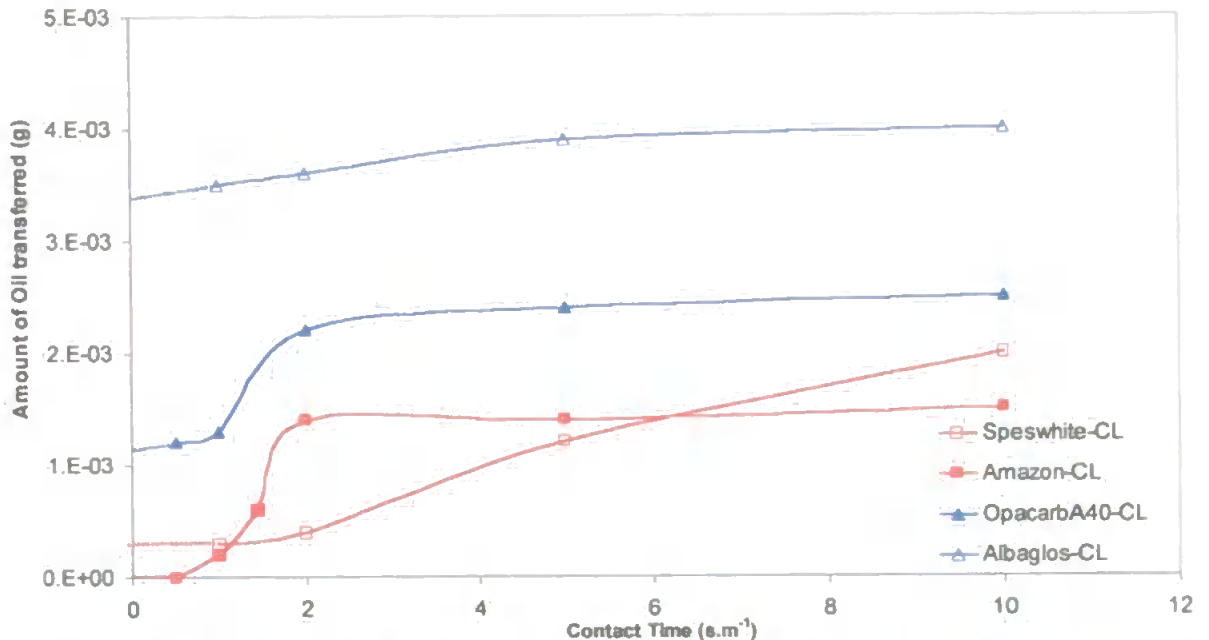


Fig. 5. 19. Amount of oil transferred from gravure roller to coating samples at 100N contact pressure.

The red coloured curves represent the coating samples belonging to the Kaolin mineral group, while the blue curves represent the samples belonging to the Precipitated Calcium Carbonate (PCC) mineral group. The curves were extrapolated to time zero as shown. The intercept at time zero was assumed to be due to almost instantaneous surface film transfer (Schoelkopf *et al.*, 2001), caused from residual oil on the surface of the gravure roller. This surface film was then subtracted to give the oil uptake additional to this transfer. Also, taking the gravure roller footprint as 1 mm as described previously, allows an absolute contact time to be estimated, Fig. 5.20.

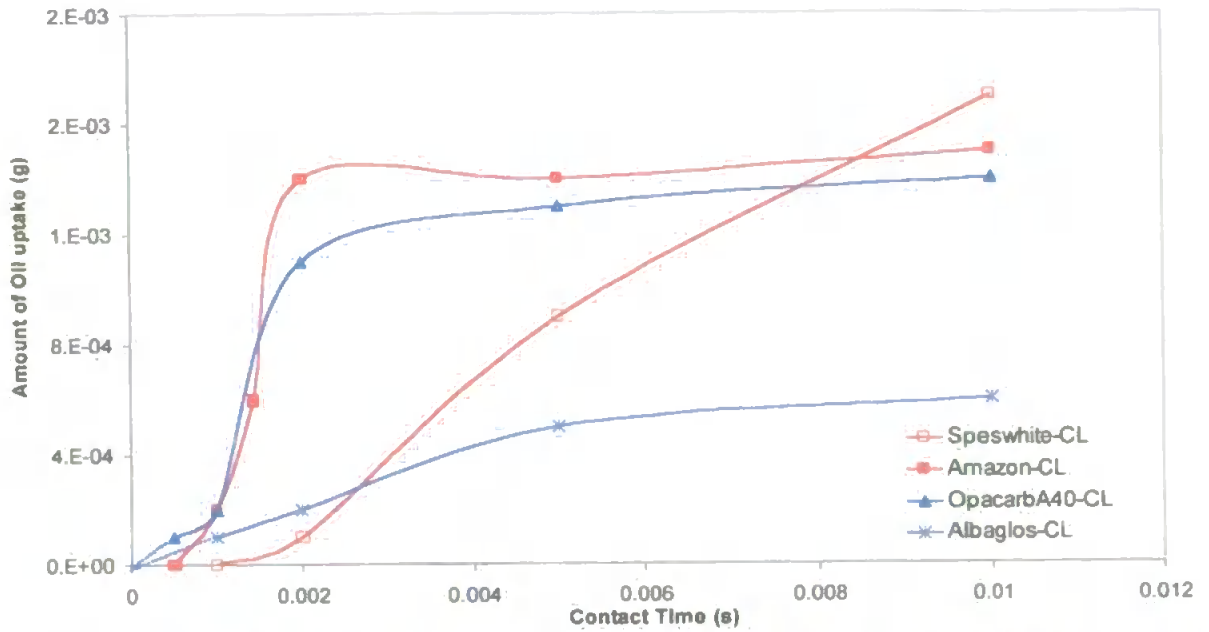


Fig. 5. 20. Results of Figure 5.20 corrected for film transfer and with respect to absolute contact time.

Inspection of Fig. 5.20 suggested that 0.002 s would be a time which revealed the trends in the experimental results before they reached a plateau. The resulting permeation rates at 0.002s contact time are shown in Fig. 5.21.

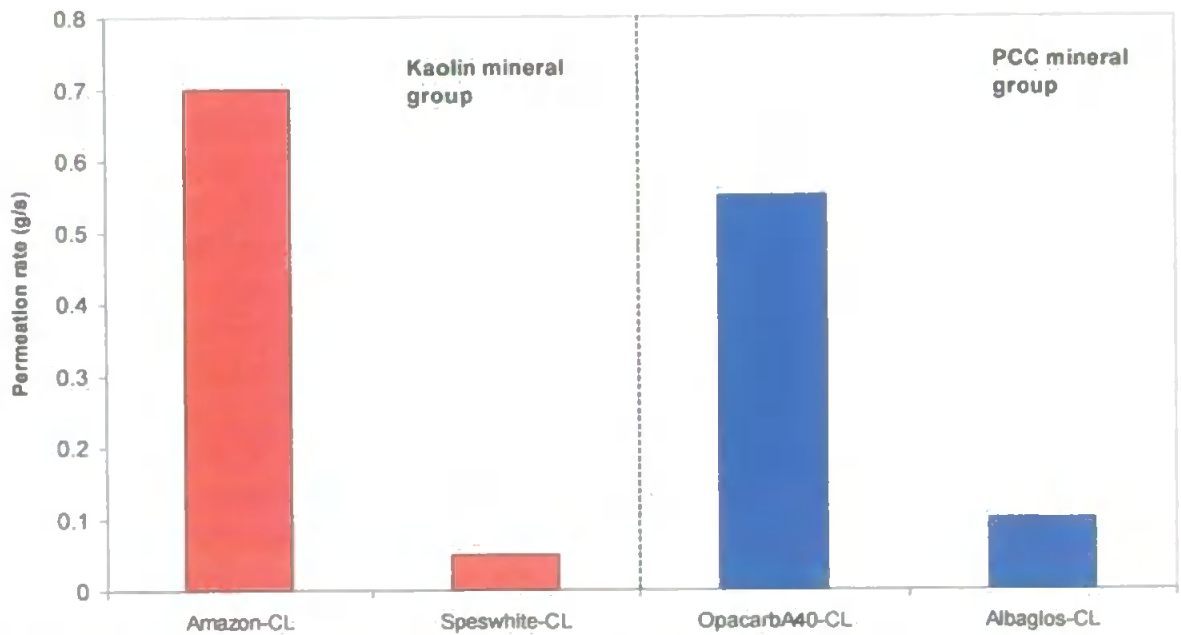


Fig. 5. 21. ISAM permeation rate of the primary samples at 0.002s contact time.

Amazon-CL and Speswhite-CL are shown to have the highest and lowest ISAM permeation rates, respectively.

5.2.5. Permeation results from Gurley Air Resistance Method (Gurley method)

Due to limited availability of coated paper samples, the Gurley method was only performed on three of the four primary samples and on one complementary sample, OpacarbA60-CL, which will be discussed in section 5.3.5. The average Gurley seconds, air permeance and permeability results for all the coated paper samples are shown in Table 5.6. Permeability measurements obtained from the Gurley method are termed as Gurley permeability measurements, and are shown to slightly vary with coat weight, Fig. 5.22.

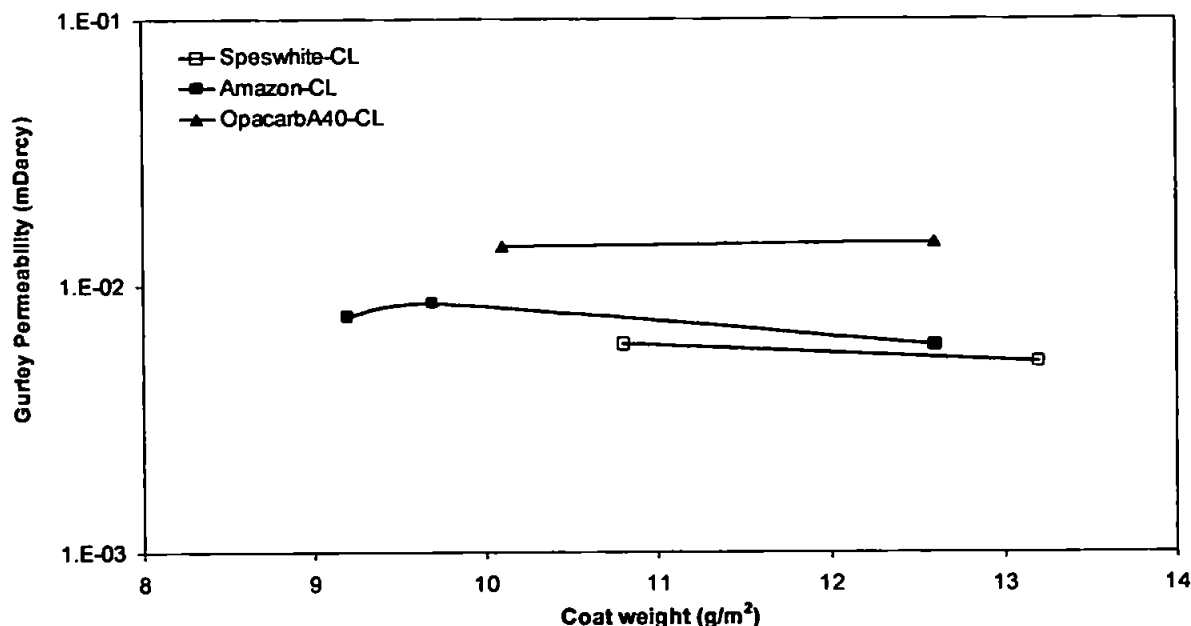


Fig. 5. 22. Gurley permeability measurements varying with coat weight. The % standard error was calculated to be between 1 to 5% for the Gurley permeability measurements of each sample (refer to Table 5.6). Error bars were therefore not shown on the curves as they would be too small in size to be clearly visible.

The permeability at a coat weight of 11 g/m² was approximated for each sample, and the results are shown in fig. 5.23.

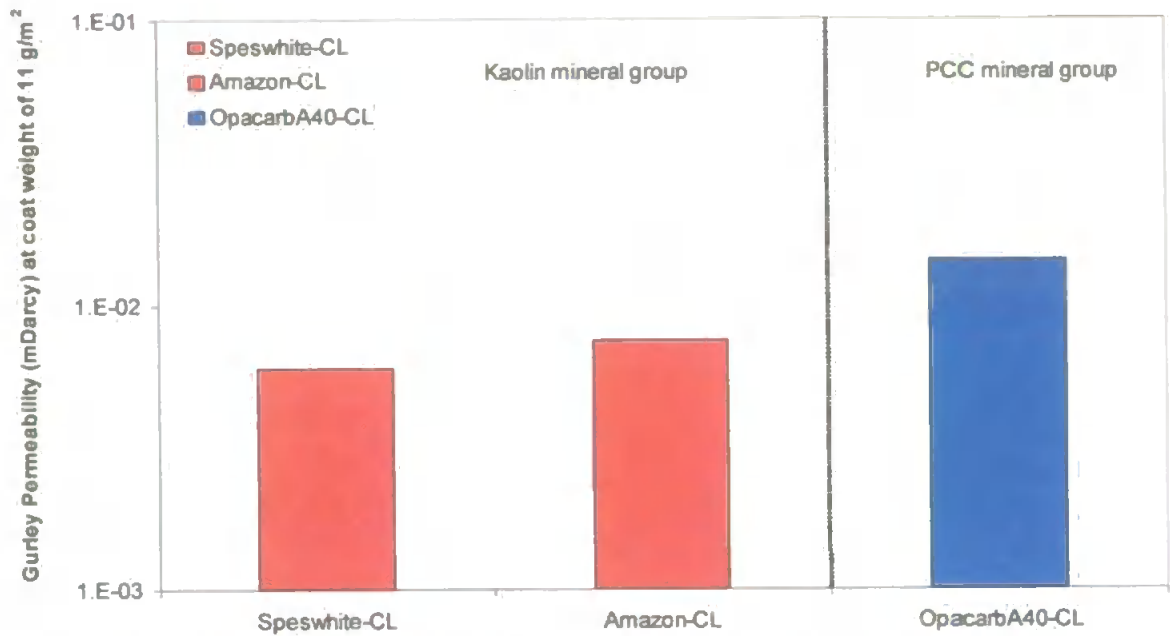


Fig. 5. 23. Gurley permeability measurements at a coat weight of 11 g/m².

The Gurley permeabilities of the Kaolin mineral group are shown to be lower than the permeabilities of the PCC mineral group. OpacarbA40-CL and Speswhite-CL are shown to have the highest and lowest permeabilities, respectively.

5.2.6. Comparison of permeation results from the primary samples

The ISAM, ISD and DAT method were all used as indirect measures of the experimental permeation rates for the samples, while the Gurley method was used as a direct measurement of permeability. All four experimental permeation methods showed Speswhite-CL to have a slower permeation than Amazon-CL. However, the ISAM and the ISD method showed Amazon-CL to have the fastest permeation while the DAT and the Gurley methods showed the samples in the PCC mineral group to have the fastest permeations. The ISAM and the ISD method also showed OpacarbA40-CL to have a faster permeation rate than Albaglos-CL; however the DAT method showed the reverse. Hence, the permeation results from the DAT method much better resembled the permeability

trends from the Gurley method than the ISAM or ISD method. The similarities in the permeation results between the ISD and the ISAM would be due to the similarities in their test procedure, as both methods showed the surface to be completely saturated with ink at the start of permeation.

The permeation results from the four experimental methods were compared to the void structure properties of the samples. A comparison between the permeation results from the four experimental permeation methods and the number density of surface throats between each sample is shown in fig. 5.24 and 5.25.

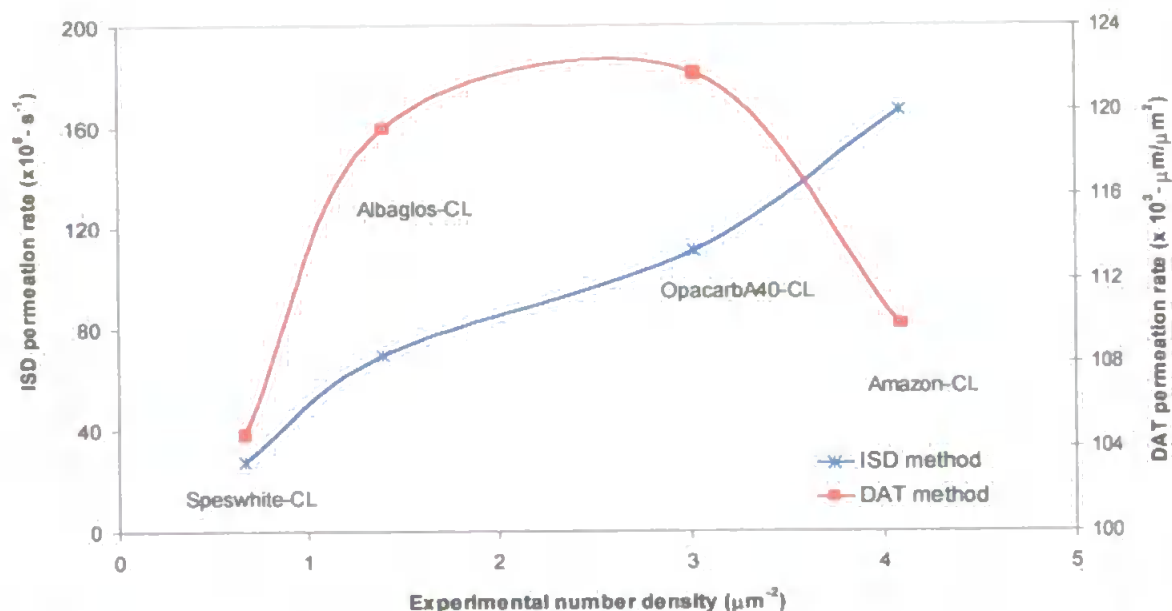


Fig. 5. 24. Comparison of the permeation results from the ISD and DAT methods with the Experimental number density of each sample.

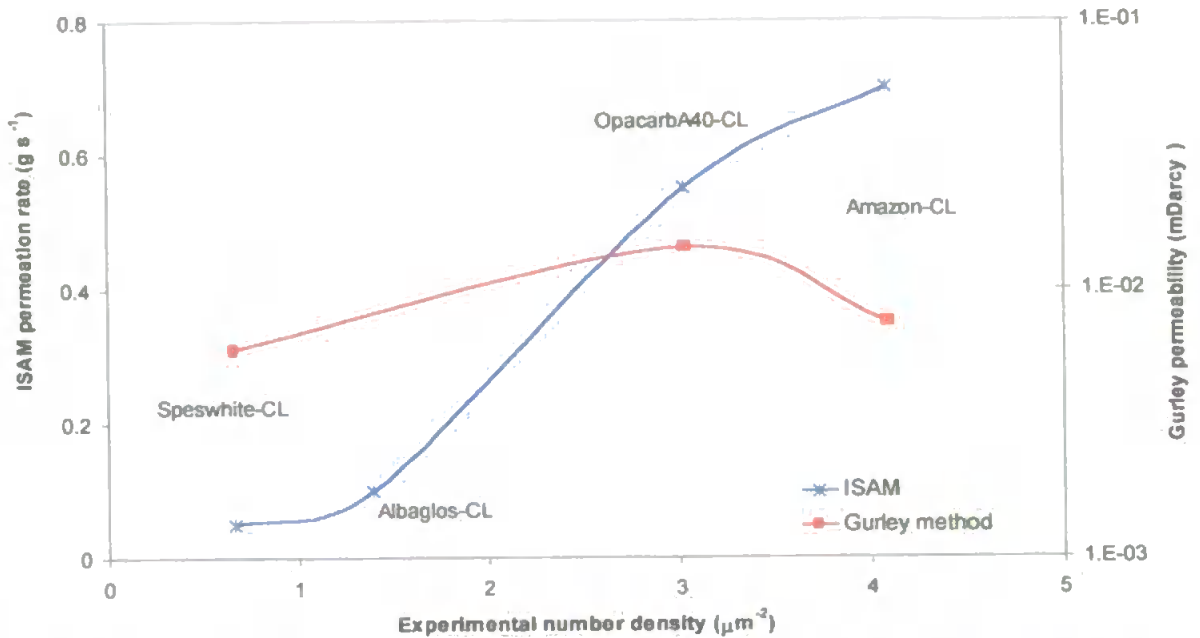


Fig. 5.25. Comparison of the permeation results from the ISAM and the Gurley methods with the Experimental number density of each sample.

The permeation results from the ISAM and the ISD method are shown to have a perfectly ranked positive correlation with number density while the DAT and the Gurley method are shown to deviate. None of the other void structure properties, such as porosity, surface area and median throat size, showed a perfectly ranked positive correlation with the four experimental permeation methods. The number density of surface throats was therefore the dominant factor in determining the permeation results of the ISD and ISAM method. This was also in agreement with the work done by Preston *et al.* (Preston *et al.*, 2001) using the ink tack test (see Section 2.3.2). In summary, the ISAM and ISD method better resembled surface number density trends than the permeability trends shown from the Gurley method.

5.3. Experimental results from the addition of complementary samples

5.3.1. Characterisation of void structures

Mercury porosimetry was also performed on the complementary samples, comprising of a mineral pigment with either CMC and latex or starch and latex. The fully-corrected mercury intrusion curves from the primary and complementary samples are shown in figures 5.26 and 5.27, for the samples containing either CMC and latex or starch and latex, respectively. However, the mercury intrusion curve for Albaglos-SL could not be obtained as the coating sample mounted on aluminium foil backing was not available.

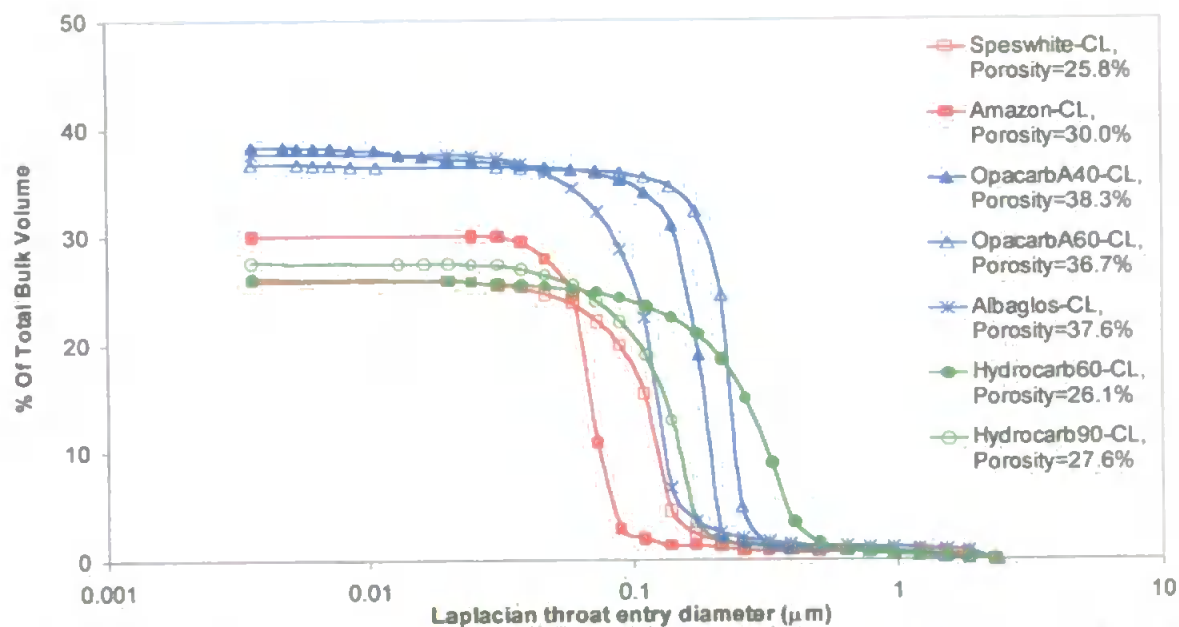


Fig. 5. 26. Fully corrected mercury intrusion curves of coating samples, comprising of a mineral pigment with CMC and latex.

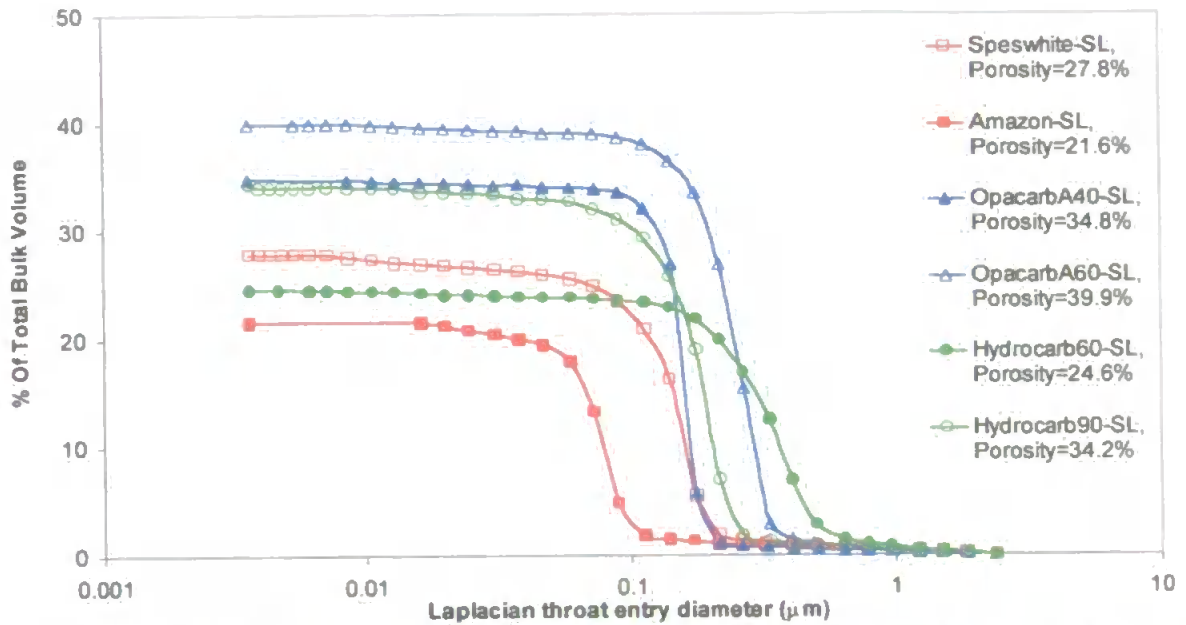


Fig. 5. 27. Fully corrected mercury intrusion curves of coating samples, comprising of a mineral pigment with starch and latex.

The characteristics of the void structures for the samples, measured by mercury porosimetry and BET surface area analysis, are shown in Table 5.5. BET surface area analysis was only performed on some of the samples.

Sample Type	Sample name	Mercury Porosimetry			BET surface area analysis
		Median throat diameter, d_{50} (μm)	Width of throat size distribution (orders of Magnitude)	Porosity (%)	Surface area (m^2/g)
PCC	Albaglos-CL	0.198	0.25	37.6	4.4056
	OpacarbA40-CL	0.192	0.5	38.3	3.9384
	OpacarbA60-CL	0.225	0.42	36.7	3.6099
	OpacarbA40-SL	0.152	0.2	34.8	-
	OpacarbA60-SL	0.241	0.33	39.9	-
Kaolin	Amazon-CL	0.064	0.24	30	7.3557
	Spes white-CL	0.119	0.37	25.8	3.3475
	Amazon-SL	0.079	0.35	21.6	-
	Spes white-SL	0.137	0.46	27.8	-
GCC	Hydrocarb60-CL	0.292	0.76	26.1	-
	Hydrocarb90-CL	0.138	0.3	27.6	-
	Hydrocarb60-SL	0.36	0.49	24.6	-
	Hydrocarb90-SL	0.18	0.42	34.2	-

Table 5. 5. Characteristics of void structure for the coating samples containing CMC and latex and starch and latex. See Section 3.2 for definitions of parameters.

The median throat size diameter, the width of the void size distribution and the porosity of the above samples are shown in Fig. 5.28 to Fig. 5.30, respectively.

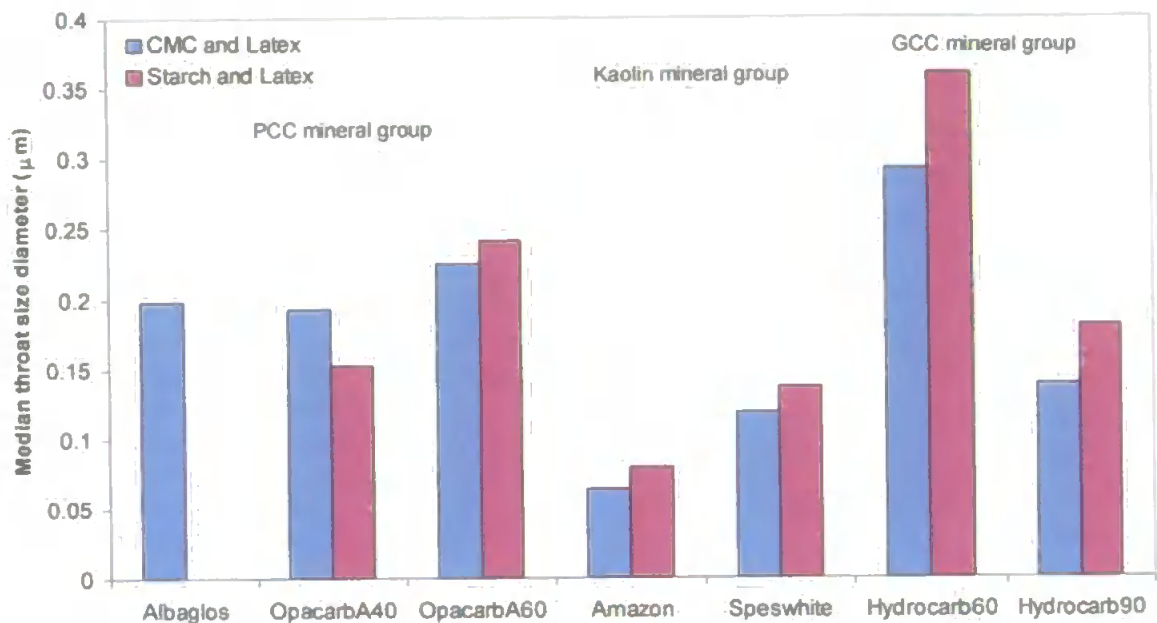


Fig. 5. 28. Median throat size diameter, d_{50} , for the CMC and latex and the starch and latex samples.

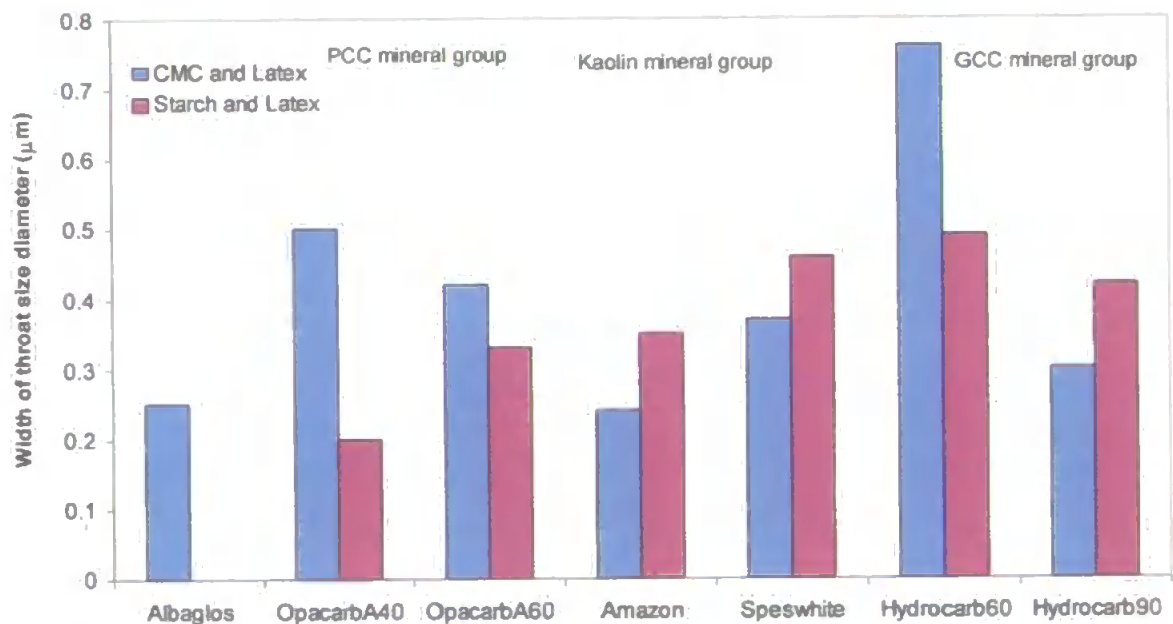


Fig. 5. 29. Width of throat size distribution for the CMC and latex and the starch and latex samples

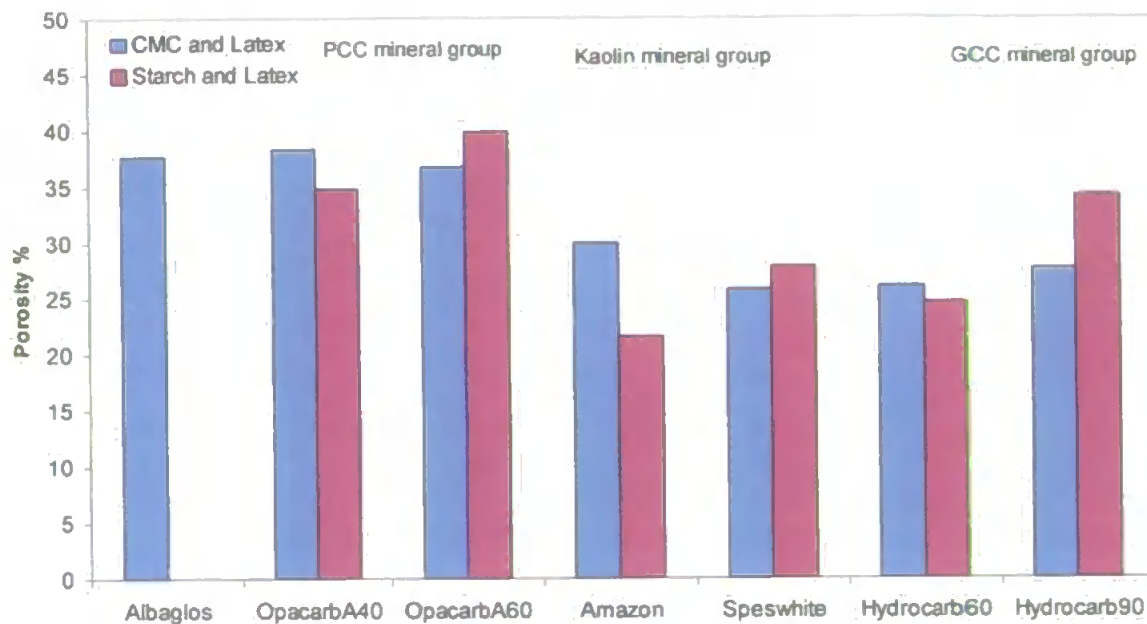


Fig. 5. 30. Porosity measurements for the CMC and latex and the starch and latex samples

Fig. 5.28 displayed how the samples containing starch, and latex are shown to have a larger median throat size diameter than the samples containing CMC and latex. The width of the throat size distribution, in fig. 5.29, and the porosity measurements of the samples, in fig. 5.30, showed no general trend between the samples containing CMC and latex and starch and latex. However, fig. 5.29 showed localised trends within the PCC and Kaolin mineral group. The PCC samples containing CMC and latex showed a greater width in throat size distribution than the PCC samples containing starch and latex; while the reverse trend is shown for the clay samples. The samples belonging to the Kaolin mineral group are shown to have much smaller median throat size diameters than the samples belonging to the PCC and GCC group, while the samples belonging to the PCC mineral group are shown to have much larger porosities than the samples belonging to the Kaolin or GCC group.

5.3.2. ISD Permeation results

The ISD permeation experiments were also performed on the complementary samples. Fig. 5.31 showed the ink stain density curves for the samples containing CMC and latex, while Fig. 5.32 showed the curves for the samples containing starch and latex.

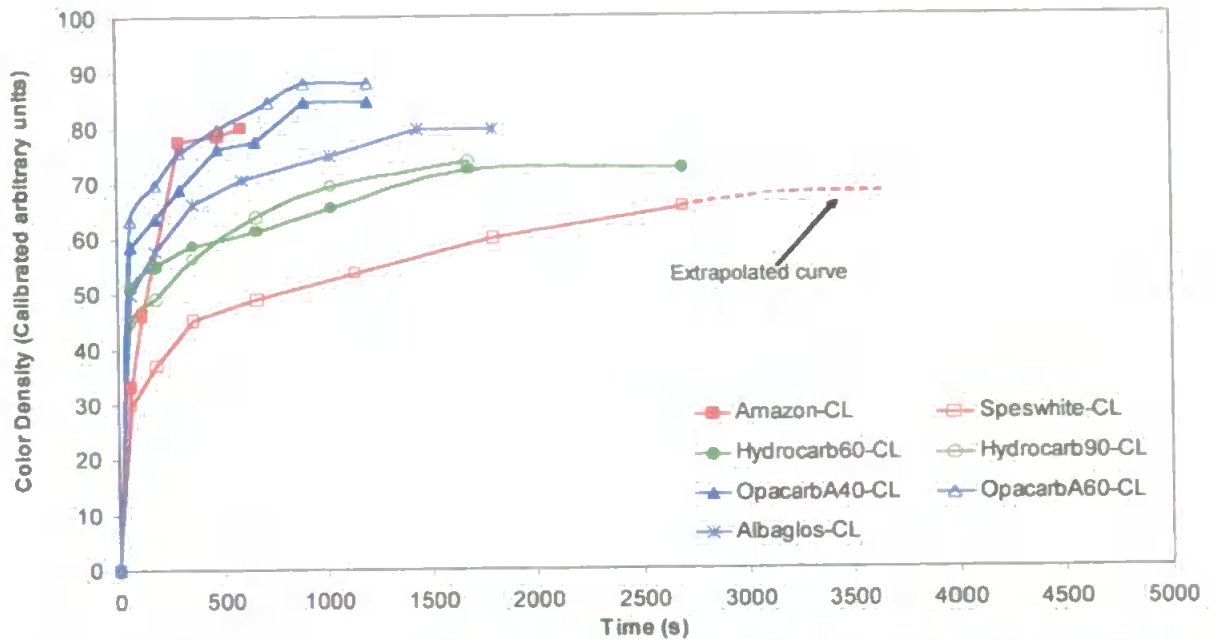


Fig. 5. 31. Comparison of the Setting Rates for coating samples, containing CMC and latex, from ink stain density experiments.

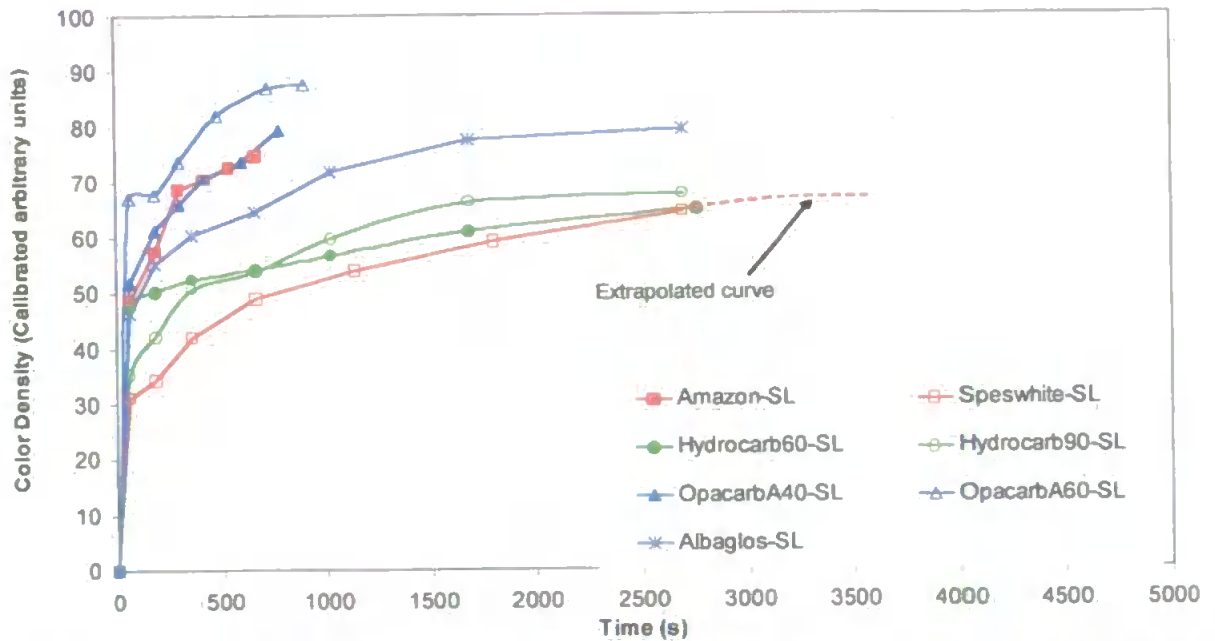


Fig. 5. 32. Comparison of the Setting Rates for coating samples, containing starch and latex, from ink stain density experiments.

The red coloured curves represent the coating samples belonging to the Kaolin mineral group, the green coloured curves represent the Ground Calcium Carbonate (GCC) mineral group, while the blue coloured curves represent the Precipitated Calcium Carbonate (PCC) mineral group. The curve for Albaglos is given a lighter blue colour as the mineral pigment has a different crystallographic habit to OpacarbA40 (refer to Section 3.1.1).

The saturation rates for the samples were calculated from the ink stain colour density curves, Fig. 5.33, and are termed as the ISD permeation rate.

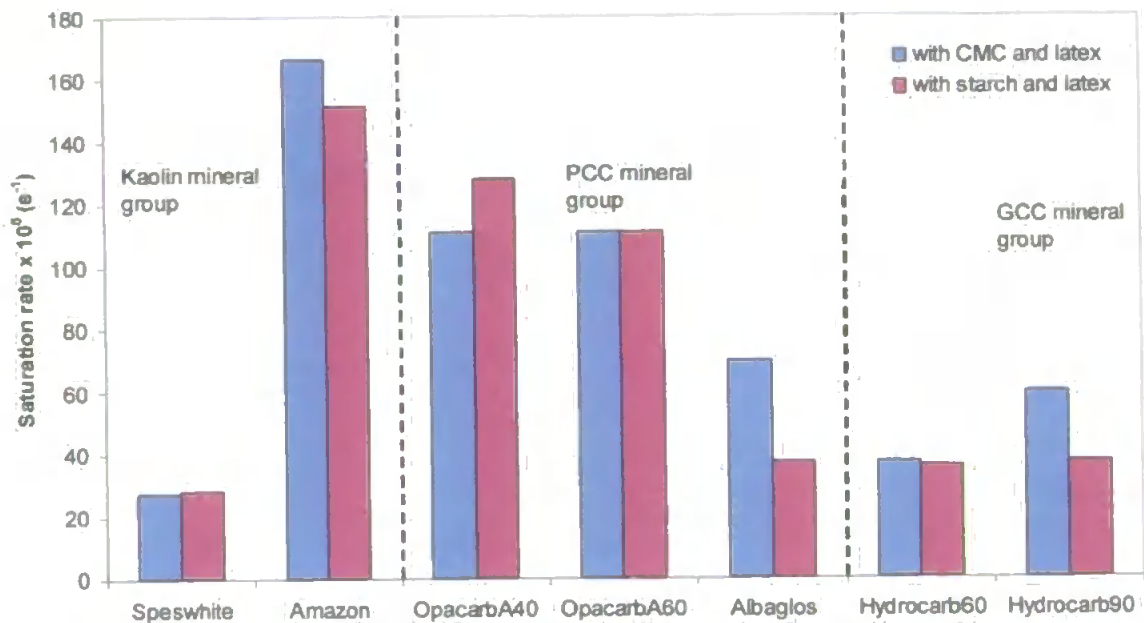


Fig. 5. 33. Saturation rate for pigment coating colours containing CMC and latex and starch and latex. The rate, measured from the Ink stain density curves, is also termed the ISD permeation rate.

Speswhite and Amazon, both belonging to the Kaolin mineral group, are shown to have the slowest and fastest ISD permeation rates, respectively, of all the coating colours. Amazon-CL showed a faster permeation rate than Amazon-SL, however, both cases of Speswhite coating showed no significant change. In the PCC coating group, both OpacarbA40 and OpacarbA60 showed a significantly faster permeation rate than Albaglos, with OpacarbA40-SL having the fastest permeation rate. The coating colours in the GCC mineral groups showed, in general, a much slower ISD permeation rate than the coating colours in the PCC mineral group. Furthermore, Hydrocarb90-CL showed a relatively faster permeation rate than the other coating colours in the GCC mineral group.

5.3.3. DAT Permeation results

The DAT method was also performed on OpacarbA60-CL, and its permeation curve is shown along with the curves from the primary samples, Fig. 5.34.

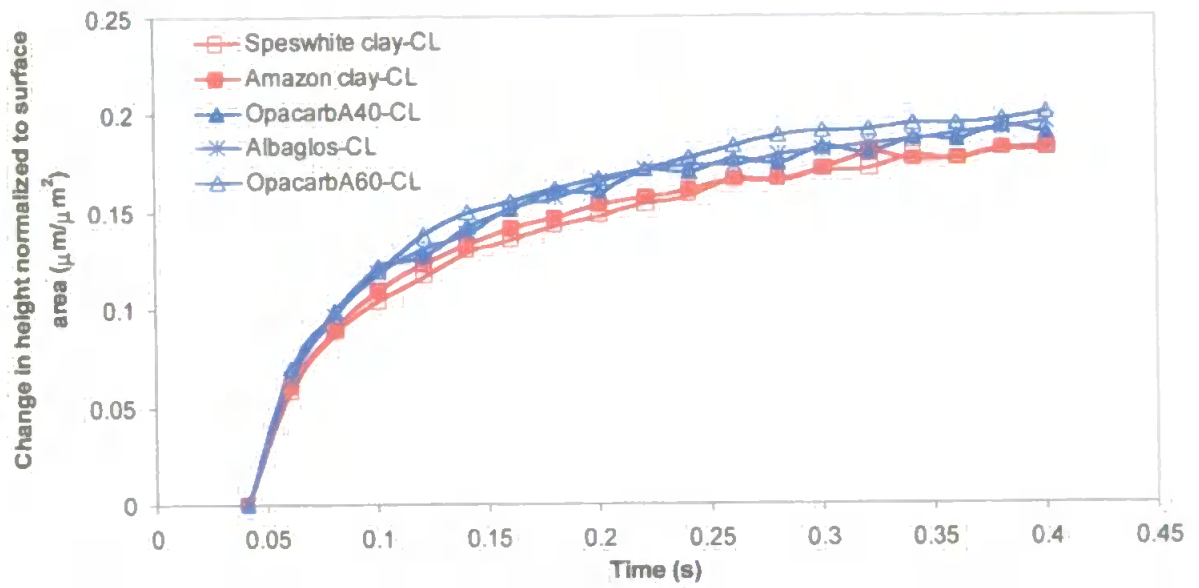


Fig. 5. 34. DAT permeation curves for the Kaolin and PCC coating samples, showing the change in height of the droplet normalized to surface area over an elapsed wetting time.

The change in normalized height for each coating sample, at approximately 0.4s, was calculated from these curves, and is shown in Fig. 5.35.

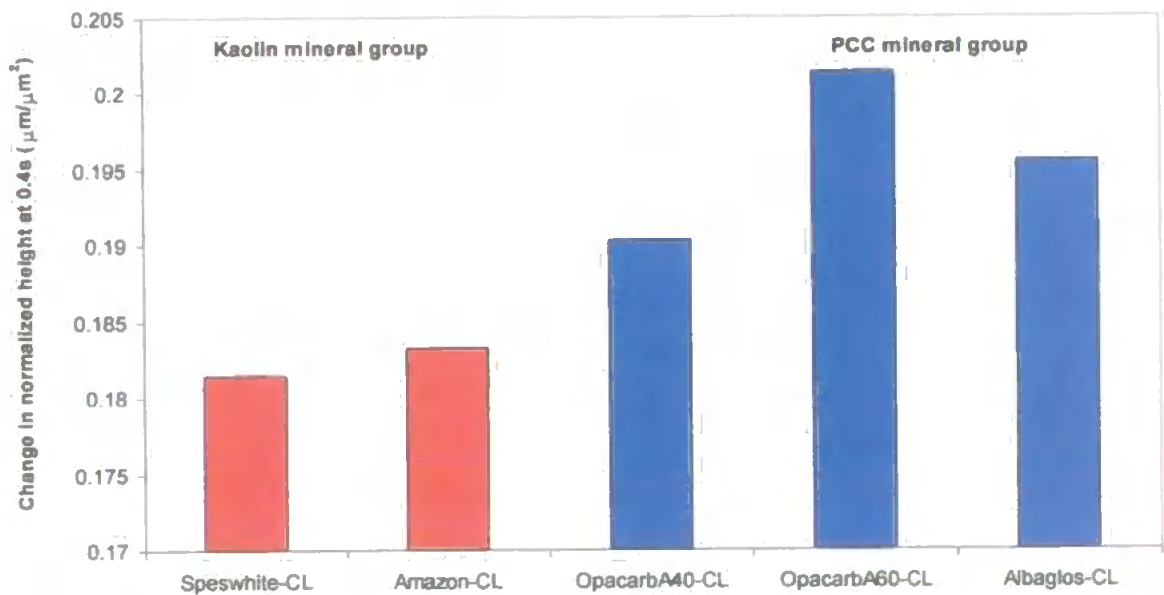


Fig. 5. 35. Change in normalized height for the droplet of oil at 0.4s for all Kaolin and PCC coatings containing CMC and latex.

The DAT permeation results were much the same as Fig. 5.18. The complementary sample, OpacarbA60-CL showed the highest permeation rate.

5.3.4. ISAM Permeation results

The ISAM was also performed on the other complementary samples comprising of a mineral pigment with CMC and latex. The results, corrected for film transfer with respect to absolute time are shown in Fig. 5.36.

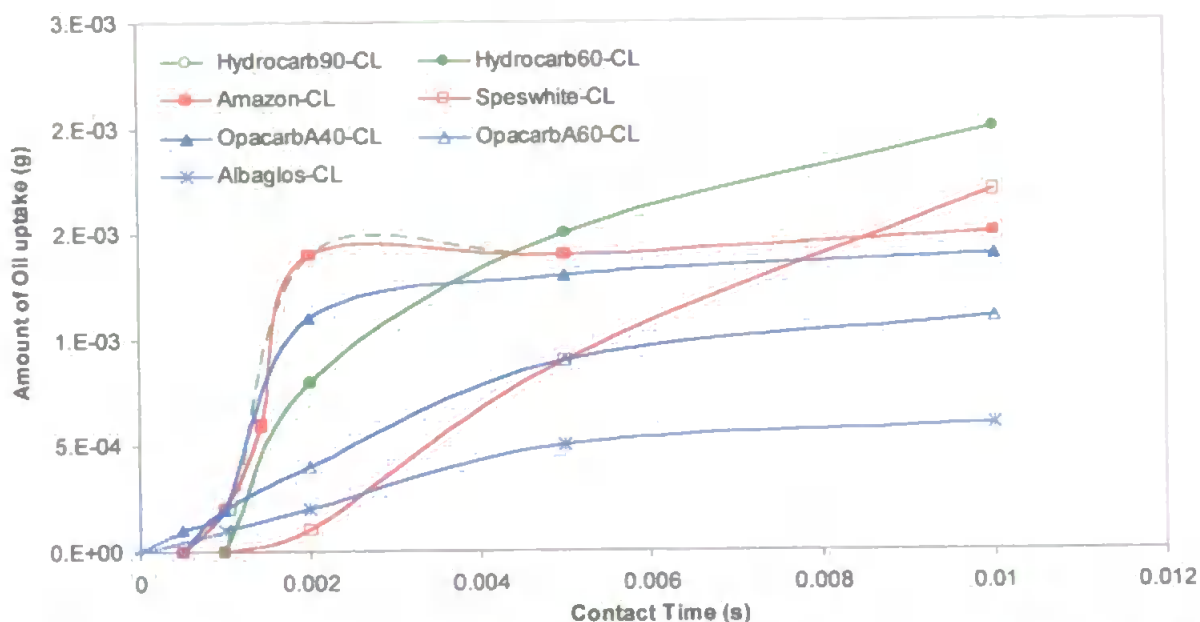


Fig. 5. 36. ISAM permeation results for the primary and complementary samples. The results were corrected for film transfer and were performed at 100N contact pressure.

The green coloured curves represent the coating samples belonging to the Ground Calcium Carbonate (GCC) mineral group. The results showed Hydrocarb90-CL and Amazon-CL to have the fastest permeation rates while Speswhite-CL was observed to have the slowest at between 1 and 2 ms. OpacarbA40-CL and Hydrocarb90-CL are also observed within this time frame to have a faster permeation rate than OpacarbA60-CL and Hydrocarb60-CL, respectively. The permeation rates at 0.002s contact time were shown for all the coating samples in fig. 5.37.

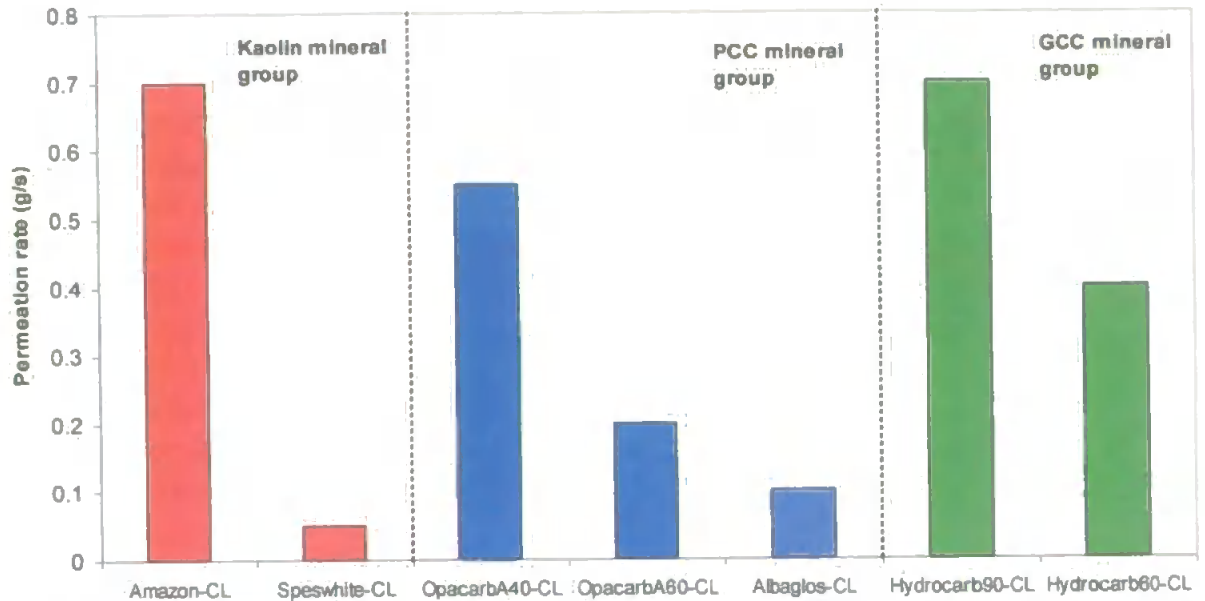


Fig. 5. 37. ISAM permeation rate of the primary and complementary samples at 0.002s contact time.

The coating samples were also arranged into their three mineral groups: Kaolin, PCC and GCC. Amazon-CL, OpacarbA40-CL, and Hydrocarb90-CL were shown to have the faster permeation rates of three mineral groups, respectively.

5.3.5. Permeation results from the Gurley method

The Gurley method was also performed on one complementary sample, OpacarbA60-CL. The results from the complementary sample along with the results from the primary samples are shown Table 5.6 and Fig. 5.38.

Sample	Coat weight (g/m ²)	Average time (Gurley seconds)	Air permeance (AP) (μm/Pa.s)	Gurley Permeability / mDarcy	% Standard error	Gurley Permeability at 11 g/m ² coat weight (mDarcy)
Speswhite-CL	13.2	584.8	0.231703146	5.14E-03	4.98	6.00E-03
	10.8	486.8	0.272745572	6.05E-03	1.35	
Amazon-CL	12.6	502.8	0.269490851	5.98E-03	1.68	7.50E-03
	9.7	351.6	0.385381115	8.55E-03	5.38	
OpacarbA40-CL	9.2	393.6	0.34425813	7.64E-03	0.70	1.43E-02
	12.6	205.6	0.659046693	1.46E-02	0.70	
OpacarbA60-CL	10.1	214.8	0.630819367	1.40E-02	0.85	1.55E-02
	11.4	197.4	0.686423506	1.52E-02	0.97	
Calibration plate	-	23.8	5.693277311	1.26E-01	-	-

Table 5. 6. Permeation results from Gurley method.

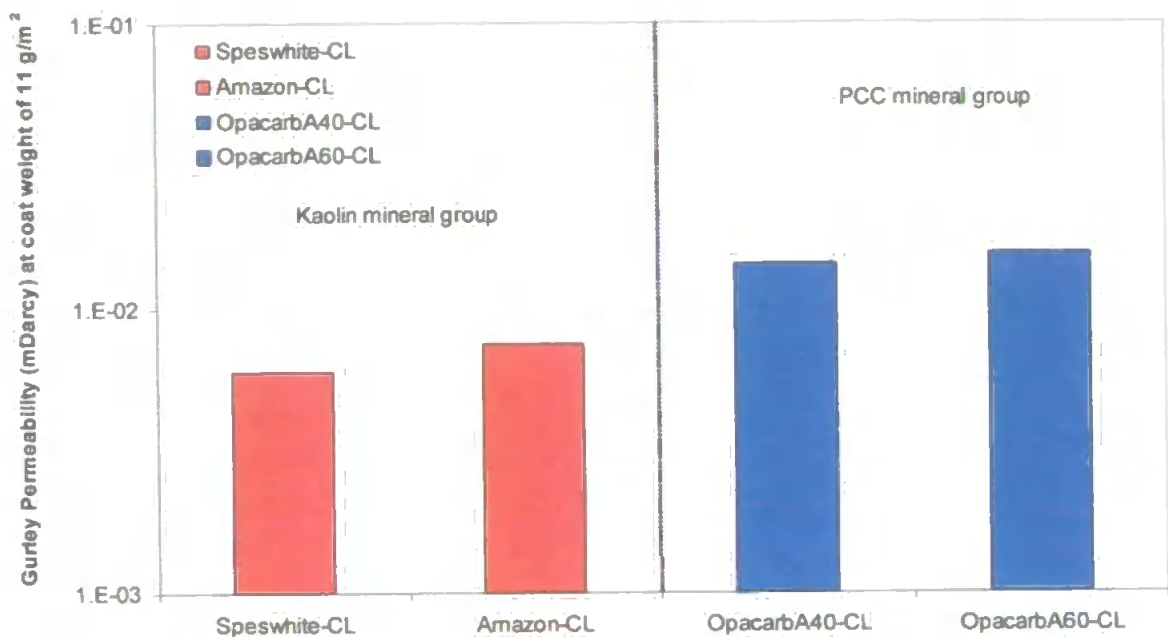


Fig. 5. 38. Gurley permeability measurements at a coat weight of 11 g/m².

The Gurley permeability measurements were much the same as Fig. 5.23, with the addition of the complementary sample, OpacarbA60-CL, showing a slightly higher permeability than OpacarbA40-CL.

5.4. Summary of results from primary samples

5.4.1. Characterisation of the particle and void structures

- The PCC samples are shown to have a larger median throat size diameter and porosity than the clay samples. Of the two mineral coating groups, OpacarbA40-CL and Speswhite-CL are shown to have the largest void size distribution. Although Amazon-CL is shown to have the smallest throat size diameter of the four samples, it was shown to have the largest surface area.

- Higher aspect ratio clay particles, structures containing aligned particles, pack more efficiently than those with lower aspect ratios. The particle packing causes a much lower number density of voids on the Speswhite surface compared to the Amazon surface.
- Although the median particle and void sizes are larger for Albaglos-CL than OpacarbA40-CL, they both have similar porosities. The particle packing, therefore, created a structure for Albaglos-CL with a lower number density than OpacarbA40-CL, as larger but fewer voids were created.

5.4.2. Experimental permeation results

- The ISAM, ISD and DAT method were all used as indirect measures of the experimental permeation rates for the samples, while the Gurley method was used as a direct measurement of permeability.
- All four experimental permeation methods showed Speswhite-CL to have a slower permeation than Amazon-CL. However, the ISAM and the ISD method showed Amazon-CL to have the fastest permeation while the DAT and the Gurley methods showed the samples in the PCC mineral group to have the fastest permeations. Hence, the permeation results from the DAT method much better resembled the permeability trends from the Gurley method than the ISAM or ISD method.
- The number density of surface throats is the dominant factor in determining the permeation results of the ISD and ISAM method. In summary, the

ISAM and ISD method better resembled surface number density trends than the permeability trends shown from the Gurley method.

5.5. Summary of results from the addition of complementary samples

5.5.1. Characterisation of the particle and void structures

The samples containing starch and latex are shown to have a larger median throat size diameter than the samples containing CMC and latex. The clay samples are shown to have much smaller median throat size diameters than the PCC or GCC samples, while the PCC samples are shown to have much larger porosities than the clay or GCC samples.

5.5.2. Experimental permeation results

- With the addition of the complementary samples, the ISD permeation results showed the clay samples, Speswhite and Amazon, to have the slowest and fastest permeation rates, respectively, of all the coating colours. The GCC samples are shown to have a much slower ISD permeation rate than the coating colours in the PCC mineral group.
- Both the DAT and Gurley permeation results showed the complementary sample, OpacarbA60-CL, to have the fastest permeation.
- The ISAM permeation results showed Hydrocarb90-CL and Amazon-CL to have the fastest permeation rates while Speswhite-CL was observed to have the slowest. Amazon-CL, OpacarbA40-CL, and Hydrocarb90-CL

were shown to have the fastest permeation rates, of three mineral groups, kaolin, PCC and GCC, respectively.

6. DEVELOPMENT OF THE PORE-COR MODEL

6.1. Basic Theory

Pore-Cor (Pore-level properties Correlator) is a computer model which has been used previously for modelling the behaviour of fluids in a wide range of materials such as porous calcium carbonate blocks (Ridgway *et al.*, 2001, Schoelkopf *et al.*, 2000) and soils (Peat *et al.*, 2000). The model generates a void structure comprising a large array of repeating, identical unit cells. Each unit cell is made up from 1000 cubic pores, in a 10 x 10 x 10 array, equally spaced from its neighbouring pores in the Cartesian co-ordinates x , y and z , and by the "pore row spacing" W . Hence, each unit cell is a cube of side length $10 W$. Cylindrical throats connect each pore and there can be up to six throats per pore – i.e. one on each face.

The percolation characteristics and the porosity of the overall void structure are matched to the experimental mercury intrusion curve of a chosen sample by adjusting the void size distribution, using the parameters of 'throat skew', 'pore skew', 'connectivity' and porosity.

Throat skew is defined as the percentage of throats of the smallest size in a log/linear distribution, as shown in Fig. 6.1. If the skew is set to 0.8 %, then 0.8 % of the total number of throats, to the nearest integer, has the smallest of the 100 sizes. The linear distribution pivots about the median, so in this case there will be 1 % of the median size, and 1.2 % of the largest size. A value of throat skew greater than one would represent a structure containing a larger proportion of smaller-sized throats; while a value of throat skew less than one would represent a

structure containing a smaller proportion of smaller-sized throats. Meanwhile, a throat skew value of one would represent an equal proportion of throat sizes.

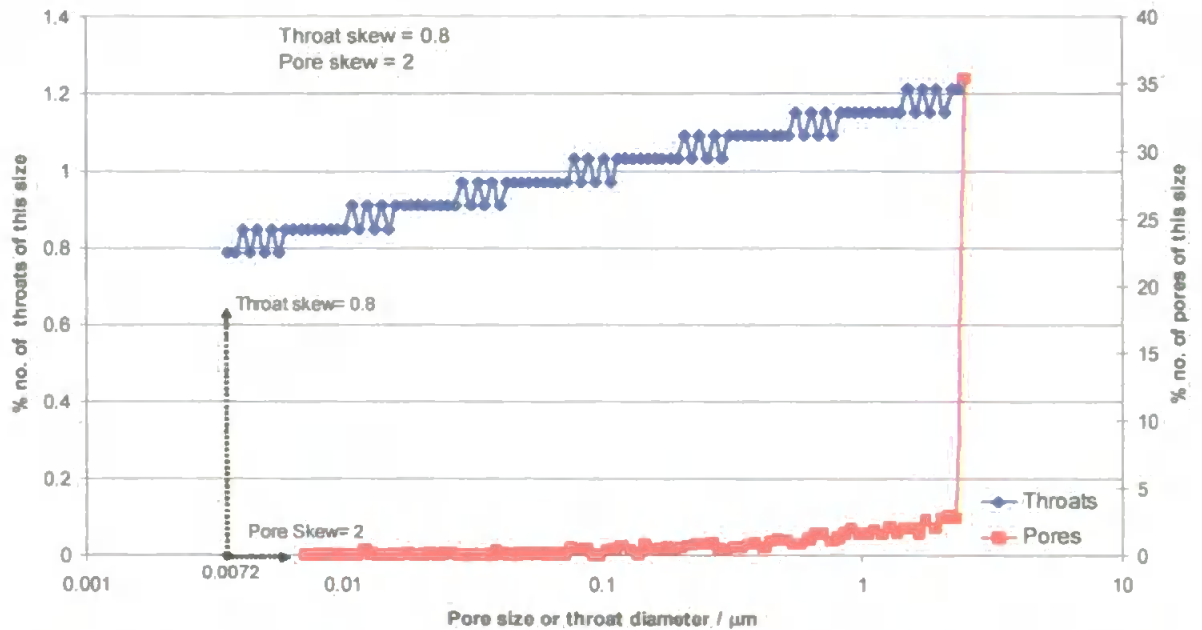


Fig. 6. 1. Example of a pore and throat size distribution for a pore skew value of 2 and a throat skew value of 0.8. The throat size distribution shows a minimum and maximum throat diameter of 0.0036 μm and 2.4 μm , respectively.

The arrangements of the pores and throats in the model were equally spaced for simplicity of calculation. However, this caused the structure to pack inefficiently, and to achieve the experimental porosity it was sometimes necessary to enlarge the pores by a factor known as the 'pore skew', giving pores sizes up to, but never exceeding, the original maximum size. The effect is shown in Fig. 6.1, in which a pore skew of 2 causes the pore size distribution to start at $0.0036 \times 2 = 0.0072 \mu\text{m}$. The size distribution is truncated at the original maximum size of 2.4 μm , and all pores above 2.4 μm are allocated that size, giving a peak in the size distribution at that point.

The pore-skew parameter therefore gives a distribution arising from the inefficiencies in the packing of features within the unit cell, rather than an

experimental feature of the sample. The pore skew parameter is therefore a somewhat unsatisfactory parameter, and is kept as low as possible consistent with achieving the correct porosity and a simulated fit close to the experimental mercury intrusion curve.

Fig. 6.1 shows that the distributions of sizes of features are simplistic, and not the Gaussian or Poisson distributions which might be expected. However, historically they have been shown to be sufficiently flexible to fit uni-modal mercury intrusion or water retention curves of a wide range of samples. Importantly, they also depend on only one parameter each for the throat and pore size distributions, and are thus easily fitted by a grid optimisation.

The number of throats connected to a particular pore is termed the 'pore co-ordination number', and the arithmetic mean of this quantity over the whole unit cell is the connectivity. Individual pore co-ordination numbers may range from 0 to 6, and a typical value of the connectivity in a real sample is 3.5. Pore-Cor is also capable of simulating size-correlated networks such as layered or laminated structures (Matthews *et al.*, 1995), but both the electron micrographs and tests with Pore-Cor showed the present structures to be random.

6.2. New developments in Pore-Cor

In this study, we have modified the structure of the unit cell to make it anisotropic by re-scaling the z axis relative to the x and y axes. When the z axis is re-scaled to make features smaller, the pores become tetragonal (slit-like in shape), and the throats in the x and y directions gain ellipsoidal cross-sections

with the major axis in the x or y direction. The effect is illustrated in Fig. 6.2, in which the z -axis is shown vertically.

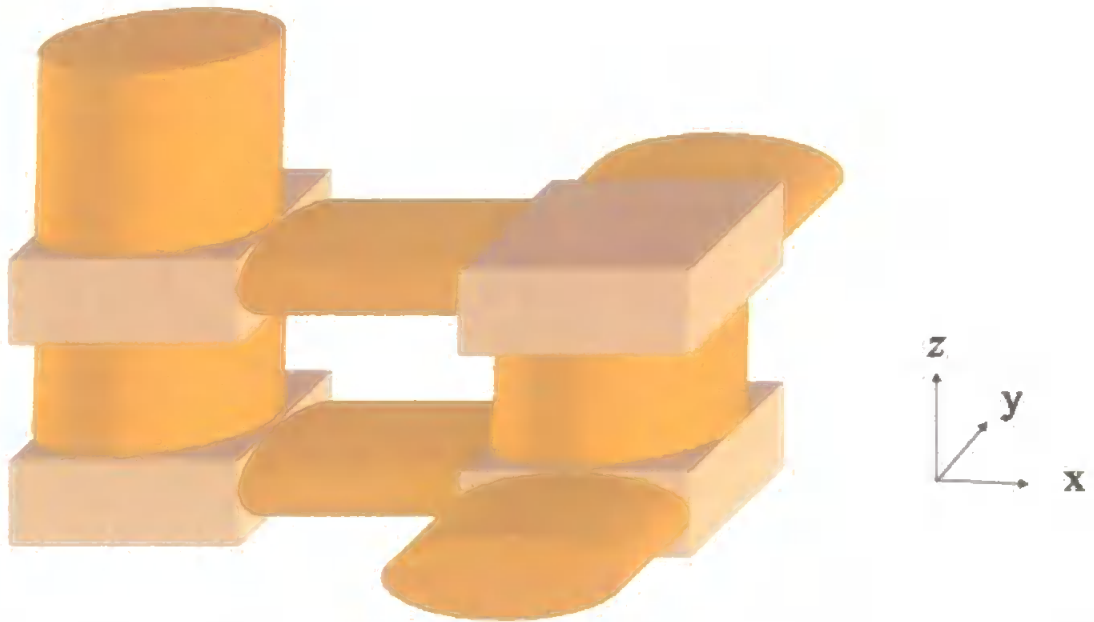


Fig. 6. 2. Example of Anisotropic Structure showing throats with elliptic cross-sections and plate-like pores with rectangular cross-sections. Aspect factor equals 0.4.

Alternatively, the z -axis was scaled so that all features had larger dimensions with respect to this axis with the dimensions remaining constant on the other two axes, Fig. 6.3.

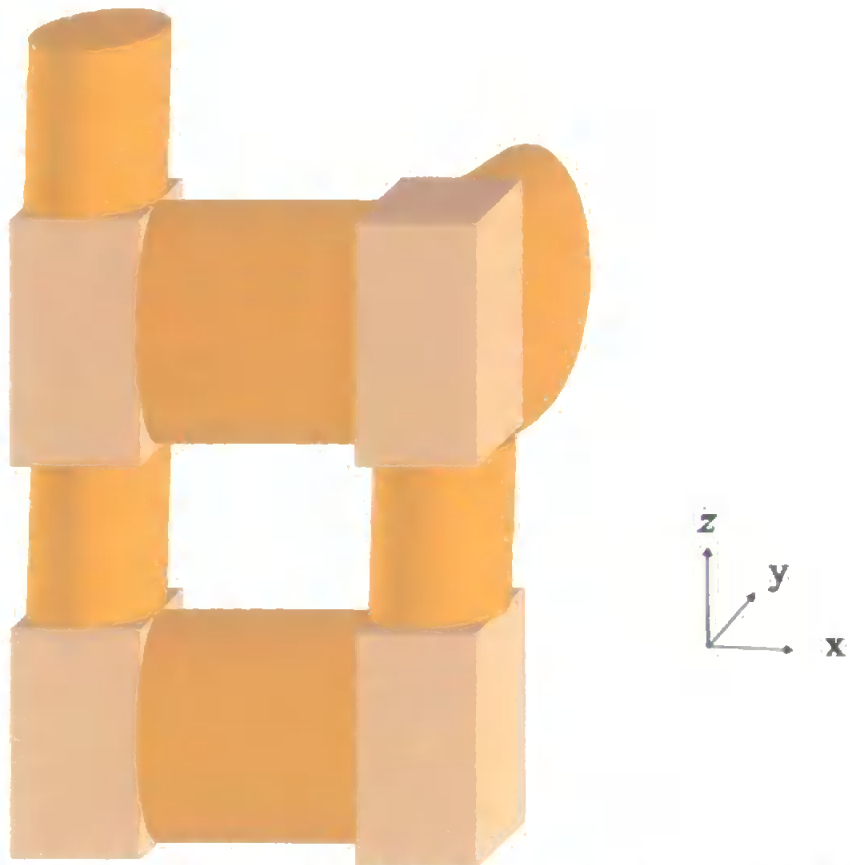


Fig. 6. 3. Example of Anisotropic Structure showing throats with elliptic cross-sections and rod-like pores with rectangular cross-sections. Aspect factor equals 2.1.

Such a transformation results in rod-like pores, and the throats in the x and y direction become ellipsoidal in cross-section, but in this case with the major axis in the z direction. The scaling factor was termed the 'aspect factor' α . The aspect factors of the structures shown in Fig. 6.2 and Fig. 6.3 are 0.4 and 2.1, respectively.

Pore-Cor was also modified to generate three different types of void structures where the layers were horizontally correlated in respect to size. These structure types were as follows:

Horizontally-banded structure #1: The largest throat and pore sizes were located at the top surface. Each descending layer from the top surface decreased in throat and pore sizes until the bottom layer was reached, as shown in Fig. 6.4.

Since the unit cell infinitely repeats itself in all directions, the bottom layer of the unit cell must contain the largest pore sizes. This made it possible for the largest throat sizes at the top surface of the repeating unit cell to properly connect to the bottom layer of the unit cell.

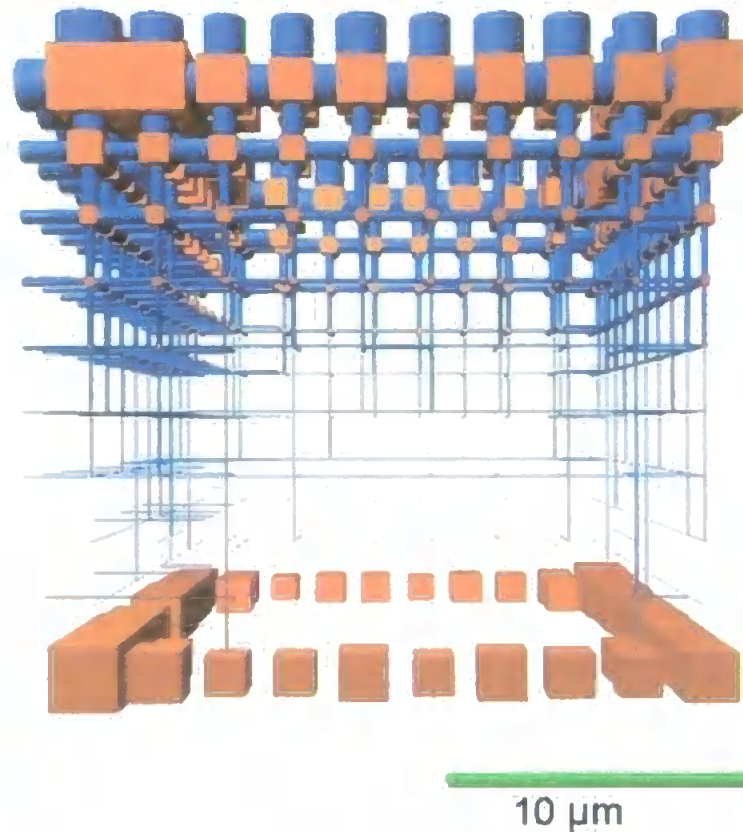


Fig. 6. 4. Horizontally-banded structure #1. The brown squares represent the pores, while the blue cylinders represent the throats.

Horizontally-banded structure #2: The largest throat and pore sizes were located at the top surface, with the smallest throat and pores sizes situated one layer below. Each next descending layer then increased in throat and pore sizes, as shown in Fig. 6.5.

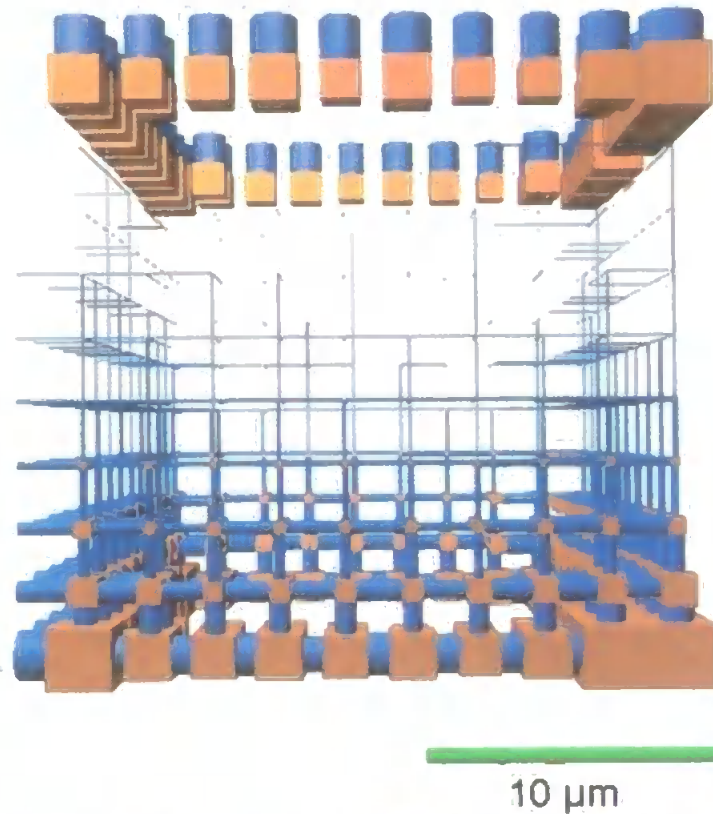
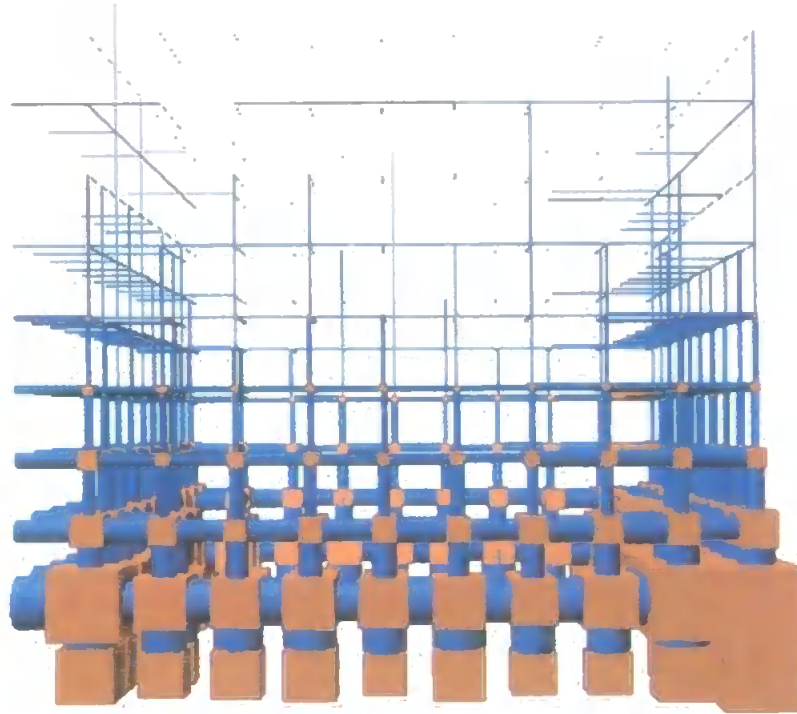


Fig. 6. 5. Horizontally-banded structure #2. The brown squares represent the pores, while the blue cylinders represent the throats.

Horizontally banded structure #3: The smallest throat and pore sizes were located at the top surface. Each descending layer from the top surface increased in throat and pore sizes, as shown in Fig. 6.6.



10 μm

Fig. 6. 6. Horizontally-banded structure #3. The brown squares represent the pores, while the blue cylinders represent the throats.

The simulated mercury intrusion curves for all three horizontally banded structures are shown in Fig. 6.7 with respect to applied pressure. Fig. 6.8 showed the simulated intrusion curves for the equivalent calculated throat diameter using an interfacial tension of 48 N m^{-1} ($480 \text{ dynes cm}^{-1}$) and an advancing contact angle of 140° .

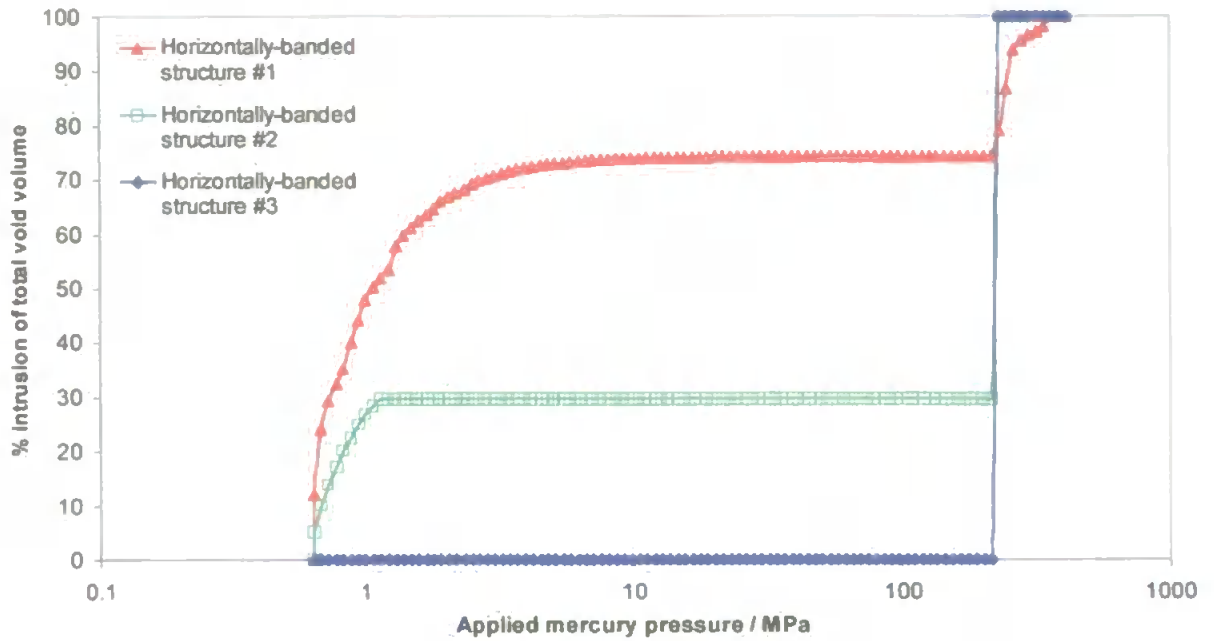


Fig. 6. 7. Simulated mercury intrusion curves for the three horizontally-banded structures shown in Fig. 6.4, 6.5 and 6.6. The parameters for the simulated structures are for a connectivity of 2.4, throat skew of 1, correlation level of 1, porosity of 7.5%, and a minimum and maximum throat diameter of approximately 2.3 μm and 0.0036 μm , respectively.

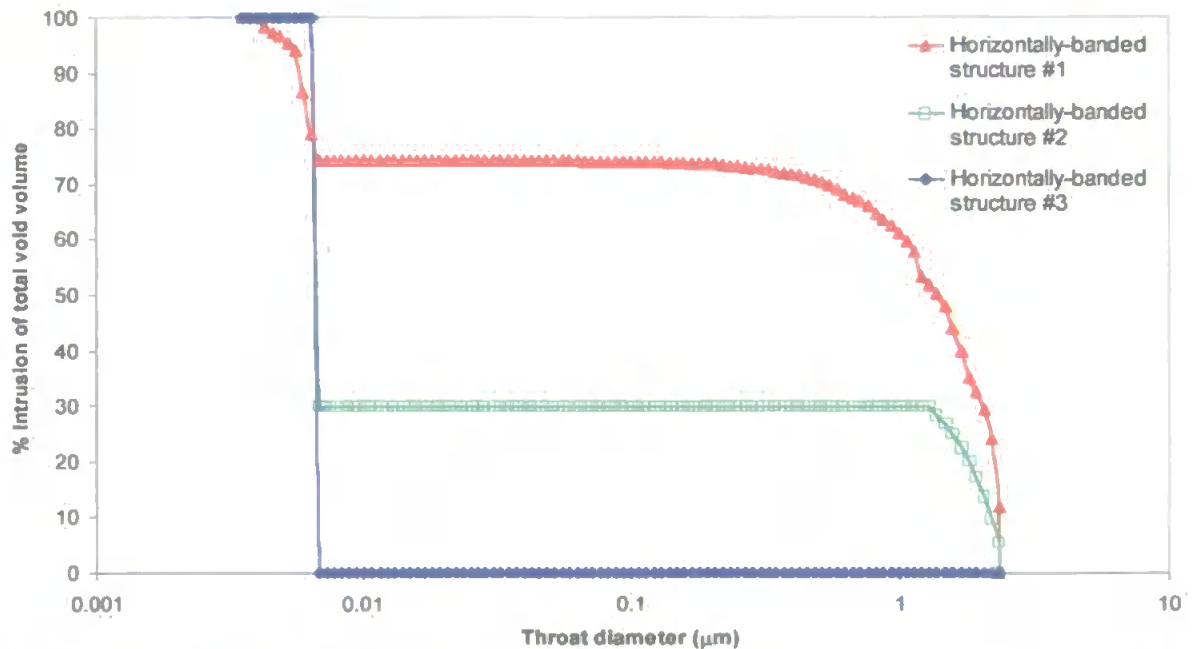


Fig. 6. 8. Same as Fig. 6.7, except the x-axis is represented by the equivalent throat diameter.

For the horizontally-banded structure #1, the mercury is shown to intrude initially at a relatively fast rate, up to an applied pressure of about 2.9 MPa (equivalent throat diameter of approximately 0.5 μm), as all of the larger throats and pores are filled

with mercury during this fast intrusion rate. The mercury then intrudes at a more gradual pace as it begins to fill the smaller pores and throats, causing 74% of the total void volume to be partially-filled, Fig. 6.9.

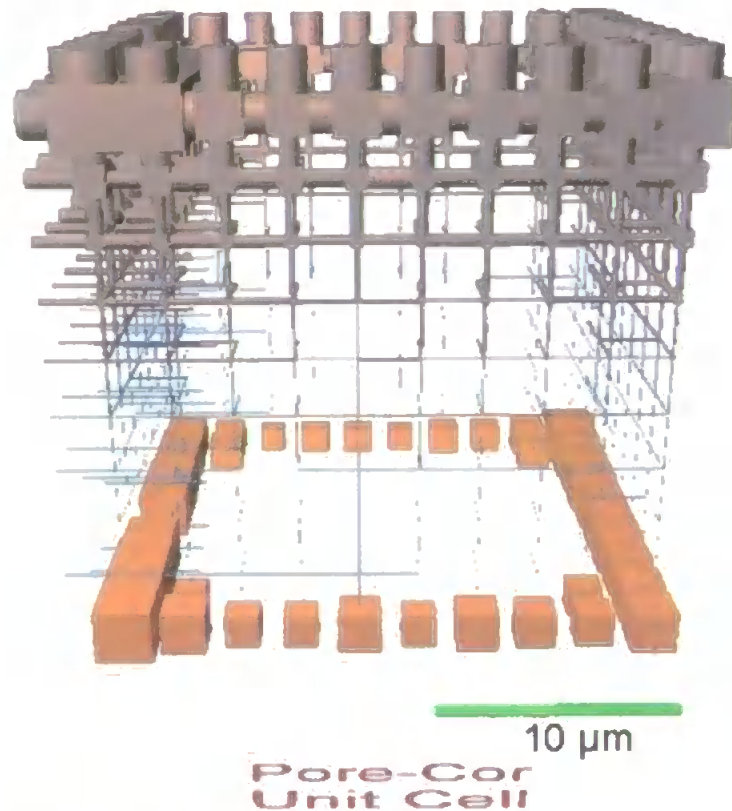


Fig. 6. 9. Horizontally-banded structure #1. A simulated partial fill of mercury at an applied pressure of about 14 MPa (equivalent throat diameter of approximately 0.1 μm). The grey colour represents the intrusion of mercury into the top surface of the void structure; the blue represents the throats and the brown the pores.

Once an applied pressure of around 210 MPa (equivalent throat diameter of around 0.007 μm) is reached, the bottom layer of larger pores, are filled at a relatively fast rate.

For the horizontally-banded structure #2, the mercury is shown to intrude initially at a fast rate, similar to structure #1, but only to an applied pressure of about 1.0 MPa (equivalent throat diameter of approximately 1.3 μm). The top layer of large surface throats and pores are filled with mercury during this fast intrusion rate, as

the applied mercury pressure was not high enough for the mercury to enter the lower throat diameters below the first layer. Approximately 30% of the total void volume is shown to be partially filled at an applied pressure of about 145 MPa (equivalent throat diameter of approximately $0.01 \mu\text{m}$), as shown in Fig. 6.10.

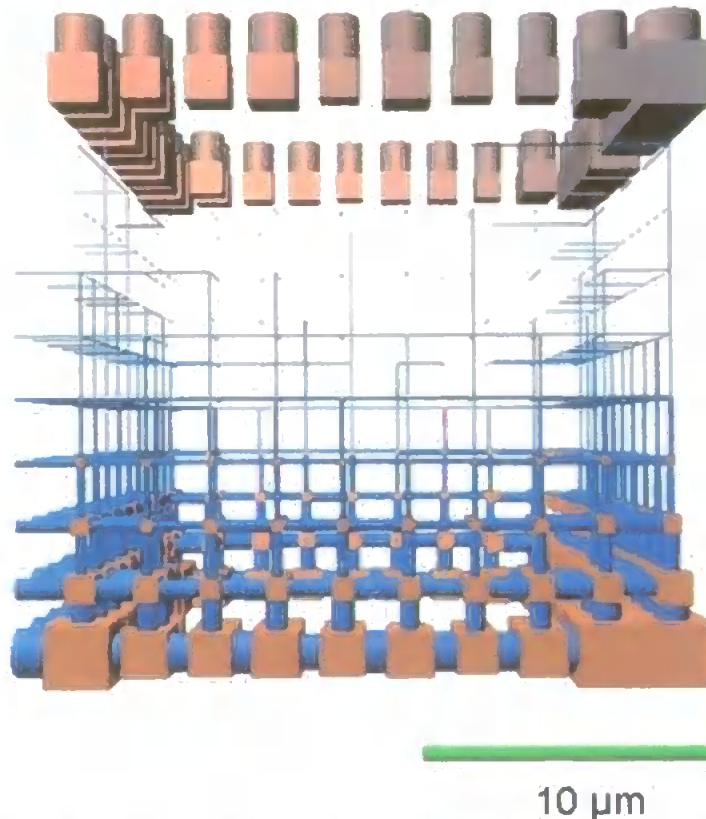


Fig. 6. 10. Horizontally-banded structure #2. A simulated partial fill of mercury at an applied pressure of about 145 MPa (equivalent throat diameter of approximately $0.01\mu\text{m}$). The grey colour represents the intrusion of mercury into the top surface of the void structure; the blue represents the throats and the brown the pores.

An increase in applied pressure, caused the mercury to intrude below a throat diameter of $0.01 \mu\text{m}$, and caused a sharp increase in the intrusion of the total void volume. The void structure was completely filled with mercury, as the throat and pore diameters of each layer become larger. A simulation is shown in Fig. 6.11 of where mercury has filled the void structure, for an applied pressure of about 296 MPa (equivalent throat diameter of approximately $0.005 \mu\text{m}$). It showed the intrusion of mercury to fill 100% of the total void volume.

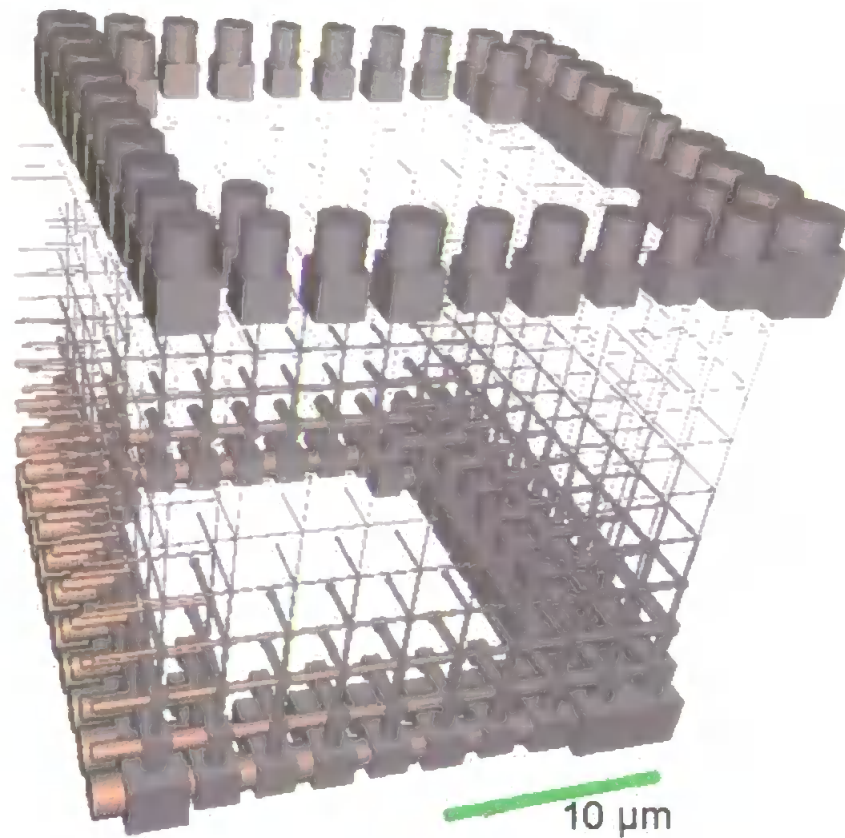


Fig. 6. 11. Horizontally-banded structure #2. A simulation for an applied mercury pressure of about 296 MPa (equivalent throat diameter of approximately 0.005 μm). The grey colour represents the intrusion of mercury into the void structure.

For the horizontally-banded structure #3, there is no intrusion of mercury until an applied pressure of about 241 MPa (equivalent throat diameter of approximately 0.006 μm) was reached, as the top layer contained the smallest pores and throats, as shown in fig. 6.6. Since the throat and pore diameters of each descending layer become larger, the mercury is then shown to fill the entire structure at a sharp intrusion rate.

6.3. Porosity algorithm in Pore-Cor

The porosity of a porous medium is defined as the percentage of void space within the total bulk medium. For an isotropic unit cell generated by the computer model, the porosity ϕ is

$$\phi = \frac{\sum_{n=1}^{1000} \left((V_{\text{pore}})_{n,i} + \sum_{i=1}^3 (V_{\text{throat}})_{n,i} \right)}{V_{\text{bulk}}} = \frac{\sum_{n=1}^{1000} \left(L_n^3 + \sum_{i=1}^3 (\pi r_{n,i}^2 h_{n,i}) \right)}{1000 W(1) W(2) W(3)}$$

Eq. 6. 1

$(V_{\text{pore}})_{n,i}$ is the volume of the n th individual pore in the network, $(V_{\text{throat}})_{n,i}$ is the volume of the throat attached to pore n in the i^{th} Cartesian direction, and V_{bulk} is the bulk or envelope volume of the unit cell. L is the side length of the cubic pore, $r_{n,i}$ and $h_{n,i}$ are the radius and length of the n^{th} throat in the i^{th} Cartesian direction, and $W(1)$, $W(2)$ and $W(3)$ are the spacing between the rows of pores in the 1st, 2nd and 3rd Cartesian (x) direction, respectively.

For anisotropic void networks, the porosity equation was modified such that it referred to the volume of throats with an elliptic cross-section and pores with a rectangular cross-section:

$$\phi = \frac{\sum_{n=1}^{1000} \left(L_{n,x} L_{n,y} L_{n,z} + \sum_{i=1}^3 (\pi r_{1,n,i} r_{2,n,i} h_{n,i}) \right)}{1000 W(1) W(2) W(3)}$$

Eq. 6. 2

where $L_{n,x}$, $L_{n,y}$ and $L_{n,z}$ refer to the width of the n th pore in the x , y and z direction, and $r_{1,n,i}$ and $r_{2,n,i}$ are the two radii of the n^{th} ellipsoidal throat in direction i .

6.4. Percolation algorithm in Pore-Cor

The Laplace equation (refer to Section 2.6) gives the diameter d of a cylindrical throat in an incompressible solid exposed to mercury, which is intruded when the pressure applied to the mercury is greater than or equal to P :

$$d = \frac{4\gamma \cos \theta}{P}$$

Eq. 6. 3

γ is the interfacial tension between mercury and air (assumed 480 dynes cm-1), and θ is the contact angle between the edge of the advancing convex mercury meniscus and the solid surface (assumed 140°). The use of this equation has many well-known shortcomings discussed by Van Brakel (Van Brakel, 1981), such as uncertainties in the values of γ and θ .

For anisotropic structures, the same form of the Laplace equation was used to calculate an 'effective' intruded throat diameter (d_{eff}) for every applied pressure of mercury. The effective throat size is related to the two diameters (d_1 and d_2) of an elliptical throat by the relation:

$$d_{\text{eff}} = \frac{4\gamma \cos \theta}{P} = \frac{2}{\left(\frac{1}{d_1} + \frac{1}{d_2}\right)} = \frac{2 d_2 \alpha}{1 + \alpha}$$

Eq. 6. 4

where $\alpha = \frac{d_1}{d_2}$

For isotropic structures, with $\alpha=1$, Eq. (6.4) reduces to Eq. (6.3) and $d_{\text{eff}} = d_1 = d_2$ as expected.

The invasion percolation algorithm applied to the entire simulated porous structure has been described previously (Matthews *et al.*, 1993). In the simulation, mercury is applied only at the top surface of the unit cell. Since the unit cell repeats infinitely in each direction, this is equivalent to applying mercury to a sheet of infinite width in the x direction and breadth in the y direction, with a thickness equal to the size of one unit cell in the z direction. The percolation of this infinite sheet in one starting direction ($-z$) is used to simulate the percolation from all directions of an experimental sample. The porosimetry of the coating was studied on collections of thin flakes, as described above, in which the thicknesses were around three orders of magnitude smaller than the other dimensions. Therefore it was reasonable to assume that percolation through the edges of the samples were negligible compared to percolation through the faces, and that there was a match between the boundary conditions of the experimental and simulated percolation. However, as the permeation proceeds, the relatively small size of the unit cell in comparison to the size of the sample will cause some problems in simulating the correct percolation characteristics.

6.5. Wetting algorithm in Pore-Cor

The equation for wetting was a modified version of the Lucas/Washburn equation as developed by Bosanquet (Bosanquet, 1923). Bosanquet considered the viscous, inertial, and capillary forces, which act as a fluid enters a capillary tube of radius r from an infinite reservoir (supersource). It was used to determine the rate of permeation of a wetting fluid into the simulated coating structures. Balancing these forces, he showed that

$$\frac{d}{dt} \left(\pi r^2 \rho x \frac{dx}{dt} \right) + 8 \pi \mu x \frac{dx}{dt} = P_e \pi r^2 + 2 \pi r \gamma \cos \theta$$

Eq. 6. 5

where x is the distance travelled by the liquid front in time t , and P_e is the external pressure applied at the entrance of the capillary tube.

For elliptical throats with major radius c and minor radius d , the Bosanquet equation becomes

$$\frac{d}{dt} \left(\rho \pi r_1 r_2 x \frac{dx}{dt} \right) + \pi \mu x \frac{dx}{dt} = P_e \pi r_1 r_2 + 4 r_1 E(e^2) \gamma \cos \theta$$

Eq. 6. 6

$E(e)$ is the elliptical integral:

$$E(e) = \int_0^{\frac{\pi}{2}} (1 - e \sin^2 \theta)^{\frac{1}{2}} d\theta$$

Eq. 6. 7

The eccentricity, e , is defined as

$$e = \sqrt{1 - \frac{r_2^2}{r_1^2}}$$

Eq. 6. 8

Abramowitz and Stegun (Abramowitz, 1965) have derived a polynomial approximation for $E(e)$:

$$E(e) = (1 + a_1 w + a_2 w^2) + (b_1 w + b_2 w^2) \log_e \left(\frac{1}{w} \right) + \text{error}$$

Eq. 6. 9

where,

$$w = 1 - e,$$

$$|\text{error}| < 4 \times 10^{-4}, \quad a_1 = 0.4630151, \quad a_2 = 0.1077812, \quad b_1 = 0.2452727$$

and $b_2 = 0.0412496$

Eq. 6.8 and 6.9 are then combined and related to $E(e^2)$ as follows:

$$E(e^2) = \left[1 + a_1 \left(\frac{r_2}{r_1} \right)^2 + a_2 \left(\frac{r_2}{r_1} \right)^4 \right] + \left[b_1 \left(\frac{r_2}{r_1} \right)^2 + b_2 \left(\frac{r_2}{r_1} \right)^4 \right] \log_e \left(\frac{r_1}{r_2} \right)^2$$

Eq. 6. 10

By integration of Eq. 6.6 and letting

$$a = \frac{8\mu}{\rho r_1 r_2} \quad \text{and} \quad b = \frac{P_c \pi r_2 + 4E(e^2)\gamma \cos \theta}{\pi \rho r_2}$$

it can be shown that

$$x_2^2 - x_1^2 = \frac{2b}{a} \left\{ t - \frac{1}{a} (1 - e^{-at}) \right\}$$

Eq. 6. 11

where x_1 is the initial position and x_2 is the position after time t .

The Bosanquet equation was used to calculate the wetting flux in each pore and throat in the void network after every time-step, using a predictor-corrector method (Schoelkopf *et al.*, 2000). This method is based on the principle of jumping the time forward by making the forward step smaller again if it proved to be too large. However because the method was being run simultaneously for many thousands of features, it was not possible to use the corrector approach. Therefore the whole combination had to be carried out with the maximum time step which was known always to be valid. This was only 1 nanosecond. Once a throat was full, the volumetric flow rate of the fluid leaving the throat was calculated and this fluid started to fill the adjacent pore. The pore could be filled by fluid from more than one throat, which may start to flow into it at different times. Once a pore was full, it started to fill the throats connected to it that were not already full and which were not already filling from other pores. If at any stage the outflow of a pore exceeded the inflow then a mass conservation restriction was applied which removed this imbalance and restricted the fluid flow further into the network.

The permeation, $\Pi(t)$, was quantified as the volumetric amount of fluid absorbed per unit area, $V_a(t)$:

$$\Pi(t) = \frac{V_a(t)}{Q_p(1) Q_p(2)}$$

Eq. 6. 12

The permeation was also expressed as a Darcy length, L , defined as

$$L(t) = 10 W(3) F_w(t)$$

Eq. 6. 13

Here $F_w(t)$ is the fraction of the total void volume filled with a wetting fluid at time t . $L(t)$ corresponds to the volume-averaged distance between the supersource and the wetting front.

It is evident that the calculation involved predictor-corrector calculations in up to 3000 features at every time step, followed by a complete mass balance summation and correction. Due to the complexities of these calculations and the limit on the time step of 1 nanosecond, and despite the efficiencies of the programming code and language, the simulation of wetting occurring in 0.1 s of real time took of the order of 10 hours on a 1 GHz personal computer.

6.6. Absolute permeability algorithm in Pore-Cor

A long-standing problem in the research of porous media have been the calculation of permeability in terms of the medium's pore level geometry. A method that has been recognised by various researchers is the combination of Darcy's Law (refer to Section 2.1 and 2.2) and Poiseuille's Equation (refer to Section 2.4) (Scheidegger, 1974).

Darcy's Law is expressed below as:

$$\frac{dV}{dt} = -\frac{k A \delta P}{\mu l}$$

Eq. 6. 14

where dV/dt is the volumetric flow rate, $\delta P / l$ is the pressure gradient across the medium, A is the cross-sectional area, and μ is the viscosity of the liquid. The dependence of the flow on the void structure of the medium is contained in the absolute permeability, k .

The Poiseuille equation is shown to be expressed as

$$\frac{dV}{dt} = -\frac{\pi r^4 \delta P}{8\mu l} = -\frac{\pi F \delta P}{8\mu}$$

Eq. 6. 15

where r is the radius of the tube and $\delta P / l$ is the pressure gradient between the ends of the tube. The term r^4 / l corresponds to the volumetric flow capacity F . In using the Poiseuille equation, we recognise that it is only a first approximation to the resistive flow of a feature within the network.

We now assume that Poiseuille flow occurs across the whole cell:

$$\left(\frac{dV}{dt}\right)_{\text{cell}} = -\frac{\pi}{8\mu} \Omega_{\text{cell}}(F_{\text{arcs}}) \frac{\delta P_{\text{cell}}}{l_{\text{cell}}}$$

Eq. 6. 16

where Ω_{cell} is an averaging operator over the whole unit cell, operating on the flow capacities of the arcs (F_{arcs}).

Again, there is an approximation in doing this. The model implicitly assumes that Poiseuille flow occurs at all points within the network. It ignores non-Poiseuille flow which occurs at corners and other feature discontinuities, which leads to effects such as hinging, and also causes the wetting front to move almost

instantaneously to a new position under some circumstances (Kent, 1989; Sell *et al.*, 1986)

An arc represents a pore-throat-pore pathway and a node is sited at the centre of each pore (Matthews *et al.*, 1993). Each arc in the flow network is the flow channel between adjacent nodes, positioned at the centre of each pore. It generates a term which is related to the effective Poiseuille capacity of the cell for flow in the $-z$ direction (from the top to the bottom face), and in the $\pm x$ and $\pm y$ direction. We do not, however, allow flow in the $+z$ direction, thereby applying an implicit positive pressure gradient with respect to z . The combination of the Eq. 6.16 with the Darcy equation, Eq. 6.14, results in an expression for the permeability independent of the pressure gradient imposed on the sample:

$$k = \frac{\pi}{8} \frac{\Omega_{cell}(F_{arcs}) l_{cell}}{A_{cell}}$$

Eq. 6. 17

A network analysis approach to this problem supplies a term $\Omega_{cell}(F_{arcs})$ as the maximal flow capacity through the network of pores and throats. It is calculated by means of the 'Dinic' network analysis algorithm (Ahuja *et al.*, 1997). There is an overall conservation of flow, so that the entire volume of fluid entering the top of the unit cell emerges at the bottom, with no build-up through the network. The value obtained, as the maximal flow, is derived from the capacity values of only the channels found to carry flow.

6.6.1. Capacity term

For the flow in a cubic pore, the equivalent equation for flow through a square tube is required. This can be shown to be:

$$\frac{dV}{dt} = -\frac{\delta P}{\mu} \cdot \frac{4L^3}{57}$$

Eq. 6. 18

where L refers to the width of the pore (Scheidegger, 1974). Thus the volume flow rate through an arc for cylindrical throats and cubic pores is:

$$\frac{dV}{dt_{arc}} = -\frac{\delta P}{\mu} \cdot \left[\frac{1}{\frac{57}{4L_1^3} + \frac{8h}{\pi r^4} + \frac{57}{4L_2^3}} \right]$$

Eq. 6. 19

where L_1 and L_2 refer to the widths of pores 1 and 2, and h the length of the throat connecting the two adjacent pores, as shown in fig. 6.12.

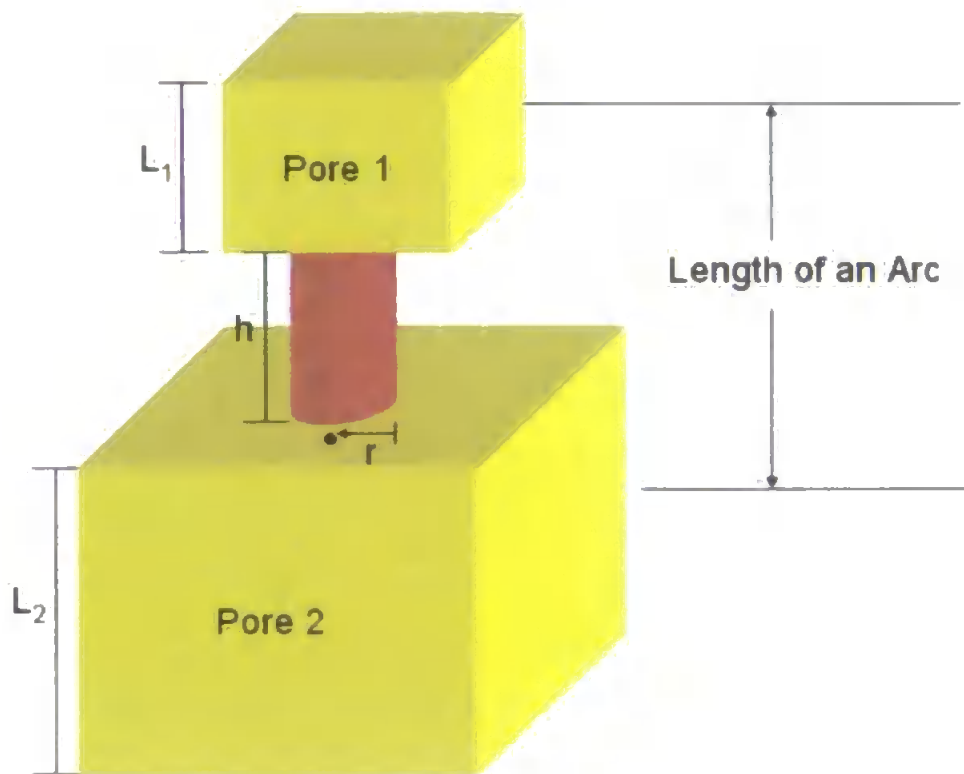


Fig. 6. 12. Schematic diagram of an arc. Representation of an isotropic structure showing cylindrical throats and cubic pores.

The approximation here is that the overall resistance of flow is equivalent to the summation of the individual effects of the pores and throat, in series-resistor style,

within each arc. Flow discontinuities between the rectangular cross-sections of the pores and the elliptic cross-sections of the throats are ignored. It has also been assumed that flow through any arc will start at the centre of one pore, and end at the centre of another. In fact flow within each pore, with its multiple entries and exits, will be much more complicated than this.

Then from Eq. 6.15

$$F_{arc} = -\frac{8}{\pi} \cdot (dV/dt)_{arc} \cdot \frac{\mu}{\delta P} = -\frac{8}{\pi} \cdot \left[\frac{1}{\frac{57}{4L_1^3} + \frac{8h}{\pi^4} + \frac{57}{4L_2^3}} \right]$$

Eq. 6. 20

For anisotropic structures, an equation describing the flow through a tube with a rectangular cross-section is as follows (O'Neill *et al.*, 1989):

$$\frac{dV}{dt} = -\frac{dP}{\mu dx} \cdot \frac{4ba^3}{3} \left[1 - \frac{192a}{\pi^5 b} \cdot \sum_{i=1,3,5,\dots}^{\infty} \frac{\tanh(i\pi b/2a)}{i^5} \right]$$

Eq. 6. 21

where a , b refer to the two radii of the tube normal to the flow, and x refers to the length of the tube in the direction of flow. For flow through a pore with a rectangular cross-section (slit-like or rod-like pores), the equation is given as follows:

$$\frac{dV}{dt} = -\frac{\delta P}{\mu} \cdot \frac{L_b L_a^3}{12 \cdot L_c} \cdot \left[1 - \frac{192L_a}{\pi^5 L_b} \cdot \sum_{i=1,3,5,\dots}^{\infty} \frac{\tanh(i\pi L_b/2L_a)}{i^5} \right]$$

Eq. 6. 22

where L_a and L_b refer to the two widths of the pore normal to the flow, and L_c refers to the width of the pore in the direction of flow.

Eq. 6.15 was modified for anisotropic void structures, for flow through an ellipsoidal throat:

$$\frac{dV}{dt} = -\frac{\delta P}{\mu} \cdot \frac{\pi r_a^3 r_b^3}{4h(r_a^2 + r_b^2)}$$

Eq. 6. 23

where r_a and r_b are the two radii of an ellipsoidal throat, and h is the length of the throat, as shown in Fig. 6.13.

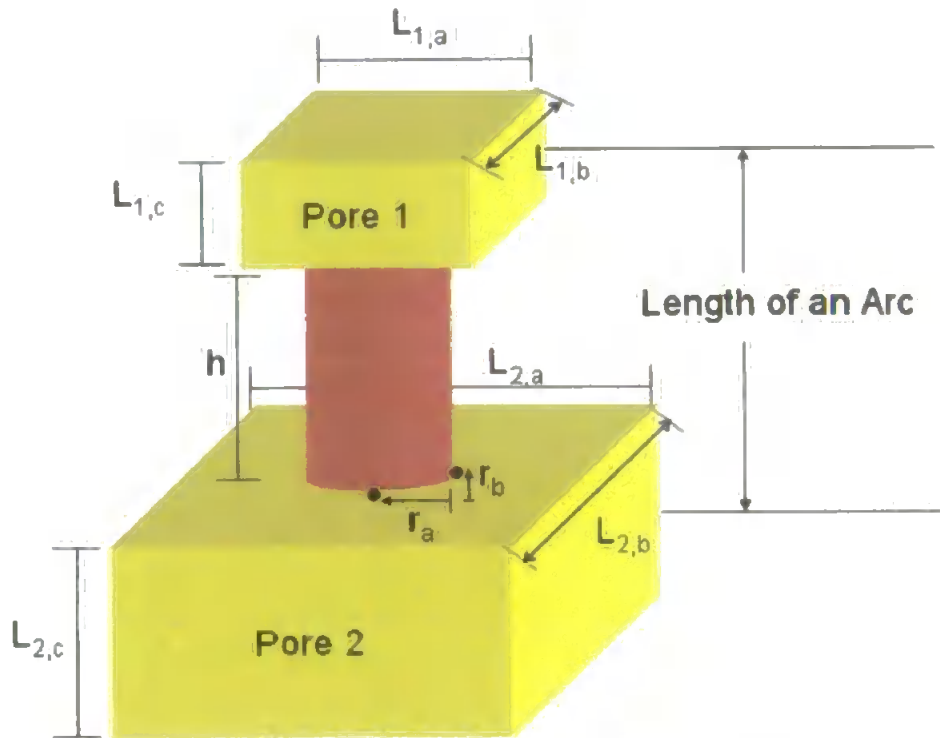


Fig. 6. 13. Schematic diagram of an arc. Representation of an anisotropic structure showing elliptical throats and a rectangular pores (slit-like or rod-like pores).

Eq. 6.20 then becomes

$$F_{arc} = -\frac{8}{\pi} \cdot \left[\frac{1}{\frac{1}{A} + \frac{1}{B} + \frac{1}{C}} \right],$$

Eq. 6. 24

where

$$A = \frac{L_{1,b} L_{1,a}^3}{12 \cdot L_{1,c}} \cdot \left[1 - \frac{192 L_{1,a}}{\pi^5 L_{1,b}} \cdot \sum_{i=1,3,5,\dots}^{\infty} \frac{\tanh(i\pi L_{1,b} / 2L_{1,a})}{i^5} \right], \quad B = \frac{\pi r_a^3 r_b^3}{4h(r_a^2 + r_b^2)}, \text{ and}$$

$$C = \frac{L_{2,b}L_{2,a}^3}{12 \cdot L_{2,c}} \left[1 - \frac{192L_{2,a}}{\pi^5 L_{2,b}} \cdot \sum_{i=1,3,5,\dots}^{\infty} \frac{\tanh(i\pi L_{2,b}/2L_{2,a})}{i^5} \right]$$

The bottom term in Eq. 6.24 ($\frac{1}{A} + \frac{1}{B} + \frac{1}{C}$) represents a resistor-network approximation for the pore-throat-pore combination. Tests of the hyperbolic tangent series showed that it converges to around 0.003% of the true answers within 4 terms.

6.6.2. Slip correction

Slip flow is an increase of the observed flow over the flow predicted from the Poiseuille equation, and is significant when the mean free path between collisions in the fluid is of the same order of magnitude as the diameter of the channel it is flowing through (Matthews *et al.*, 1993). Only gases will exhibit significant slip flow, because the mean free path for liquids is very small compared to the throat and pore sizes. The Knudsen number, K_n , is indicative of the flow regime occurring in a channel.

$$K_n = \lambda / d$$

Eq. 6. 25

where λ is the mean free path and d is the channel diameter. K is about 10^{-5} for laminar flow, 10^{-3} for slip/laminar flow and 10^{-1} for slip flow. Dawe (Dawe, 1973) has applied a correction for slip to capillary gas viscometers.

For laminar flow with slip through cylindrical tubes, the Poiseuille equation becomes

$$\frac{dv}{dt} = -\frac{\delta P}{\mu} \cdot \frac{\pi r^4}{8h} \left[1 + \frac{s\lambda}{r} \right]$$

Eq. 6. 26

for an incompressible fluid where s is a constant which may vary with temperature, capillary and molecular species and r is the radius of the tube. Also

$$s\lambda = 4\mu / \varepsilon$$

Eq. 6. 27

where the ratio μ/ε is the coefficient of slip, and ε is the coefficient of external friction. Rigorous calculations show that $\mu / \varepsilon \approx 1.1\lambda$, and therefore from equation 18, it follows that $s \approx 4.4$. Inspection of the above equation shows that the effect of slip is negligible when r is large compared to λ . Slip correction becomes increasingly significant in 'tighter' samples in which the pores and throats are smaller.

When the slip correction is added to the capacity term, Eq. 6.23 becomes:

$$F_{acc} = -\frac{8}{\pi} \cdot \left[\frac{1}{\frac{57}{4L_1^3 \left(1 + \frac{8.8\lambda}{L_1}\right)} + \frac{8h}{\pi r^4 \left(1 + \frac{4.4\lambda}{r}\right)} + \frac{57}{4L_2^3 \left(1 + \frac{8.8\lambda}{L_2}\right)}} \right]$$

Eq. 6. 28

For anisotropic structures, an effective radius (r_{eff}) for the throats and pores must be used when calculating slip correction. For flow through a pore with a rectangular cross-section (slit-like or rod-like pores), an effective length is calculated as the reciprocal of the sum of the two pore sides' lengths perpendicular to the direction of flow through the arc:

$$\frac{4}{L_{eff}} = \frac{2}{L_x} + \frac{2}{L_y}, \text{ or } L_{eff} = \frac{2L_x L_y}{L_x + L_y}$$

Eq. 6. 29

L_{eff} is the effective length of the pore sides, perpendicular to the direction of flow through the arc. The volumetric flow rate, Eq. 6.22, is adjusted for slip correction and becomes:

$$\frac{dV}{dt} = -\frac{\delta P}{\mu} \cdot \frac{L_b L_a^3}{12 \cdot L_c} \cdot \left[1 - \frac{192 L_a}{\pi^5 L_b} \cdot \sum_{i=1,3,5,\dots}^{\infty} \frac{\tanh(i\pi L_b / 2L_a)}{i^5} \right] \cdot \left[1 + \frac{8.8\lambda}{L_{eff}} \right]$$

Eq. 6. 30

For flow through an ellipsoidal throat, an effective radius (r_{eff}) is calculated as the reciprocal of the sum of its two radii:

$$\frac{2}{r_{eff}} = \frac{1}{r_a} + \frac{1}{r_b} \quad , \text{ or } r_{eff} = \frac{2r_a r_b}{r_a + r_b}$$

Eq. 6. 31

The volumetric flow rate, Eq. 6.23, is adjusted for slip correction and becomes:

$$\frac{dV}{dt} = -\frac{\delta P}{\mu} \cdot \frac{\pi r_a^3 r_b^3}{4h (r_a^2 + r_b^2)} \cdot \left[1 + \frac{4.4\lambda}{r_{eff}} \right]$$

Eq. 6. 32

The capacity term of Eq. 6.24 with slip correction will then become:

$$F_{arc} = -\frac{8}{\pi} \cdot \left[\frac{1}{\frac{1}{A} + \frac{1}{B} + \frac{1}{C}} \right]$$

Eq. 6. 33

where,

$$A = \frac{L_{1,b} L_{1,a}^3}{12 \cdot L_{1,c}} \cdot \left[1 - \frac{192 L_{1,a}}{\pi^5 L_{1,b}} \cdot \sum_{i=1,3,5,\dots}^{\infty} \frac{\tanh(i\pi L_{1,b} / 2L_{1,a})}{i^5} \right] \cdot \left[1 + \frac{8.8\lambda}{L_{1,eff}} \right],$$

$$B = \frac{\pi r_a^3 r_b^3}{4h (r_a^2 + r_b^2)} \cdot \left[1 + \frac{4.4\lambda}{r_{eff}} \right], \text{ and}$$

$$C = \frac{L_{2,b} L_{2,a}^3}{12 \cdot L_{2,c}} \cdot \left[1 - \frac{192 L_{2,a}}{\pi^5 L_{2,b}} \cdot \sum_{i=1,3,5,\dots}^{\infty} \frac{\tanh(i\pi L_{2,b} / 2L_{2,a})}{i^5} \right] \cdot \left[1 + \frac{8.8\lambda}{L_{2,eff}} \right]$$

6.7. Matching of the model to the experimental characteristics

There were two problems which had to be overcome to match the simulated void structures to the experimental ones. The first concerned the allocation of aspect factors (refer to section 6.2 for definition). Although experimental techniques are available to measure the sizes and aspect ratios of particles in a porous solid, it is impossible to measure the aspect factors of the voids. By definition, the void phase of a porous solid is continuous, and so needs to be split arbitrarily into pores and throats. Then the outline of a pore needs to be mapped, and there is no simple way of doing this. The outlines of even surface voids are ambiguous or hidden in scanning electron micrographs of surfaces, and in scanning or transmission micrographs of slices only a single cross-section of the void can be mapped. To overcome this problem, we tried different values of aspect factor (rather than aspect ratio) to the experimental samples, on the basis of visual inspection of the micrographs.

The criteria for the choice of these parameters were: (i) whether the particles were rod-like (implying voids with aspect factor > 1), isotropic (aspect factor = 1) or plate-like (aspect factor < 1); (ii) that aspect factors for voids should be less than the aspect ratios of the particles, because the particles are not completely aligned; and (iii) that the aspect factors should give pore-row spacings which were realistic relative to the dimensions of the experimental sample. The resulting values of aspect factor are listed below in Table 6.1. An aspect factor of one was used for Albaglos-CL since its pores were relatively isometric.

Primary samples	Aspect factor (α)	Number density of surface throats (μm^{-2})			Surface throat number density correction factor, f
		Experimental	Experimental % standard error of mean	Model	
Albaglos-CL	1	1.4	11	12.13	0.12
OpacarbA40-CL	1.5	3.02	4	13.54	0.22
Amazon-CL	0.8	4.09	4	10.66	0.38
Speswhite-CL	0.6	0.66	15	7.89	0.084

Table 6. 1. The resulting values of aspect factor, f , used for each sample, and the estimates of number density of surface throats and the correction factor, f , used for each sample.

Due to the difficulty in choosing accurate aspect factors for the clay samples, it was necessary to try a lower aspect factor for Speswhite-CL ($\alpha=0.1$), so that the effects of anisotropy and the change of anisotropy within the coating structures could be investigated more closely. The sensitivity of the choice of value was also tested by running simulations with an aspect factor of one ($\alpha=1$) for each anisotropic sample.

The second problem concerned the number density of surface throats. The structures which were used for the modelling purposes had virtually identical percolation characteristics to the experimental samples, the same porosity, and a realistic aspect factor. One would have hoped, then, that another important feature of the model, namely the number of throats at the surface, would have matched the number density observed in the sample. In fact, as described below, there were significantly higher number densities generated by the model than observed for the experimental samples, as shown in Table 6.1.

One could suggest that the implicit particles within the model were therefore not platey enough, and one should make the model's aspect factor an even smaller fractional number until a match of the number densities was obtained. However, this proved unrealistic in another sense. For example, for the modelled number density of Speswhite coating to match the experimental number density 0.66

throats/ μm^2 , an aspect factor of around 0.1 would have had to be used. However, this would have created a simulated structure with a pore row spacing in the x and y direction of approximately $13.1 \mu\text{m}$; one order of magnitude larger than would seem realistic from an observation of the electron micrographs. So the best that could be done was to multiply the modelled permeabilities and wetting calculations by a correction factor for surface throat number density, f .

$$f = \frac{N_{\text{exp}}}{N_{\text{mod}}},$$

Eq. 6. 34

where N_{exp} and N_{mod} refer to the number density of surface throats obtained experimentally and from the model, respectively. The correction factors and number densities are listed in Table 6.1.

This correction is valid when calculating the volumetric flow rate obtained from the surface throats, and also while the wetting front is contained in the surface throats. However, it becomes increasingly invalid as the flow rate is calculated throughout the structure, as the body of the modelled structure would then have a porosity which was a factor of f greater than the experimental sample. Therefore the results in following chapters are compared to experiment both with and without the correction factor.

6.7.1. Fit of the simulated to the experimentally measured void properties

Fig. 6.14 and 6.15 show the close fit of the simulated to the experimental percolation characteristics for the primary samples. The simulated and experimental porosities matched to within 0.1 %. The Pore-Cor fitting parameters

used to generate the simulated structures are shown in Table 6.2, and included the chosen aspect factor of each sample, as discussed previously in Section 6.7.

Primary samples	Minimum throat entry diameter (μm)	Maximum throat entry diameter (μm)	Connectivity	Throat skew	Pore skew	Aspect factor, α	Porosity (%)
Albaglos-CL	0.0036	2.39	5	1.3	2	1	37.6
OpacarbA40-CL	0.0036	2.38	3.3	0.78	1.6	1.5	38.3
Amazon-CL	0.0036	2.31	4.6	1.84	3.1	0.8	30
Speswhite-CL	0.0036	2.32	4.8	1.63	1.8	0.6	25.8

Table 6. 2. The Pore-Cor fitting parameters used to generate the simulated structures for each sample.

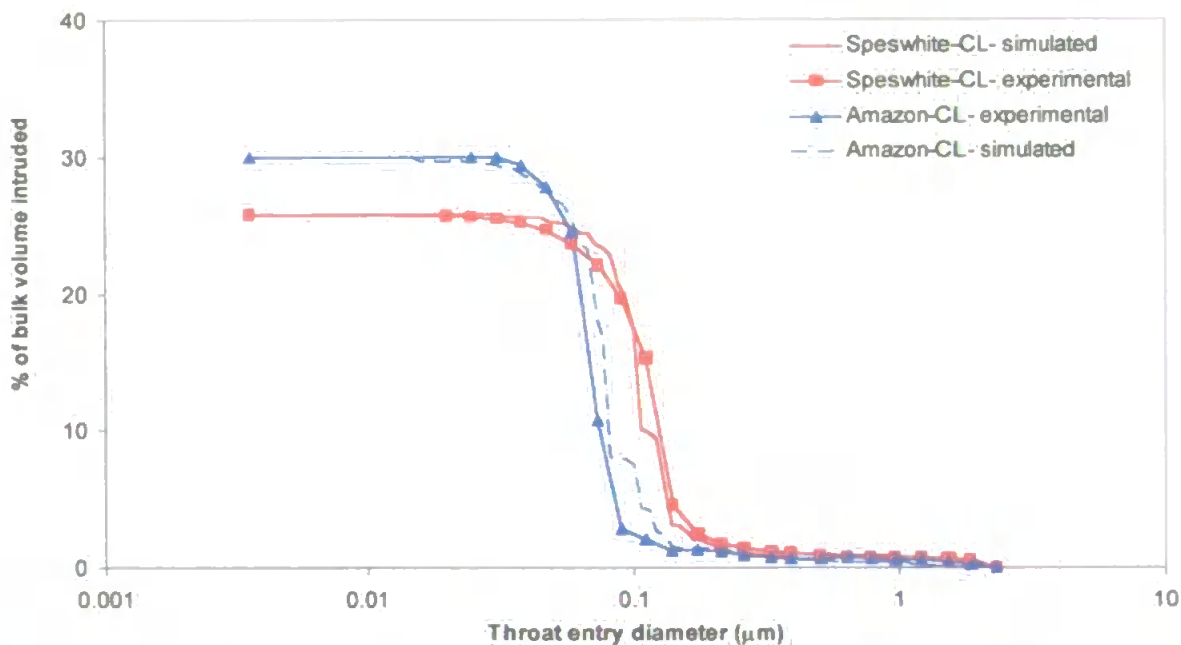


Fig. 6. 14. Experimental and simulated mercury intrusion curves for the clay coating samples.

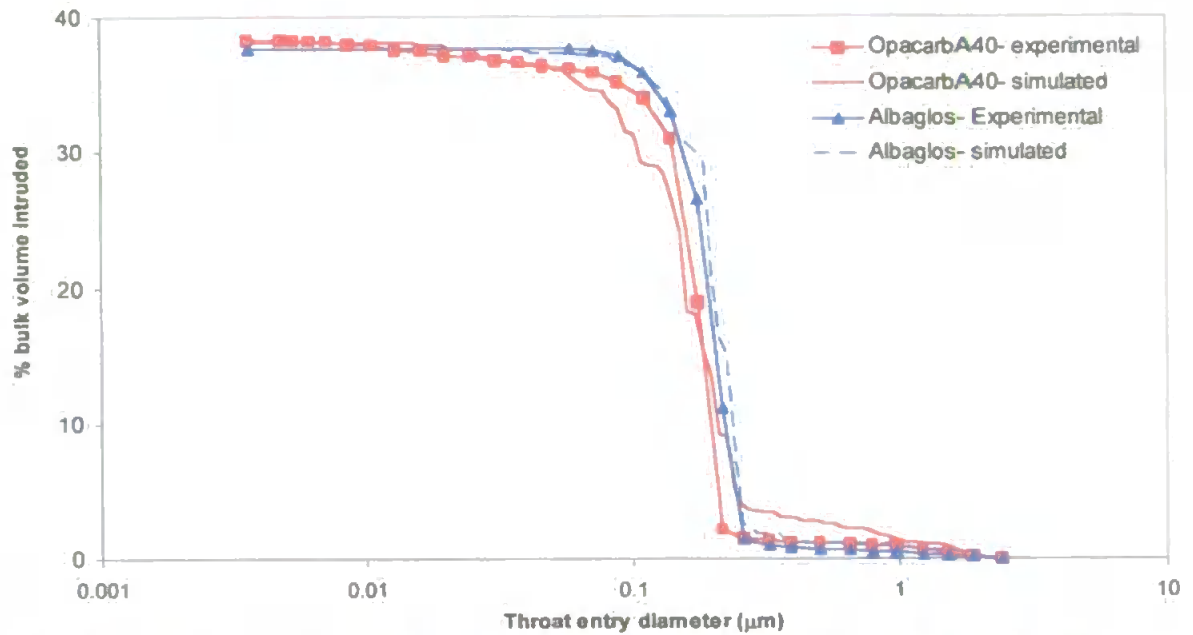


Fig. 6. 15. Experimental and simulated mercury intrusion curves for the PCC coating samples.

6.8. Comparing the Pore-Cor model to much simpler approaches

The Pore-Cor simulations, from the permeability and wetting algorithms presented in this work, are only worthwhile if they represent a substantial improvement over much simpler approaches. Therefore, the permeability simulations were compared to the Kozeny and Aligned cylinders models, described in Section 3.5.1 and 3.5.2, respectively. The results are discussed in Chapter 7.

The wetting simulations were compared to Effective Hydraulic Radius (EHR) calculations, described in Section 3.5.3. The calculated wetting distances, x , from the EHR model, were compared to the volume-averaged distances (Darcy lengths) calculated from the Pore-Cor wetting algorithm. The simulated wetting results from the models are discussed in Chapter 9.

6.9. Summary

- The structure of the unit cell was modified in the Pore-Cor model to anisotropic by re-scaling the z axis relative to the x and y axes. When the z axis was re-scaled, the pores became either slit-like or rod-like in shape, and the throats in the x and y directions gain ellipsoidal cross-sections with the major axis in the x or y direction.
- Pore-Cor was also modified to generate three different types of void structures where the layers were horizontally correlated in respect to size. Different percolation characteristics were shown for each horizontally banded structure.
- The equation for wetting was a modified version of the Lucas/Washburn equation as developed by Bosanquet (Bosanquet, 1923). For anisotropic structures, the wetting equation was further modified to refer to elliptical throats, and used to calculate the wetting flux in each pore and throat in the void network after every time-step, using a predictor-corrector method (Schoelkopf *et al.*, 2000).
- The Pore-Cor model calculated the maximal flow capacity through the network of pores and throats by means of the 'Dinic' network analysis algorithm (Ahuja *et al.*, 1997). For anisotropic structures, the equations for network flow capacity were modified to describe the flow through ellipsoidal throats and a pore with a rectangular cross-section.

- To model the flow rate of gases, the slip flow correction was added to the Poiseuille equation. The slip flow correction was also modified for anisotropic structures.
- The criteria for the choice of aspect factors were: (i) whether the particles were rod-like, isotropic or plate-like; (ii) that aspect factors for voids should be less than the aspect ratios of the particles and (iii) that the aspect factors should give pore-row spacings which were realistic relative to the dimensions of the experimental sample.
- The structures which were used for the modelling purposes had virtually identical percolation characteristics to the experimental samples, the same porosity, and a realistic aspect factor. However, there were significantly higher number densities generated by the model than observed for the experimental samples. Hence, a correction factor for number density was used to multiply the modelled permeabilities and wetting calculations.
- The Pore-Cor model generated a close fit of the simulated to the experimental percolation characteristics for the primary samples.

7. COMPUTER MODELLING OF PERMEABILITY

It will be seen that a very important benefit of explaining the effects of anisotropy by use of a computer model is that it is possible to hold individual properties constant. For example, in this study, we changed the anisotropy of the model while holding its throat size distribution, connectivity and sometimes its percolation characteristics and porosity constant.

In recognition of our use of the Darcy equation, we have expressed all permeabilities in Darcy units, where 1 Darcy = $9.87 \times 10^{-13} \text{ m}^2$.

7.1. Modelling the flow capacity of a non-isometric structure

A change in aspect factor, α , caused different effects to the shape of the throats and pores in the network model. For example, a decrease in aspect factor caused the cross sectional face of the throats and pores normal to the flow in the x or y direction to resemble a 'compressed' ellipse and a slit-like rectangle, respectively (Fig. 6.2). However, the cross sectional face of the throats and pores normal to the flow in the -z direction resembled a larger-diameter circle and a larger-sized square, respectively, as these faces are only affected by the increase in the x and y axes. Meanwhile, an increase in aspect factor has an obverse effect on the throats and pores. The cross-sectional face of the throats and pores normal to the flow x or y direction resembled a stretched ellipse and a rod-like rectangle, respectively, (Fig. 6.3), while in the -z flow direction, they resembled a smaller-diameter sized circle and a smaller-sized square.

The permeability of a void structure is dependent on the route that the liquid flows through the network. It is calculated from the flow capacities of all the arcs that

are part of the flow route, in the $\pm x$, $\pm y$ and $-z$ directions. The volumetric flow rate (Q) of a throat and pore, and the flow capacity of an arc (F_{arc}) were calculated for the flow of a liquid in both the $\pm x$, $\pm y$ and $-z$ direction from using Eq. 6.23 and Eq. 6.24, and for a range of aspect factors from 0.001 to 1 000. Fig. 7.1 displays the volumetric flow rate (Q_{pore}) and throat (Q_{throat}) in the x or y direction, by using an effective diameter, d_{eff} , of $1 \mu\text{m}$ and a throat height, h , equal to $1 \mu\text{m}$.

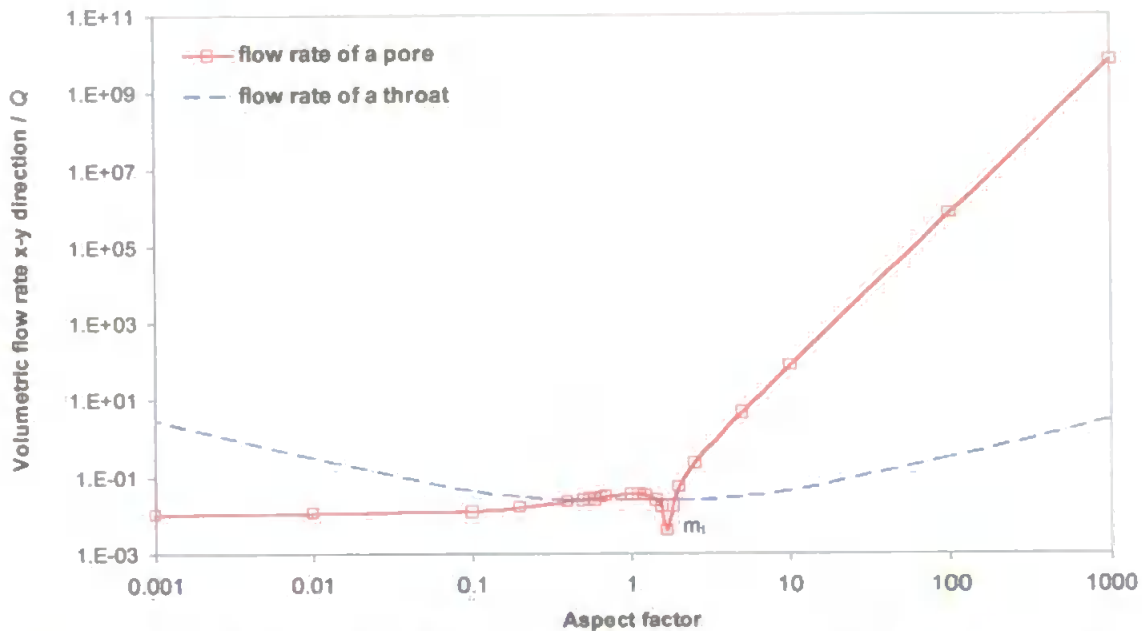


Fig. 7. 1. The volumetric flow rate of a pore (Q_{pore}) and throat (Q_{throat}) in the x - y direction.

The two faces of the pores are calculated as having equal size dimensions to the connecting throat and is known as the 'pore-throat size ratio', having a value in this case of one. Hence, for an aspect factor of 10, the throat in the x or y direction will have the shape of a 'stretched' elliptical cylinder, having r_a and r_b being equal to 2.75 and 0.275, respectively. The face of the pore normal to the flow in the x or y direction will have a rod-like rectangular shape, having L_a being equal to 5.5, and L_b and L_c being both equal to $0.55 \mu\text{m}$. The pore and throat dimensions are labelled in reference to the direction of the flow of fluid, as explained in section 6.6.1 (Eq. 6.24), and are illustrated below, in Fig. 7.2.

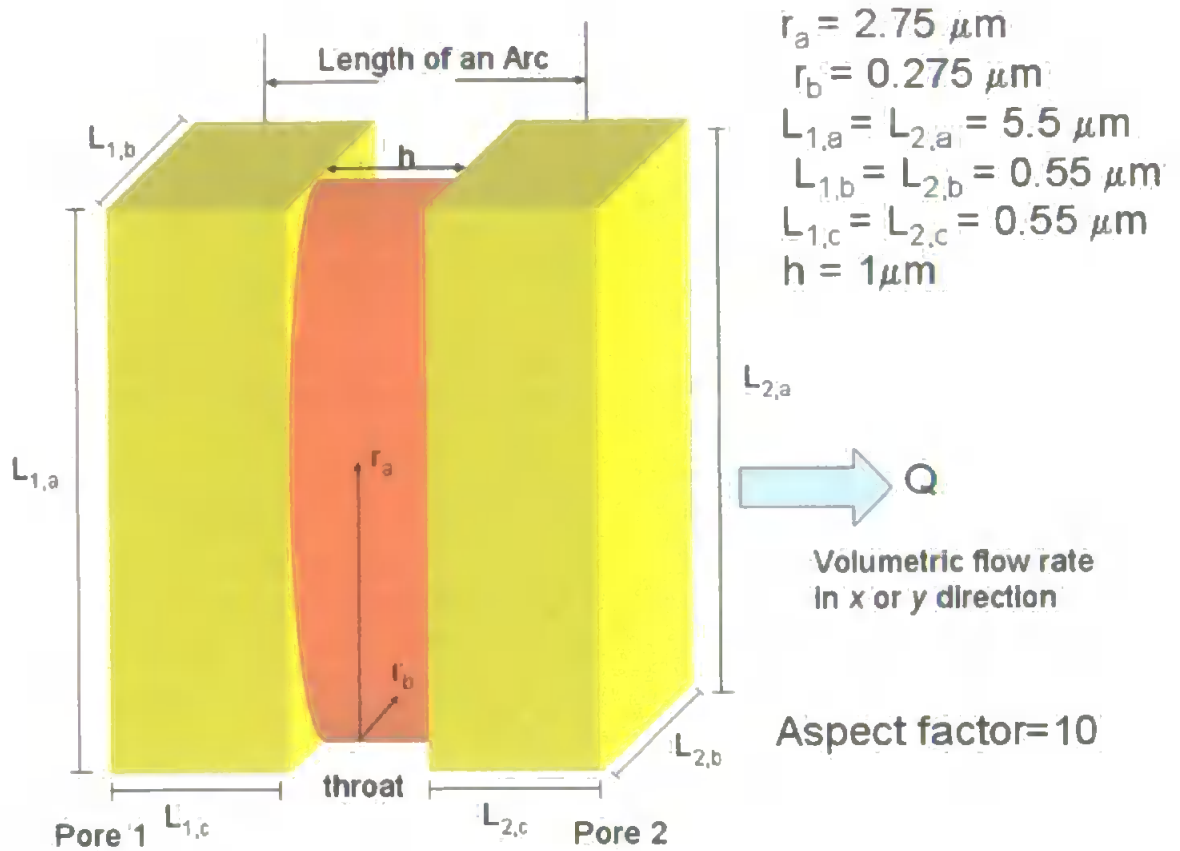


Fig. 7. 2. Volumetric flow rate (Q) in the x or y direction, showing the typical size dimensions for the pore and throat, when $\alpha=10$.

Q_{throat} in the x or y direction accelerated at the same speed when 'compressing' ($\alpha < 1$) or 'stretching' ($\alpha > 1$) the elliptical throat normal to the flow, and approached a minimum at an aspect factor of one (fig. 7.1). Meanwhile, Q_{pore} is shown to decelerate slowly for slit-like ($\alpha < 1$) pores; while for rod-like ($\alpha > 1$) pores, the flow rate is shown to accelerate much faster. The curve is also shown to contain a local minimum, labelled m_1 on the graph, having an aspect factor value close to 1.67. This minimum arises due to the flow capacity equation containing a hyperbolic -tangential term, Eq. 6.24.

Since the three side lengths of the pore are related to d_{eff} (Eq. 6.5), an increase in L_a (z direction) for a particular value of d_{eff} causes a compensatory decrease in L_b and L_c (x and y direction). Correspondingly, a decreasing thickness of the pore in the z direction would be offset by an increase in the width of the pore in the x and

y direction, thus causing the flow rate in the x and y direction to have a slow deceleration, for aspect factors below one. However, a much different flow rate is shown in Fig. 7.3, when L_a and L_b are held constant with respect to L_c .

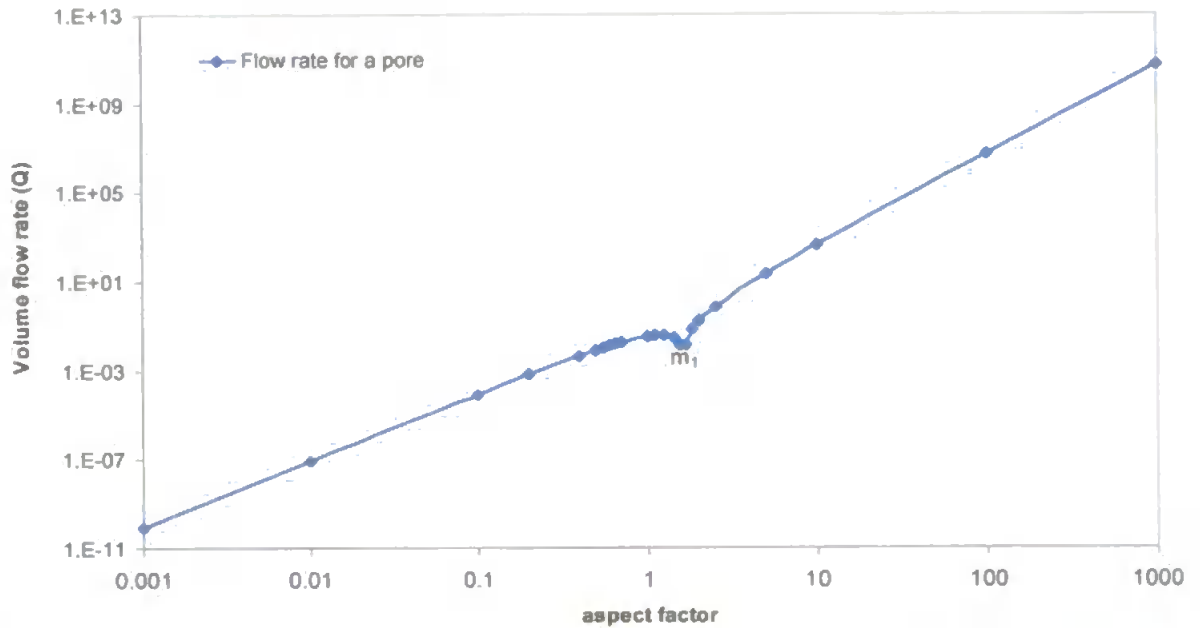


Fig. 7. 3. The volumetric flow rate (Q) in the x and y direction when L_a and L_b are held constant with respect to L_c .

The flow rate is now shown to decelerate much faster for aspect factors below one, as the width of the pore would remain constant with a decrease in the thickness of the pore (z direction). The local minimum, m_1 , observed in Fig. 7.1 is also shown in Fig. 7.3, both showing the same value for its aspect factor.

Fig. 7.4 shows the volumetric flow rate of a pore and throat in the -z direction. Similar to Fig. 7.1, an effective diameter of $1 \mu\text{m}$, throat height of $1 \mu\text{m}$, and a 'pore-throat size ratio' of one was used to calculate the flow rate.

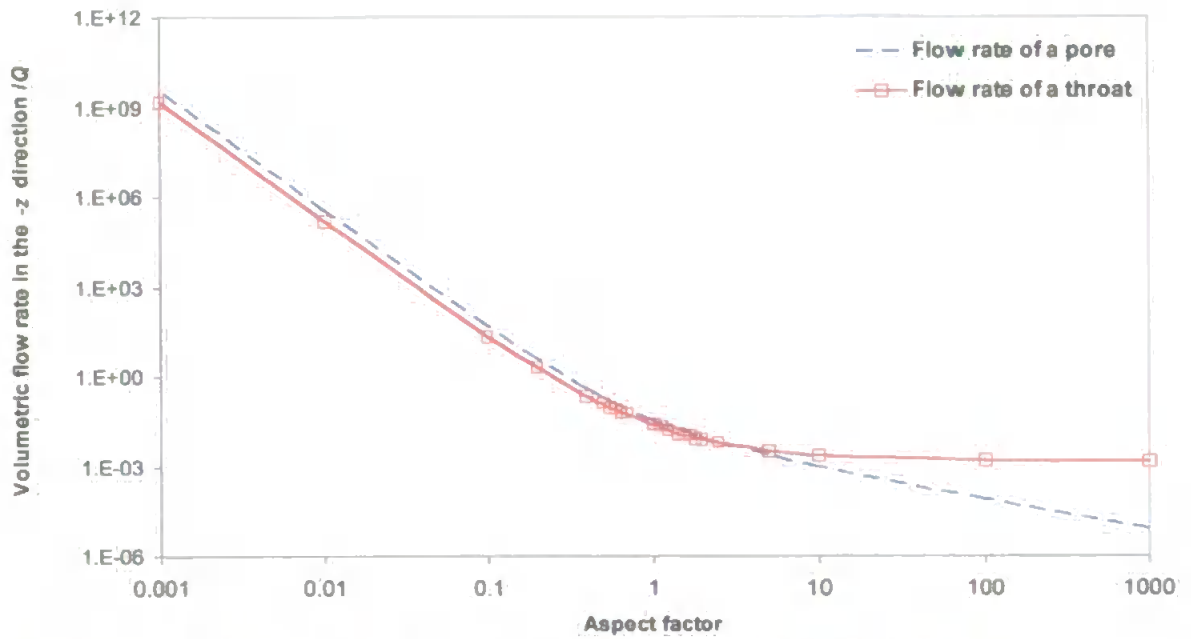


Fig. 7. 4. The volumetric flow rate, Q , of a pore and throat in the $-z$ direction.

Hence, for an aspect factor of 10, the throat in the $-z$ direction will have the shape of a circular cylinder, while the face of the pore normal to the flow in the $-z$ direction will have the shape of a square. The size of the throat and pore will also be reduced; r_a and r_b and L_a and L_b will be equal to 0.275 and 0.55 μm , respectively, and L_c will be equal to 5.5 μm . The pore and throat dimensions are labelled in reference to the direction of the flow of fluid, as explained in section 6.6.1 (Eq. 6.24), and are illustrated below, in Fig. 7.5.

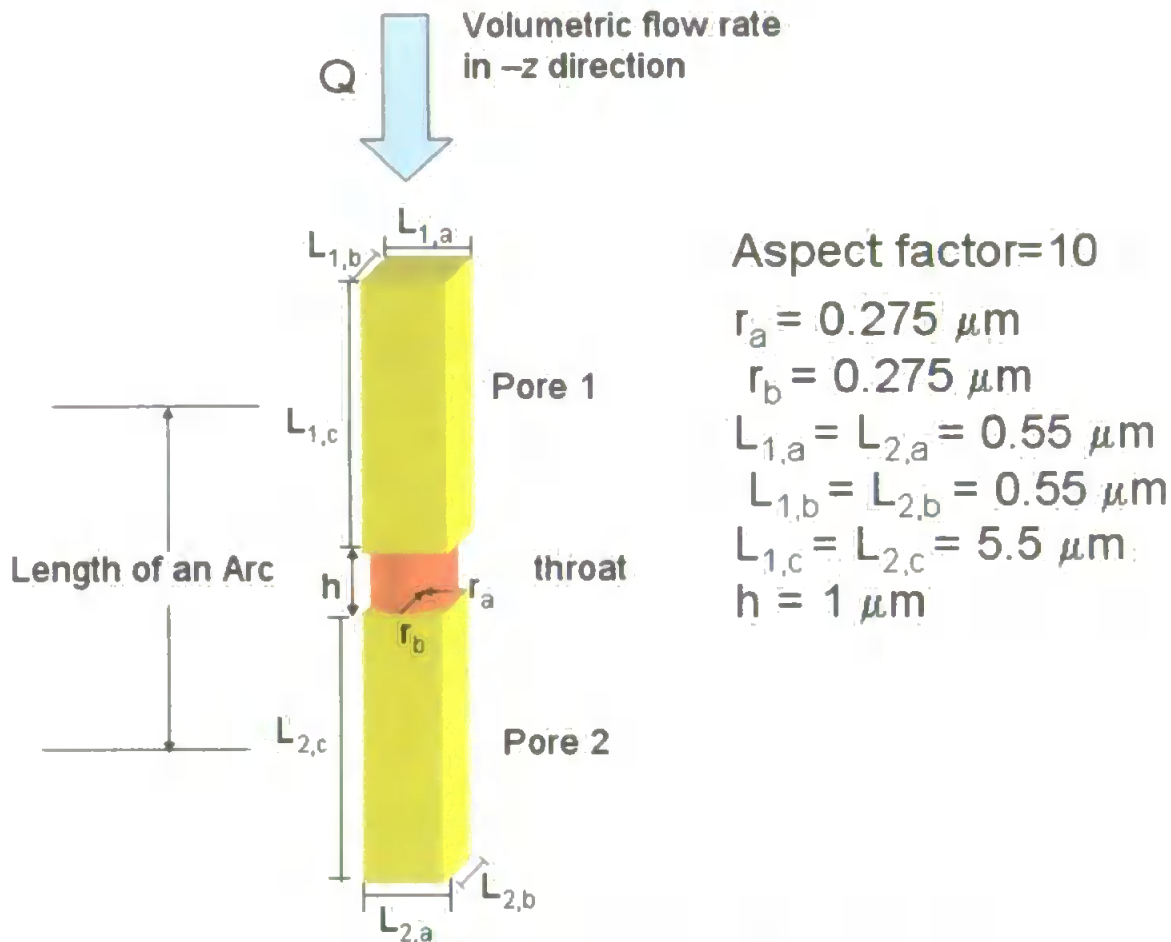


Fig. 7. 5. Volumetric flow rate (Q) in the $-z$ direction, showing the typical size dimensions for the pore and throat, when $\alpha=10$.

Q_{throat} in the $-z$ direction increased sharply when $\alpha < 1$, and showed an increase in the diameter of the throat normal to the direction of flow, Fig. 7.4. However when $\alpha > 1$, Q_{throat} decreased and gradually approach an asymptote, as the throat diameter decreased. Meanwhile, Q_{pore} in the $-z$ direction decreased when $\alpha > 1$, Fig. 7.4, as the face of the pore normal to the flow decreased in size.

The flow capacity of an arc, F_{arc} , (Eq. 6.24) in the $\pm x$, $\pm y$ or $-z$ direction was calculated from the combination Q_{pore} and Q_{throat} , Fig. 7.1 and 7.4, respectively. The same pore and throat size dimensions used to calculate Q were used to calculate F_{arc} , as illustrated in Fig. 7.2 and 7.6.

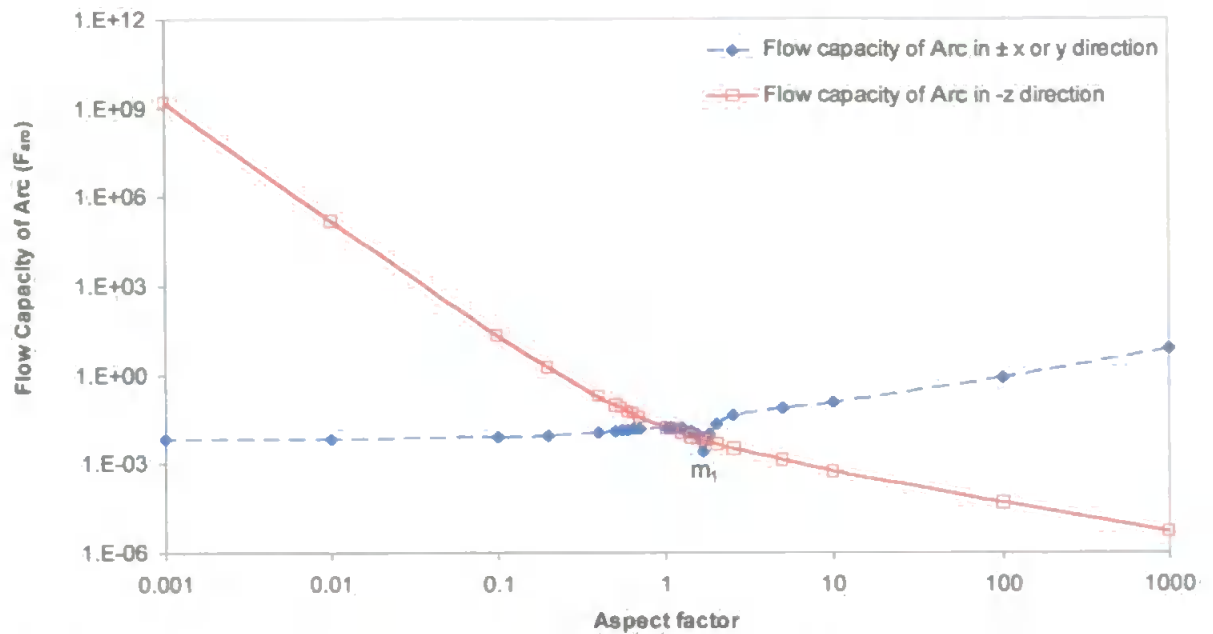


Fig. 7. 6. The flow capacity of an Arc (F_{arc}) in the $\pm x$, $\pm y$ or $-z$ direction.

F_{arc} in the $\pm x$ and $\pm y$ direction is shown to decrease at a relatively slow rate with a decrease in α . For $\alpha > 1$, F_{arc} is largely dependent on the Q of the throat, while for $\alpha < 1$, F_{arc} is largely dependent on the Q of the pore. The local minimum, m_1 , is also shown, and is located at the same α value found in Fig. 7.1.

When $\alpha > 1$, F_{arc} in the x and y direction acts inversely with F_{arc} in the $-z$ direction, as an increase in α caused an increase in F_{arc} in the x - y direction but a decrease in the $-z$ direction. There will therefore be no significant effect on the network flow capacity of a void structure when $\alpha > 1$. The network permeabilities of a void structure for two stochastic generations were calculated by holding all other parameters constant, and then varying the aspect factor. The permeabilities for both stochastic generations, when $\alpha > 1$, were found to fluctuate within around one order of magnitude of each other, showing no overall significant trend, Fig. 7.7. However, at relatively high aspect factors ($\alpha > 100$) both stochastic generations showed a gradual decrease in permeability. Hence, in agreement with Fig. 7.6, a change in aspect factor, from an isotropic pore structure to a rod-like pore

structure, is shown to generally have very little to no significant effect on permeability. Even at relatively high aspect factors the change in permeability is shown to be less than one order of magnitude.

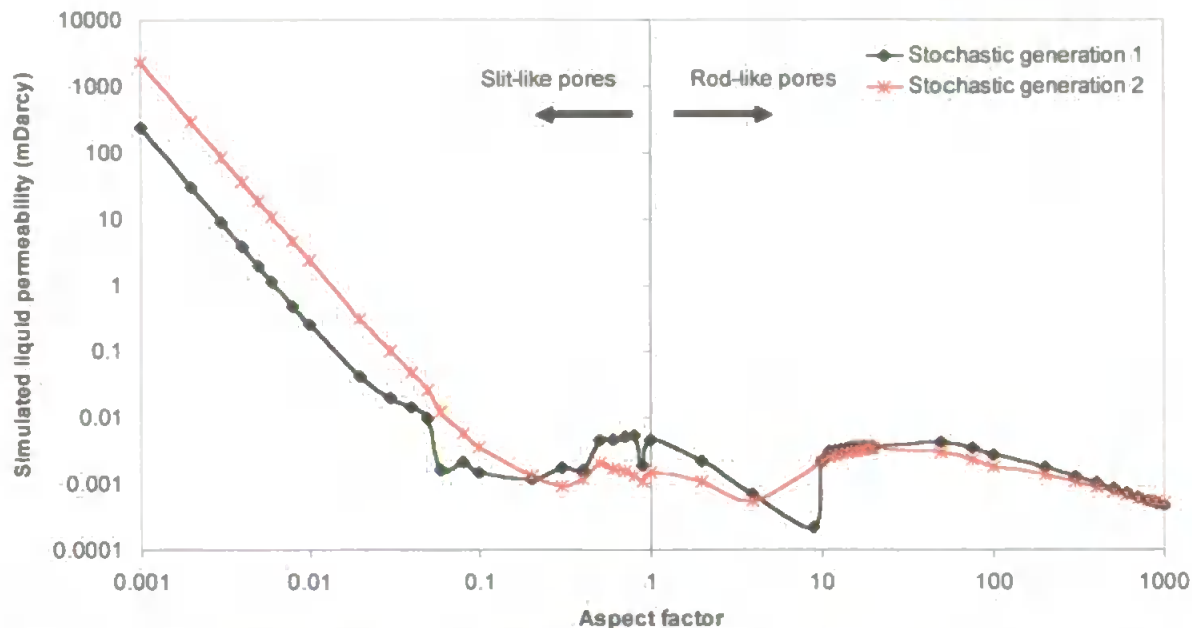


Fig. 7. 7. Simulated liquid permeabilities at various aspect factors for two stochastic generations. All other parameters are held constant and are as follows: Random structure, Connectivity=5, pore-skew=2, throat skew=1, minimum throat diameter=3.6e-3 μ m, maximum throat diameter 2.4 μ m.

When $\alpha < 1$, F_{arc} in the x and y direction also acts inversely with F_{arc} in the $-z$ direction, but at a slower rate. There will therefore be an increasing effect on the network flow capacity of a void structure when $\alpha < 1$. The network permeabilities of a void structure for two stochastic generations, when the $\alpha < 1$, was again calculated by holding all other parameters constant and varying the aspect factor. Only small permeability fluctuations (less than one order of magnitude) were found around an aspect factor between 0.1 and 1. However lower aspect factors showed a significant increase in permeability of orders of magnitude, for both stochastic generations. This is in agreement with Fig. 7.6, which showed that although the flow capacity of an arc decreased in the $\pm x$ and $\pm y$, it is masked by a larger increase in the $-z$ direction. Hence, a change in aspect factor, from an

isotropic pore structure to a slit-like pore structure, is shown to generally have an increasing effect on permeability.

7.2. Modelled flow capacity trends

The parameters of h , d_{eff} , and *pore-throat size ratio* were altered for an arc to show the effects on the flow capacity of a coating structure, in the $\pm x$, $\pm y$ and $-z$ directions, shown in Fig. 7.8 and 7.9. An increase of one order of magnitude in d_{eff} caused a steady rise in F_{arc} of approximately three orders of magnitude, in all the directions. However, an increase of one order of magnitude in length of the throats, h , had an inverse effect on F_{arc} as the F_{arc} decreased by approximately one order of magnitude in all the directions.

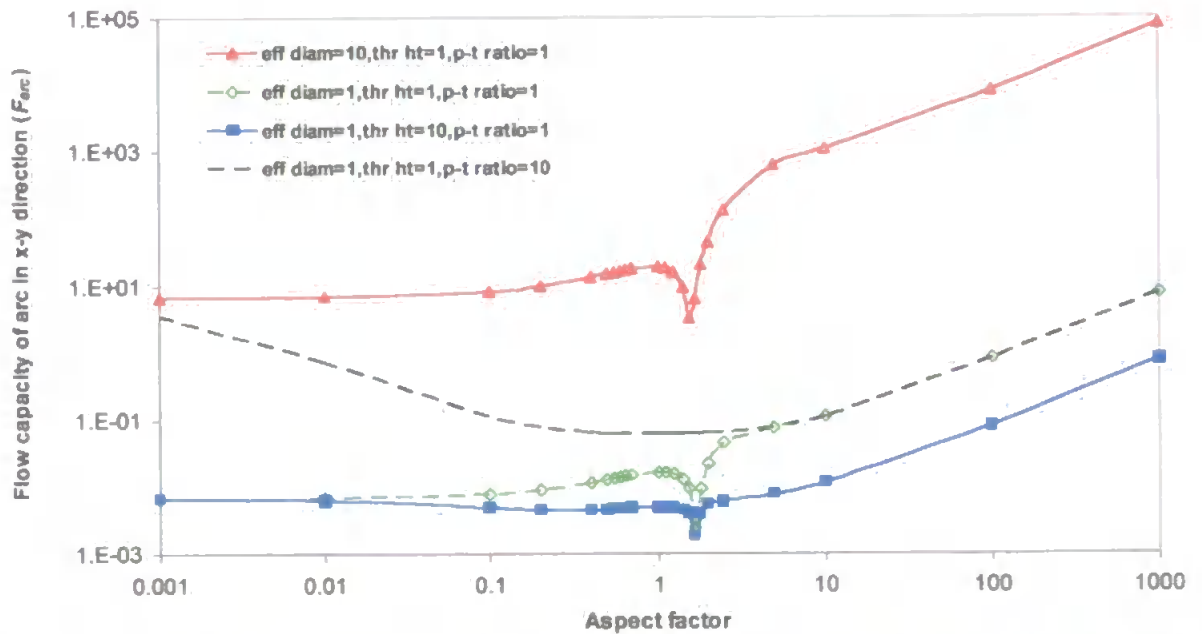


Fig. 7. 8. Flow capacity modelling trends in $\pm x$ and $\pm y$ direction. The abbreviations in the legend are deciphered as follows: 'eff diam' refers to effective diameter, 'thr ht' refers to throat height, p-t ratio refers to pore-throat ratio.

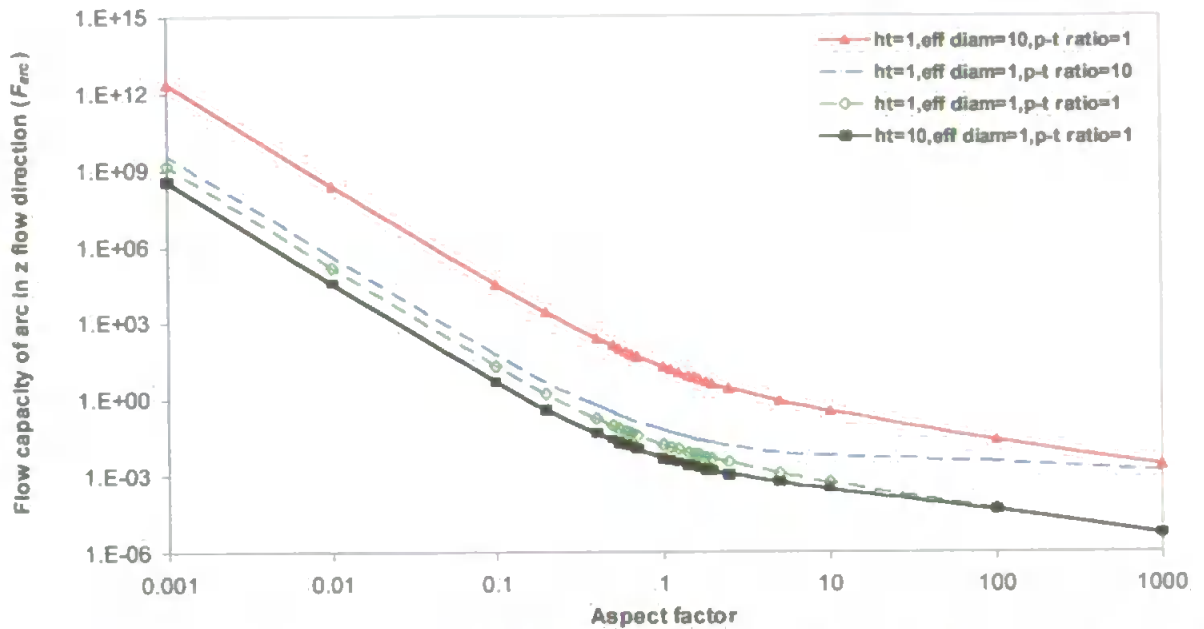


Fig. 7. 9. Flow capacity modelling trends in the $-z$ direction. The abbreviations in the legend are deciphered as follows: 'eff diam' refers to effective diameter, 'thr ht' refers to throat height, p-t ratio refers to pore-throat ratio.

An increase of one order of magnitude for the *pore-throat size ratio* caused varying effects to F_{arc} depending on the aspect factor and direction of flow. For $\alpha > 1$, the increase in *pore-throat size ratio* caused no change to F_{arc} in the $\pm x$ and $\pm y$ direction; while F_{arc} in the $-z$ direction is shown to rise by an increasing rate with an increase in aspect factor. For $\alpha < 1$, the increase in *pore-throat size ratio* caused the flow capacity in the $\pm x$ and $\pm y$ direction to rise by an increasing rate with a decrease in aspect factor; while F_{arc} in the $-z$ direction is shown to increase by less than a half an order of magnitude.

From the observed results of the above three parameters, a conclusion could be drawn that the lengths of the throats, h , had the least effect on the network flow capacity of a structure, while the diameters of the throats, d_{eff} , had the greatest effect. The *pore-throat size ratio* parameter had a much greater effect on the network flow capacity when using low and high aspect factors.

7.3. Modelling the permeabilities of isotropic and anisotropic structures

An initial fit was made for isotropic structures ($\alpha=1$) by optimising throat skew and connectivity, until the simulated percolation curve closely matched the experimental percolation curve for the primary samples (Speswhite-CL, Amazon-CL, OpacarbA40-CL and Albaglos-CL, in which 'CL' refers to samples containing CMC and latex). The optimisation was performed by running through a grid of possible values for throat skew and connectivity. The pore-skew was minimized for each stochastic generation, and caused the pore-row spacing to adjust so that the porosity of the simulated network was equal to that of the experimental sample, as an increase in pore row spacing would lengthen the throats, increase the unit cell size, and reduce the porosity. The pore skew parameter was kept the same as for the isotropic case, but the throat skew and connectivity were again optimised for each estimated aspect factor. The pore row spacing parameter was also adjusted for each structure to match the experimental porosity.

Liquid, nitrogen and methane gas network permeabilities of each sample, at $\alpha=1$ and at their chosen aspect factors, were then calculated from five to eight stochastic generations, as full network permeabilities could not be calculated for some stochastic generations due to the limitations of the Dinic algorithm. The calculation of a flow route becomes increasingly difficulty for the algorithm when the simulated network structure contains arcs with an extremely wide range of flow capacities. The calculated network permeabilities and their optimised Pore-Cor parameters for each stochastic generation, and at their chosen and isotropic aspect factors, are shown in Tables 7.1 to 7.8. Calculated network permeabilities at a lower aspect factor for Speswhite-CL ($\alpha=0.1$) was also simulated such that the effects of a much larger change in anisotropy could be tested (Table 7.3).

Speswhite-CL		Aspect factor = 1.0					
Stochastic generation	Liquid Permeability (mDarcy)	Methane Permeability (mDarcy)	Nitrogen Permeability (mDarcy)	Connectivity	Throat Skew	Pore-Row Spacing	Pore Skew
1	2.73E-05	3.31E-04	3.19E-04	4.80	1.57	2.48	1.80
2	1.72E-05	2.07E-04	1.99E-04	4.60	1.50	2.55	1.80
3	5.50E-05	5.09E-04	4.91E-04	4.20	1.32	2.65	1.80
4	1.94E-05	2.26E-04	2.18E-04	4.20	1.44	2.53	1.80
5	2.82E-05	2.85E-04	2.74E-04	3.50	1.00	2.76	1.80
6	1.91E-05	2.22E-04	2.14E-04	4.20	1.44	2.53	1.80
7	6.13E-05	5.82E-04	5.79E-04	4.30	1.38	2.63	1.80
Mean	3.25E-05	3.37E-04	3.28E-04	4.26	1.38	2.59	1.80
Median	2.73E-05	2.85E-04	2.74E-04	4.20	1.44	2.55	1.80
Geometric mean	2.88E-05	3.12E-04	3.02E-04	4.24	1.37	2.59	1.80

Table 7. 1. The optimised Pore-Cor parameters for Speswhite-CL, for an isotropic aspect factor ($\alpha=1$), at each stochastic generation. The Calculated liquid permeabilities and its mean, median and geometric mean are also calculated.

Speswhite-CL		Aspect factor = 0.60					
Stochastic generation	Liquid Permeability (mDarcy)	Methane Permeability (mDarcy)	Nitrogen Permeability (mDarcy)	Connectivity	Throat Skew	Pore-Row Spacing	Pore Skew
1	2.71E-05	3.26E-04	3.14E-04	4.80	1.57	3.30	1.80
2	1.29E-05	1.46E-04	1.41E-04	4.60	1.50	3.40	1.80
3	6.09E-05	4.81E-04	4.64E-04	4.20	1.32	3.54	1.80
4	1.53E-05	2.01E-04	1.93E-04	4.20	1.44	3.37	1.80
5	1.73E-05	1.82E-04	1.76E-04	3.50	1.00	1.80	1.80
6	1.49E-05	1.94E-04	1.87E-04	4.20	1.44	3.37	1.80
7	7.25E-05	5.74E-04	5.54E-04	4.30	1.38	3.50	1.80
Mean	3.15E-05	3.01E-04	2.90E-04	4.26	1.38	3.18	1.80
Median	1.73E-05	2.01E-04	1.93E-04	4.20	1.44	3.37	1.80
Geometric mean	2.50E-05	2.66E-04	2.56E-04	4.24	1.37	3.11	1.80

Table 7. 2. The optimised Pore-Cor parameters for Speswhite-CL, for a chosen aspect factor of $\alpha=0.6$, at each stochastic generation. The Calculated network permeabilities and its mean, median and geometric mean are also calculated.

Speswhite-CL		Aspect factor = 0.10					
Stochastic generation	Liquid Permeability (mDarcy)	Methane Permeability (mDarcy)	Nitrogen Permeability (mDarcy)	Connectivity	Throat Skew	Pore-Row Spacing	Pore Skew
1	1.06E-04	5.51E-04	5.34E-04	4.80	1.57	13.60	1.80
2	1.00E-04	4.43E-04	4.30E-04	4.60	1.50	14.00	1.80
3	7.11E-05	3.91E-04	3.79E-04	4.20	1.32	14.80	1.80
4	3.46E-05	1.71E-04	1.65E-04	4.20	1.44	13.90	1.80
5	1.47E-05	9.78E-05	9.45E-05	3.50	1.00	15.20	1.80
6	3.27E-05	1.69E-04	1.63E-04	4.20	1.44	13.90	1.80
7	1.03E-04	4.53E-04	4.40E-04	4.30	1.38	14.40	1.80
Mean	6.60E-05	3.25E-04	3.15E-04	4.26	1.38	14.23	1.80
Median	7.11E-05	3.91E-04	3.79E-04	4.20	1.44	14.00	1.80
Geometric mean	5.37E-05	2.76E-04	2.67E-04	4.24	1.37	14.22	1.80

Table 7. 3. The optimised Pore-Cor parameters for Speswhite-CL, for a lower aspect factor of $\alpha=0.1$, at each stochastic generation. The Calculated network permeabilities and its mean, median and geometric mean are also calculated.

Amazon-CL		Aspect factor = 1.0					
Stochastic generation	Liquid Permeability (mDarcy)	Methane Permeability (mDarcy)	Nitrogen Permeability (mDarcy)	Connectivity	Throat Skew	Pore-Row Spacing	Pore Skew
1	6.87E-06	1.30E-04	1.25E-04	4.30	1.76	2.43	3.10
2	5.53E-06	9.19E-05	8.85E-05	4.40	1.70	2.52	3.10
3	1.56E-05	2.00E-04	1.92E-04	4.60	1.76	2.56	3.50
4	9.02E-06	1.41E-04	1.36E-04	4.60	1.80	2.58	4.00
5	9.87E-06	1.56E-04	1.50E-04	4.40	1.74	2.53	3.50
6	1.17E-05	1.80E-04	1.73E-04	4.20	1.65	2.61	3.50
7	1.97E-05	2.58E-04	-	4.60	1.89	2.36	3.50
Mean	1.12E-05	1.65E-04	1.44E-04	4.44	1.76	2.51	3.46
Median	9.87E-06	1.71E-04	1.43E-04	4.40	1.76	2.53	3.50
Geometric mean	1.03E-05	1.87E-04	1.40E-04	4.44	1.76	2.51	3.45

Table 7. 4. The optimised Pore-Cor parameters for Amazon-CL, for an isotropic aspect factor ($\alpha=1$), at each stochastic generation. The Calculated network permeabilities and its mean, median and geometric mean are also calculated.

Amazon-CL		Aspect factor = 0.80					
Stochastic generation	Liquid Permeability (mDarcy)	Methane Permeability (mDarcy)	Nitrogen Permeability (mDarcy)	Connectivity	Throat Skew	Pore-Row Spacing	Pore Skew
1	7.30E-06	1.30E-04	1.25E-04	4.80	1.57	3.30	1.80
2	5.31E-06	9.09E-05	8.76E-05	4.60	1.50	3.40	1.80
3	2.01E-05	2.24E-04	2.16E-04	4.20	1.32	3.54	1.80
4	8.90E-06	1.31E-04	1.26E-04	4.20	1.44	3.37	1.80
5	9.36E-06	1.35E-04	1.31E-04	3.50	1.00	1.80	1.80
6	1.01E-05	1.48E-04	1.43E-04	4.20	1.44	3.37	1.80
7	1.90E-05	1.89E-04	1.82E-04	4.30	1.38	3.50	1.80
Mean	1.14E-05	1.50E-04	1.44E-04	4.44	1.76	2.83	3.46
Median	9.36E-06	1.35E-04	1.31E-04	4.40	1.76	2.85	3.50
Geometric mean	1.03E-05	1.45E-04	1.39E-04	4.44	1.76	2.83	3.45

Table 7. 5. The optimised Pore-Cor parameters for Amazon-CL, for a chosen aspect factor of $\alpha=0.8$, at each stochastic generation. The Calculated network permeabilities and its mean, median and geometric mean are also calculated.

OpacarbA40-CL		Aspect factor = 1.0					
Stochastic generation	Liquid Permeability (mDarcy)	Methane Permeability (mDarcy)	Nitrogen Permeability (mDarcy)	Connectivity	Throat Skew	Pore-Row Spacing	Pore Skew
1	1.81E-05	2.23E-04	2.15E-04	3.40	0.77	2.56	1.80
2	5.18E-05	3.84E-04	3.71E-04	2.50	0.23	2.56	1.80
3	1.98E-05	-	-	2.60	0.34	2.55	1.80
4	3.59E-05	2.55E-04	2.47E-04	3.40	0.90	2.47	1.80
5	1.95E-05	2.35E-04	2.27E-04	2.60	0.33	2.56	1.80
Mean	2.90E-05	2.74E-04	2.65E-04	2.90	0.51	2.54	1.80
Median	1.98E-05	3.10E-04	2.89E-04	2.60	0.34	2.56	1.80
Geometric mean	2.64E-05	2.65E-04	2.66E-04	2.87	0.45	2.54	1.80

Table 7. 6. The optimised Pore-Cor parameters for OpacarbA40-CL, for an isotropic aspect factor ($\alpha=1$), at each stochastic generation. The Calculated network permeabilities and its mean, median and geometric mean are also calculated.

OpacarbA40-CL		Aspect factor = 1.5				Throat Skew	Pore-Row Spacing	Pore Skew
Stochastic generation	Liquid Permeability (mDarcy)	Methane Permeability (mDarcy)	Nitrogen Permeability (mDarcy)	Connectivity				
1	3.43E-05	1.84E-04	1.77E-04	3.40	0.77	2.13	1.80	
2	2.09E-05	1.84E-04	1.77E-04	2.50	0.23	2.13	1.80	
3	2.15E-05	8.37E-04	8.08E-04	2.60	0.34	2.13	1.80	
4	1.13E-05	-	2.75E-04	3.40	0.90	2.06	1.80	
5	2.24E-05	2.25E-04	2.17E-04	2.60	0.33	2.13	1.80	
Mean	2.21E-05	3.58E-04	3.31E-04	2.80	0.51	2.12	1.80	
Median	2.15E-05	5.11E-04	2.17E-04	2.60	0.34	2.13	1.80	
Geometric mean	2.08E-05	4.73E-04	2.73E-04	2.87	0.45	2.12	1.80	

Table 7. 7. The optimised Pore-Cor parameters for OpacarbA40-CL, for a chosen aspect factor of $\alpha=1.5$, at each stochastic generation. The Calculated network permeabilities and its mean, median and geometric mean are also calculated.

Albagios-CL		Aspect factor = 1.0				Throat Skew	Pore-Row Spacing	Pore Skew
Stochastic generation	Liquid Permeability (mDarcy)	Methane Permeability (mDarcy)	Nitrogen Permeability (mDarcy)	Connectivity				
1	5.56E-04	3.67E-03	3.55E-03	5.00	1.30	2.56	2.00	
2	2.65E-04	1.81E-03	1.74E-03	4.40	1.15	2.60	2.00	
3	3.97E-04	2.45E-03	2.37E-03	4.60	1.18	2.61	2.00	
4	4.58E-04	2.74E-03	2.65E-03	4.60	1.19	2.62	2.00	
5	5.21E-04	2.78E-03	2.69E-03	4.70	1.12	2.68	2.00	
6	2.76E-04	-	-	5.00	1.31	2.55	2.00	
7	2.30E-04	-	-	4.30	1.10	2.60	2.00	
8	3.88E-04	1.38E-03	1.33E-03	5.00	1.29	2.60	2.00	
Mean	3.86E-04	2.47E-03	2.39E-03	4.70	1.21	2.60	2.00	
Median	3.93E-04	2.45E-03	2.36E-03	4.65	1.19	2.60	2.00	
Geometric mean	3.69E-04	2.61E-03	2.52E-03	4.69	1.20	2.60	2.00	

Table 7. 8. The optimised Pore-Cor parameters for Albagios-CL, for an isotropic aspect factor ($\alpha=1$), at each stochastic generation. The Calculated network permeabilities and its mean, median and geometric mean are also calculated.

The liquid permeability changes with stochastic generation number for each sample at $\alpha=1$ were compared to the permeability changes at their estimated aspect factors (figures 7.10 to 7.14), and the geometric means of the network permeabilities were calculated for each aspect factor and are shown in figure 7.15, and Table 7.1 to 7.8.

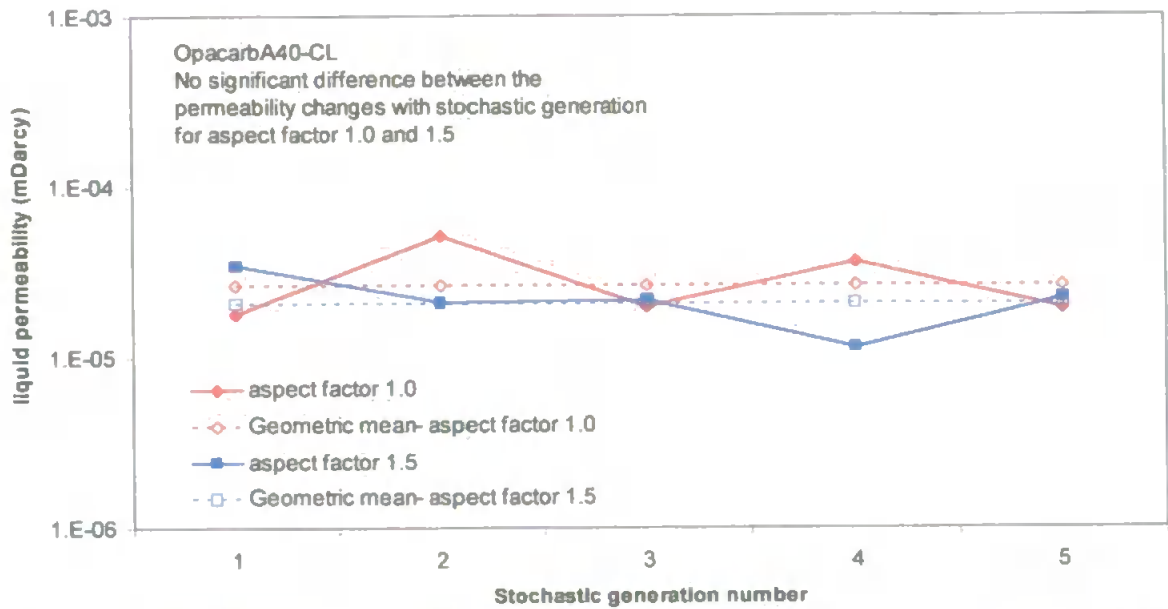


Fig. 7. 10. OpacarbA40-CL. Permeability changes with stochastic generation number at aspect factors 1.5 and 1.0.

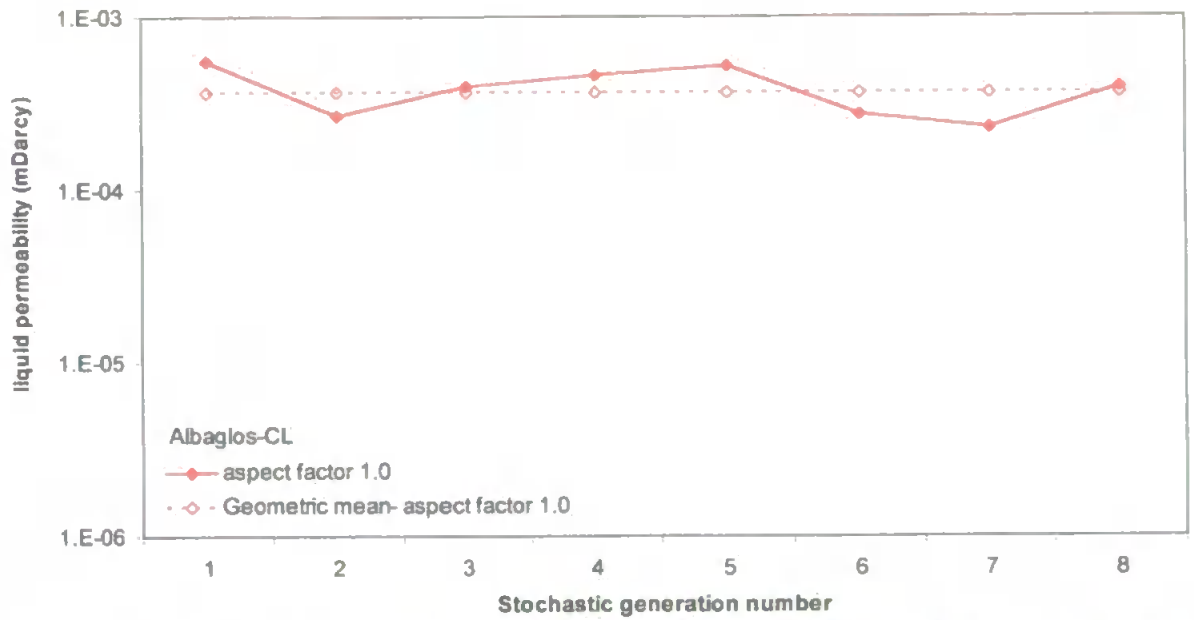


Fig. 7. 11. Albaglos-CL. Permeability changes with stochastic generation number at aspect factor of 1.0.

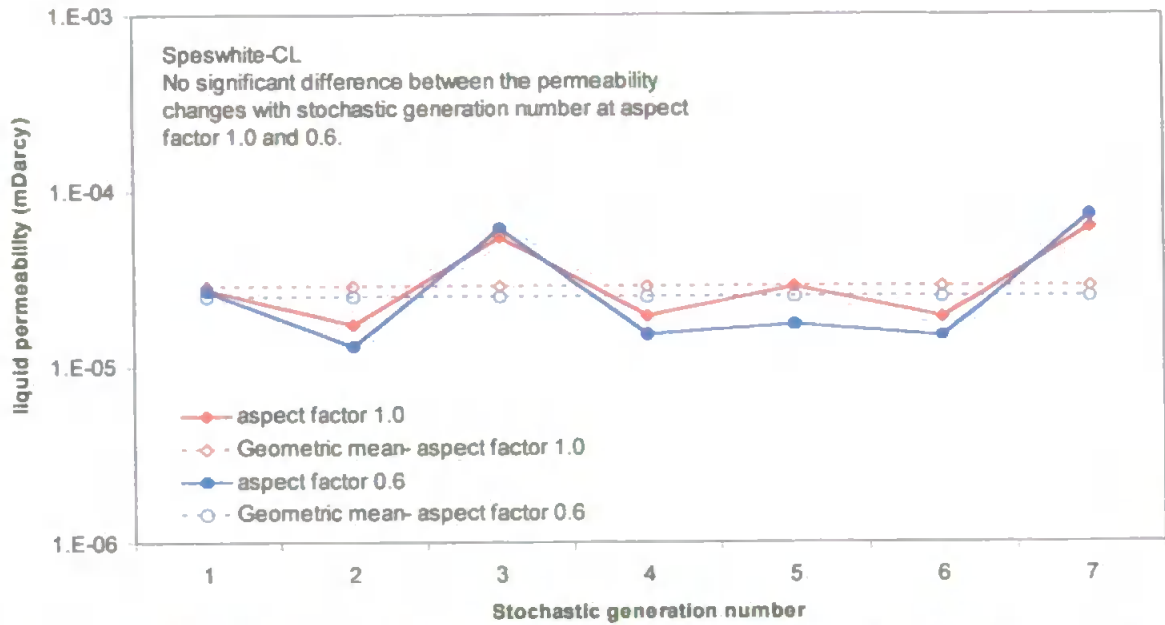


Fig. 7. 12. Speswhite-CL. Permeability changes with stochastic generation number at aspect factors 1.0 and 0.6.

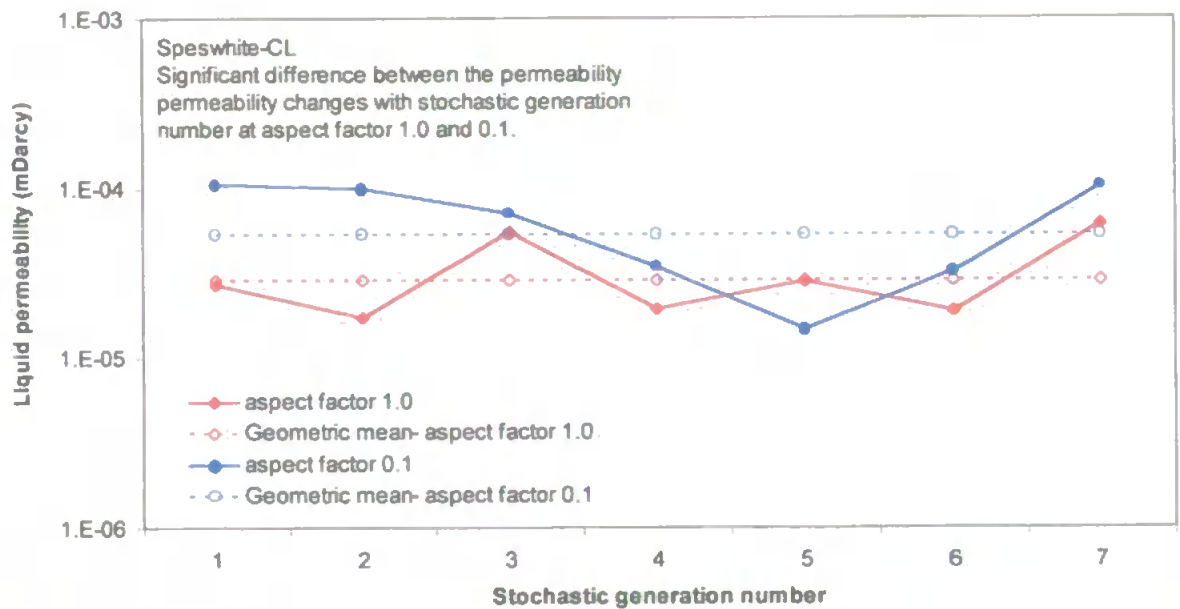


Fig. 7. 13. Speswhite-CL. Permeability changes with stochastic generation number at aspect factors 1.0 and 0.1.

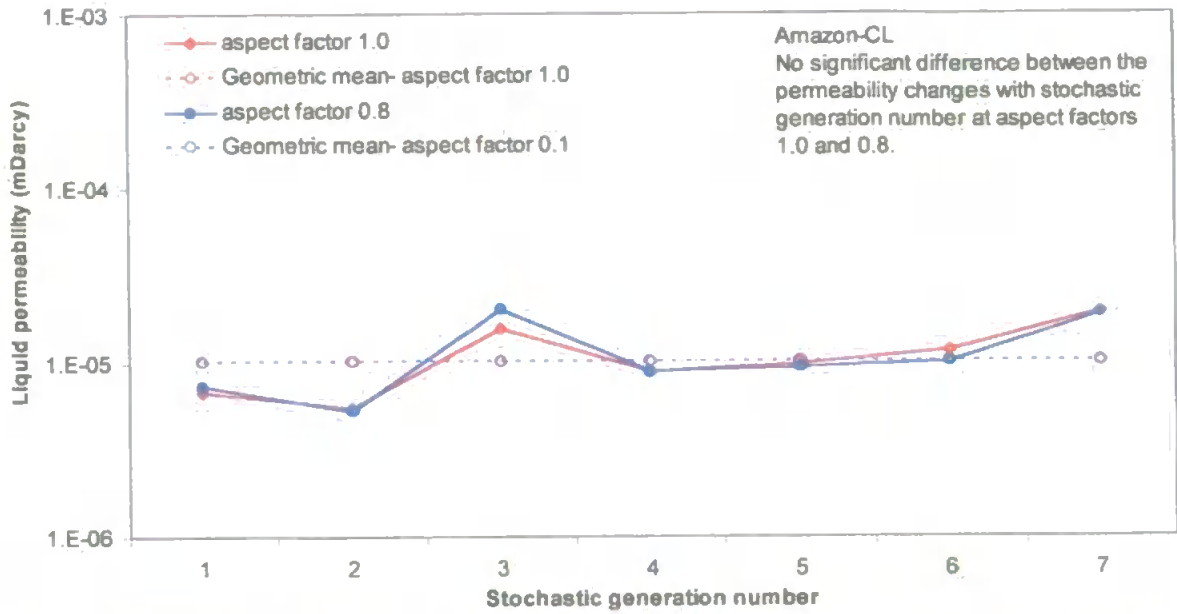


Fig. 7. 14. Amazon-CL. Permeability changes with stochastic generation number at aspect factors 1.0 and 0.8.

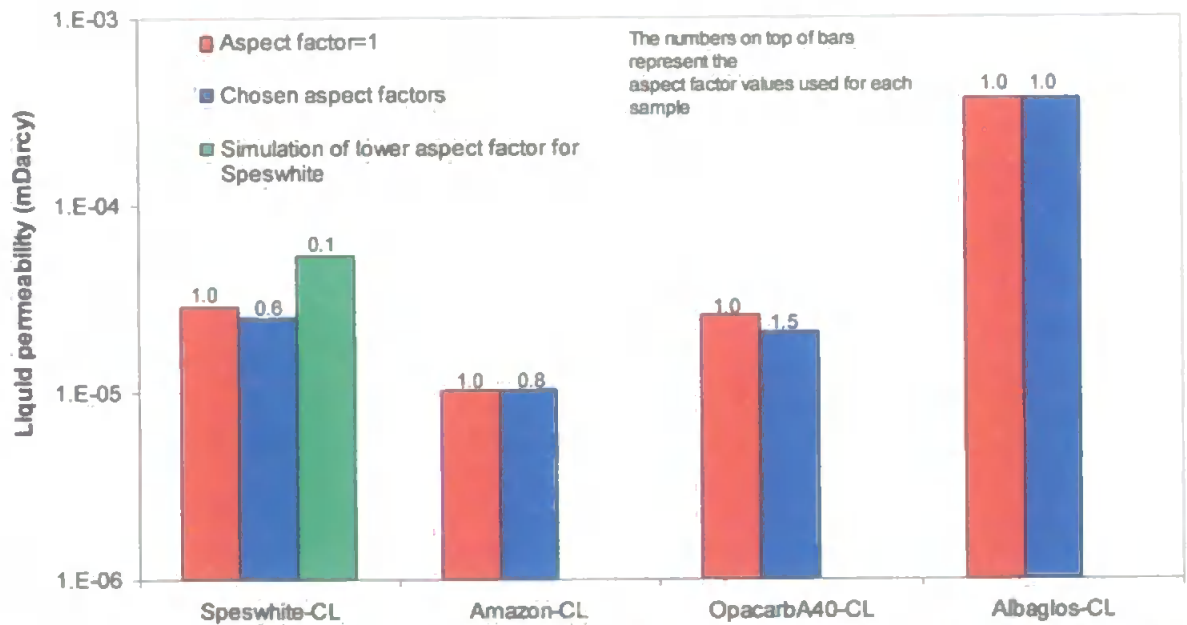


Fig. 7. 15. Calculated geometric means of the network permeabilities for each sample, at their chosen and isotropic aspect factors.

Statistical paired-t tests were performed on the permeability trends of the four samples, at their chosen and isotropic aspect factors, to determine if there was any significant difference in the two (at 95% confidence level), and are shown in Table 7.9.

Sample	Aspect factor, α	Mean liquid permeability (mDarcy)	Variance (mDarcy)	t	t Critical two-tail	Result of paired t-test (95% confidence level)
OpacarbA40-CL	1	2.90E-05	2.16E-10	0.77	2.78	No significant difference between means
	1.5	2.21E-05	6.68E-11			
Speswhite-CL	1	3.25E-05	3.28E-10	0.34	2.45	No significant difference between means
	0.6	3.15E-05	6.09E-10			
Speswhite-CL	1	3.25E-05	3.28E-10	-2.46	2.45	Significant difference between means
	0.1	6.60E-05	1.48E-09			
Amazon-CL	1	1.12E-05	2.48E-11	-0.34	2.45	No significant difference between means
	0.8	1.14E-05	3.33E-11			

Table 7. 9. Statistical paired t-test and the mean liquid permeability results for the four samples at their chosen and isotropic aspect factors. A significant difference between the mean permeabilities is observed within 95% confidence level, if the absolute value of t is greater than the value of t critical two-tail.

The calculated geometric means for OpacarbA40-CL showed the geometric mean permeability to be lower at its chosen aspect factor; however, the t-test measured no significant difference in the calculated permeabilities at their chosen and isotropic aspect factors (see fig. 7.10 and 7.15). This is in agreement with figure 7.7, in which the permeability for a simulated void structure showed no considerable difference when $\alpha > 1$.

For the clay samples, Speswhite-CL and Amazon-CL showed a relatively small decrease and increase, respectively, in their geometric mean permeabilities at their chosen aspect factors (see fig. 7.12, 7.14 and 7.15). However, the t-test showed the clay samples to have no significant difference at their chosen and isotropic aspect factors. The calculated permeabilities at a lower aspect factor for Speswhite-CL ($\alpha = 0.1$) was also simulated such that the effects of a much larger change in anisotropy could be tested (see fig. 7.13 and 7.15). The t-test showed Speswhite-CL to have a significant difference in their mean permeabilities when a lower aspect factor is used, and is in agreement with figure 7.7, where the

permeability for a void structure when $\alpha < 1$ is shown to increase sharply at lower aspect factors.

Methane and nitrogen gas network permeabilities are shown for Speswhite-CL, at $\alpha = 1$ and at $\alpha = 0.6$, in Fig 7.16 and 7.17.

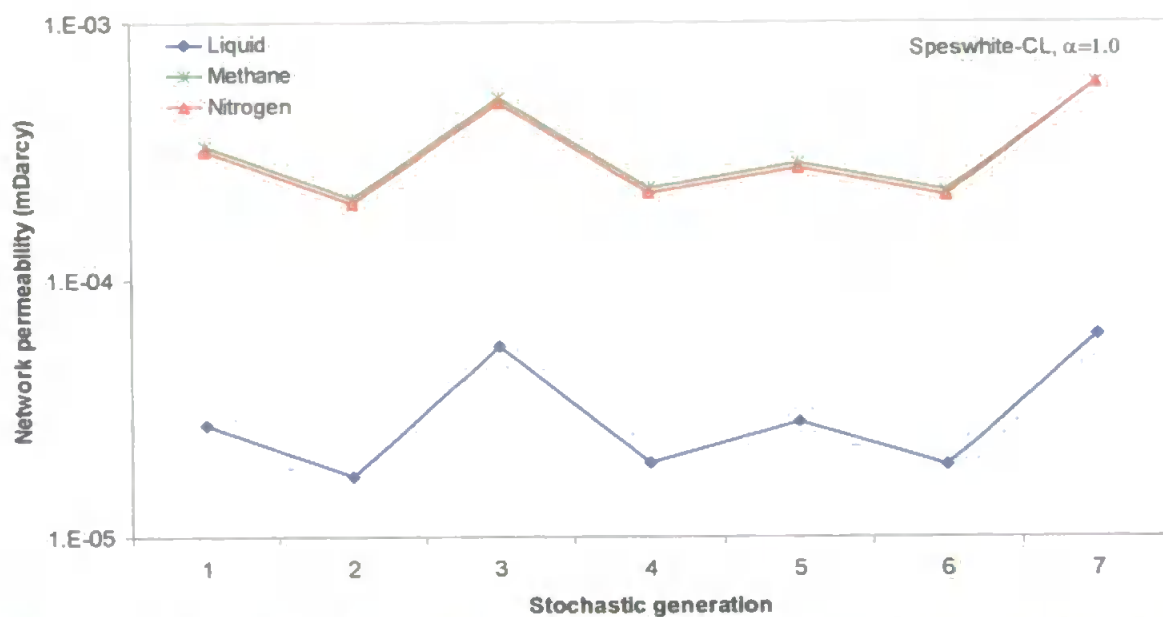


Fig. 7. 16. Speswhite-CL. Network permeabilities of liquid, methane and nitrogen gas with stochastic generation number, at $\alpha=1.0$.

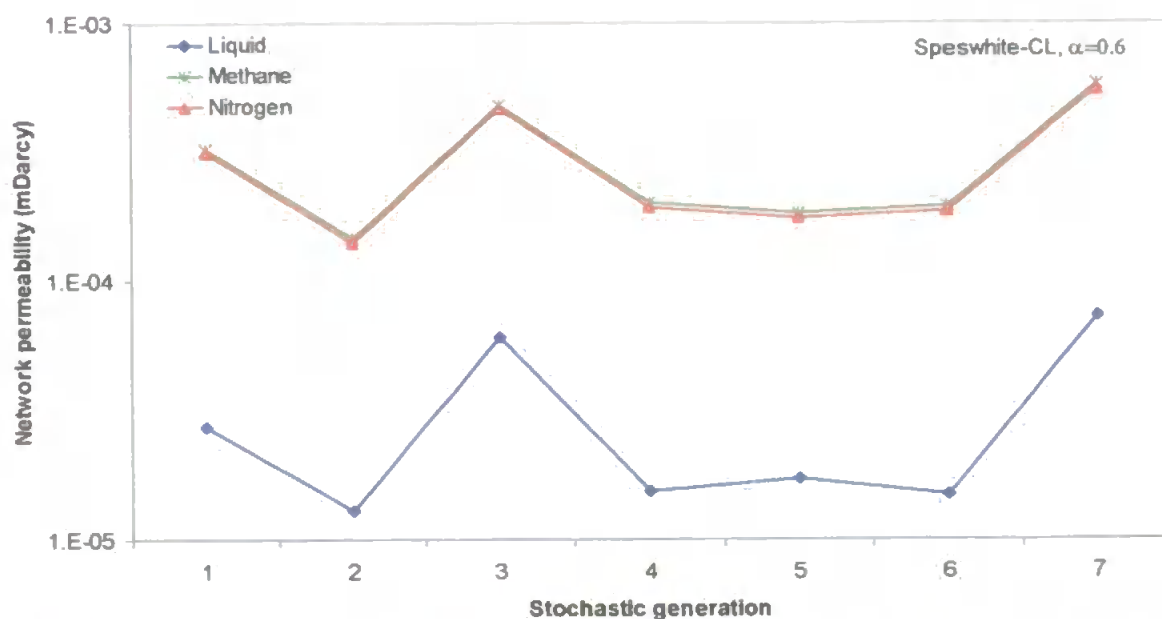


Fig. 7. 17. Speswhite-CL. Network permeabilities of liquid, methane and nitrogen gas with stochastic generation number, at $\alpha=0.6$.

The liquid permeabilities at $\alpha=1.0$ and $\alpha=0.6$ are shown to be around one order of magnitude lower than the permeabilities for both methane and nitrogen gas. This is a much greater difference than seen in sandstones, where the slip effect causes a reduction in liquid permeability relative to gas typically between 3% and 32% (Matthews *et al.*, 1993).

Although a statistical paired-t test showed no significant difference between the liquid permeabilities at $\alpha=1.0$ and $\alpha=0.6$, it did show a significant difference between the gas permeabilities. The anisotropic structure ($\alpha=0.6$) showed the gas permeabilities to be around 0.1 orders of magnitude lower than the gas permeabilities calculated for an isotropic structure ($\alpha=1.0$). The difference in the permeability curves for a liquid and gas is due to the slip flow phenomena, as discussed in Section 6.6.2 (Matthews *et al.*, 1993). The differences between the gas and liquid permeabilities are slightly lower for an anisotropic than an isotropic structure, as the slip flow correction has less of an effect for elliptical throats and slit-like or rod-like pores.

The two major parameters affecting permeability are connectivity and throat skew. Connectivity affects the ability of a liquid to find a flow route through the network that maximizes its overall flow capacity. A structure with a high connectivity would enable the liquid to uncover a less tortuous route through the network, and cause an increase in permeability. Meanwhile, throat skew affects the flow capacity of each individual arc in the network. A high throat skew would skew the size distribution to smaller sizes. Therefore a high throat skew would cause the flow of fluid to become impeded from the larger proportion of tiny capillaries in the void structure, and cause a decrease in permeability. The calculated mean values for the optimised connectivity and throat skew parameters of each sample are shown

figure 7.18. The optimised structures for the samples at $\alpha=1$ had very similar the percolation characteristics to the optimised structures at their chosen aspect factors, as the connectivity and throat skew are calculated to be the same.

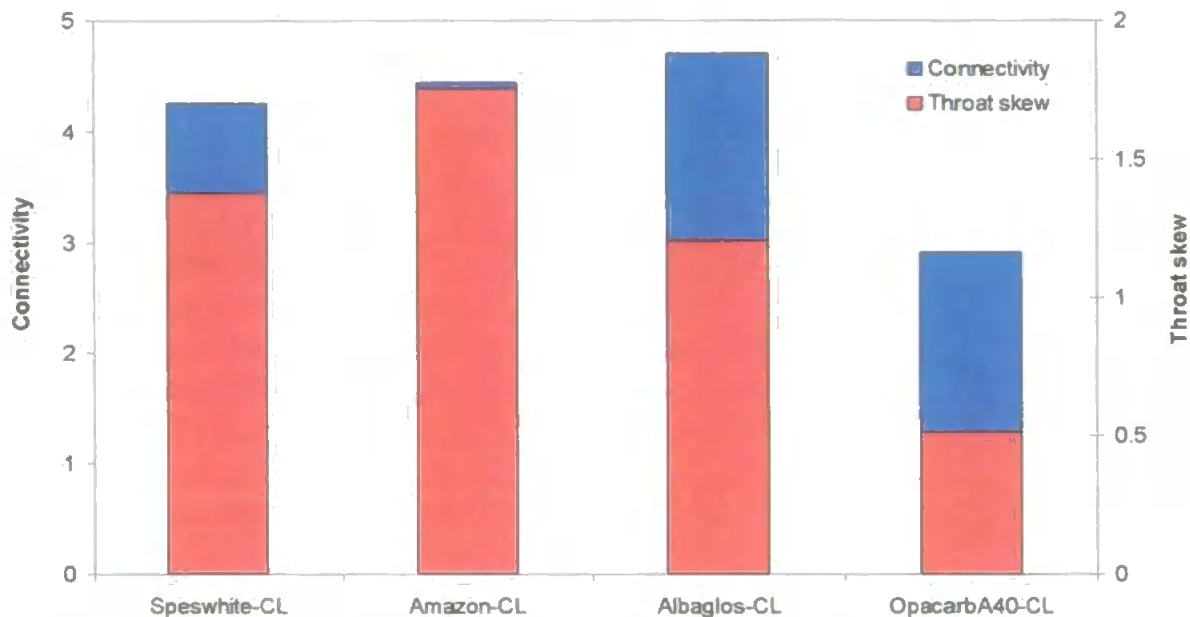


Fig. 7. 18. The mean connectivity and throat skew of the four samples.

Albaglos-CL is shown to have a much higher throat skew than OpacarbA40-CL, but also contains a much higher connectivity. As Albaglos-CL is calculated as having a higher calculated permeability than OpacarbA40-CL (Fig. 7.15), the connectivity of the void structure must play a greater role than throat skew in determining network permeability.

7.4. Permeability results from Pore-Cor and other existing models

The geometric mean network permeability calculations for the primary samples were calculated by three versions of the Pore-Cor model; the Isotropic and Anisotropic Pore-Cor model, and the Anisotropic Pore-Cor model with the application of the correction factor. The Pore-Cor permeability calculations were also compared to other existing models; the Aligned Cylinders, Kozeny and the

Kozeny-Carman model (refer to Section 3.4). The parameters used by the Aligned cylinders (Eq. 3.7) and the Kozeny models (Eq. 3.8 and 3.9) are shown in Table 5.1, while the results from all the permeability models are shown below, in Table 7.10.

Permeability models	Network Permeability calculations	Speswhite-CL	Amazon-CL	Albaglos-CL	OpacarbA40-CL
Pore-Cor models					
Isotropic Pore-Cor model (mDarcy)	Liquid	2.88E-05	1.03E-05	3.69E-04	2.57E-05
	Methane	3.12E-04	1.58E-04	2.36E-03	2.65E-04
	Nitrogen	3.02E-04	1.40E-04	2.28E-03	2.56E-04
Anisotropic Pore-Cor model (mDarcy)	Liquid	2.50E-05	1.03E-05	3.69E-04	2.08E-05
	Methane	2.66E-04	1.45E-04	2.36E-03	4.73E-04
	Nitrogen	2.56E-04	1.39E-04	2.28E-03	2.73E-04
Anisotropic Pore-Cor model with correction factor (mDarcy)	Liquid	2.34E-06	4.63E-06	4.26E-05	5.10E-06
	Methane	2.49E-05	6.49E-05	2.72E-04	1.16E-04
	Nitrogen	2.40E-05	6.26E-05	2.63E-04	6.67E-05
Other existing models					
Aligned cylinders model (mDarcy)	Liquid	3.31E-03	1.71E-03	5.33E-02	1.02E-01
Kozeny Model (mDarcy)	Liquid	2.76E-01	1.01E-01	6.57E-01	7.96E-01
Kozeny-Carmen Model (mDarcy)	Liquid	1.10E-01	4.04E-02	2.63E-01	3.19E-01

Table 7. 10 Calculated permeabilities for the primary samples, from using the Pore-Cor models and other existing models.

The calculated liquid permeability trends from the Pore-Cor models, along with the permeability trends from the other existing models, are discussed and compared to the experimental ISD and DAT permeation rates in the following sections (Section 7.5 and 7.6). However, nitrogen gas permeability trends from the Pore-Cor models were used in comparing the Gurley air permeability trends, as nitrogen gas would be closest in representing the flow of air used in the Gurley method (Section 7.7). The permeability trends from the other existing models were also compared to the Gurley permeability trends.

7.5. Comparison of ISD permeation rates with the modelled permeabilities

The trends from the ISD permeation rates were used to compare the trends from the six permeability models; the Aligned Cylinders model, the Isotropic Pore-Cor model, the Anisotropic Pore-Cor model, Anisotropic Pore-Cor Model with correction factor, the Kozeny model and the Kozeny-Carman model. The results from the six permeability models are shown in Table 7.10, and the experimental ISD permeation rates are shown in Table 5.3.

The permeability results from the Pore-Cor models are shown in fig. 7.19 while the permeability results from the Kozeny and Aligned cylinders models are shown in fig. 7.20. In both figures, the experimental ISD permeation rates were graphed on the secondary y axis. To enable a better comparison of the experimental permeation and modelled permeability trends, both axes were made into a log scale spanning the same orders of magnitude.

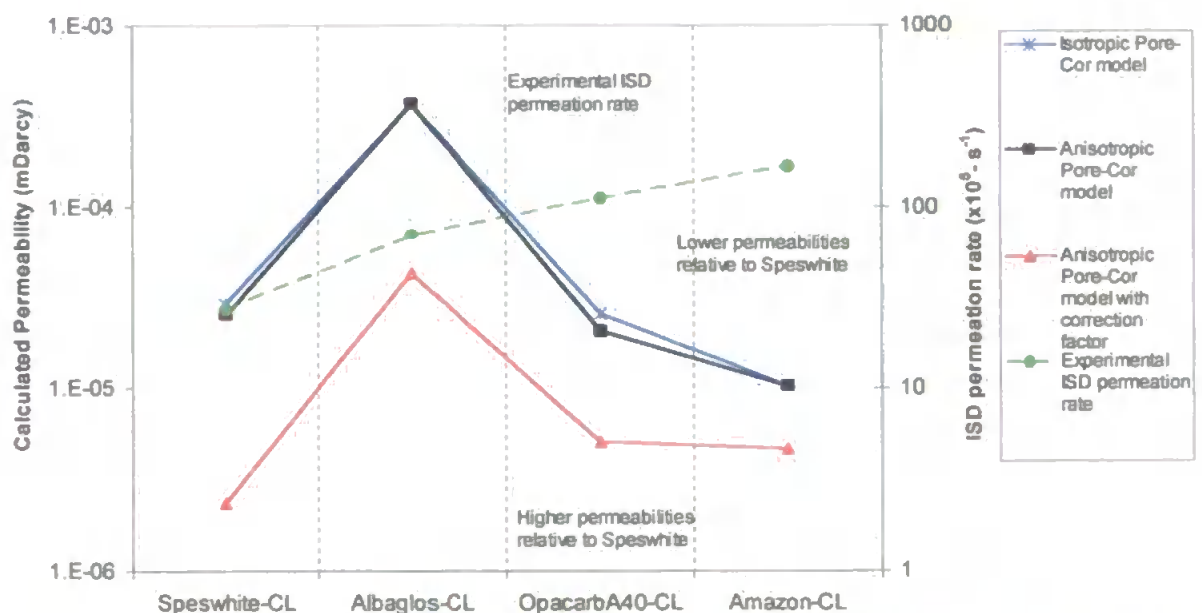


Fig. 7. 19. Comparison of the simulated permeabilities of the four samples from the three Pore-Cor models. The experimental ISD permeation rates of the four samples were graphed on the secondary y axis.

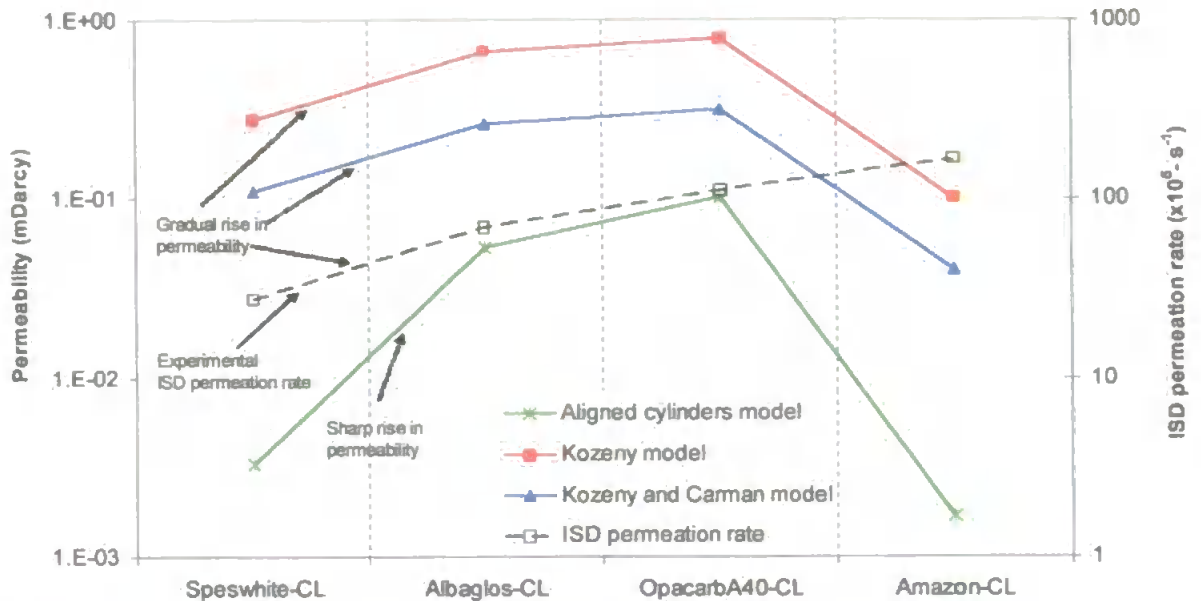


Fig. 7. 20. Comparison of the simulated permeabilities of the four samples from the Kozeny and Aligned cylinders models. The experimental ISD permeation rates of the four samples were graphed on the secondary y axis.

Fig. 7.19 showed very little difference between the Isotropic and Anisotropic Pore-Cor model. These two models showed the permeability trends for Speswhite and Albaglos to be in agreement with the ISD permeation trends; however the calculated permeabilities for OpacarbA40-CL and Amazon-CL were much lower than of Speswhite, which is in contrast to the experimental ISD permeation results. Better agreement is shown when the correction factor is applied to the anisotropic model, causing the permeabilities for the OpacarbA40-CL and Amazon-CL to now be greater than Speswhite-CL. However, the model still showed the permeability for OpacarbA40-CL and Amazon-CL to be lower than Albaglos-CL, in contrast to the experimental ISD permeation results.

The permeabilities for the Kozeny and Aligned cylinders models are shown in Fig. 7.20 to be two to three orders of magnitude higher than the Pore-Cor models. The Kozeny-Carman model is shown to have slightly lower permeabilities than the Kozeny model, while the Aligned cylinders model was shown to have

permeabilities of approximately one order of magnitude lower than the Kozeny models.

All three models in fig. 7.20 showed poor correlation in regards to Amazon-CL, as it is shown to have the lowest permeability of all the samples although it has highest ISD permeation rate. However, Speswhite-CL, Albaglos-CL and Amazon-CL are shown to have an increasing permeability trend for all three of the models, which is in agreement with the ISD permeation trend. The slope of the ISD permeation trend for these three samples is more similar to the Kozeny models than to Aligned cylinders model, as the latter shows a much sharper rise in permeability between Speswhite-CL and Albaglos-CL than predicted by the Kozeny models. In summary, the permeabilities from Speswhite-CL, Albaglos-CL and OpacarbA40-CL were shown to be in best agreement with the experimental ISD permeation trends by using either one of the Kozeny models.

7.5.1. Ranking of modelled permeabilities to ISD permeation rates

An alternative approach in comparing the different permeability models was performed by ranking the experimental permeation rates and their respective modelled permeabilities between each sample, in ascending order. For example, a sample with the highest modelled permeability would have the highest modelled permeability ranking of four, while the sample with the highest ISD permeation rate would have the highest ISD permeation ranking of four.

The rankings of the ISD permeation rates were plotted on the x-axis, while the rankings of the modelled permeabilities were plotted on the y-axis, accordingly (fig. 7.21). A line of perfect fit between the two rankings would represent a curve with a

slope of one; as an increase in ranking of ISD permeation rate would represent an increase in ranking of modelled permeability, showing a positive trend.

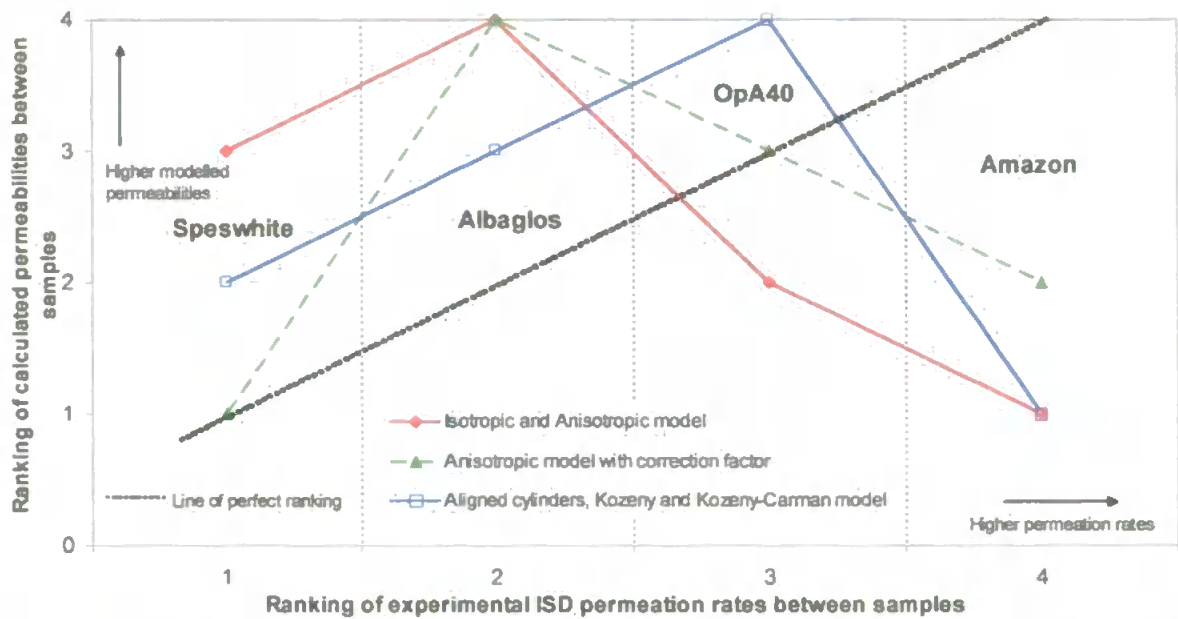


Fig. 7. 21. The ranking scheme between samples for the ISD permeation rates and the permeability models.

As evident in Fig. 7.21, only a qualitative assessment can be used to judge which model shows closer agreement with the experimental permeation trends. A quantitative measure was used to show how close the trends from the different models resemble the experimental permeation trends. The sum of the square of the difference between each pair of modelled and experimental ranking points of each sample (also known statistically as the L2-norm) was calculated for each model, with the result expressed as the modelling trend error for each model, M_T .

$$M_T = \sum_1^i (R_{m,i} - R_{e,i})^2,$$

Eq. 7. 1

where R_m and R_e refers to the modelled and experimental permeation ranking of each sample, i . The modelling trend errors for the ISD permeation rates were calculated on each permeability model, and are shown in Fig. 7.22.

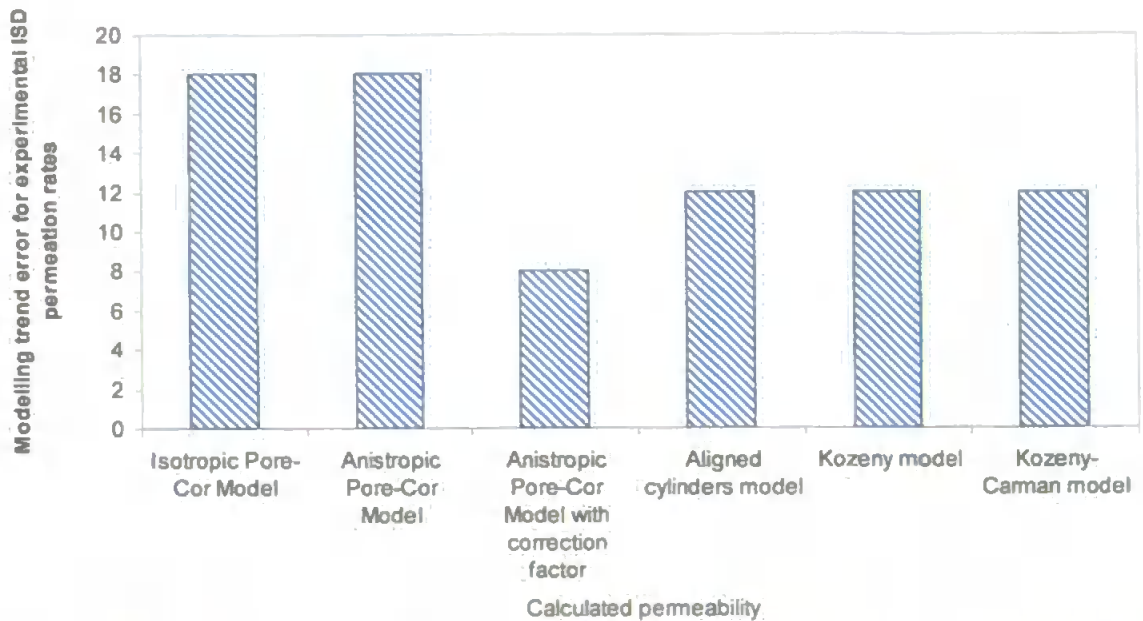


Fig. 7. 22. Modelling trend error on the calculated permeabilities for the ISD permeation rates.

Both the Isotropic and Anisotropic Pore-Cor model had the worst fit to the experimental ISD permeation results than all the other permeability models. There was also no difference in the rankings for the two Pore-Cor models, as the use of the estimated aspect factors did not produce any significant improvement in their trend. However, when the correction factor was applied to the anisotropic Pore-Cor model, the modelling trend error was calculated to be the lowest of all the permeability models.

7.5.2. Comparison of experimental ISD permeation rates with samples of similar surface throat number densities

Although the aligned cylinders model and Kozeny models are much simpler models than the Pore-Cor model, their permeability calculations are based on two factors that Pore-Cor does not directly measure: the number density of throats, used in the aligned cylinders model (see Eq. 3.7), and specific surface area used in the Kozeny models (see Eq. 3.5 and 3.6). The aligned cylinders and the Kozeny model have been shown to better resemble the experimental trends than

either the Isotropic or Anisotropic Pore-Cor model. It follows that the number density of throats and the specific surface area are particularly good modelling parameters for calculating permeability, when these calculations are judged against experimental ISD permeation trends. By contrast, the anisotropic Pore-Cor model predicted permeabilities which compared less well with the ISD permeation trends. This was because the anisotropic effects on permeability were masked by the packing errors within the Pore-Cor model which caused a discrepancy between the simulated and actual number density of surface throats. However, once the correction factor, f , was applied to the anisotropic Pore-Cor model it has been shown to predict permeabilities at more accurate than those predicted by the Kozeny and aligned cylinders models.

The application of the correction factor, f , is needed if the samples have number densities that are significantly different from each other. Amazon-CL and Speswhite-CL provide an example of two samples with significant difference in number densities, as Amazon-CL is shown to be around six times larger than Speswhite-CL (Table 6.1). The Anisotropic Pore-Cor model is shown to calculate a larger permeability for Speswhite-CL than Amazon-CL, even though the experimental ISD permeation rate is much smaller for Speswhite-CL, Fig. 7.17. Once the correction factor is applied to the model, the calculated permeabilities fall in agreement with the experimental trends. The correction factor is not needed, however, when the permeabilities are calculated for samples with similar number densities. A comparison is made between Amazon-CL (containing CMC and latex) and Amazon-SL (containing starch and latex), as the number density for Amazon-CL is shown only to be 1.3 times larger than Amazon-SL, Fig. 5.5 and Fig. 7.23 (refer to Table B.2 of Appendix B.1)

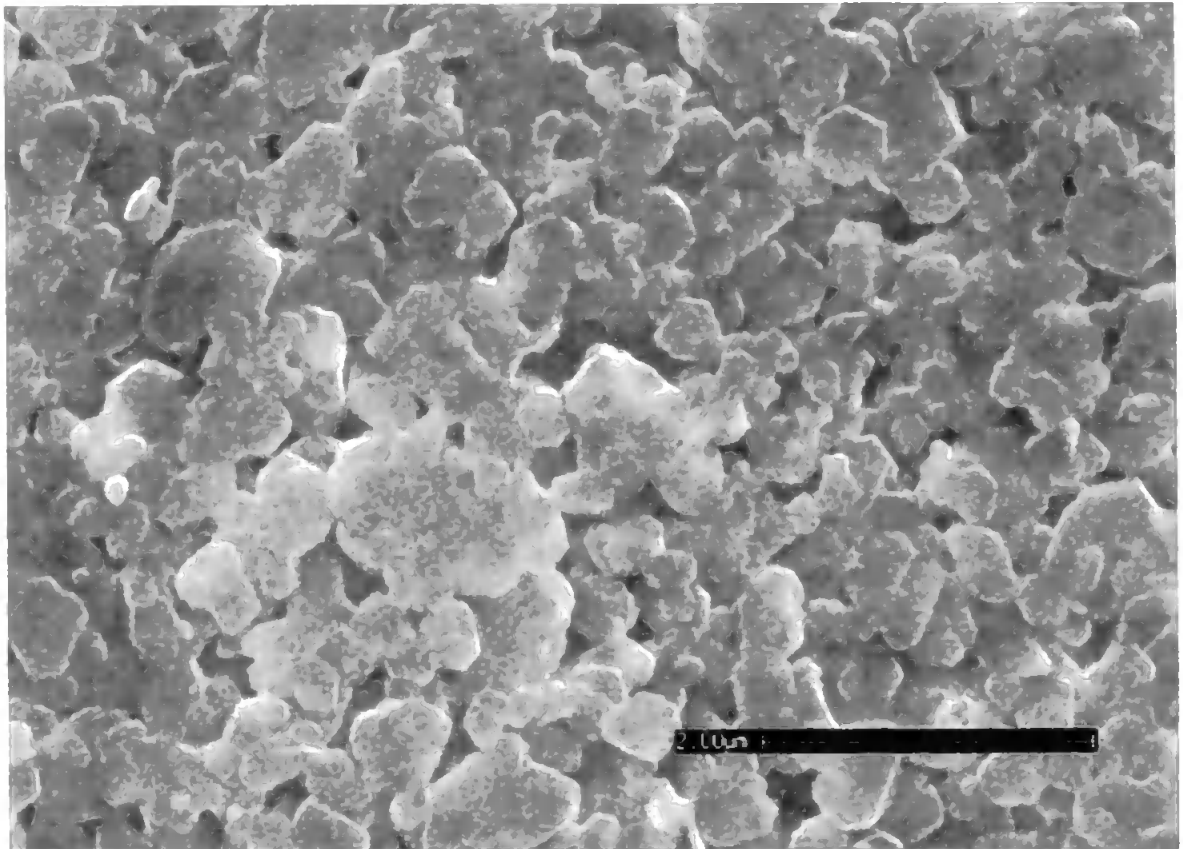


Fig. 7. 23. Amazon-SL: scanning electron micrographs of surface scan. Scale bar: $2\mu\text{m}$. The number density of surface throats was calculated to be $3.16\ \mu\text{m}^{-1}$.

The Anisotropic Pore-Cor model was used to calculate the geometric mean network permeability for Amazon-SL, from a range of stochastic generations, at an estimated aspect factor of 0.8. The optimised Pore-Cor parameters and their respective network permeabilities are shown in Table B.4 of Appendix B.2. The ISD permeation rates and the calculated permeabilities from the Anisotropic Pore-Cor Model are shown for the two Amazon samples, in Fig. 7.24.

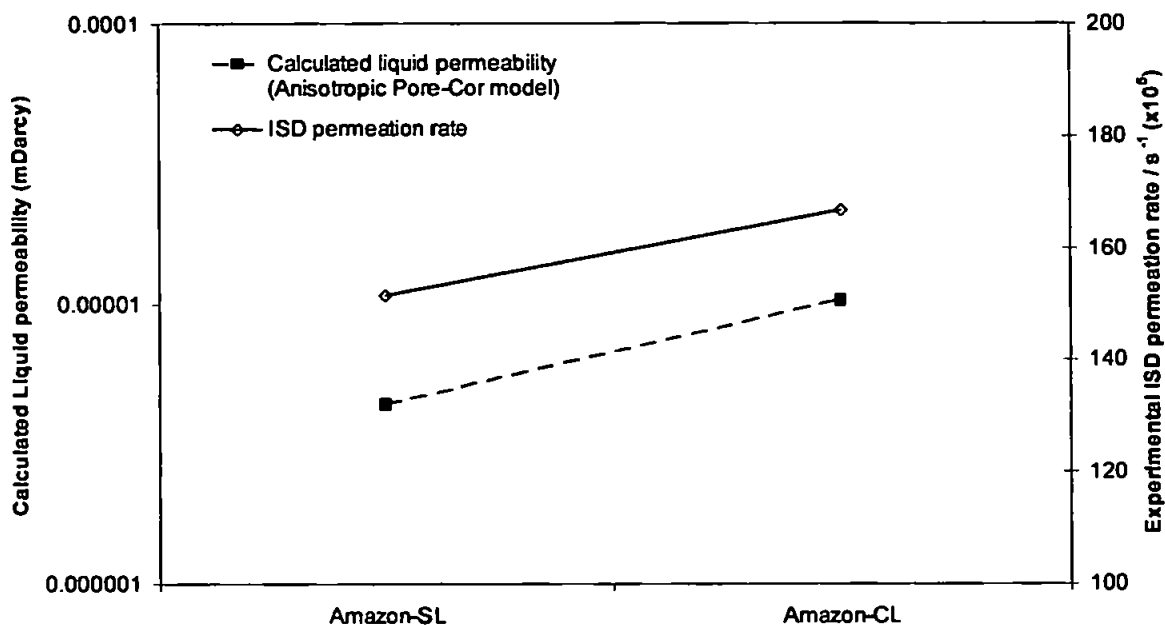


Fig. 7. 24. Comparison of the calculated liquid permeability and the experimental ISD permeation rate for Amazon-CL and Amazon-SL, using an aspect factor of 0.6 for both samples.

Amazon-CL is shown to have both a greater experimental permeation rate and calculated permeability than Amazon-SL, exhibiting a positive trend for both curves. For this case, the use of the correction factor is not needed for the Pore-Cor model to simulate realistic trends.

7.6. Comparison of DAT permeation rates with the modelled permeabilities

The DAT permeation results are shown in section 5.2.6 to better represent permeability measurements than the ISD permeation results, as their trends closely resembled the trends from the Gurley permeability measurements. The DAT permeation rates showed less dependency on number density, as confirmed in fig. 5.23, since no perfect positive rank correlation with permeation rate was revealed. In this case, Amazon is shown to have the highest number density, but is shown to have a lower DAT permeation rate than the PCC samples.

Using the experimental DAT permeation rates, the permeability calculations for the six models were compared in similar fashion as the experimental ISD permeation rates. The permeability results from the Pore-Cor models are shown in fig. 7.25 while the permeability results from the Kozeny and aligned cylinders models are shown in fig. 7.26. In both figures, the calculated permeabilities, and the experimental DAT permeation rates were graphed on the primary and secondary axis, respectively.

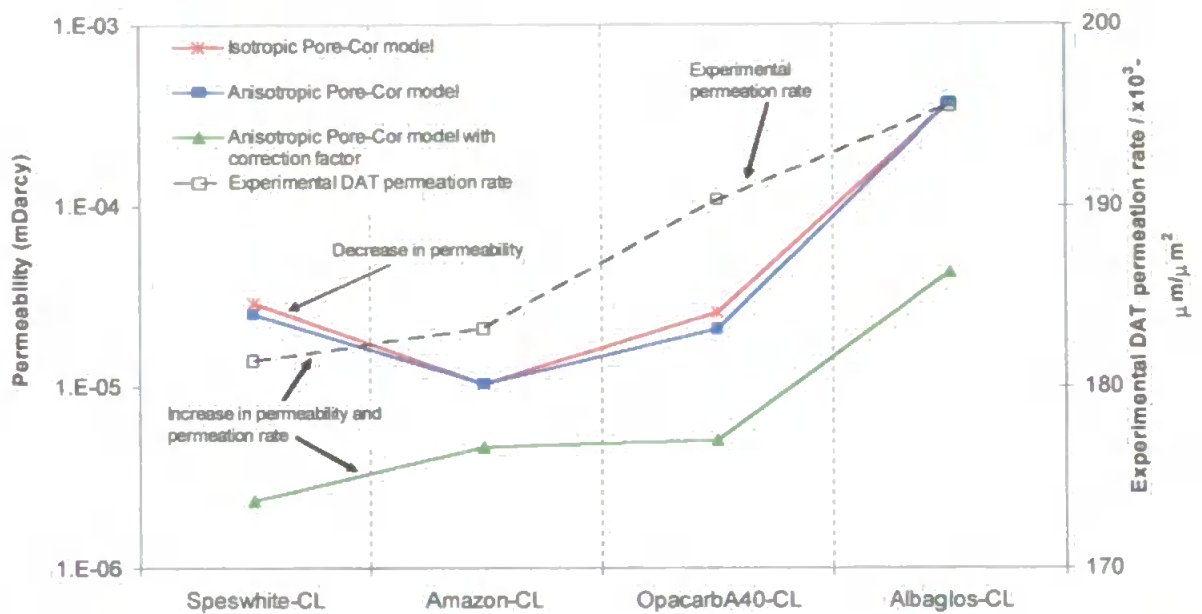


Fig. 7. 25. Comparison of the simulated permeabilities of the four samples from the three Pore-Cor models. The DAT permeation rates of the four samples were graphed on the secondary y axis.

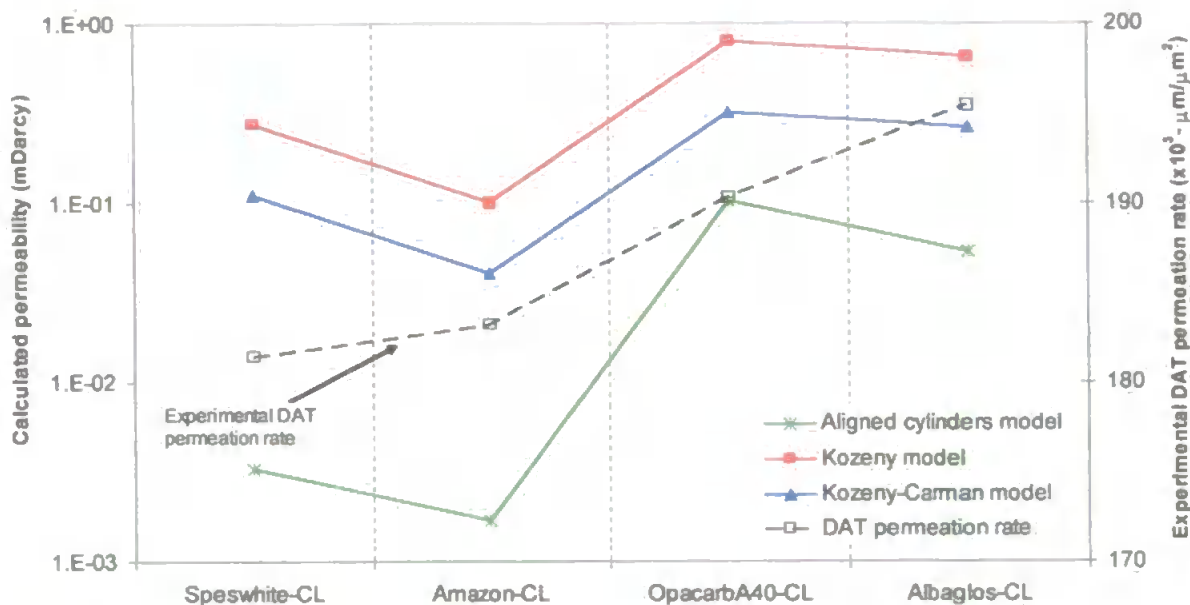


Fig. 7. 26 Comparison of the simulated permeabilities of the four samples from the Kozeny, Kozeny-Carman and the Aligned cylinders models. The experimental DAT permeation rates of the four samples were graphed on the secondary y axis.

Fig. 7.25 showed very little differences between the Isotropic and Anisotropic Pore-Cor model, when the estimated aspect factors were used and showed positive correlation with the experimental DAT permeation rates for three of the four samples. However, Speswhite-CL is shown to have a higher permeability than Amazon-CL, which is the reverse trend shown in the experimental results. The application of the correction factor to the Anisotropic Pore-Cor model caused the calculated permeabilities of the samples to decrease by one order of magnitude, and displayed an increase in permeability for all four of the samples. Hence, the simulated permeability trend is shown to be in close agreement with the DAT permeation trend.

In Fig. 7.26, the permeability trend for all three models is shown to fluctuate rather than follow a gradual increase, as observed in the DAT permeation trend. However, all three models showed the clay samples (Speswhite-CL and Amazon-CL) to have a lower permeability than the PCC samples (Albaglos-CL and OpacarbA40-CL), which is in agreement with the experimental trend.

7.6.1. Ranking of modelled permeabilities to DAT permeation rates

A ranking scheme was used for the DAT permeation rates, and is shown in Fig. 7.27, while the modelling trend error for each permeability model is shown in Fig. 7.28.

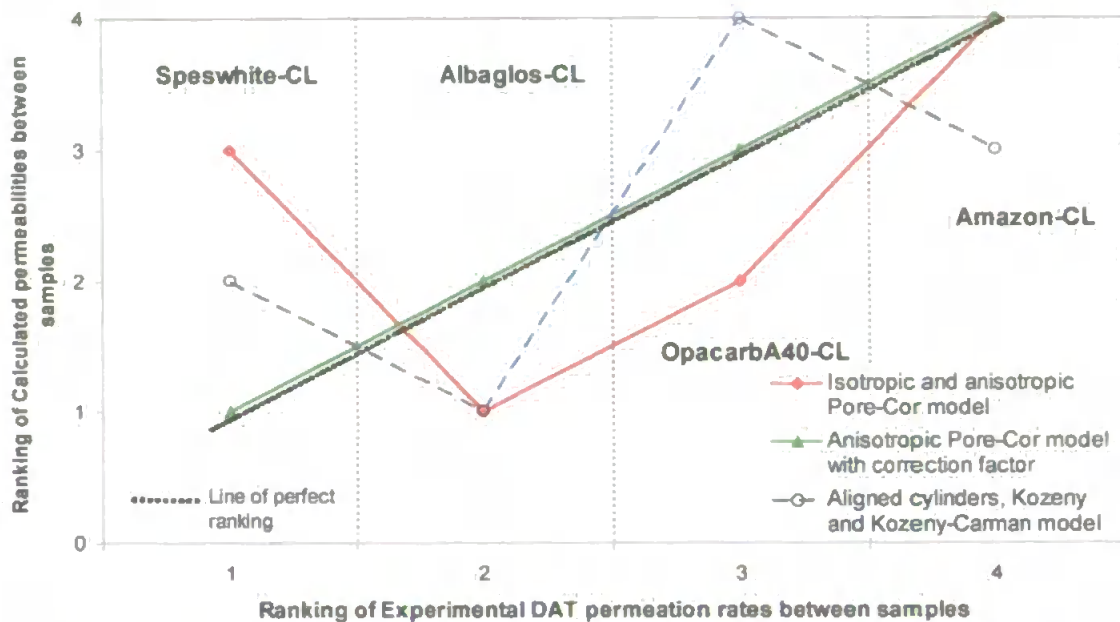


Fig. 7. 27. The ranking scheme between samples for the experimental DAT permeation rates and the permeability models. The anisotropic Pore-Cor model with correction factor is shown to give a better qualitative prediction than any other model.

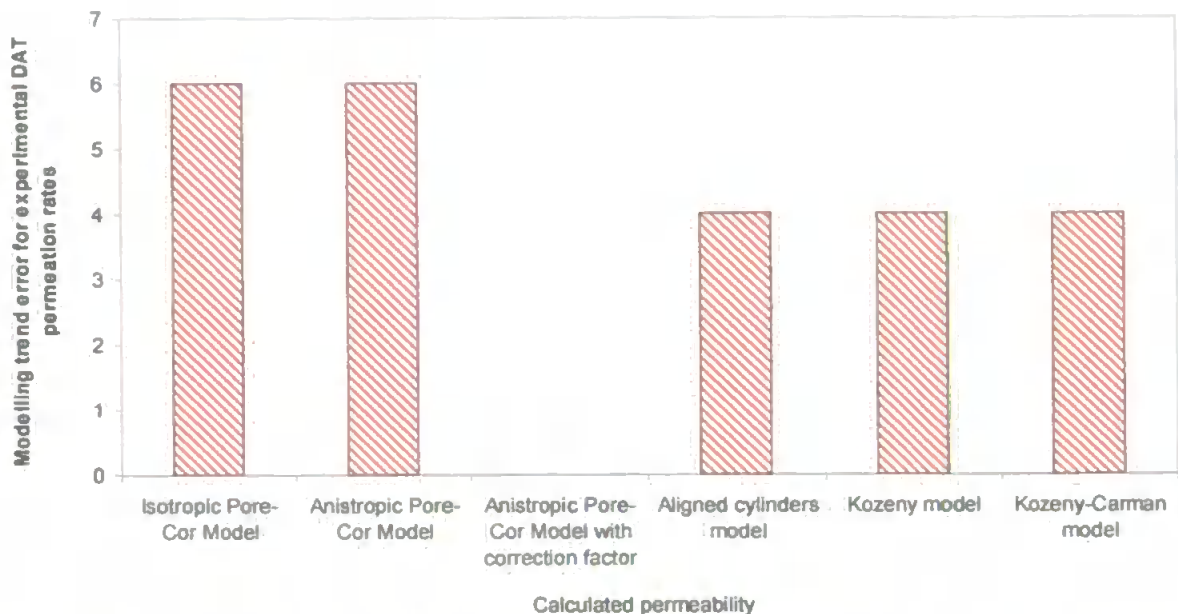


Fig. 7. 28. The modelling trend errors for the DAT permeation rates. The anisotropic Pore-Cor model with correction factor has a zero modelling trend error – i.e. it is shown to give a perfect prediction.

The isotropic and anisotropic Pore-Cor model showed the largest modelling trend error of all the permeability models. There was also no difference in the rankings for the two Pore-Cor models, as the use of an estimated aspect factor showed no significant improvement in their trend. The Kozeny, Kozeny-Carman and the Aligned cylinders model had a lower modelling trend error than the two Pore-Cor models, showing better agreement with the experimental DAT results. However, once the correction factor was applied to the Anisotropic Pore-Cor model, the modelling trend error was reduced to zero, indicating a trend which exactly matched that of the DAT permeation results.

7.6.2. Comparison of experimental DAT permeation rates with samples of similar surface throat number densities

As shown with the experimental ISD permeation trends, the Pore-Cor model gave much better correlation when comparing experimental DAT permeation trends for samples of similar surface throat number densities. An

example is made between OpacarbA60-CL and OpacarbA40-CL, as the number density for OpacarbA40-CL is shown only to be 1.05 times larger than OpacarbA60-CL, Fig. 5.7 and Fig. 7.29 (refer to Table B.2 of Appendix B.1)

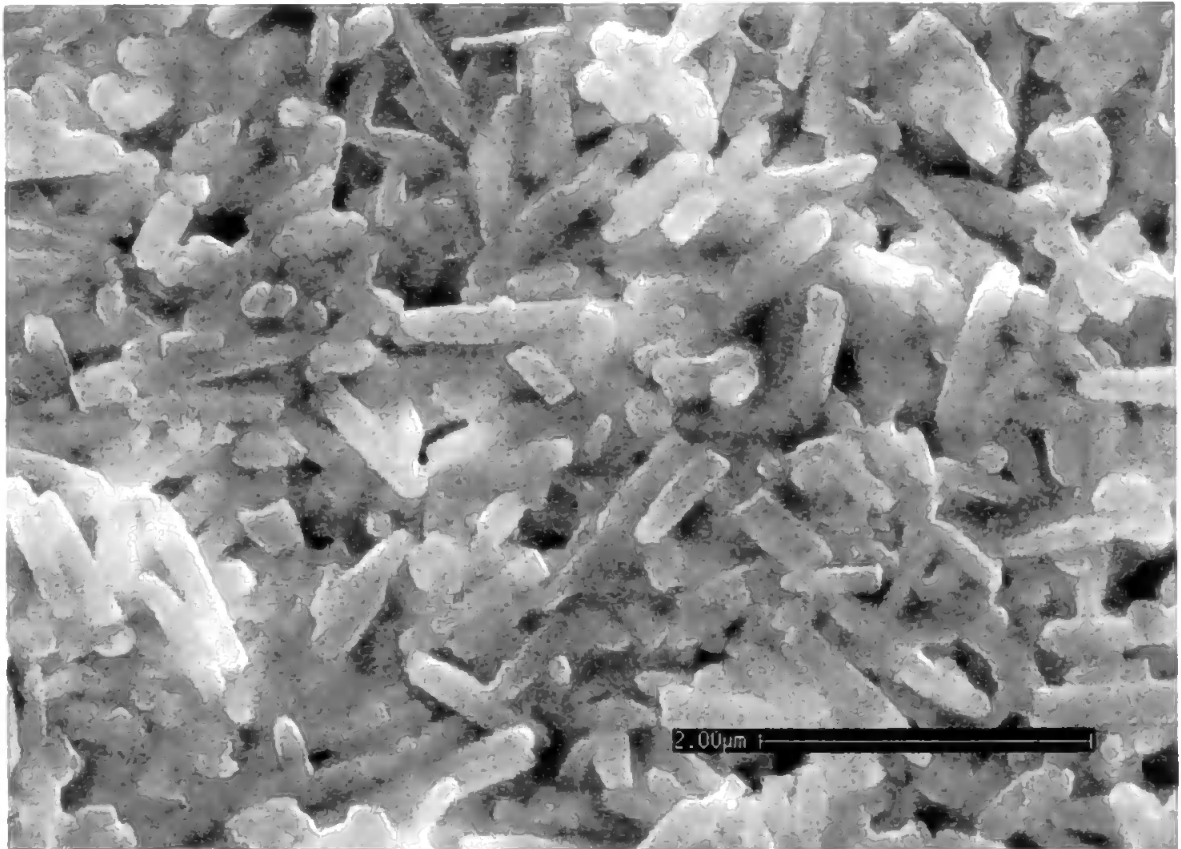


Fig. 7. 29. OpacarbA60-CL: scanning electron micrographs of surface scan. Scale bar: $2\mu\text{m}$. The number density of surface throats was calculated to be $2.87\ \mu\text{m}^{-1}$.

The anisotropic Pore-Cor model was used to calculate the geometric mean network permeability for OpacarbA60-CL, from a range of stochastic generations, at an estimated aspect factor of 2.0. The optimised Pore-Cor parameters and their respective network permeabilities are shown in Table B.3 of Appendix B.2. The DAT permeation rates and the calculated permeabilities from the anisotropic Pore-Cor model are shown for the two precipitated calcium carbonate (PCC) samples, in Fig. 7.30.

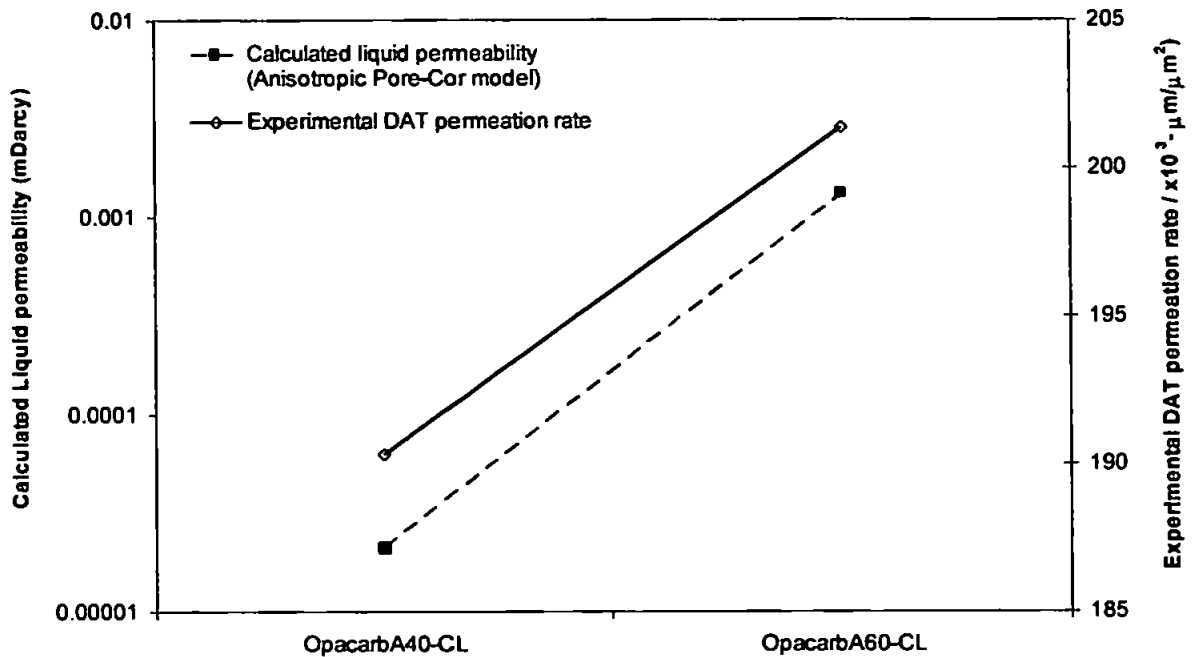


Fig. 7. 30. Comparison of the calculated liquid permeability and the experimental DAT permeation rate for OpacarbA40-CL and OpacarbA60-CL, using an aspect factor of 1.5 and 2.0, respectively.

OpacarbA40-CL is shown to have both a greater experimental permeation rate and calculated permeability than OpacarbA60-CL, exhibiting a positive trend for both curves. As such is the case in Fig. 7.24, the use of the correction factor is not needed for the Pore-Cor model to simulate realistic trends,

7.7. Comparison of the Gurley permeability results with the modelled permeabilities

The Gurley permeability trends for three of the four samples were compared to the trends from the six permeability models, in similar fashion as the experimental ISD and DAT permeation rates. The permeability results from the Pore-Cor models are shown in fig. 7.31 while the permeability results from the Kozeny and aligned cylinders models are shown in fig. 7.32. In both figures, the calculated permeabilities and the experimental Gurley permeabilities were graphed on the primary and secondary axis, respectively.

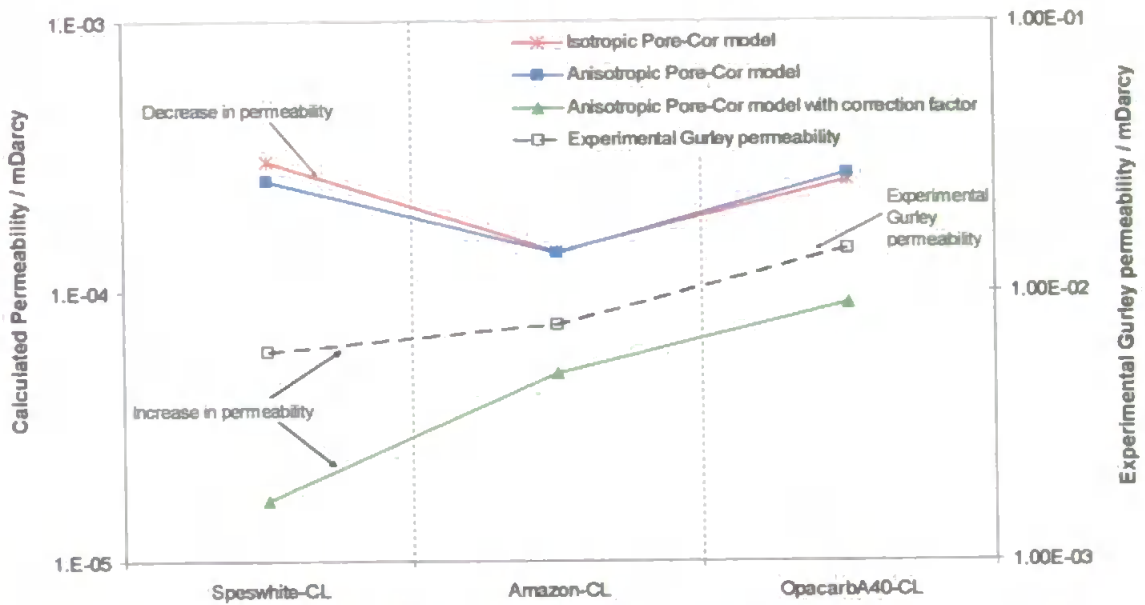


Fig. 7. 31. Comparison of the simulated nitrogen gas permeabilities from the three Pore-Cor models for three of the four samples. The experimental Gurley permeability of the three samples were graphed on the secondary y axis.

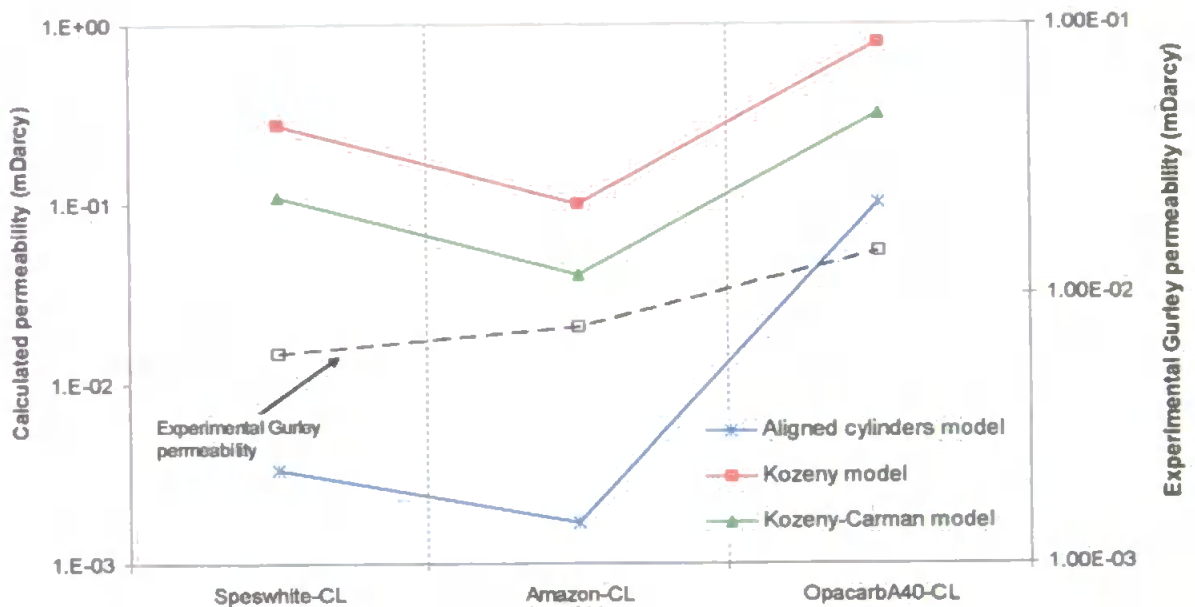


Fig. 7. 32. Comparison of the simulated permeabilities for three of the four samples from the Kozeny, Kozeny-Carman and the Aligned cylinders models. The experimental Gurley permeability of the three samples was graphed on the secondary y axis.

Both the Isotropic and Anisotropic Pore-Cor model showed positive correlation with the experimental Gurley permeabilities for only two of the three samples, as Speswhite-CL is shown to have a higher calculated permeability than Amazon-CL, in contrast to experimental results. The application of the correction factor caused

the calculated permeabilities to have a positive correlation with the Gurley permeability results for all three of the samples. Hence, the simulated permeability trend for Pore-Cor is now shown to be in close agreement with the experimental Gurley permeability trends. However, the experimental Gurley permeability results are shown to be around two orders of magnitude higher than the permeability results from the isotropic and anisotropic Pore-Cor model.

Fig. 7.32 showed the permeabilities from the Kozeny and the Kozeny-Carman model to be around one order of magnitude higher than the experimental Gurley permeabilities, while the Aligned cylinders model showed permeabilities around the same order of magnitude as the Gurley permeabilities. However, all three models showed Speswhite-CL to have a higher calculated permeability than Amazon-CL, in contrast to the experimental Gurley permeability trend.

7.7.1. Ranking of modelled permeabilities to Experimental Gurley permeabilities

A ranking scheme was used for the Gurley permeabilities, and is shown in fig. 7.33, while the modelling trend error for each permeability model is shown in fig. 7.34.

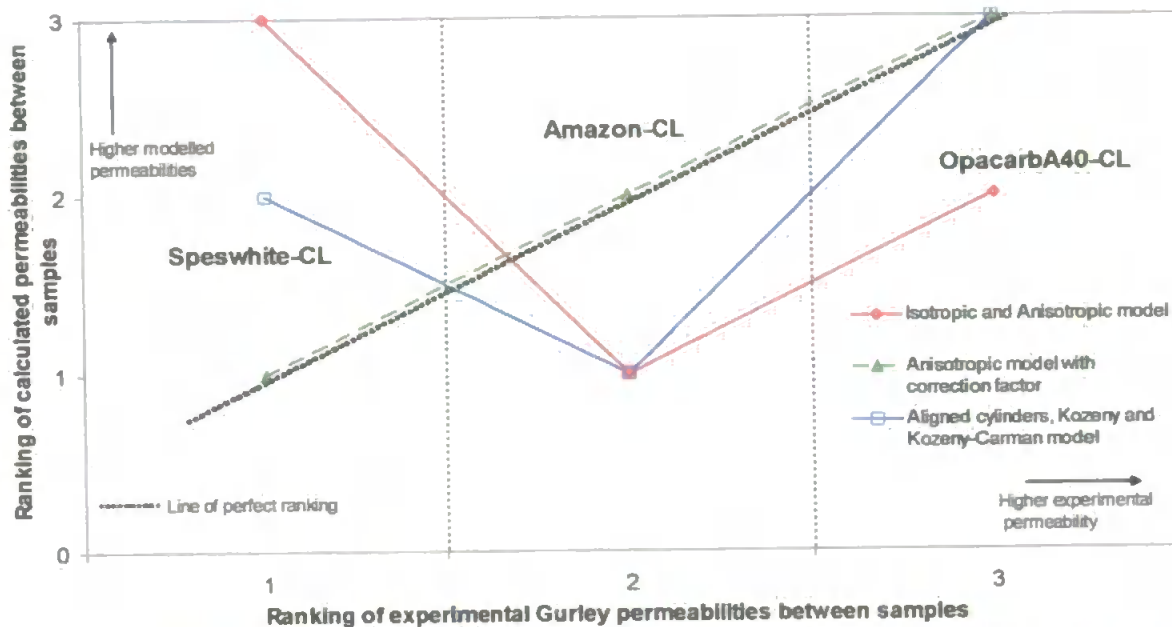


Fig. 7. 33. The ranking scheme between samples for the experimental Gurley permeabilities and the permeability models. The anisotropic Pore-Cor model with correction factor is shown to give a better qualitative prediction than any other model.

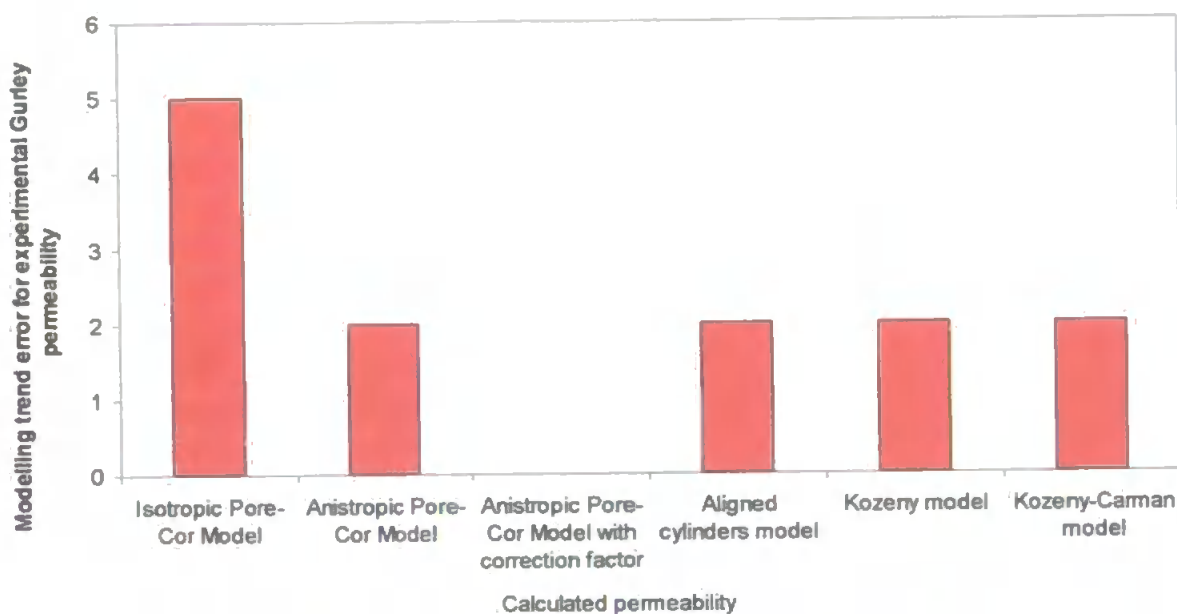


Fig. 7. 34. The modelling trend error for the experimental Gurley permeabilities. The anisotropic Pore-Cor model with correction factor has a zero modelling trend error – i.e. it is shown to give a perfect prediction.

The modelling trend errors for the experimental Gurley permeabilities showed the isotropic Pore-Cor model to have the largest modelling trend error of all the permeability models. The Kozeny, Kozeny-Carman and the Aligned cylinders model showed the same modelling trend error as the Anisotropic Pore-Cor model. However, once the correction factor was applied to the Anisotropic Pore-Cor

model, the modelling trend error was reduced to zero. This indicated a trend which exactly matched that of the experimental Gurley permeability results.

7.7.2. Comparison of experimental Gurley permeability with samples of similar surface throat number densities

As shown with the experimental ISD and DAT permeation trends, the Pore-Cor model gave much better correlation when comparing experimental Gurley permeabilities for samples of similar surface throat number densities. An example is made again between OpacarbA60-CL and OpacarbA40-CL, as the two samples showed similar number densities, Fig. 5.7 and Fig. 7.29. The calculated permeabilities from the anisotropic Pore-Cor model and the experimental Gurley permeabilities are shown for the two precipitated calcium carbonate (PCC) samples, in Fig. 7.35.

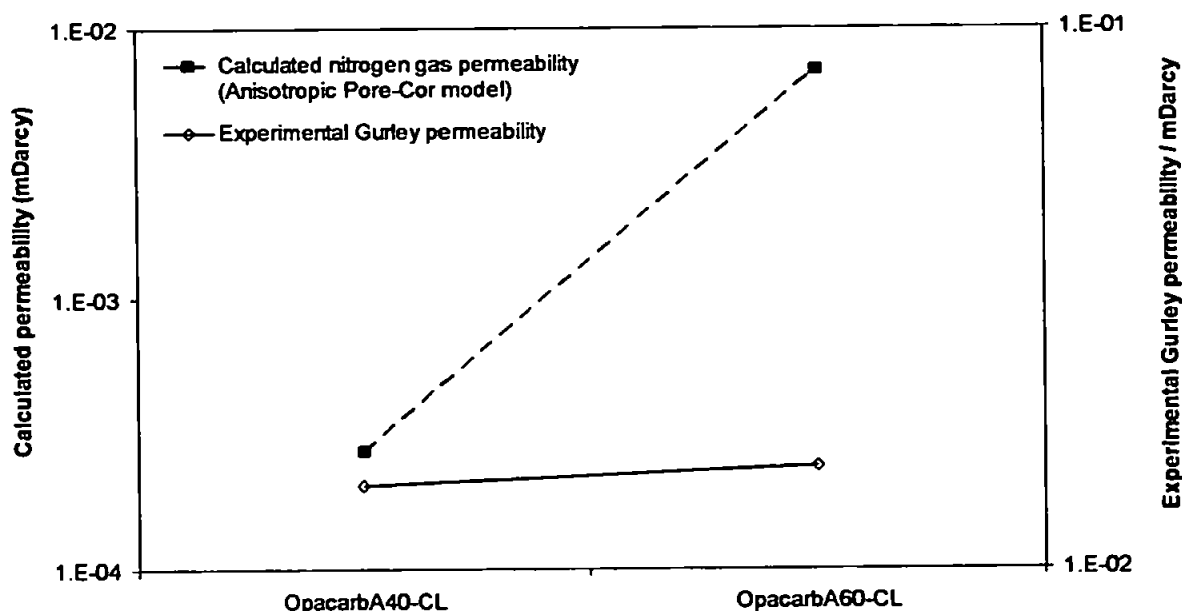


Fig. 7. 35. Comparison of the calculated nitrogen gas permeabilities from the Anisotropic Pore-Cor model and the experimental Gurley permeabilities for OpacarbA40-CL and OpacarbA60-CL, using an aspect factor of 1.5 and 2.0, respectively.

OpacarbA40-CL is shown to have both a greater experimental and calculated permeability than OpacarbA60-CL, as it exhibits a positive trend for both curves. However, the change in calculated permeability is shown to be an order of a magnitude greater than the change in Gurley permeability. Hence, for samples of similar number density, the Pore-Cor model was able to simulate correct permeability trends, but is shown to simulate differences in permeabilities between the samples of around an order of magnitude larger than reality.

7.8. Summary

- The lengths of the throats, h , had the least effect on the network flow capacity of a structure, while the diameters of the throats, d_{eff} , had the greatest effect. The *pore-throat size ratio* parameter had a much greater effect on the network flow capacity when using low and high aspect factors.
- The Pore-Cor model showed Albaglos-CL to contain a much higher throat skew (more smaller throat sizes relative to larger throat sizes) than OpacarbA40-CL, but also contained a much higher connectivity. As Albaglos-CL is calculated as having a higher calculated permeability than OpacarbA40-CL (Fig. 7.13), the connectivity of the void structure must play a greater role than throat skew in determining network permeability.
- A change in aspect factor, from an isotropic to a rod-like pore structure, is shown to generally have very little to no significant effect on permeability. This is confirmed with OpacarbA40-CL, as the mean calculated permeability, at its estimated and isotropic aspect factor, showed no significant difference.

- A change in aspect factor, from an isotropic to a slit-like pore structure, is shown to generally have an increasing effect on permeability. However, this was only observed within the clay samples when a lower aspect factor was used ($\alpha=0.1$), as the permeability is shown to increase sharply.
- The calculated liquid permeabilities are around one order of magnitude lower than the permeabilities for both methane and nitrogen gas. The gas permeabilities were slightly lower for an anisotropic than an isotropic structure, as the slip flow correction had less of an effect for slit-like or rod-like pore structures.
- The permeabilities from the Kozeny and Aligned cylinders models are two to three orders of magnitude higher than the permeabilities from the Pore-Cor models. The Kozeny-Carman model is shown to have slightly lower permeabilities than the Kozeny model, while the Aligned cylinders model was shown to have permeabilities of approximately one order of magnitude lower than the Kozeny models.
- Overall, the aligned cylinders and the Kozeny models have been shown to be generally better in resembling the experimental trends than either the Isotropic or Anisotropic Pore-Cor model. However, once the correction factor, f , was applied to the anisotropic Pore-Cor model it has been shown to predict permeabilities more accurate than those predicted by the Kozeny and aligned cylinders models.

- The application of the correction factor, f , to the Pore-Cor model is only necessary when the samples have number densities that are significantly different from each other. Hence, for samples of similar number density the Pore-Cor model was able to simulate correct permeability trends, but was shown to simulate differences in permeabilities between samples much larger than reality (experimental Gurley permeability results).

8. COMPUTER MODELLING OF THE WETTING OF COATING STRUCTURES

8.1. Introduction

In the previous chapter, permeabilities predicted by the anisotropic Pore-Cor model were compared with DAT, ISD and Gurley experimental results. There was a good match between experiment and the model once a correction factor was added to allow for the number density of surface throats. However, the experiments involved progressive wetting from the surface, whereas the permeability calculation was based on the flow capacity of the entire modelled network. A major part of this work was therefore to modify a wetting algorithm developed by Schoelkopf and Ridgway (Ridgway *et al.*, 2001; Schoelkopf *et al.*, 2001; Schoelkopf *et al.*, 2000) so that it could model the wetting of anisotropic structures, so that both the model and the experiments involved progressive wetting from the surface.

8.2. Volume-averaged extent of wetting

In all the simulations the fluid was hexadecane, for reasons described in Section 4.3, with a contact angle of 40° representing an aged solid surface.

A number of trials were initially carried out without considering the correction factor f (see section 6.7). The wetting algorithm was first tested on Speswhite-CL (CMC and latex), and it generated a set of absorption curves for a range of aspect factors from 0.01 to 1.0, fig. 8.1.

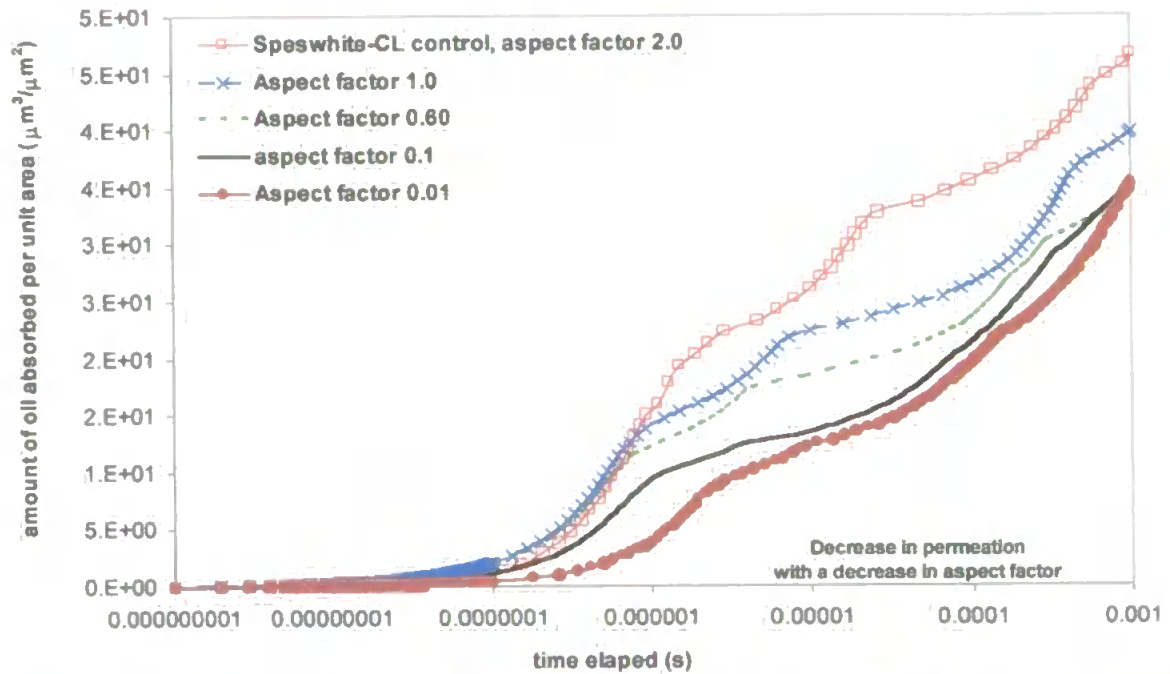


Fig. 8. 1. Simulated absorption of oil per unit area ($\mu\text{m}^3/\mu\text{m}^2$) for aspect factors from 0.01 to 2.0 for the Speswhite-CL sample, up to an elapsed wetting time of 1 millisecond.

It can be seen that in general, there was a decrease in the amount of oil absorbed per unit area with a decrease in aspect factor, i.e. as the simulated voids became less rod-like and more slit-like. This effect was especially noticeable for the lowest aspect factors at the shortest times. However, several of the curves cross over each other at various times. It can also be seen that the curves show a series of steps and points of inflexion, corresponding to the filling of successive layers. This is shown in more detail in fig. 8.2, where the points of inflexion for the absorption simulations with lower aspect factors occur earlier than those with the higher aspect factors, as shown.

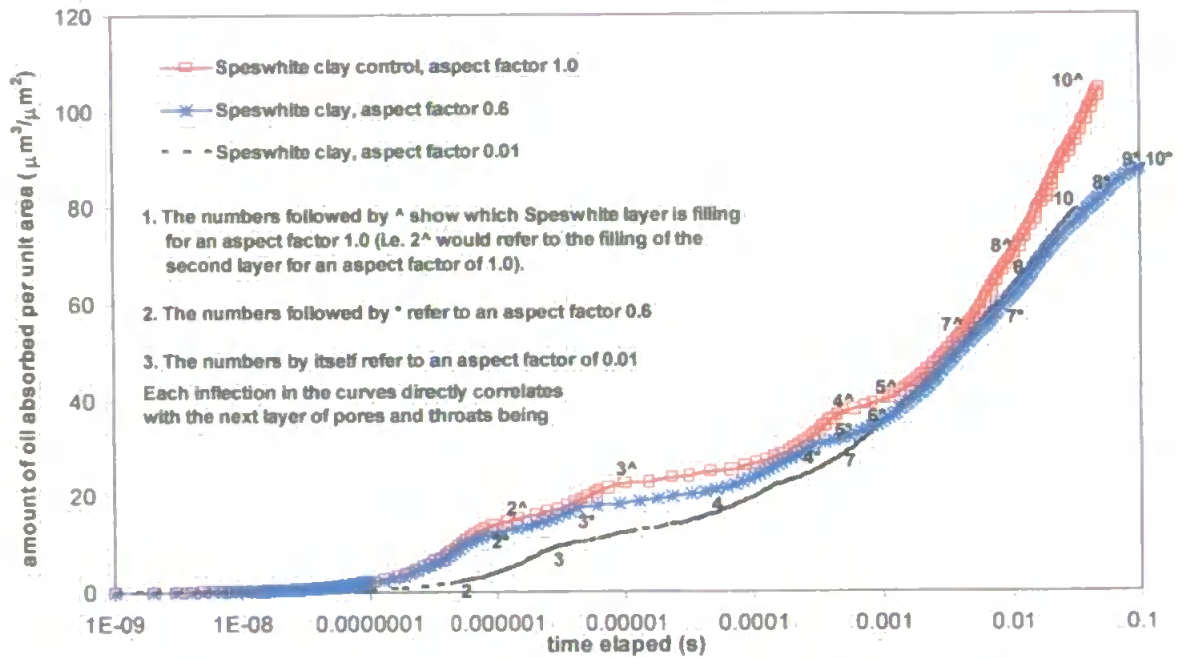


Fig. 8. 2. Simulated absorption of oil per unit area ($\mu\text{m}^3/\mu\text{m}^2$) for aspect factors of 0.01, 0.6 and 1.0 for the Speswhite-CL sample, up to an elapsed wetting time of 1 millisecond, showing steps due to filling of successive layers.

The wetting algorithm was then used to calculate the amount of oil absorption for each of the primary samples, using the estimated aspect factors. 'Control' simulations were also performed for comparison. These had the experimental percolation and porosity of the particular experimental sample, but were isotropic (aspect factor = 1.0). Fig. 8.3 confirms that the use of aspect factors of less than one for the clays caused the simulated absorption of oil to decrease relative to isotropic structures.

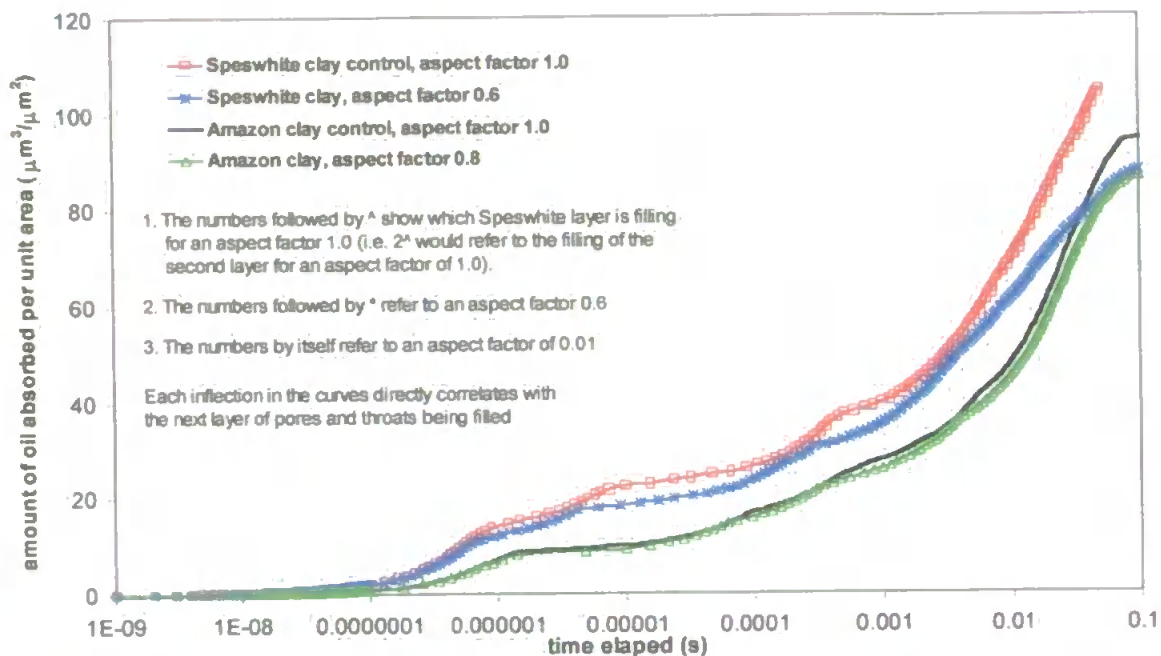


Fig. 8. 3. Simulated absorption of oil per unit area ($\mu\text{m}^3/\mu\text{m}^2$) for the clay coating samples, Speswhite-CL and Amazon-CL, at their estimated ($\alpha=0.6$ and 0.8 , respectively) and isotropic ($\alpha=1$) aspect factors, and up to an elapsed wetting time of 0.1 seconds.

It can also be seen that Speswhite-CL absorbs a higher amount of oil than Amazon-CL. However, as time proceeds, the absorption curves for Speswhite-CL and Amazon-CL start to converge upon each other. Fig. 8.4 shows the amount of oil absorbed into the precipitated calcium carbonate coatings, using both estimated and isotropic aspect factors (which are both the same for Albaglos-CL).

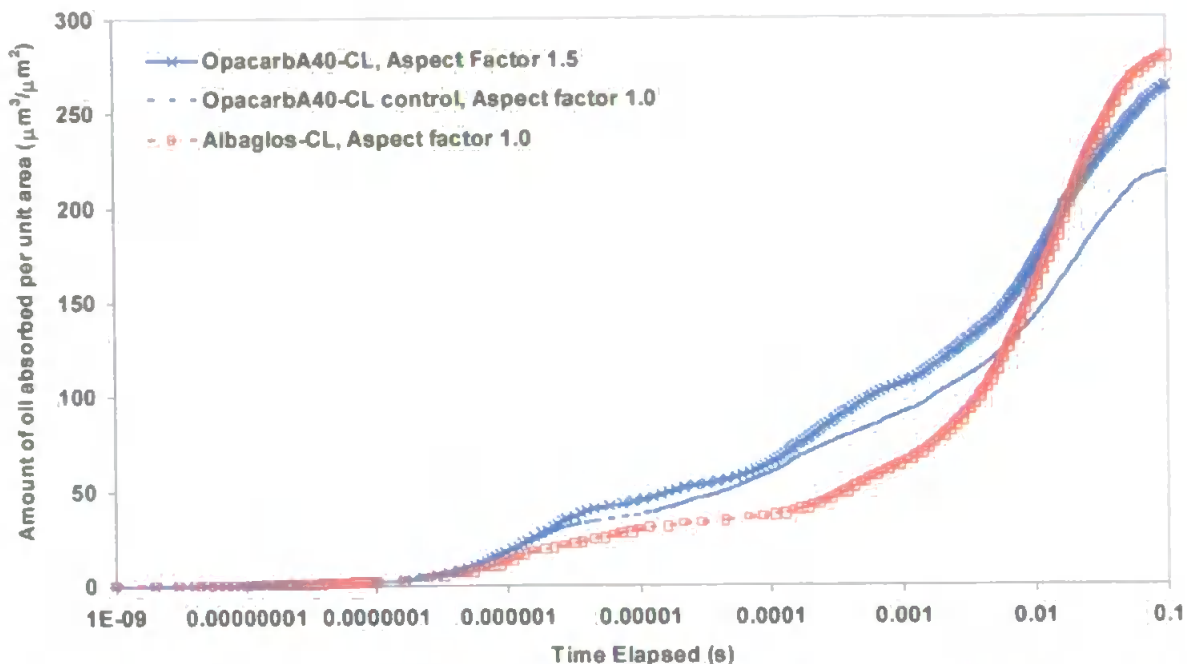


Fig. 8. 4. The amount of oil absorbed for the PCC samples, OpacarbA40-CL and Albaglos-CL, at their estimated ($\alpha=1.5$ and 1.0 , respectively) and isotropic ($\alpha=1$) aspect factors.

The simulation for Albaglos-CL is shown to be lower than the isotropic curve for OpacarbA40-CL until a time of approximately $0.007s$ is reached, in which the simulated absorption for OpacarbA40-CL control becomes lower than Albaglos-CL. However, comparing simulations with the appropriate estimated aspect factor, the simulation for Albaglos-CL is shown to be lower than OpacarbA40-CL for a longer time of approximately $0.02s$. A comparison of the vertical scales of Figs 9.3 and 9.4 shows that overall the simulated absorption for the clays is less than half of that predicted for the PCCs.

8.2.1. Visual examination of structure

All the wetting results so far, both experimental and simulated, have been volume or mass-averaged measures of the extent of permeation and the position of the wetting front. However, the steps in fig. 8.2, 8.3 and 8.4 show that there is also a fine structure within the simulated wetting which bears closer examination. To illustrate this fine structure, we took snapshots at 0.1 seconds of the primary

samples, with features coloured from dark blue (100 % wet), through light blue and purple to red (empty), with colours chosen according to a logarithmic scale of filling.

Fig. 8.5 showed the extent of filling by the model fluid (hexadecane) into Speswhite-CL. A detail of Fig. 8.5, shown in Fig. 8.6, reveals advance wetting into small features.

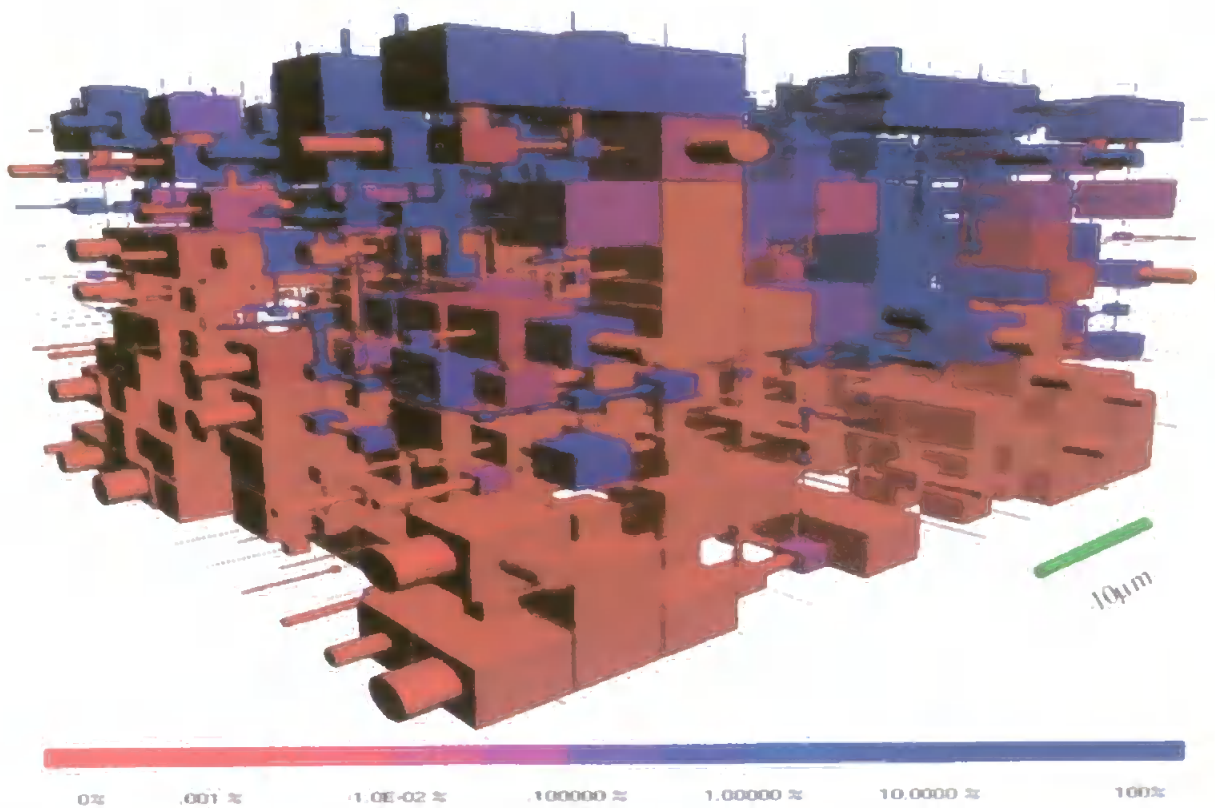


Fig. 8. 5. Simulation of the absorption of oil into Speswhite-CL at 0.1 seconds, and at an aspect factor=0.6. Red voids are empty of wetting fluid, dark blue voids are full, and intermediate colours are allocated on a logarithmic scale, as shown on the colour bar.

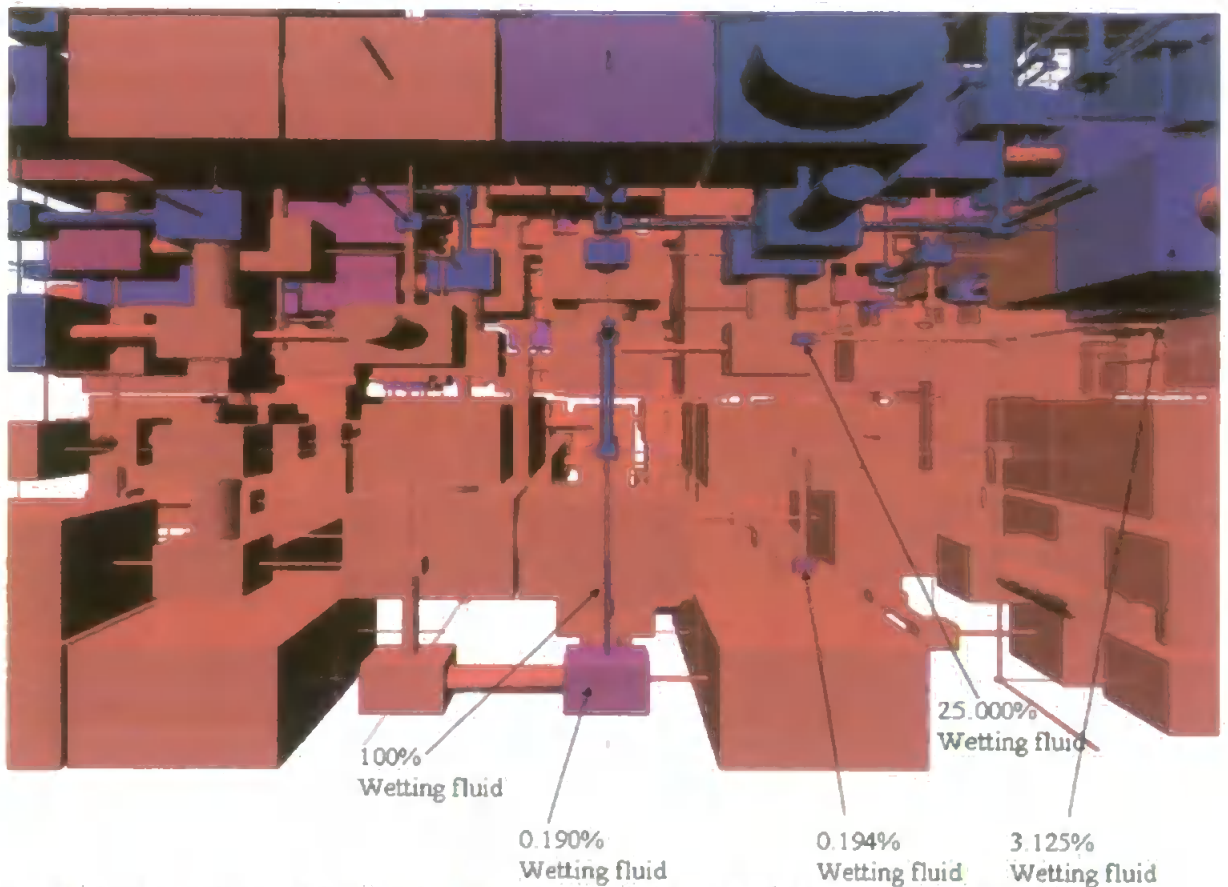


Fig. 8. 6. Detail of Fig. 8.5, showing permeation into Speswhite-CL at 0.1 seconds.

This would not be visible by any experimental technique which measured the volume averaged position of the wetting front. It represents a type of preferential flow which is normally overlooked because of the low volumes of the void features which are wetted.

Fig. 8.7 shows that there is a lack of advance wetting in Amazon-CL.

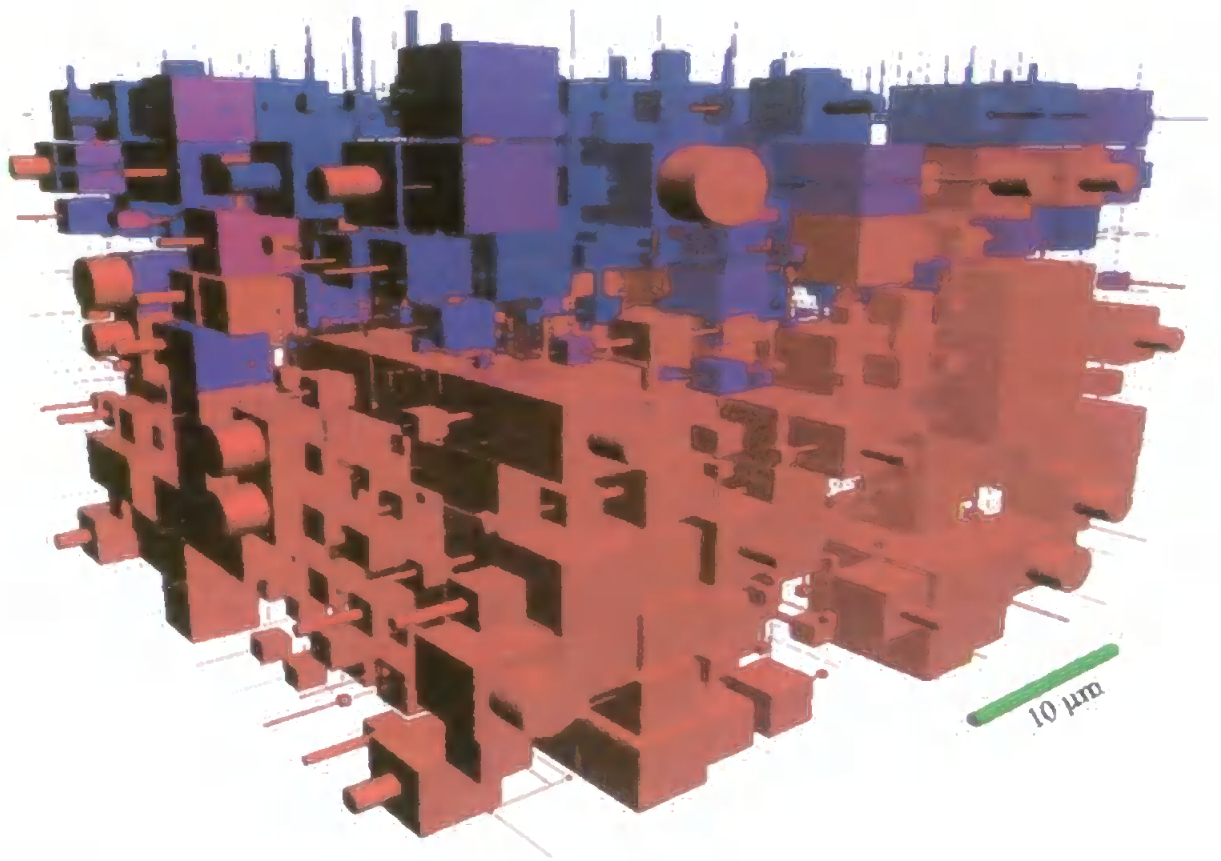


Fig. 8. 7. The permeation of Amazon-CL sample at 0.1 seconds.

Fig. 8.8 and 8.9 showed the extent of permeation for OpacarbA40-CL and Albaglos-CL at 0.1 seconds after initial contact of the fluid reservoir.

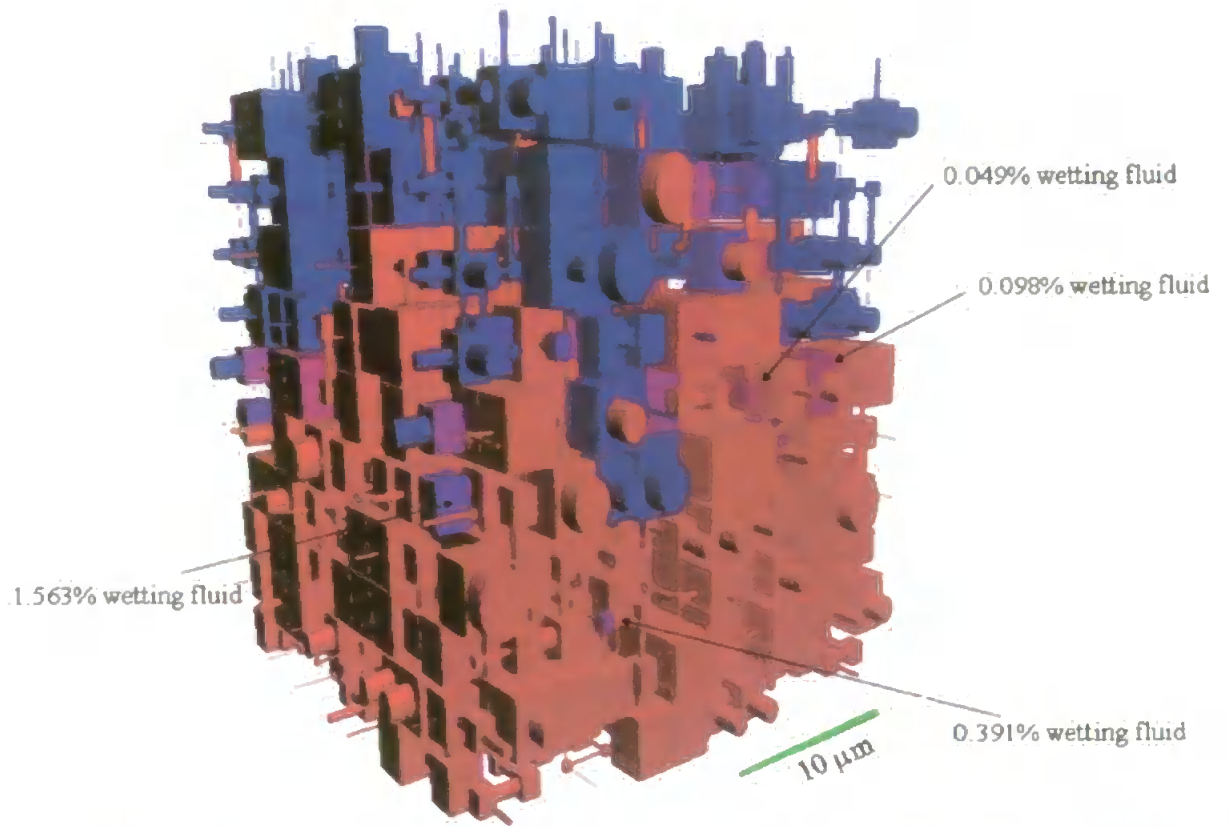


Fig. 8. 8. Simulation of the absorption of oil into OpacarbA40-CL at 0.1 seconds, and at an aspect factor=1.5. Colours as fig. 8.17.

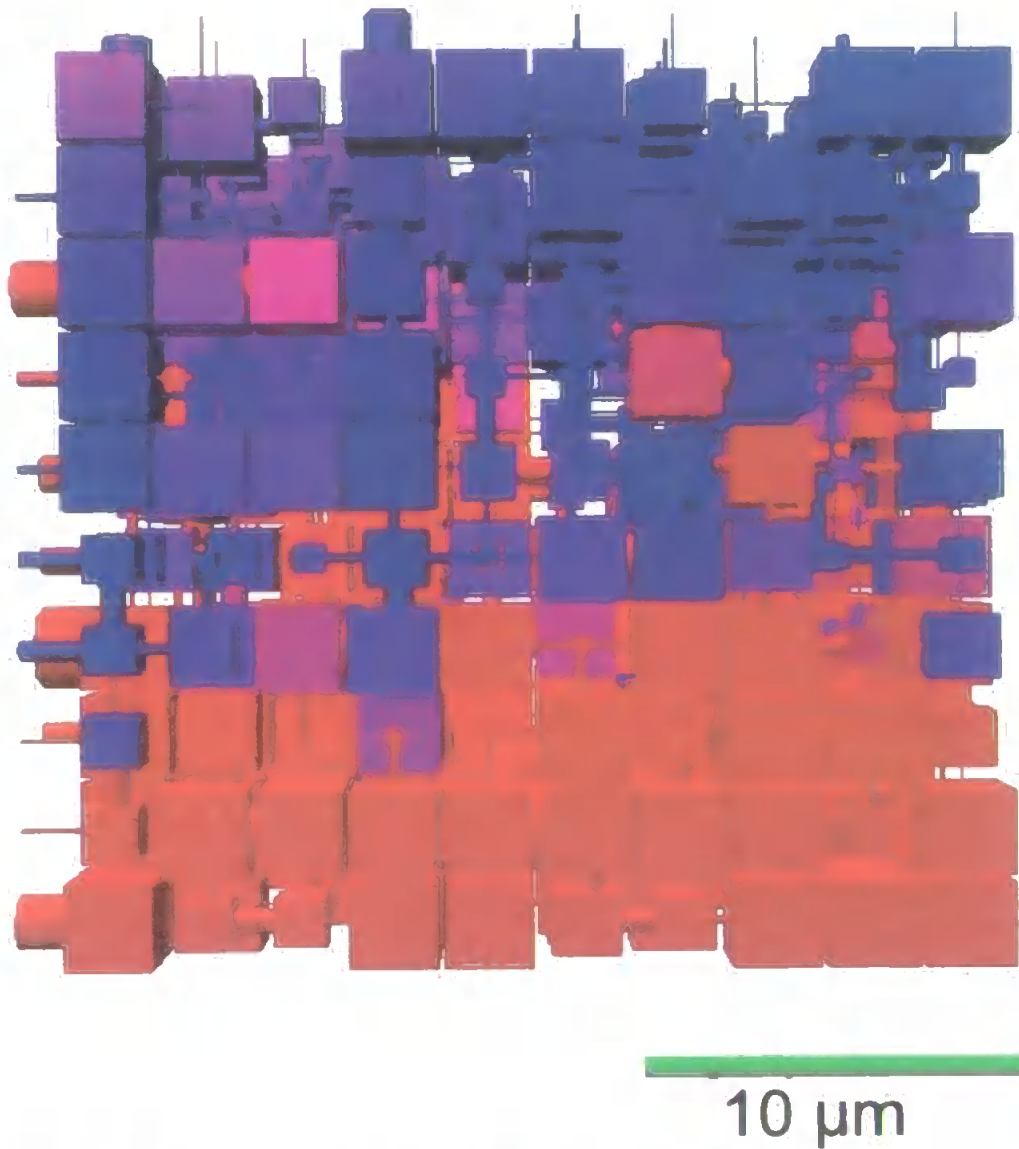


Fig. 8. 9. The permeation of Albaglos-CL sample at 0.1 seconds.

Fig. 8.10 shows a detail of Fig. 8.8 and reveals some advance wetting in OpacarbA40-CL, which is not evident in Albaglos-CL, Fig. 8.9.

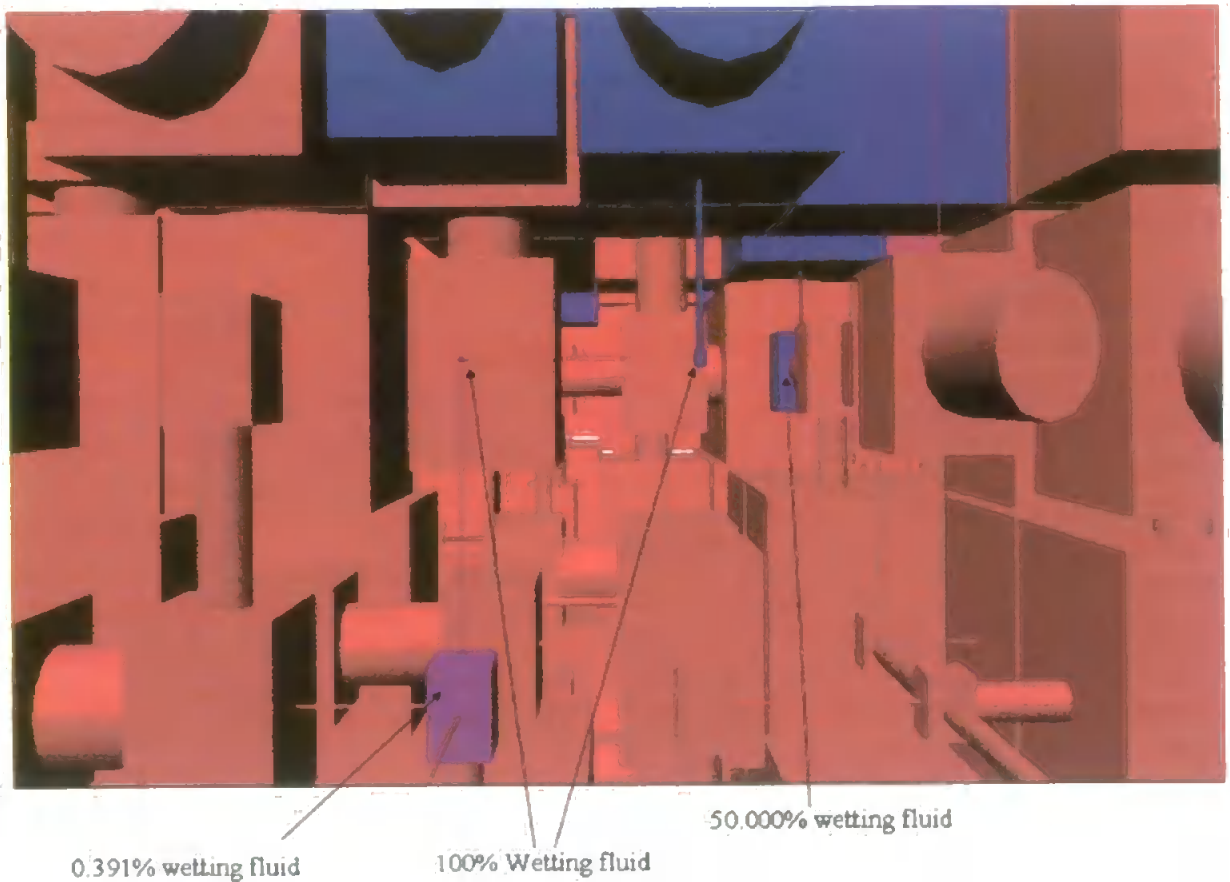


Fig. 8. 10. Detail of Fig. 8.8, showing permeation into OpacarbA40-CL at 0.1 seconds.

Speswhite-CL and OpacarbA40-CL are both shown to have a much broader void size distribution (Table 5.2) than Amazon-CL and Albaglos-CL, and coincided with advance wetting within their network structure. This is in agreement with Ridgway *et al.* (Ridgway *et al.*, 2002) where they observed a preferred pathway of permeation when a broad size distribution occurred within a network structure (refer to Section 2.9.2.2).

8.3. The effects of anisotropy on the wetting profile of a structure

The effect of anisotropy on the wetting profile for both the Lucas-Washburn and Bosanquet equation was examined by modelling Speswhite-CL and OpacarbA40-CL. The inclusion of an inertial term to the Bosanquet equation is the only difference between the Bosanquet and the Lucas-Washburn equation. These two samples were chosen as they exhibited two different types of void shapes; slit-

like and rod-like pores, respectively. Wetting simulations using both equations were tested on the two structures at their isotropic aspect factor and at their respective estimated aspect factors. The Wetting simulations were performed up to an elapsed time of 0.1s, using hexadecane as the wetting fluid.

8.3.1. Effects of anisotropy for a slit-like pore structure ($\alpha < 1$)

Fig. 8.11 shows the simulated wetting curves for Speswhite-CL at its estimated ($\alpha=0.6$) and isotropic ($\alpha=1.0$) aspect factor, and also shows when applying the Lucas-Washburn or Bosanquet equation.

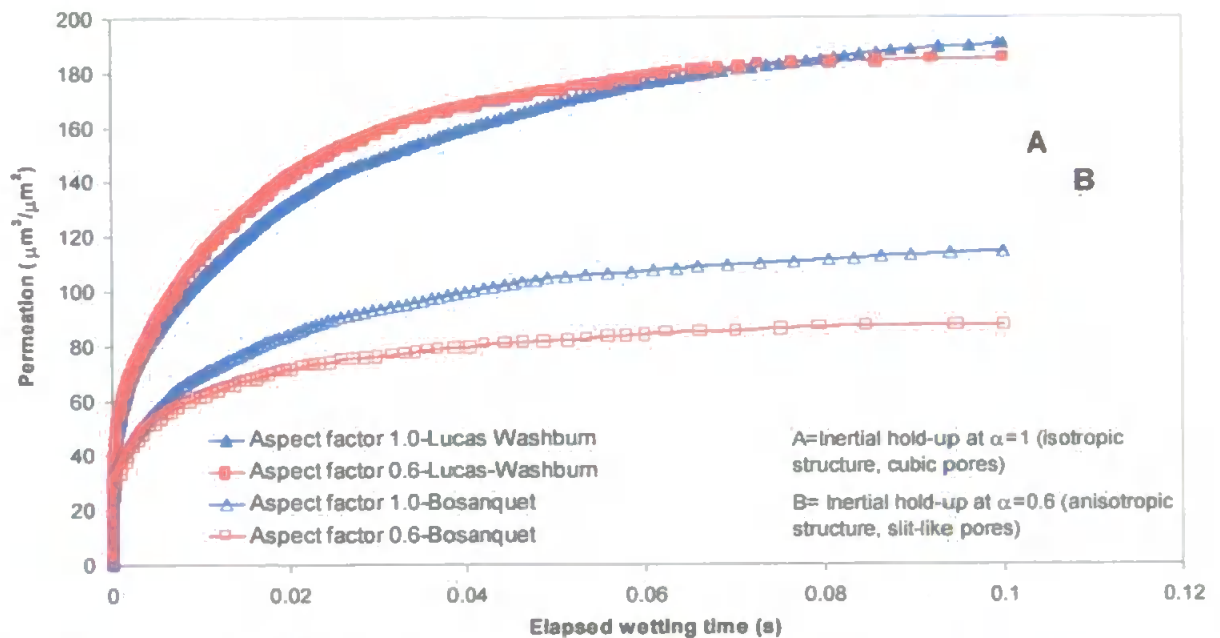


Fig. 8. 11. Simulated permeation curves for Speswhite-CL at its estimated ($\alpha=0.6$) and isotropic ($\alpha=1.0$) aspect factor, and also shows the results when applying the Lucas-Washburn or the Bosanquet equation.

The inertial effects cause the fluid to initially hold-up at the entrance of each throat, and as result, the amount of permeation is shown to be significantly greater when using the Lucas-Washburn in replace of the Bosanquet equation, as evident in fig. 8.11. The effect of anisotropy on wetting calculated from the Bosanquet equation has a much more significant effect than it does on wetting calculated from the

Lucas-Washburn equation. With the Bosanquet equation, a reduction in permeation of about 23% was observed when an estimated aspect factor was applied to the structure. However, with the Lucas Washburn equation only a reduction of about 3% was observed. Hence, a decrease in aspect factor caused a significant decrease in permeation when inertial effects are introduced in the wetting simulation.

The permeation curves have been converted to a Darcy length approximation, Fig. 8.12. Since the same porosity was used for the simulated structures, the results for all four curves, showed the same trends as the permeation curves in Fig. 9.11.

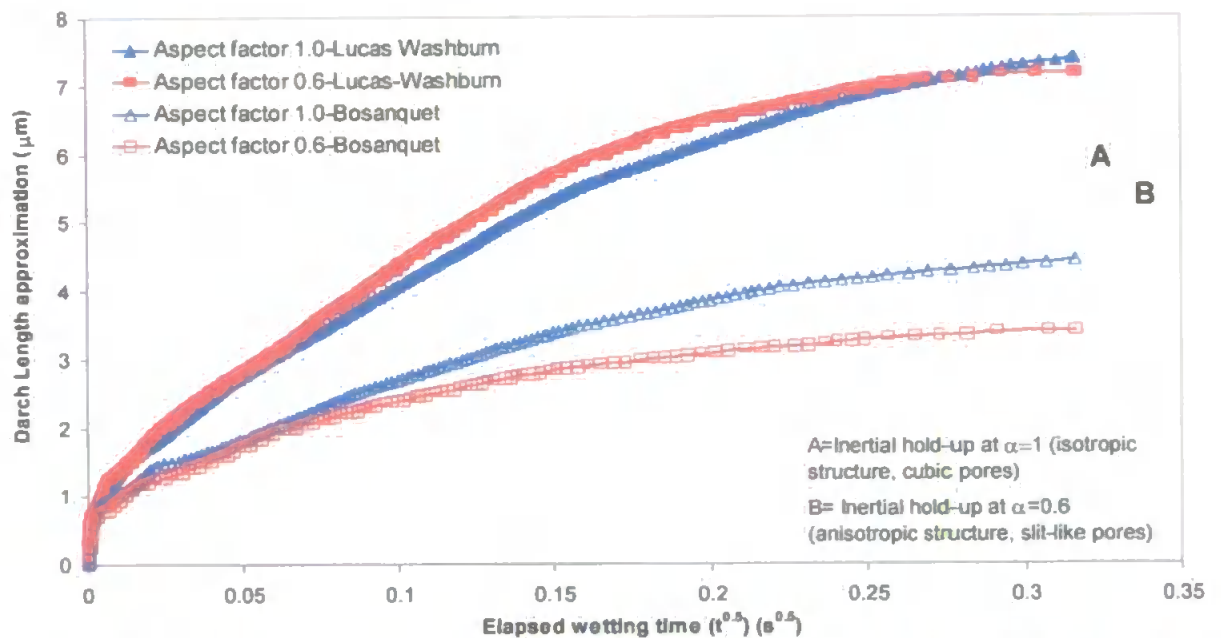


Fig. 8. 12. Simulated Darcy length curves for Speswhite-CL at its estimated ($\alpha=0.6$) and isotropic ($\alpha=1.0$) aspect factor, and also shows the results when applying the Lucas-Washburn or the Bosanquet equation.

The Darcy length curves were graphed with respect to the square root of time ($t^{0.5}$) due to the Bosanquet equation having a square root of time ($t^{0.5}$) dependency with respect to the distance travelled of the wetting front. As expected, the curves showed a linear trend at the beginning of permeation, but as the wetting fluid permeates through the network, the curves are shown to deviate, and become

hindered due to the cumulative wetting effects of the many pores and throats in the network structure.

When inertial effects were ignored the simulated wetting fronts travelled a Darcy length twice the distance, and the use of an estimated aspect factor in replace of an isotropic aspect factor showed very little difference in the Darcy length curves. However, when inertial effects were included into the simulation the use of an estimated aspect factor caused the wetting front to travel a much shorter Darcy distance.

8.3.1.1. The effects of Inertia ignored in the wetting simulation (Lucas-Washburn equation)

Visual inspection of the extent of the wetting front when inertial effects are ignored is shown in fig. 8.13 and 8.14, at its isotropic and its estimated aspect factor, respectively. A snapshot of the wetting of the simulated structures was taken at an elapsed time of 0.1s. Although the two structures have similar Darcy lengths, the use of an estimated aspect factor, in Fig. 8.14, caused greater preferential flow near the edges of the structure than when compared to the isotropic structure, fig. 8.13. However, within the preferential flow regions of Fig. 8.14 and 8.15, the advance wetting in the small features is less noticeable, as the filling of other features has kept pace.

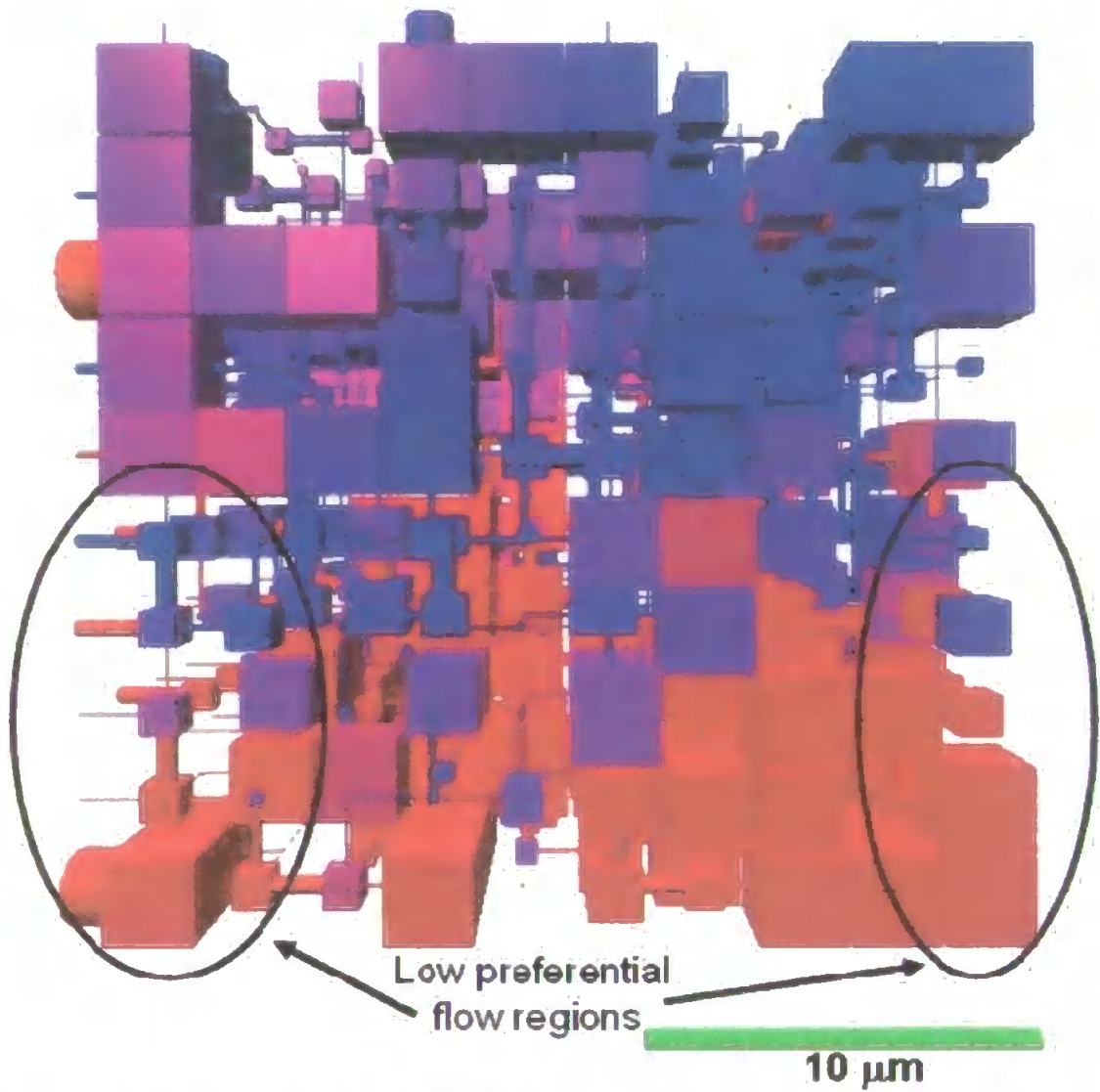


Fig. 8. 13. Simulated absorption of oil into Speswhite-CL control (isotropic aspect factor) at 0.1 seconds, but ignoring inertial effects (Lucas-Washburn equation).

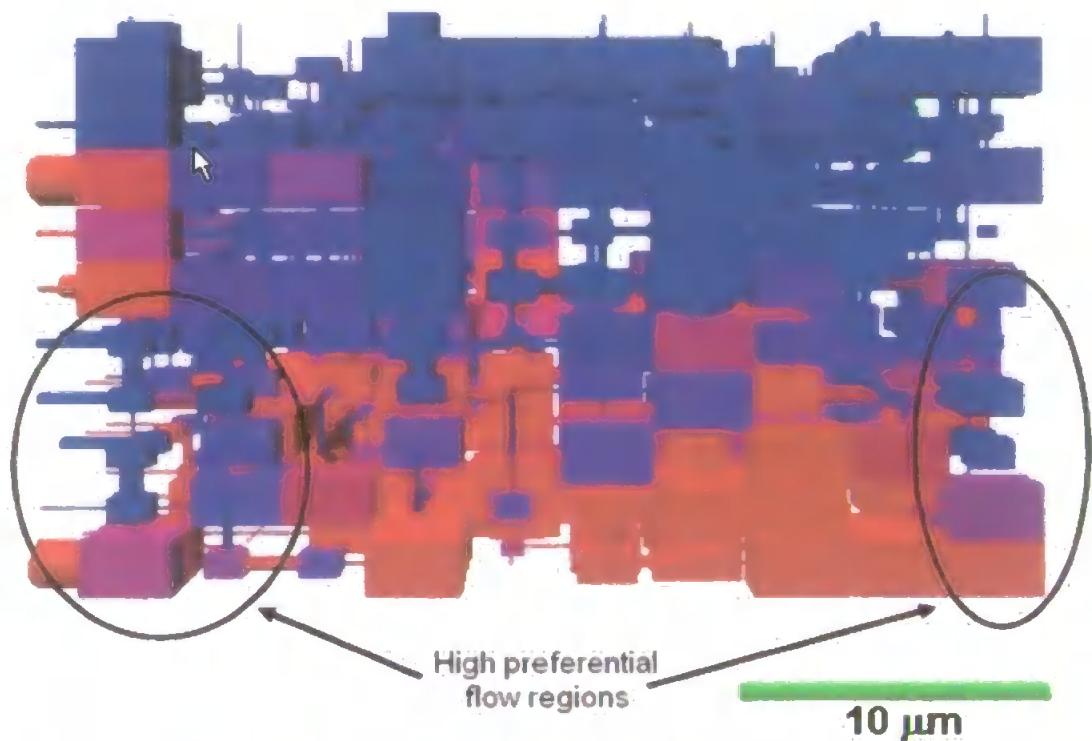


Fig. 8. 14. Simulated absorption of oil into Speswhite-CL at its estimated aspect factor ($\alpha=0.6$) at 0.1 seconds, but ignoring inertial effects (Lucas-Washburn equation).

8.3.1.2. *The Effects of inertia included in the wetting simulation (Bosanquet Equation)*

A visual comparison is shown of the extent of the wetting front when inertial effects are now included in the wetting calculation. A snapshot of the wetting of the simulated structures was taken at an elapsed time of 0.1s, at its isotropic and estimated aspect factor, fig. 8.15 and 8.16.



Fig. 8. 15. Simulated absorption of oil into Speswhite-CL control ($\alpha=1$) at 0.1 seconds, including inertial effects (Bosanquet equation).

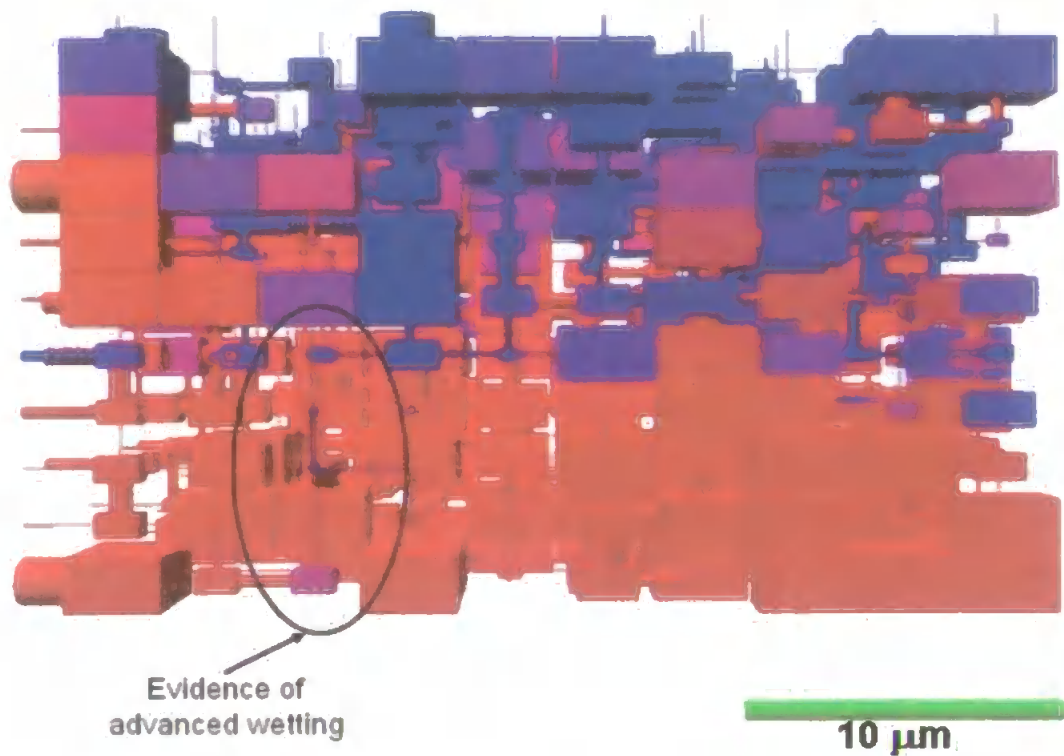


Fig. 8. 16. Simulated absorption of oil into Speswhite-CL at its estimated aspect factor ($\alpha=0.6$) at 0.1 seconds, including inertial effects (Bosanquet equation).

The amount of permeation and the overall extent of the wetting front are shown to be significantly reduced with the addition of inertial effects, as compared to fig. 8.13 and 8.14. However, the use of an estimated aspect factor in Fig. 8.16 caused advanced wetting in narrow features of the structure. No evidence of advanced wetting was seen in the same equivalent region for an isotropic aspect factor, fig. 8.15.

A detail of Fig. 8.14 and 8.16 are shown in Fig. 8.17 and 8.6, respectively.

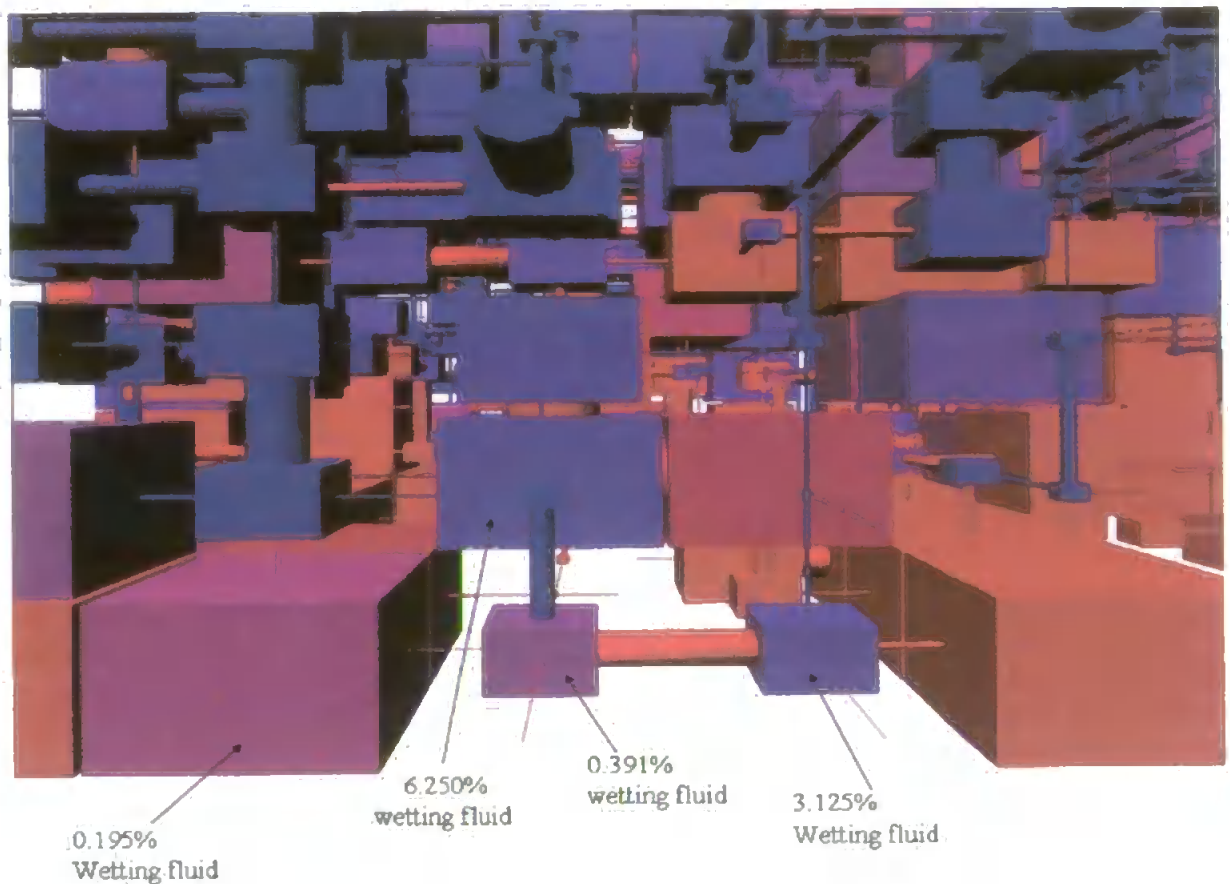


Fig. 8. 17. Detail of Fig. 8.14.

It can be seen that there is a substantial difference in the extent of the filling, and that the advance wetting in the small features is less noticeable when effects of inertia are not included in the simulation, Fig. 8.17. These findings are in agreement with those of Shoelkopf *et al.* (Schoelkopf *et al.*, 2000) in porous calcium carbonate blocks.

Another snapshot of the wetting of the simulated structures when inertial effects are included was taken at an elapsed time of 0.001s, fig. 8.18 and 8.19. Similar to the 0.1s wetting time, the effects of anisotropy on permeation play much more of an important role, as the extent and profile of the wetting front is very different when using an estimated or an isotropic aspect factor. The area in the circle of figure 8.18, displays a region of advanced wetting, in which wetting is observed into the narrow features of the anisotropic structure. The same equivalent region

is shown in the isotropic structure, and the equivalent pores are labelled with the same letters, Fig. 8.19.

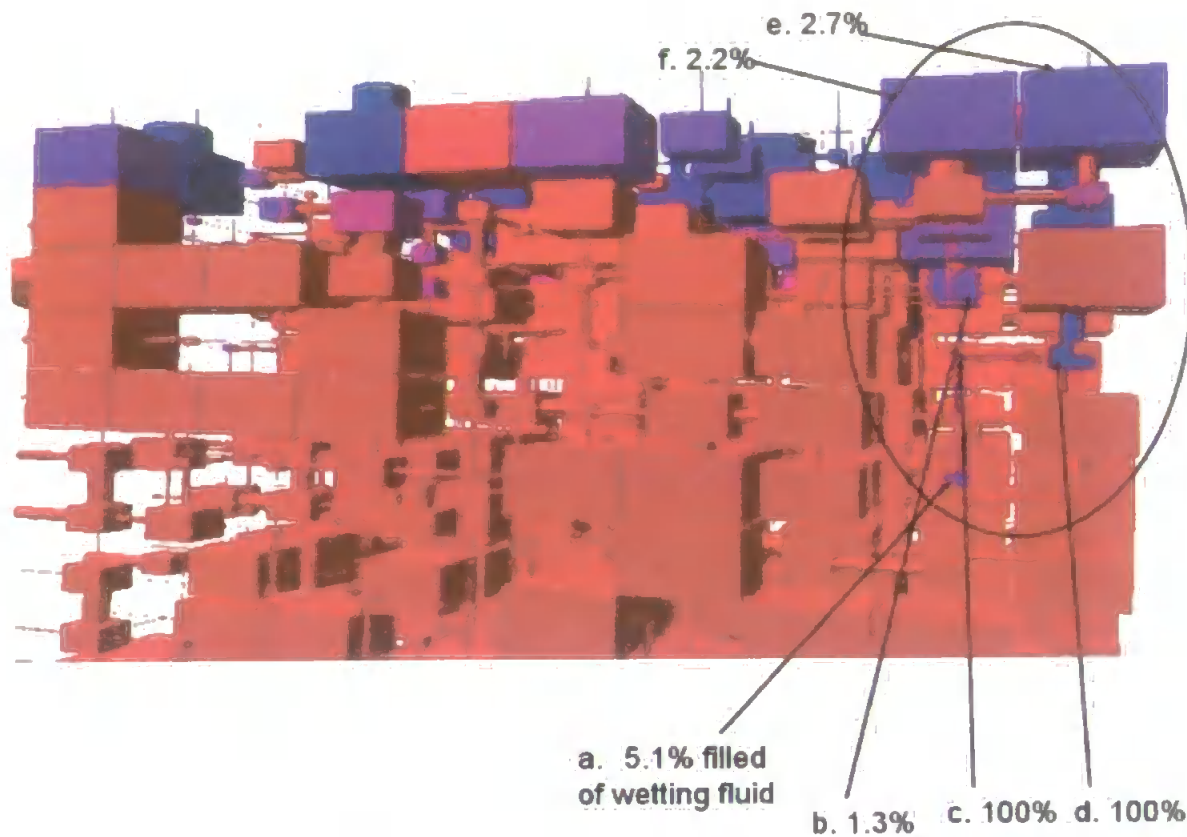


Fig. 8. 18. Simulated absorption of oil into Speswhite-CL at its estimated aspect factor ($\alpha=0.6$) at 1 millisecond, including inertial effects (Bosanquet equation).

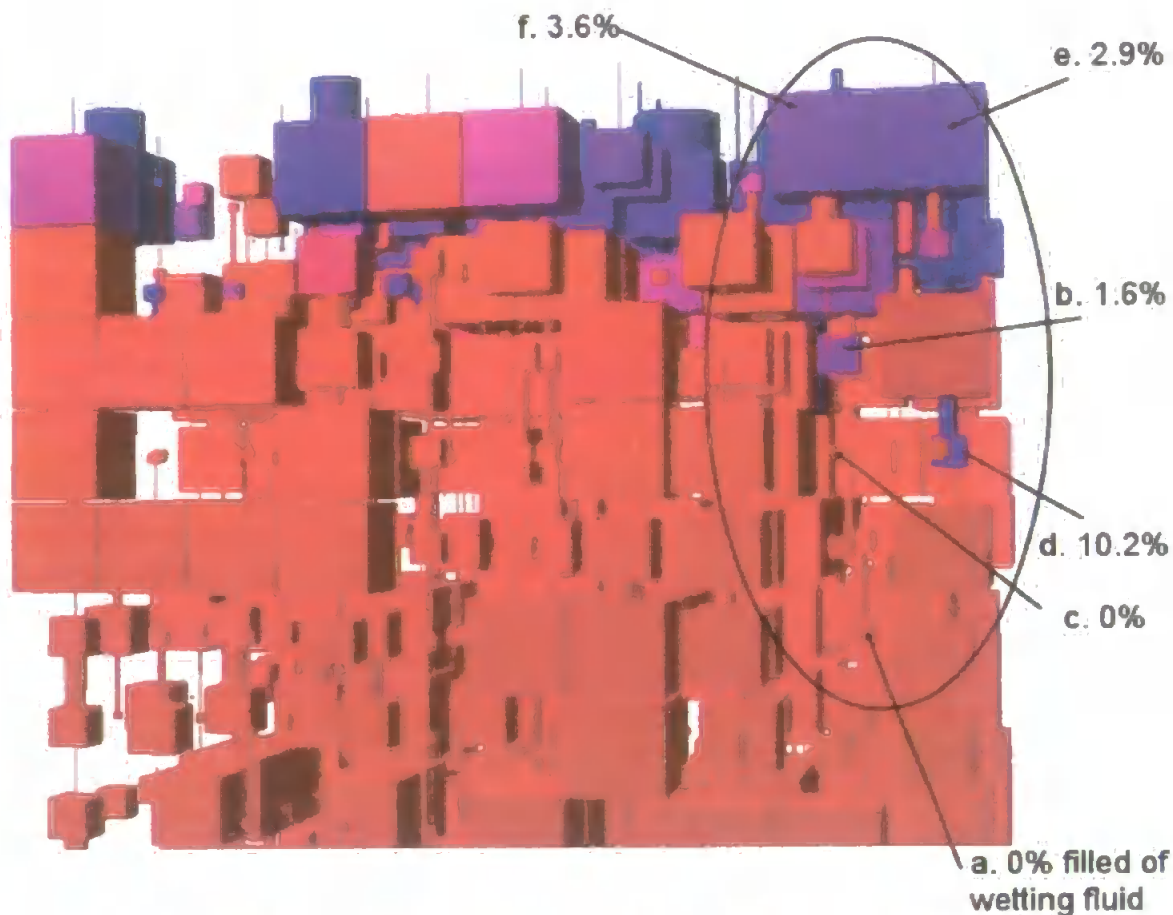


Fig. 8. 19. Simulated absorption of oil into Speswhite-CL at its isotropic aspect factor ($\alpha=1.0$) at 1 millisecond, including inertial effects (Bosanquet equation).

The equivalent region in the isotropic structure is shown to have significantly less advanced wetting, with most of the equivalent pores containing no fluid, Fig. 8.19. For example, in Fig. 8.18 the pores labelled letter a, c and d represents 5.1%, 100%, and 100% filled with wetting fluid. However, in Fig. 8.19 the same equivalent pores are shown to be filled with none to very little fluid; showing 0%, 0% and 10.2%, respectively.

Another example of localised preferential flow is seen near the back of the simulated anisotropic structure, Fig. 8.20. Due to the shadowing effect in the back of the structure a headlamp feature had to be imposed to enable sufficient lighting to view the features. This caused the colouring to be much brighter than in figures Fig. 8.18 and Fig. 8.19.

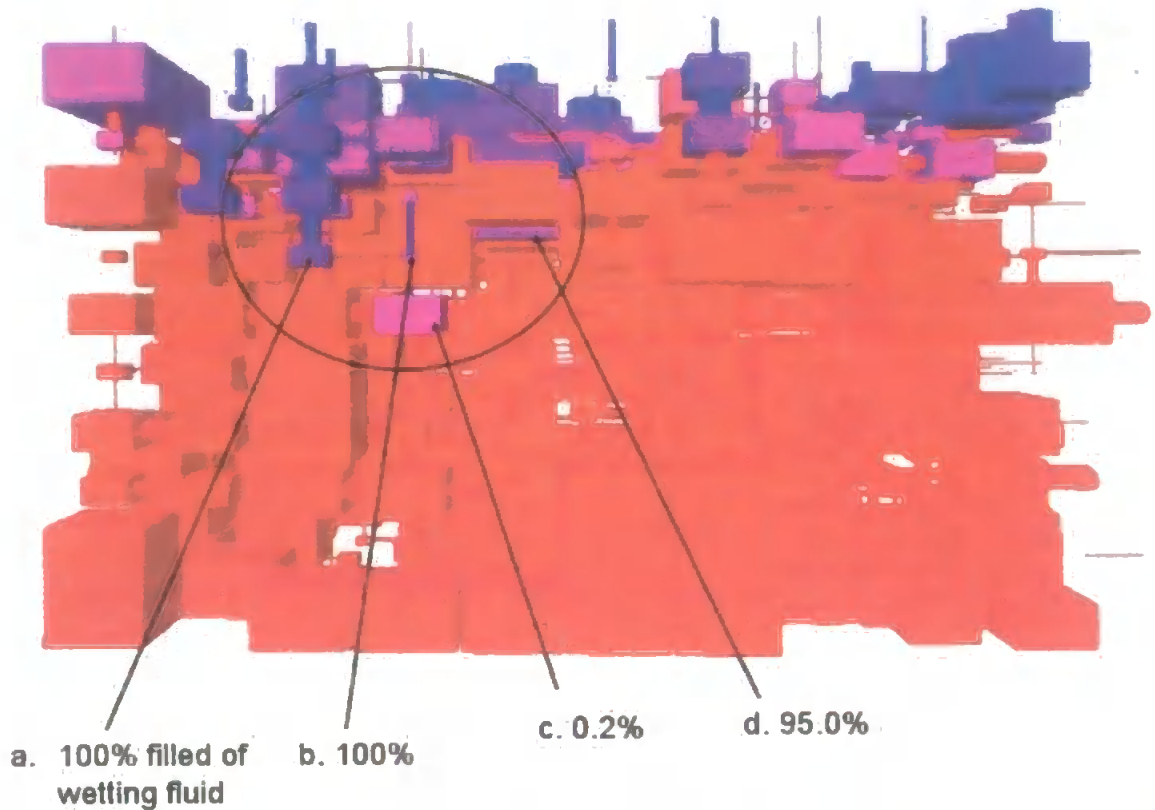


Fig. 8. 20. Simulated absorption of oil into Speswhite-CL at its estimated aspect factor ($\alpha=0.6$) at 1 millisecond, including inertial effects (Bosanquet equation). The back of the structure is shown in the figure, and it is brightened by a 'headlamp' for better visibility.

The equivalent region in the isotropic structure is, again, shown to have significantly less advanced wetting, with all of the equivalent labelled pores containing little to no fluid, Fig. 8.21.

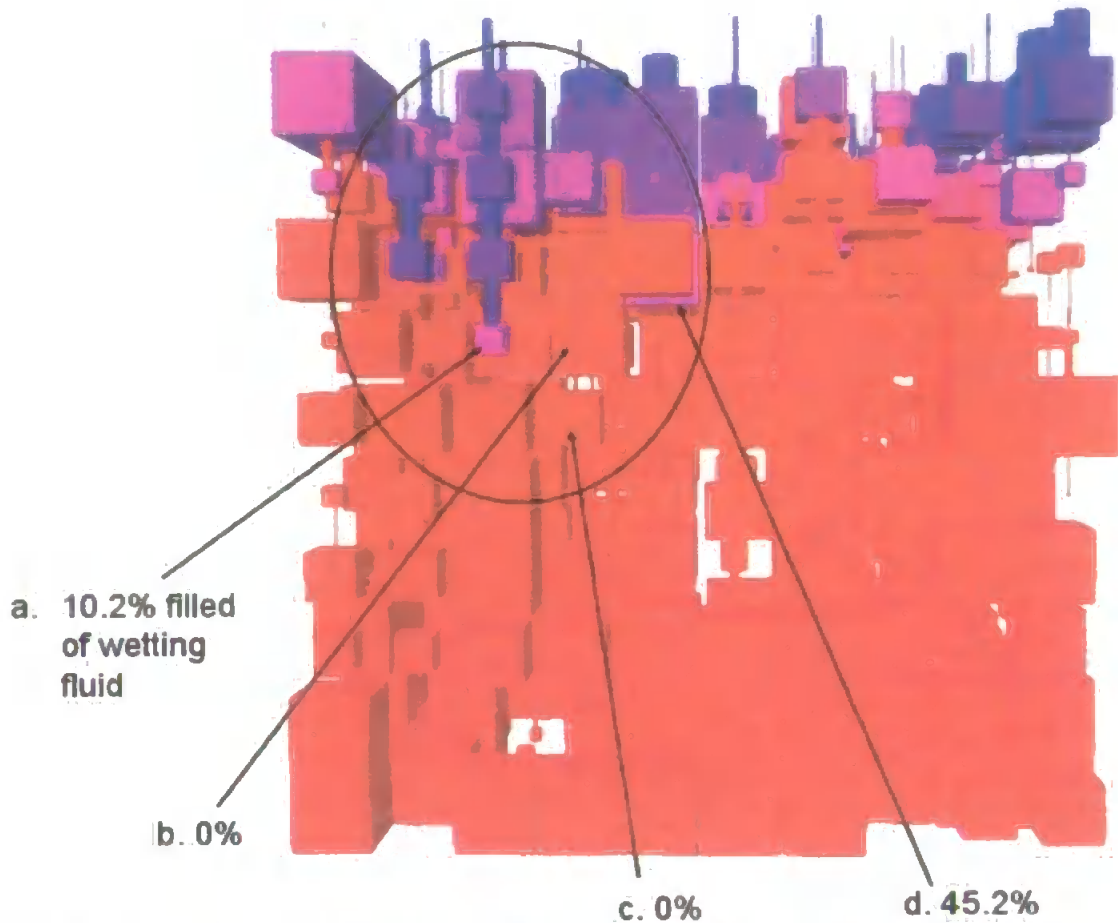


Fig. 8. 21. Simulated absorption of oil into Speswhite-CL at its estimated aspect factor ($\alpha=0.6$) at 1 millisecond, including inertial effects (Bosanquet equation). The back of the structure is shown in the figure, and it is brightened by a 'headlamp' for better visibility.

For example, in Fig. 8.20 the pores labelled letter a, b, c and d represents 100%, 100%, 0.2% and 95% filled with wetting fluid. However, Fig. 8.21 the same equivalent pores are shown to be filled with none to very little fluid; showing 10.2%, 0%, 0% and 45.2%, respectively.

8.3.2. Effects of anisotropy for rod-like pore structure ($\alpha > 1$)

Fig. 8.22 shows the simulated wetting curves for OpacarbA40-CL at its estimated ($\alpha=1.5$) and isotropic ($\alpha=1.0$) aspect factor, and also shows the results when applying the Lucas-Washburn or Bosanquet equation.

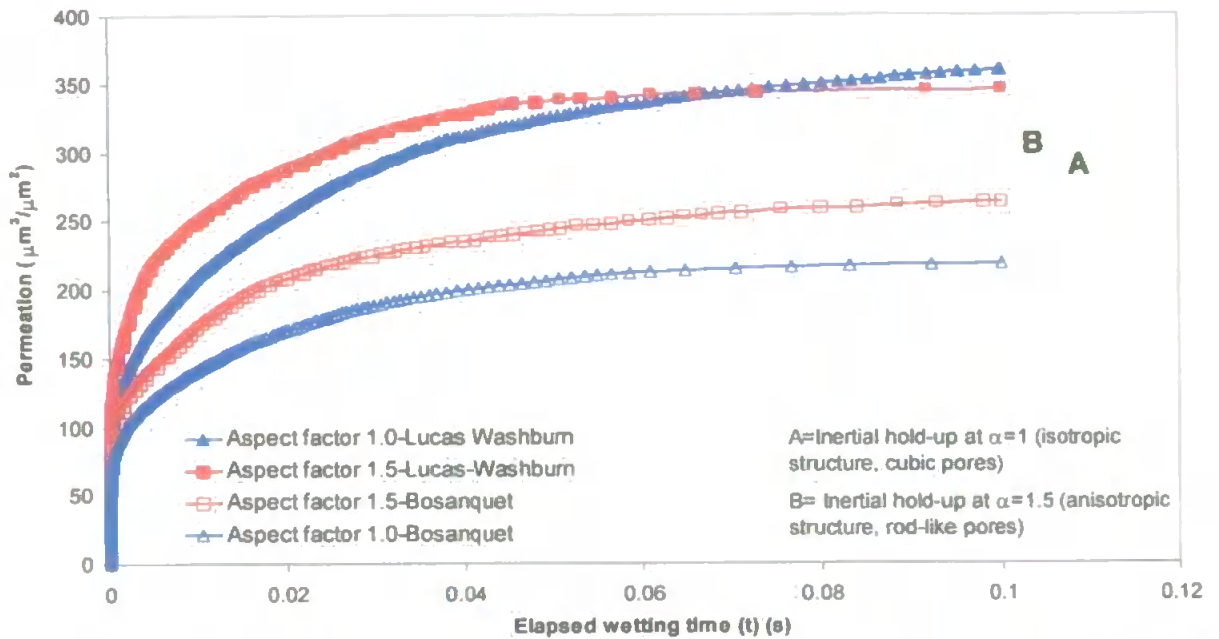


Fig. 8. 22. Simulated permeation curves for OpacarbA40-CL at its estimated ($\alpha=1.5$) and isotropic ($\alpha=1.0$) aspect factor, and also shows the results when applying the Lucas-Washburn or the Bosanquet equation.

In agreement with the results from Speswhite-CL, Fig. 8.11, the amount of permeation is shown to be significantly larger when applying the Lucas-Washburn over the Bosanquet equation. The effect of anisotropy on wetting is also shown to have a much more significant effect on permeation with the application of the Bosanquet than the Lucas-Washburn equation, and is also in agreement with Speswhite-CL. With the Bosanquet equation, an increase in permeation of about 21% was observed when an estimated aspect factor was applied to the structure, however, the Lucas Washburn equation caused only small reduction of about 4%. Hence an increase in aspect factor caused a significant increase in permeation when the effects of inertia are included in the wetting simulation.

The permeation curves have been converted to Darcy length approximation curves, Fig. 8.23. Since the same porosity was used for the simulated structures, the results for all four curves, showed the same trends as the permeation curves in Fig. 8.22.

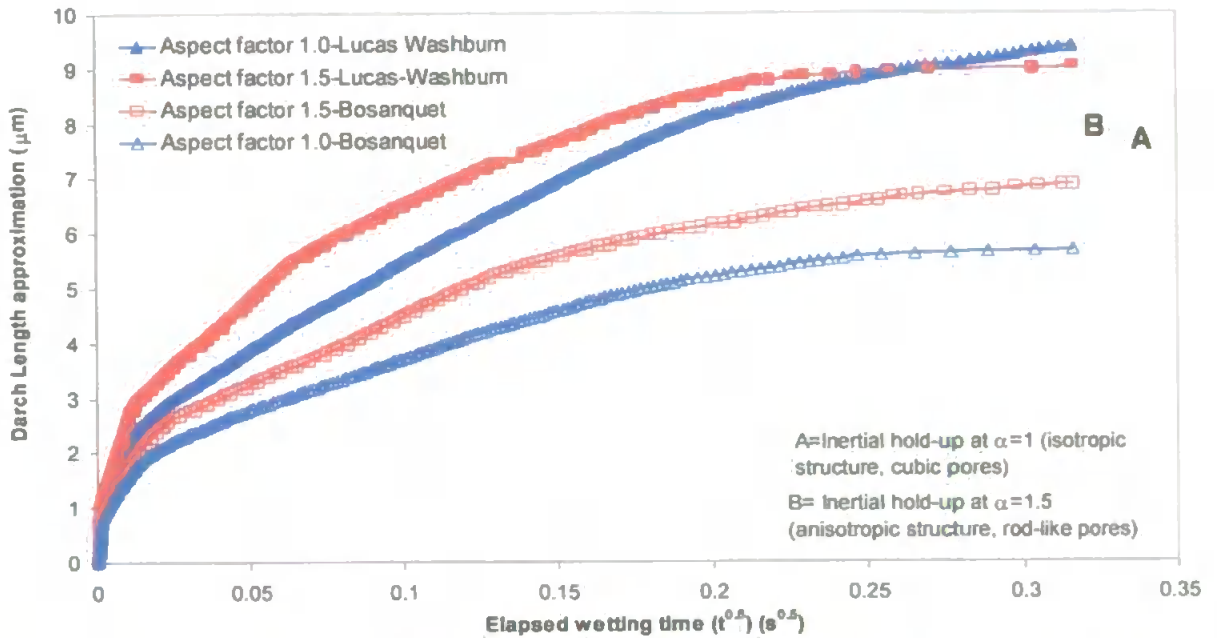


Fig. 8. 23. Simulated Darcy length curves for OpacarbA40-CL at its estimated ($\alpha=1.5$) and isotropic ($\alpha=1.0$) aspect factor, and also shows the results when applying the Lucas-Washburn or the Bosanquet equation.

Similar to Fig. 8.12, the Darcy length curves were graphed with respect to the square root of time ($t^{0.5}$). The simulated wetting fronts travelled a Darcy length almost twice the distance when inertial effects were ignored, and the use of an estimated aspect factor showed very little difference in the Darcy length curves. However, when inertial effects were included into the wetting simulation, the use of an estimated aspect factor caused the wetting front to travel a much longer Darcy distance. This is in contrast to the Fig. 8.12, as the application of the estimated aspect factor for Speswhite-CL caused the wetting front to travel a much smaller distance. Hence, an increase in aspect factor, from a slit-like to a rod-like porous structure, causes an increase in the volume-averaged distance travelled by a wetting front.

8.3.2.1. The effects of inertia ignored in the wetting simulations (Lucas-Washburn equation)

Visual inspection of the extent of the wetting front when the inertial term is ignored is shown in fig. 8.24 and 8.25, at its isotropic and its estimated aspect factor, respectively. A snapshot of the wetting of the simulated structures was taken at an elapsed time of 0.1s.

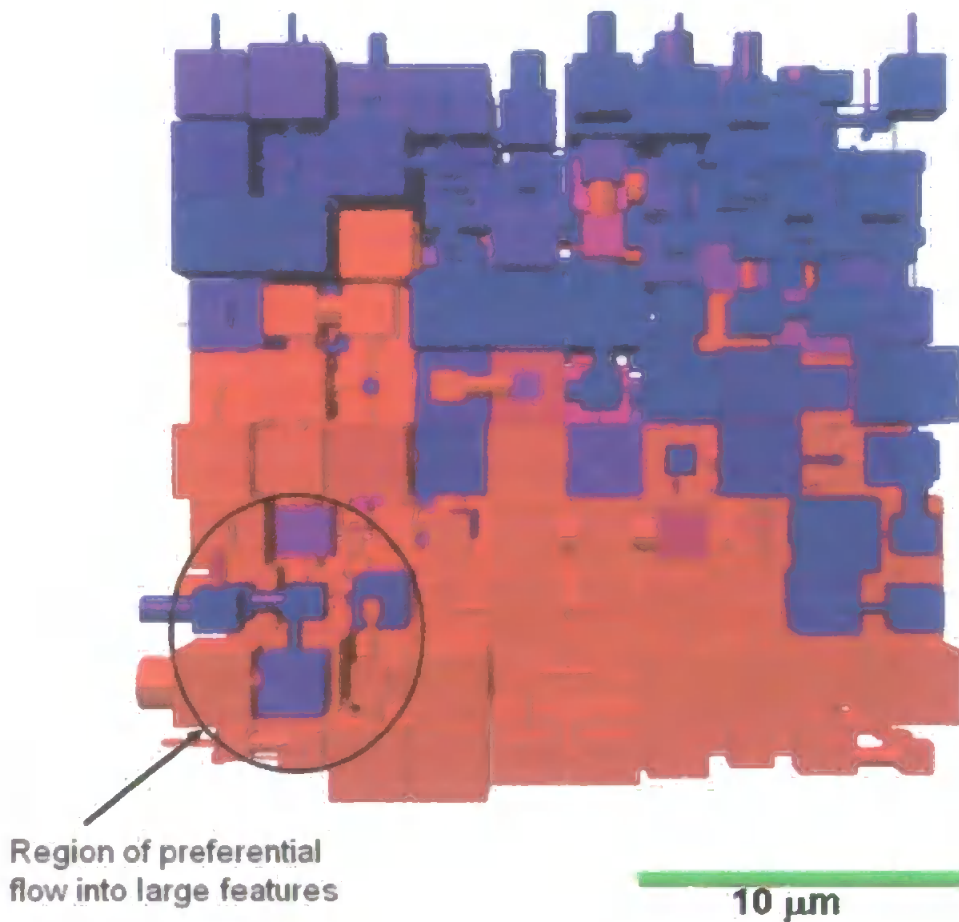


Fig. 8. 24. Simulated absorption of oil into OpacarbA40-CL using the isotropic aspect factor ($\alpha=1.0$) at 0.1 seconds, but ignoring inertial effects (Lucas-Washburn equation).



Fig. 8. 25. Simulated absorption of oil into OpacarbA40-CL using the estimated aspect factor ($\alpha=1.5$) at 0.1 seconds, but ignoring inertial effects (Lucas-Washburn equation).

Both figures showed areas of localised preferential flow into the large features of the structure. However, the anisotropic structure, Fig. 8.25, also showed some advanced wetting into the narrow features of the structure.

The transition line of where the wetting front ends and where the advanced wetting begins was taken to be the layer where the number of empty voids outweighs the number of voids containing fluid. This is best visualized by rendering the isotropic and anisotropic structure into a wire frame, Fig 8.26 and 8.27, respectively. The voids containing any amount of fluid are outlined with a blue colour, while voids containing no fluid are outlined with a red colour.

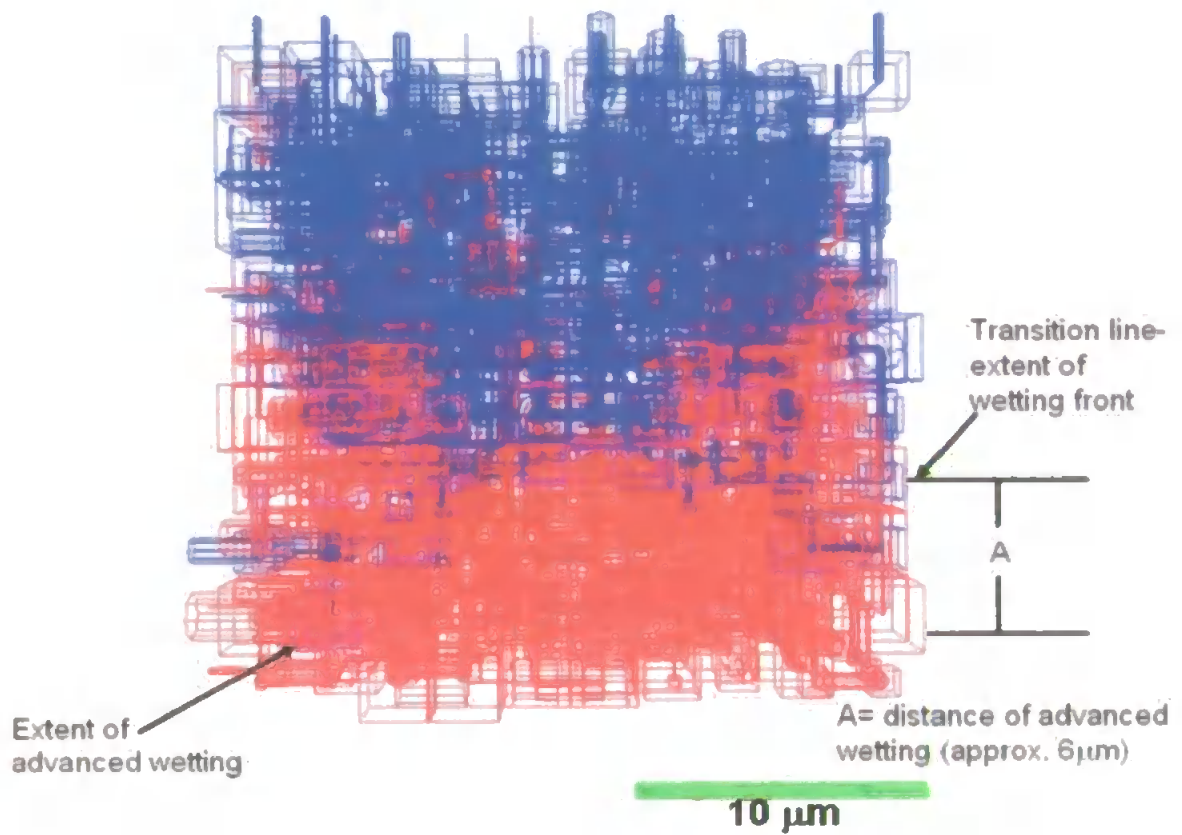


Fig. 8. 26. Simulated absorption of oil into OpacarbA40-CL applying the isotropic aspect factor ($\alpha=1.0$) at 0.1 seconds, but ignoring inertial effects (Lucas-Washburn equation). The structure is rendered into a wire frame in which the voids containing any amount of fluid are outlined with a blue colour, while voids containing no fluid are outlined with a red colour.

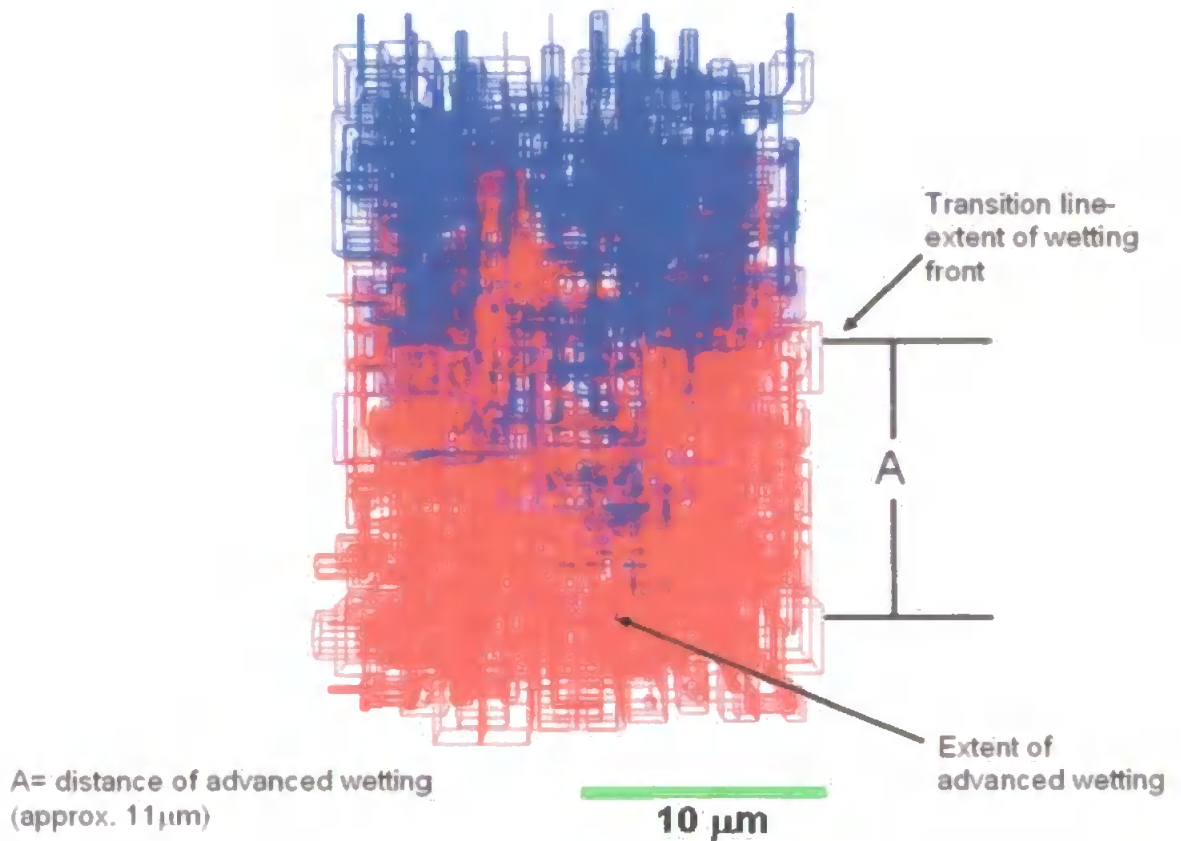


Fig. 8. 27. Simulated absorption of oil into OpacarbA40-CL applying the estimated aspect factor ($\alpha=1.5$) at 0.1 seconds, but ignoring inertial effects (Lucas-Washburn equation). The structure is rendered into a wire frame in which the voids containing any amount of fluid are outlined with a blue colour, while voids containing no fluid are outlined with a red colour.

The wetting profile in Fig. 8.26 showed that the vertical extent of the advanced wetting to be relatively close to the vertical extent of the wetting front, showing a distance for the advanced wetting of only approximately $6\mu\text{m}$. However when the estimated aspect factor is applied to the structure, Fig. 8.27 showed a much longer advanced wetting distance of approximately $11\mu\text{m}$. Hence, the application of the estimated aspect factor caused much further advanced wetting and showed preferential flow not only in the large features but also in the narrow features of the structure.

8.3.2.2. The effects of inertia included in the wetting simulations (Bosanquet equation)

A visual comparison is now shown of the extent of the wetting front when inertial effects are now included in the wetting calculation. A snapshot of the wetting of the simulated structures was taken at an elapsed time of 0.1s, at its isotropic and estimated aspect factor, Fig. 8.28 and 8.29.

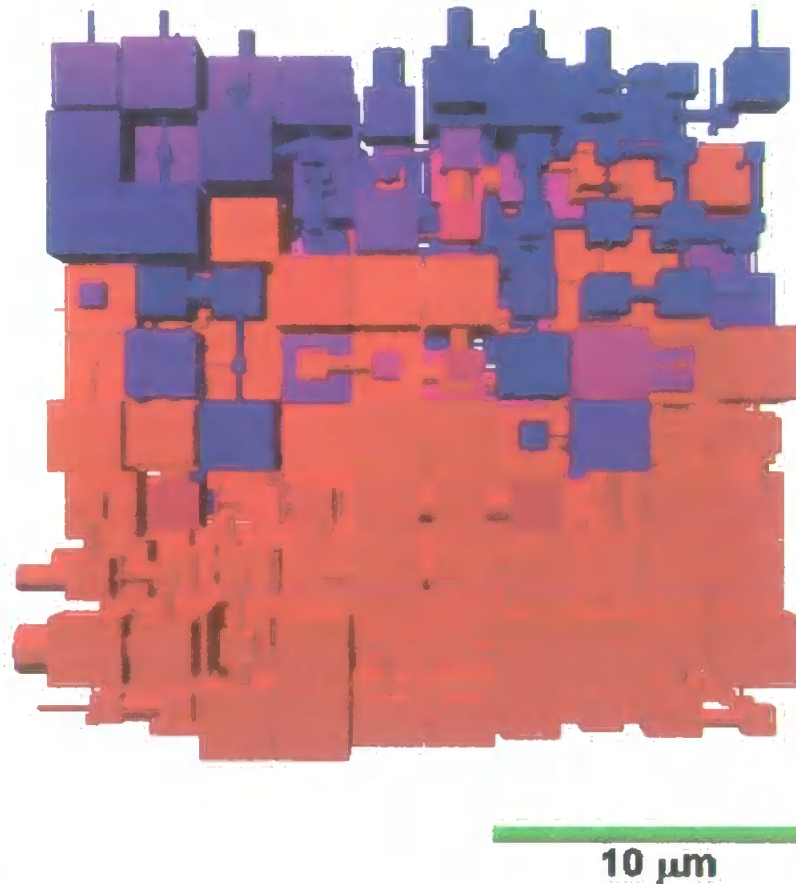
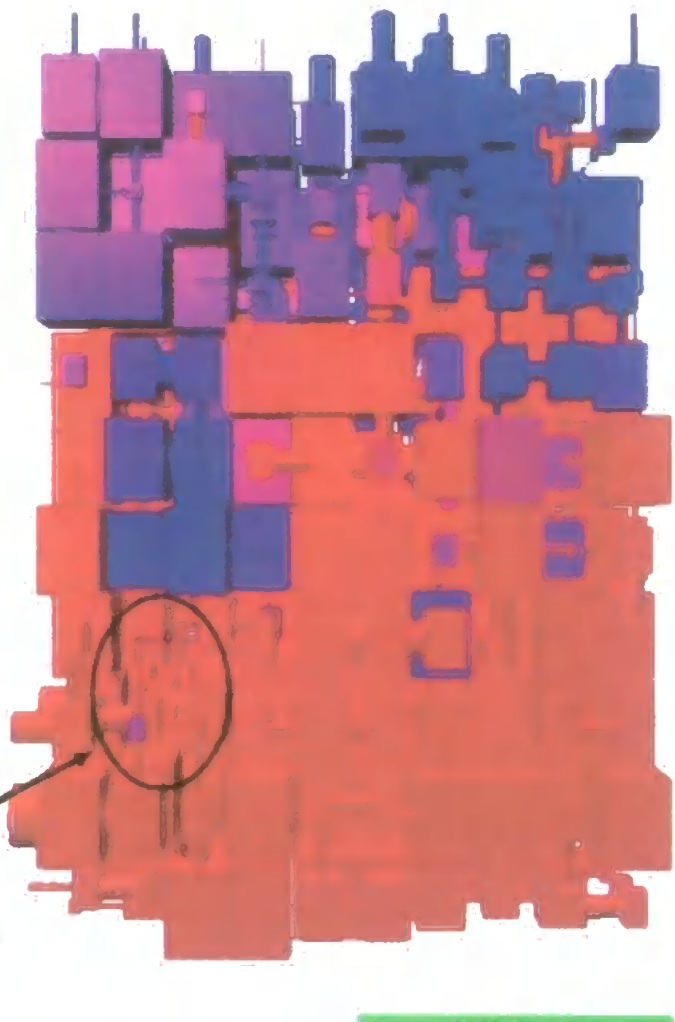


Fig. 8. 28. Simulated absorption of oil into OpacarbA40-CL showing an isotropic structure ($\alpha=1.0$) at 0.1 seconds, including inertial effects (Bosanquet equation).



Evidence of advanced wetting into narrow features

10 μm

Fig. 8. 29: Simulated absorption of oil into OpacarbA40-CL using the estimated aspect factor ($\alpha=1.5$) at 0.1 seconds, including inertial effects (Bosanquet equation).

As confirmed in Fig. 8.29 and Fig. 8.28, the amount of permeation and the overall extent of the wetting front are shown to be significantly reduced with the addition of inertial effects, as compared to fig. 8.24 and 8.25. However, the use of an estimated aspect factor in Fig. 8.29 caused advanced wetting in the narrow features of the simulated structure. No evidence of any significant advanced wetting was seen in the same equivalent region for an isotropic aspect factor, fig. 8.28.

8.4. Summary

- In general, there was a decrease in the amount of oil absorbed per unit area with a decrease in aspect factor, i.e. as the simulated voids became less rod-like and more slit-like. This effect was especially noticeable for the lowest aspect factors at the shortest times. The curves showed a series of steps and points of inflexion, corresponding to the filling of successive layers.
- The simulated absorption for the clay samples is less than half of that predicted for the PCC samples. Advance wetting into small features of Speswhite-CL and OpacarbA40-CL is revealed from visual inspection of the structure and represents preferential flow, although preferential flow is usually an experimentally observed quantity and therefore tends to overlook advance wetting into low-volume features.
- The amount of permeation is shown to be significantly larger without an inertial term being included in the wetting simulations.
- The Lucas-Washburn Equation is shown to be insensitive to anisotropy as very little difference is shown in permeation. However, by contrast, the inclusion of inertial effects, incorporated into the Bosanquet equation, caused a considerable difference in permeation.
- From visual inspection of the modelled structures, the effect of anisotropy revealed advance wetting in the narrow features of Speswhite-CL and OpacarbA40-CL. This represents a type of preferential flow which is normally overlooked because of the low volumes of the void features which

are wetted. The advance wetting in the narrow features was much more evident when the effects of inertia were included in the simulation.

- The advance wetting observed within these two samples coincided with their broad void size distribution, which was in agreement with observations made by Ridgway *et al.* (Ridgway *et al.*, 2002).

9. DISCUSSION OF SIMULATED WETTING AND EXPERIMENTAL TRENDS

9.1. Comparison of the permeation rates from the Ink Surface Absorption Method (ISAM) with the modelled wetting results

The Ink Surface Absorption Method (ISAM) was similar to the simulated wetting of the coating structures, as the top surface is saturated with fluid and absorbed downwards into the structure. The ISAM also showed absorption times similar to the simulated wetting results. For both the above reasons, the ISAM absorption rates (Table 5.3) were used in comparing the absorption trends from the simulated wetting results. Hence, as discussed in Section 5.2.3, the wetting rates of the primary samples were calculated at time t equals 0.002s by three versions of the Pore-Cor model; the Isotropic and Anisotropic model, and the Anisotropic model with the application of the correction factor. The volume-averaged Pore-Cor distance penetrated by the wetting fronts, expressed as Darcy lengths, Eq. 6.13 (at t equals 0.002s), were compared to the calculated distance by the much simpler Effective Hydraulic Radius (EHR) model, Eq. 3.10. The median void sizes of the samples, used as approximate values for R (Eq. 3.10), are shown in Table 5.1, while the wetting results from the different versions of the Pore-Cor model and the EHR model are shown below, in Table 9.1.

Pore-Cor Model	Wetting measurement	Speswhite-CL	Albaglos-CL	OpacarbA40-CL	Amazon-CL
Isotropic Pore-Cor model	absorption rate ($\mu\text{m}^3 \mu\text{m}^{-2} \text{s}^{-1}$)	22464.44	38893.50	51001.83	15997.21
	Darcy length (μm)	1.73	2.06	1.90	1.05
Anisotropic Pore-Cor model	Absorption rate ($\mu\text{m}^3 \mu\text{m}^{-2} \text{s}^{-1}$)	20720.91	38893.50	60879.92	15291.55
	Darcy length (μm)	1.61	2.06	3.12	0.99
Anisotropic Pore-Cor model with correction factor	Absorption rate ($\mu\text{m}^3 \mu\text{m}^{-2} \text{s}^{-1}$)	1732.81	4488.88	13574.69	5867.27
	Darcy length (μm)	0.13	0.24	0.70	0.38
Other models					
Effective Hydraulic Radius (EHR) model	Darcy length (μm)	36.64	47.27	46.55	26.87

Table 9. 1. Wetting measurements from the different versions of the Pore-Cor model and the Effective Hydraulic Radius (EHR) model, comparing the absorption rates and the Darcy lengths of the primary samples.

The experimental absorption rates calculated from the ISAM was compared to the isotropic and anisotropic Pore-Cor model. The two models showed some correlation between the simulated and the experimental trends for Speswhite-CL, Albaglos-CL and OpacarbA40-CL, but not for Amazon-CL.

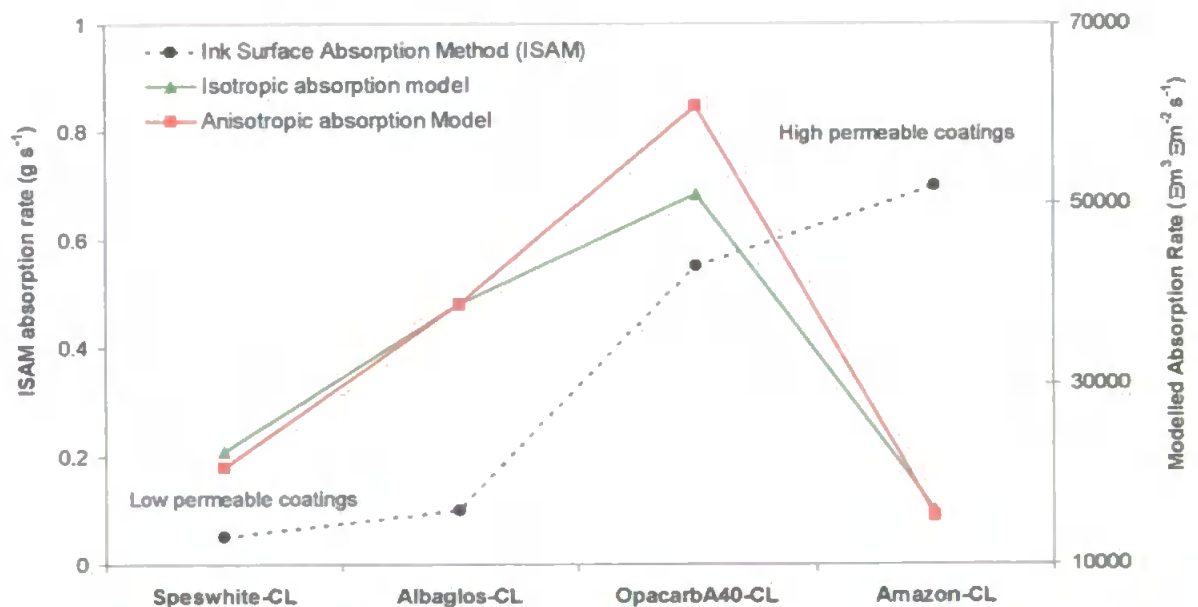


Fig. 9. 1. The modelled absorption rates of the four coatings, before applying the correction factor, compared to the experimental absorption rates at a time, t , of approximately 0.002s. The modelled absorption rate is measured in $\mu\text{m}^3/\mu\text{m}^2/\text{s}$ at the respective estimated aspect factors, while the experimental absorption rate is measured in g/s.

The correction factor f for each coating structure (refer to Table 6.1) was then applied to the simulated oil absorption curves, and the results for the four samples are shown in Fig. 9.2. This gives a significant improvement in the agreement, as Amazon is now shown to have a modelled absorption rate higher than the experimentally low permeable coating samples.

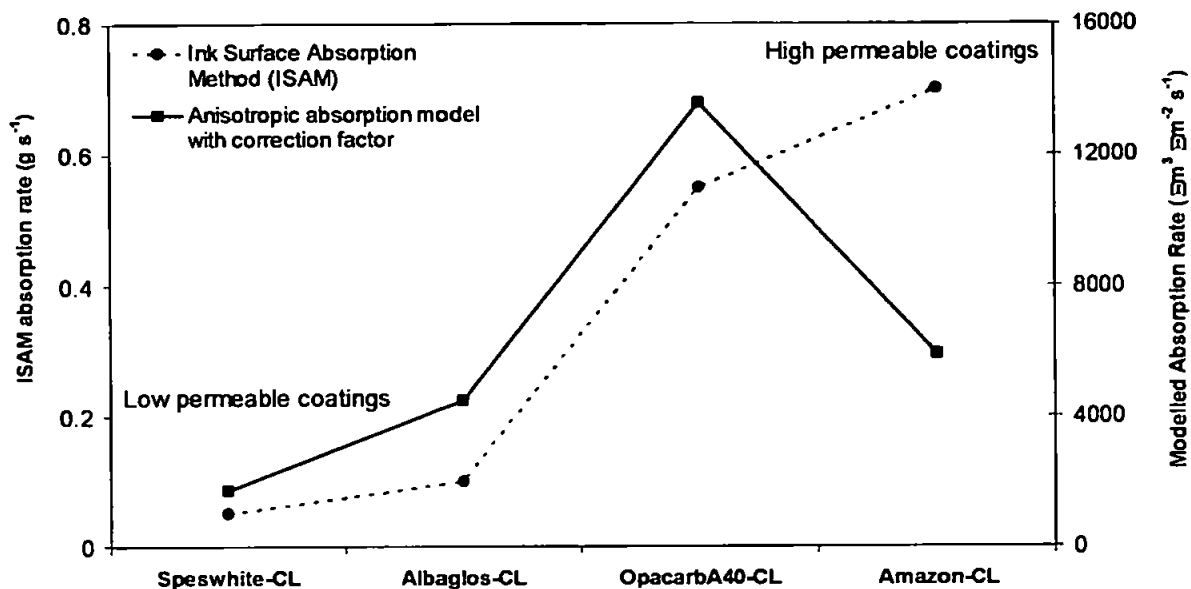
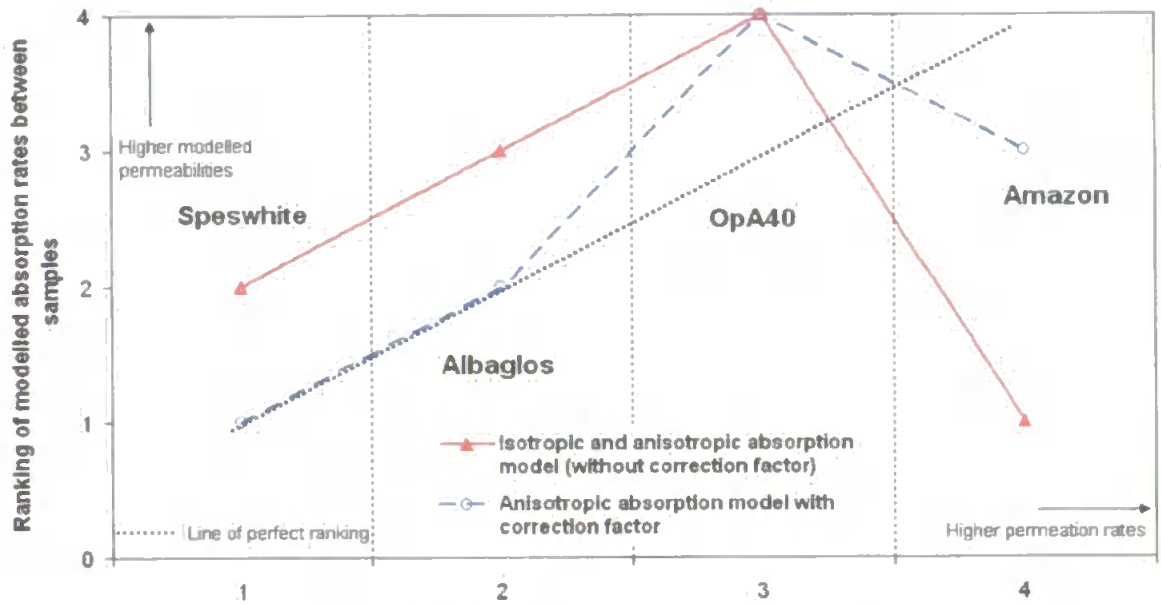


Fig. 9. 2. The modelled absorption rates of the four coatings, after applying the correction factor, compared to the experimental absorption rates at a time, t , of approximately 0.002s. The modelled absorption rate is measured in $\mu\text{m}^3/\mu\text{m}^2/\text{s}$ and at their respective estimated aspect factors, while the experimental absorption rate is measured in g/s.

An alternative approach in comparing the experimental and modelled absorption trends was performed by ranking the experimental ISAM absorption rates and their respective modelled rates, between each sample, in ascending order. This was done in similar fashion to the ranking scheme of the modelled permeability results in Section 7.5.1. For example, a sample with the highest modelled absorption rate would have the highest modelled absorption ranking of four, while the sample with the highest ISAM absorption rate would have the highest ISAM absorption ranking of four.

The rankings of the ISAM absorption rates were plotted on the x-axis, while the rankings of the modelled absorption rates were plotted on the y-axis, accordingly, Fig. 9.3. A line of perfect fit between the two rankings would generate a best fit line with a slope of one.



Ranking of ISAM absorption rates between samples

Fig. 9. 3. Ranking of ISAM and modelled absorption rates between samples

The modelling trend error (Eq. 7.1) was then calculated for each model such that a quantitative measure could be used to show how close the trends from the different models resembled the experimental absorption trends. The results are shown in fig. 9.4.

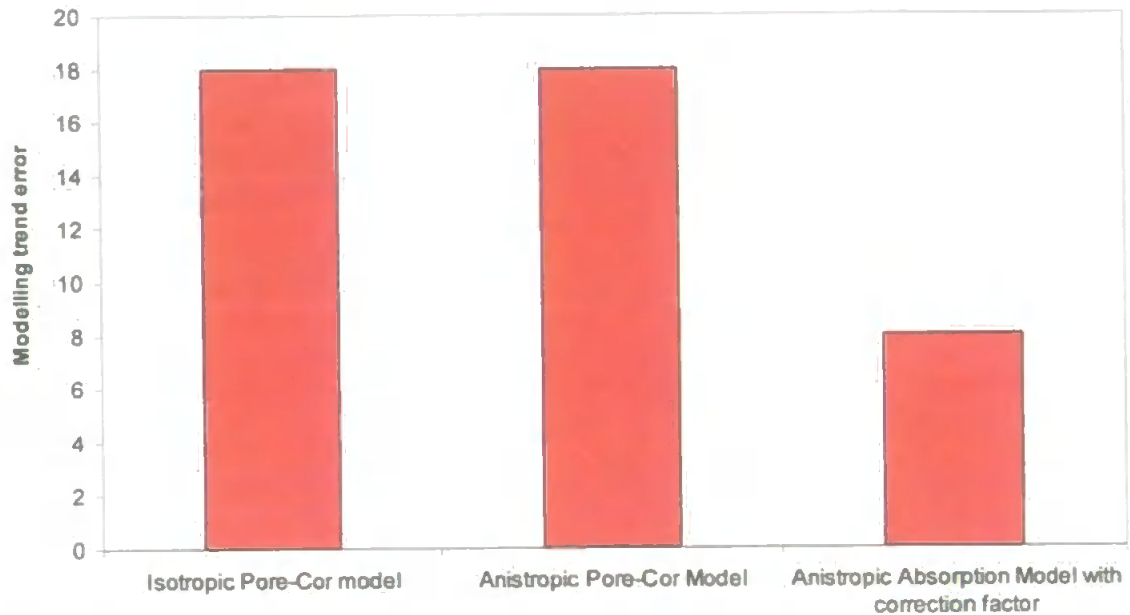


Fig. 9. 4. Modelling trend error for each of the absorption models

The modelling trend error for the anisotropic absorption model, with the correction factor, was calculated to be the lowest of the three models. It would therefore most closely resemble the experimental absorption trends shown by the ISAM. Meanwhile, the anisotropic absorption model, without the application of the correction factor, showed no reduction in the modelling trend error when compared to the isotropic absorption model; it therefore showed no improvement in resembling the experimental absorption trends.

9.1.1. Comparison of Volume-averaged Pore-Cor distance and the Effective Hydraulic Radius (EHR) model

Fig. 9.5 shows the volume-averaged Pore-Cor distance penetrated by the wetting fronts, expressed as Darcy lengths, Eq. 6.13, at t equals 0.002s, and is compared to the calculated distance by the much simpler Effective Hydraulic Radius (EHR) model, Eq. 3.7. The Pore-Cor modelling results are displayed both before and after the application of the correction factor f , (refer to Eq. 6.32, and table 9.1) and the experiment absorption rates are graphed on its secondary axis.

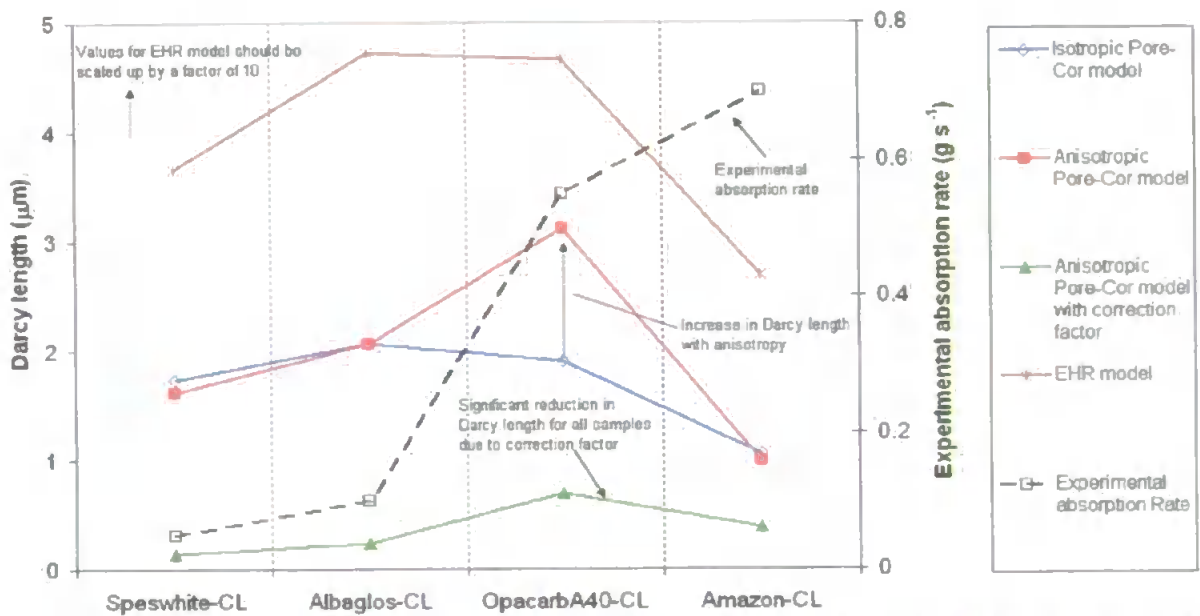


Fig. 9.5. Distance travelled by a wetting front, from the absorption of oil after 0.002 s. The modelled Darcy length calculated from the Effective hydraulic radius (EHR) model has been scaled down by one order of magnitude, and the ISAM absorption rate has been graphed on the secondary y-axis.

OpacarbA40-CL exhibits an increase in Darcy length when an estimated aspect factor is applied to its structure, and, hence, is shown to have a better fit to the experimental permeation rates. The application of the correction factor to the Pore-Cor model caused all the samples to have a significant reduction in Darcy length. However, Amazon-CL is now shown to have a higher Darcy length greater than the Speswhite-CL and Albaglos-CL, which more closely resembles the trend from the experimental absorption rates. The anisotropic modelled Darcy lengths (both with and without applying the correction factor) showed the same improvement when compared to experiment as do the volume and mass absorption rate comparisons in the previous figures.

The calculated Darcy lengths for the EHR model have been scaled down by a factor of ten such that the results could be shown on the same axis with the three Pore-Cor models. The Darcy distance is shown to be approximately one to two orders of magnitude longer than the volume-averaged distance from the Pore-Cor

models. The explanation is that firstly that the EHR model does not take into consideration any interconnectivity. Secondly, it does not allow any distribution of void sizes, as the characteristic throat diameter of the sample is used as the effective hydraulic radius. Finally, it does not take into consideration the inertial effects which would also retard the movement of wetting front.

The experimental ISAM absorption rates between each sample, and their respective modelled wetting distances (Darcy lengths) were also similarly ranked in ascending order. In this scheme, the sample with the longest modelled Darcy length would have the highest modelled Darcy length ranking of four; while the sample with the highest ISAM absorption rate would have the highest ISAM absorption ranking of four. The results of the ranking scheme are shown in Fig. 9.6 below.

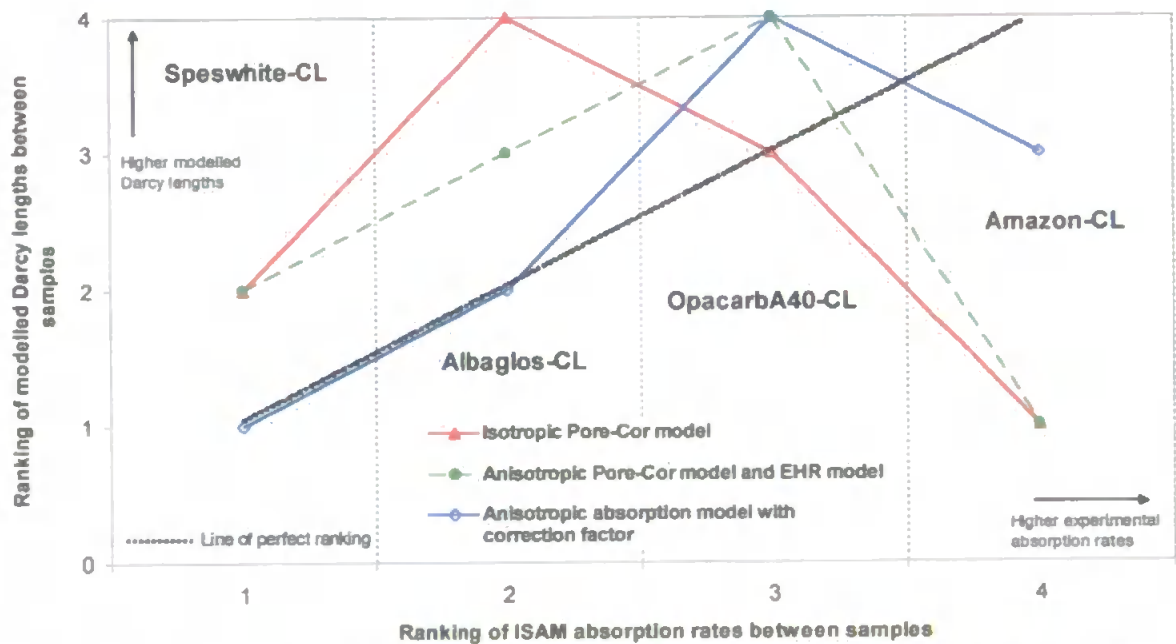


Fig. 9. 6. Ranking of ISAM absorption rates and the modelled Darcy lengths between samples.

The modelling trend error for each absorption model was also similarly performed to quantitatively show how close the trends from the different

absorption models fit to the experimental permeation trends. Figure 9.7 shows the modelling trend error for the calculated Darcy distances of each of the absorption models.

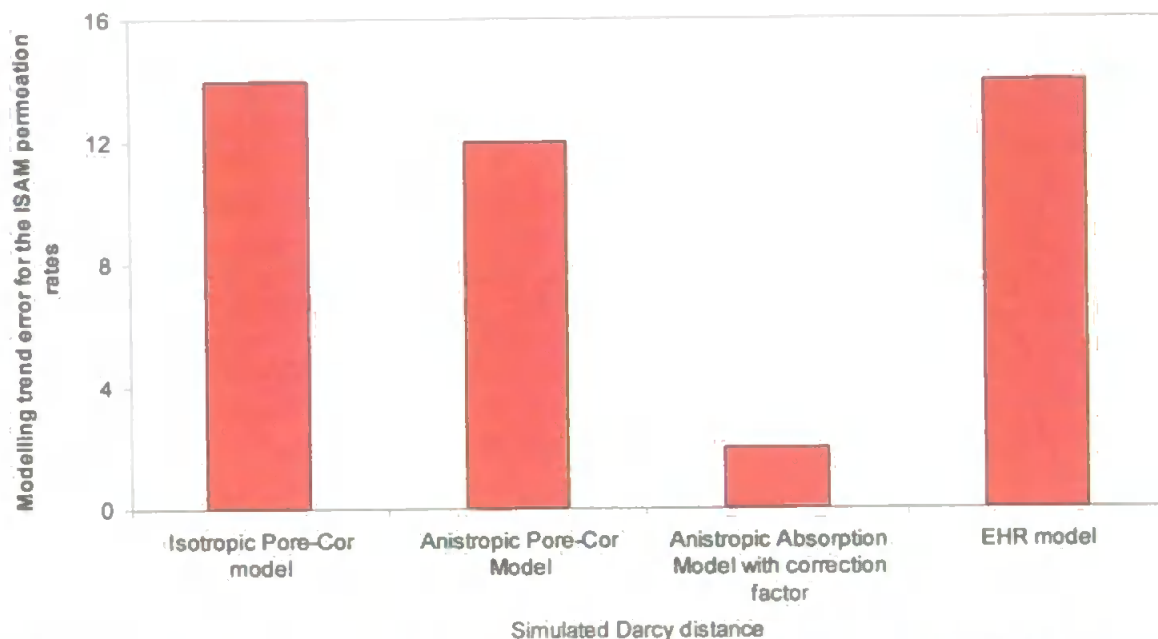


Fig. 9. 7. Modelling trend error of the calculated Darcy distances on the ISAM absorption rates.

The Anisotropic Pore-Cor model revealed a fit to the ISAM absorption rates better than both the Isotropic and the EHR model, as it showed a lower modelling trend error. Furthermore, when the correction factor was applied to the anisotropic Pore-Cor model, the modelling trend error was calculated to be the lowest of the four models, showing a similar result to the volume and mass absorption rates. It therefore most closely resembled the experimental absorption trends shown by the ISAM.

9.2. Summary

- The isotropic and anisotropic Pore-Cor models showed some correlation between the simulated and the experimental trends for Speswhite-CL,

Albaglos-CL and OpacarbA40-CL, but not for Amazon-CL. The application of the correction factor, f , to the simulated oil absorption curves of each coating structure, gave significant improvement in the agreement, as Amazon is now shown to have a modelled absorption rate higher than the experimentally low permeable coating samples.

- OpacarbA40-CL exhibits an increase in Darcy length when an estimated aspect factor is applied to its structure, and, hence, is shown to have a better fit to the experimental permeation rates. The application of the correction factor to the Pore-Cor model caused all the samples to have a significant reduction in Darcy length. However, Amazon-CL is now shown to have a higher Darcy length greater than the Speswhite-CL and Albaglos-CL, which more closely resembles the trend from the experimental absorption rates.
- The Darcy distance for the EHR model is shown to be approximately one to two orders of magnitude longer than the volume-averaged distance from the Pore-Cor models. This is due to EHR model not taking into consideration any interconnectivity, not allowing any distribution of void sizes, and it does not take into consideration the inertial effects which would also retard the movement of wetting front.
- The calculated Darcy lengths from the Anisotropic Pore-Cor model revealed a fit to the ISAM absorption rates better than both the Isotropic and the EHR model. Furthermore, when the correction factor was applied to the anisotropic Pore-Cor model, it most closely resembled the experimental absorption trends shown by the ISAM.

10. OVERVIEW

10.1. Hypotheses

The aim of this final chapter is to give an overview of the whole project, in the context of the initial hypotheses stated in Section 1.3. These hypotheses were as follows:

- That highly controlled application of fluid, using an experimental technique with minimal unknown parameters, can provide useful insights into the effect of void structure on printability.
- That computer modelling of the behaviour of fluids in porous media can shed new light on the complicated relationship between permeation, void structure and properties.
- That computer modelling can allow anisotropy to be isolated from other characteristics of void structure, and hence explain effects which are otherwise intractable.

The sub-hypotheses gave additional criteria, namely:

Success, as judged by

- A close fit to experimental percolation characteristics and porosity.
- Better explanation of trends in permeation experiments than using either a straight aligned-tubes model or an isotropic three-dimensional network.

Usefulness, as judged by

- Explanatory and predictive capabilities.

So to what extent have the overall hypotheses been proven, and the sub-hypotheses achieved?

10.2. Experimental methods

We start by considering the experimental methods. We needed accurate and precise methods to be able to study effects as subtle as anisotropy. The traditional instrument to study liquid uptake is the Prufbau printability tester (refer to Section 4.1). This has the advantage of being able to use identical delivery and uptake sheets, so there was a symmetry in the fluid delivery and uptake system which initially seemed welcome. In practice, however, it proved impossible to determine whether the delivery strip was flooded or not – a factor which dominates the delivery characteristics. Also, because so little fluid was taken up at the contact speed of 1 m s^{-1} , it could not be measured gravimetrically. It was also evident from visual inspection that there was a very uneven uptake of fluid onto the sample. For all these reasons, the traditional Prufbau tester was abandoned.

The next most obvious instrument to use was the Dynamic Absorption Tester (DAT) (refer to Section 3.3.2). This device has the advantage that the delivered fluid droplet has no additional application pressure to take into account. However, the size of each droplet can be slightly variable. Also, although the droplet volume is only $4 \mu\text{l}$, it does flood the surface in the small area of its application. To deal with the last two problems, we used as our measure of permeation the change in height of the drop on the surface with time, and normalised the droplet height

using the droplet's surface area. This approach also avoided other problems, such as assumed droplet shape and pixel-limited image resolution, associated with the instrument's standard analysis software. With these modifications, the DAT provided useful and usable data about the permeation of fluids.

However, there was still a worry that the DAT droplet was flooding the local area which it contacted. So an even more controlled fluid application system was used, namely a gravure roller (refer to Section 4.2). Such rollers have a precisely machined array of tiny pits on the surface, which deliver a calibrated amount of fluid absolutely evenly over the surface which they contact. Since the fluid is recessed in the gravure pattern, the fluid itself had a delivery pressure of zero when in contact with the sample. The gravure roller was mounted on a modified ISIT apparatus. The instrument also delivered sufficient fluid such that the fluid uptake could be measured gravimetrically.

The only worry about the modified ISIT method was that the contact time between the gravure roller and the sample was short and arbitrary. For a footprint of width about 1 mm and rolling rate of 1 m s^{-1} , the contact time was around 1 millisecond. This was appropriate for studies of the fast wetting of the samples – i.e. the short-time absorption through the surface pores, without dominant effects from the rest of the network. Permeation, however, involves the rest of the porous network. So the ISIT was also used in a mode which allowed the fluid much longer times for penetration. The gravure roller was replaced by an inked rubber roller, which delivered excess ink, which was then wiped off at successive intervals (refer to Section 3.3.1).

The final device used was a Gurley permeameter (refer to Section 3.4), necessary to test whether the modelled permeability predictions were any better than those of much simpler models. The permeameter required special calibration for the task, as it is normally only used as a quality control instrument comparing its relative results with those of other Gurley instruments.

10.3. Samples

Armed with a suitable array of experimental methods, we also needed a suitable set of samples to study (refer to Section 3.1.4). Clearly, these had to include void structures which were anisotropic, generated by using anisotropic particles. Isotropic particles, such as spheres, needed to be used to provide control samples. The sample set also needed to include a wide range of void sizes to demonstrate the general applicability of the findings about anisotropy. Finally, three different substrates were required – foil for mercury porosimetry, base paper for the Gurley permeameter, and Syntepaper for all the other measurements.

With these requirements in mind, a large number of samples were studied experimentally - around 60 characterisations in all. As the experiments developed, and the results were modelled, it became evident that the hypotheses could be best tested by examining in detail a sample subset.

10.4. Results

To test the first hypothesis, we need to interpret the results themselves, without any recourse to the use of models.

Overall, the ISAM and ISD methods gave similar trends, and the DAT and Gurley also gave similar trends (refer to Section 5.2.6). However, the trends from one

pair of methods differed from those of the other. Such a difference might be expected from the previous discussion. The ISAM and ISD methods both involved a carefully controlled application, or application and removal, of fluid from the surface. The DAT and Gurley methods both flooded the surface of the sample with excess fluid, in the form of a liquid droplet or pressurised gas respectively. These latter two methods therefore had greater dependence on the body of the porous sample than the first two which are most greatly affected by the surface throats.

This consideration also explains the next finding. This is that the ISAM and ISD methods had a perfectly ranked positive correlation with the number density of surface throats. They did not show a positive rank correlation with any other measured property, namely porosity, mean throat diameter, surface area, width of void size distribution, width of particle size distribution, or mean particle diameter.

Ideally, when comparing trends, it would have been better to carry out fully quantitative measures of correlation, rather than semi-quantitative comparison of ranks. However, the results for all but the Gurley permeameter were so disparate that only rank comparisons could reveal whether relationships between data sets existed or not.

10.5. Modelling

The importance of the Pore-Cor model used in this work was that it related directly to the experimental void structure of the sample (refer to Section 6.1). The percolation curves of the simulated and experimental structures, and the simulated and experimental porosities, were almost identical. So it is important to re-

emphasise that the foundations of the model were much more sophisticated than those normally cited in the literature, which typically compare experimental trends against models which have arbitrary void size distributions and connectivities (refer to Section 2.8). The Pore-Cor structures were also more sophisticated than others often used to analyse experimental data, which implicitly involve the straight capillary approximation (refer to Section 2.5). So the model was based on a strong foundation of experimental data. Nevertheless, it was clearly removed from reality by the gross over-simplification of its geometry. So in this overview, we examine whether the strengths of the model are such that, despite its weaknesses, we can successfully and usefully use it with respect to anisotropic samples.

So first we consider the modelling on its own – i.e. we consider whether the simulated structures based on the experimental porosity and percolation could in themselves provide useful information about the samples. The primary information which derived from the model was the values of the fitting parameters used to match the model with the percolation curves and porosities of the samples. The simulated characteristic throat diameters track closely with the experimental characteristic throat diameters from the intrusion curves (refer to Section 6.7.1). This was expected because of the very close link between these parameters in the model, so does not tell us anything new about the samples. The only strong message from the fitting parameters themselves is that the modelled network for OpacarbA40-CL has a low throat skew (i.e. fewer small throats and more large throats) and a lower connectivity than Albaglos. The simulated permeability arises from a balance between these two parameters (refer to Section 7.3). With Speswhite-CL and Amazon-CL, the fitting parameters are much more

similar to each other, and work to produce the same effect on permeability, so there is less of interest to conclude.

Structures with different aspect factors were simulated to study the effect of anisotropy on permeability (refer to Section 7.3). A change in aspect factor, from an isotropic to a rod-like pore structure, was shown to have very little to no significant effect on permeability. This was confirmed with OpacarbA40-CL, as the mean calculated permeability, at its estimated and isotropic aspect factor, was shown to have no significant difference. Meanwhile, a change in aspect factor from an isotropic to a slit-like pore structure was shown to have an increasing effect on permeability. However, this was only observed within the clay samples when lower aspect factor were used, e.g. $\alpha = 0.1$ (refer to Sections 7.1 and 7.3). The effect of anisotropy on slip flow was also investigated for methane and nitrogen gas, and showed the gas permeabilities to be slightly lower for an anisotropic than an isotropic structure. Hence, the slip flow correction is shown to have less of an effect for slit-like or rod-like pore structures.

The model is clearly limited when dealing with only fitting parameters. Also, it is not telling us much more about the experimental structures than we know already. So how can more information be gained? The answer is to wet the simulated structures from one surface (the top) and compare the results with experiment. Now we begin to see wetting fine structure which cannot be directly observed experimentally, and the model begins to come into its own. We can see for example the fine structure of the wetting process as it wets successive layers, corresponding to a series of steps and points of inflexion in the wetting curves (refer to Section 8.2). From visual inspection of the modelled structures, the effect of anisotropy revealed advance wetting in the narrow features of Speswhite-CL

and OpacarbA40-CL. This represents a type of preferential flow which is normally overlooked because of the low volumes of the void features which are wetted (refer to Section 8.3). The advance wetting observed within these two samples coincided with their broad void size distribution, which was in agreement with observations made by Ridgway *et al.* (Ridgway *et al.*, 2002).

The Lucas-Washburn Equation is shown to be insensitive to anisotropy as very little difference is shown in permeation. However, by contrast, the inclusion of inertial effects, incorporated into the Bosanquet equation, caused a considerable difference in permeation, and also caused advance wetting in the narrow features of OpacarbA40-CL and Speswhite-CL to be much more evident (refer to Section 8.3). Furthermore, permeation was found to be strongly dependent on surface throat number density, to the extent that a correction factor had to be included to allow for this characteristic (refer to Section 6.7). So overall there is clear message that *both* inertia and surface throat density need to be included to gain a clear understanding of the permeation of anisotropic structures – previously only surface throat number density has been considered (Preston *et al.*, 2001).

10.6. Results in the context of modelling

The discussions in the previous section concerned simulated void structures based on experimental data. From these simulated void structures, different new properties were generated. These new properties are fascinating in themselves, but it would have been unsatisfactory to leave it at that, simply examining simulated parameters which are not themselves validated by experiment.

So we needed to relate the model to the real world again, by comparing the simulated properties with experimental ones where possible. On doing this, we discovered a good positive rank correlation between experimental permeabilities inferred from both the DAT and Gurley instruments, and the simulated permeabilities, but only when the number density of surface throats was included as an additional parameter (refer to Section 7.6 and 7.7). We discovered a positive but imperfect rank correlation between the simulated permeabilities and wetting characteristics and those inferred from the ISAM and ISD measurements, but again only when the number density of surface throats was included (refer to Section 9.1 and 7.5, respectively). So there was confirmation that the model was producing successful and useful results but only with the inclusion of the number density of surface throats. However, when comparing samples with similar surface densities of throats, the model provided successful comparisons without the need for a correction factor (refer to Section 7.5.2, 7.6.2 and 7.7.2).

Of the four experimental methods used, the Gurley permeameter provided measurements most analogous to simulated properties. So in this case, a quantitative comparison was made to complement the semi-quantitative rank comparisons of the other properties. This showed that the simulated permeabilities were around two orders of magnitude lower than those measured experimentally, but followed the same trend (refer to Section 7.7). This was much as expected from other types of samples in other projects (MacDonald, 2000), and arose from the fact that the Pore-Cor model was much simpler, and had fewer intricacies and connections, than the void network in the experimental sample.

The Pore-Cor model permeabilities were also compared to the much simpler Kozeny and Aligned cylinders models. As already described (refer to Section

2.5.5), the Kozeny model and Kozeny-Carman model are partly phenomenological, because of two of its parameters, c (a fitting parameter) and T (a fitting parameter dressed up as a primary parameter, which we therefore set at 1). However, even without the help of these parameters, the Kozeny models, along with the Aligned cylinders model, have been shown to be generally better in resembling the experimental trends than either the Isotropic or Anisotropic Pore-Cor model. We have shown that wetting and permeation in anisotropic void structures is very sensitive to the number density of surface throats. This property is included in the equation for the Aligned cylinders model, and maps closely onto the surface area term of the Kozeny and Kozeny-Carman equation. The success of these models is therefore fortuitous.

By contrast, the anisotropic Pore-Cor model predicted permeabilities which compared generally less well with the experimental permeation trends. This was because the anisotropic effects on permeability were masked by the packing errors within the Pore-Cor model causing a discrepancy between the simulated and actual number density of surface throats. However, once the correction factor was applied to the anisotropic Pore-Cor model it was able to successfully predict permeabilities more accurate than those predicted by the Kozeny and aligned cylinders models.

10.7. Implications for design of paper coatings

Designers of paper coatings should most concern themselves with the most important properties for the absorption of fluids into the structure, as well as with other properties such as gloss and opacity. The implication of this thesis is that for anisotropic void structures, generated by the use of particles with high aspect

ratio, a feature of prime importance is the number density of surface throats. However, this is a parameter generally ignored because it is not easily measured. Success in the design of paper coatings must therefore have come from the serendipitous obtaining of the correct number of surface throats, from the manipulation of other factors such as particle size distribution width, and aspect ratio.

Controlled preferential flow is also an important factor regarding the absorption of fluid into the structure. It can promote fast absorption of the ink vehicle into the base paper of the coating, and hence encourage faster drying of the ink. A broad void size distribution is shown to be a contributing factor in causing such advance wetting features in paper coatings. The porosity of a paper coating will also play a dominant role in determining ink density, as a low porosity structure needs less volume of ink to obtain a certain required ink density.

The design of high-performance and specialist paper coatings should take into account the design characteristics which derive from this thesis. There are also other characteristics that are not discussed in this thesis, but it should be noted that such properties as print gloss are affected by the absorption rate of fluids (Preston *et al.*, 2002).

Of the primary samples investigated, OpacarbA40-CL and Amazon-CL are shown to have the best performance. Both coatings are shown experimentally to have a relatively high number density (Table 5.3) and, subsequently, a fast absorption rate (Fig. 5.21). However, the modelled void structure revealed evidence of preferential flow for only OpacarbA40-CL (Fig. 8.8 and 8.29), as the anisotropy of the void structure and its broad void size distribution contributed to this advance

wetting feature (Fig. 5.4). Although both Amazon-CL and OpacarbA40-CL showed a narrow particle size distribution (Fig. 5.1), the particle packing caused OpacarbA40-CL to have a much broader void size distribution than Amazon-CL (refer to section 5.1.4). On the other hand, the particle packing of Amazon-CL caused a much lower porosity than OpacarbA40-CL, which would be beneficial in regards to ink density (Fig. 5.5).

Although not all experimental and modelling analysis was performed on the complementary samples, an assessment on the performance of the complete data set of samples could still be given based on the design characteristics which derive from this thesis. Hydrocarb90 and Amazon would demonstrate the best performance of all the samples. The samples are shown to have the fastest absorption rate of all the samples (Fig. 5.37), and also have relatively low porosities (Fig. 5.30). Although the application of starch and latex as a binder, rather than CMC and latex, increased the porosity of these two samples, it also caused the two samples to have a broader void size distribution (Fig. 5.29), which would be beneficial for achieving controlled preferential flow.

The thesis also had an environmental mission to assist in the design of paper coatings (refer to Section 1.9). Paper coatings produced from the PCC or GCC mineral group would have a higher pH than the Kaolin mineral group, as they use calcium carbonate rather than clay as their pigment. The higher pH would cause less of an impact on the environment, from the disposal and recycling practices of coated papers. The calcium carbonate pigments also have a much lower mine-waste factor than the Kaolin (clay) pigments. The PCC and GCC coatings would therefore cause less environmental degradation from their mining practices. The application of starch as a binder would also be more environmentally-friendly than

the use of CMC and latex, as starch is naturally-produced and a renewable resource. When an environmental factor is incorporated into the design of paper coatings, OpacarbA40-CL is shown to have the best performance of the primary samples investigated; while Hydrocarb90-SL is shown have the best performance of the complete data set of samples investigated.

10.8. Implications for future work

The successful design of better instruments to measure the permeability and wetting of fluids in paper coatings can be used with great benefit in future work. Paper coatings, comprising of a combination of different pigment types (i.e. 75% weight clay to 25% weight calcium carbonate), could be measured with these instruments to optimise their absorption properties. The effect of permeation from the calendering of different paper coatings could also be measured and related to anisotropy. Different void structure properties of the paper coatings, such as anisotropy, number density and void size distribution, could also be investigated in regards to other printing quality properties, such as gloss and opacity.

With regard to simulation, it is clear that the Pore-Cor model can usefully give information about fine structure, from which paper coating manufacturers can glean useful advice. However, for the Pore-Cor model to be able to produce reliable permeability trends for anisotropic media, the packing of the voids within the anisotropic structure will need to be made more sophisticated. The Pore-Cor model currently is only capable of modelling 100 different sizes in the void structure. An increase in the number of throat sizes (i.e. from 100 to 1000 sizes) would produce more accurate permeability and wetting results. The theory of the

partial wetting of pores in a network structure is also an important phenomenon that should be further studied and included in the Pore-Cor model.

APPENDIX

A. LIST OF SYMBOLS

Each symbol is cross-referenced to an example showing its application in an equation or figure caption.

A	Cross-sectional area (Eq. 2.1)
A_s	Absorption (Eq. 2.29)
A_{cell}	Cross-sectional area of the unit cell (Eq. 6.17)
AP_{smp}	Air permeance of the sample (Eq. 3.7)
AP_{cal}	Air permeance of calibration plate (Eq. 3.7)
a, b	The two radii for a rectangular cross-sectioned tube normal to the flow (Eq. 6.21)
d_{base}	Diameter of the base of the droplet (Eq. 3.3)
C	Curvature of a meniscus (or capillary pressure) (Eq. 2.27)
C_d	Drainage penetration curvature (Fig. 2.6)
C_i	Imbibition curvature (Fig. 2.6)
c	Permeability coefficient also referred to as the 'Kozeny constant' (Eq. 2.23)
d	Diameter of a cylindrical tube or throat (Eq. 2.12)
d_{50}	Median void or particle size (Table 5.1)
d_{base}	Diameter of the base of the droplet (Eq. 3.3)
d_{eff}	Effective throat diameter (Eq. 6.4)
D	Fractal dimension (Eq. 2.32)
dp/dx	Pressure gradient along the capillary (Eq. 2.12)
d_j	Length of a segment (Eq. 2.30)
e	Eccentricity (Eq. 6.8)
$E(e)$	Elliptical integral (Eq. 6.7)

F	Volumetric flow capacity (Eq. 6.16)
F_{arc}	Flow capacity of an arc (Eq. 6.16)
F	Volume-force per unit mass (Eq. 2.9)
$f(d)$	Pore size distribution (Eq. 2.18)
$F(\phi)$	Porosity factor (Eq. 2.20)
F_w	Fraction of the total void volume filled with a wetting fluid (Eq. 6.13)
f	Surface throat number density correction factor (Eq. 6.34)
G	Shape factor- definition from Mason and Morrow {621} (Fig. 2.6)
g	Acceleration due to gravity (Eq. 2.3)
$g(d)$	Differential pore size distribution (Eq. 2.18)
h	Measurement of height (Eq. 2.1)
h_n	Normalized height of droplet (Eq. 3.3)
h_0	Height of the droplet at the initial time of contact (Eq. 3.3)
i	represents a segment (Eq. 2.30)
K	Permeability of a certain medium to a particular fluid (Eq. 2.1)
K_n	Knudson number (Eq. 6.25)
K_s	Saturated permeability of a material (Eq. 2.7)
k	Intrinsic (specific) permeability of a material, independent of the fluid used to measure it (Eq. 2.6)
k_{samp}	absolute permeability of the sample runs
k_{cal}	permeability of the calibration plate
L, l	Measurement of length (Eq. 2.2)
L_a, L_b	Two widths of the pore normal to the flow (Eq. 6.22)
L_c	Width of the pore in the direction of flow (Eq. 6.22)
l_{cell}	Length of the unit cell (Eq. 6.17)
$L(t)$	Volume-averaged distance between the supersource and the wetting front (Eq. 6.13)
m	number of sides (Eq. 2.26)

$L(t)$	Volume-averaged distance between the supersource and the wetting front (Eq. 6.13)
m	number of sides (Eq. 2.26)
M_{ss}	Bulk modulus of the solid sample (Eq. 3.1)
M_T	Modelling trend error (Eq. 7.1)
n	Number of capillaries per unit area of cross section (Eq. 2.12)
N_{exp}	Number density of surface throats obtained experimentally (Eq. 6.34)
N_{mod}	Number density of surface throats obtained from the model (Eq. 6.34)
P_e	External pressure (Eq. 2.34)
P	Pressure potential equivalent to the hydrostatic head (Eq. 2.8)
P	Pressure difference generated across the fluid meniscus (Eq. 2.25)
P^1	Atmospheric pressure (Eq. 3.1)
p	pressure (Eq. 2.3)
Δp	Hydrostatic pressure difference (Eq. 2.2)
ΔP	Difference between the capillary pressure and the externally applied pressure (Eq. 2.31)
$\delta P / l$	Pressure gradient across the medium
Q	Volumetric flow rate (Eq. 2.1)
q	Referred to as the flux, Darcy velocity, macroscopic velocity, filter velocity, or flow per unit area (Eq. 2.5)
\mathbf{q}	Vector flow velocity (Eq. 2.7)
R_e	Experimental permeation ranking (Eq. 7.1)
R_m	Modelled permeation ranking (Eq. 7.1)
r	measurement of a radius (Eq. 2.10)
r_a, r_b	Two radii of an ellipsoidal throat (Eq. 6.23)
r_e	Effective hydraulic radius (Eq. 3.13)
r_{eff}	Effective radius (Eq. 6.4)

r_m	'average' radius of the capillaries (Eq. 3.8)
R	Radius of a segment (Eq. 2.30)
R_A	Absorption rate (Eq. 3.4)
Re	Reynolds number (Eq. 2.11)
R_H	Hydraulic radius (Eq. 2.20)
R_S	Saturation rate (Eq. 3.2)
S	Average specific surface area (surface area per unit bulk volume) (Eq. 2.22)
S_d	Surface area of droplet (Eq. 3.3)
S_o	'specific' surface exposed to the fluid (e.g. the surface exposed to the fluid per unit volume of <i>solid</i> material (Eq. 2.24)
S_w	Water saturation (Fig. 2.5)
T	Tortuosity (Eq. 2.16)
t	measurement of time (Eq. 2.9)
t_p	thickness of paper (Eq. 2.29)
T_s	Saturation point (Eq. 3.2)
V	Measurement of Volume (Eq. 2.29)
V_a	Volumetric amount of fluid absorbed (Eq. 6.12)
V_{int}	Volume intrusion into the sample (Eq. 3.1)
V_{obs}	Intruded mercury volume reading (Eq. 3.1)
δV_{blank}	Change in the blank run volume reading (Eq. 3.1)
V'_{bulk}	Sample bulk volume at atmospheric pressure (Eq. 3.1)
V_{bulk}	bulk or envelope volume of the unit cell (Eq. 6.1)
V_{pore}	Volume of pore (Eq. 6.1)
V_{throat}	Volume of throat (Eq. 6.1)
\mathbf{v}	Local velocity-vector of a point of the fluid (Eq. 2.29)
v	Average flow velocity in a tube (Eq. 2.11)
W	Pore-row spacing (Eq. 6.1)

x	distance travelled by the wetting front (Eq. 2.28)
z	Height of elevation from datum (refer to Fig. 2.1)
α	Aspect factor (Eq. 6.4)
α_c	Half of the angle of a corner (Eq. 2.26)
λ	Mean free path (Eq. 6.25)
ε	Coefficient of external friction (Eq. 6.27)
δ	'Average' pore diameter of a porous medium (Eq. 2.17)
ϕ	Porosity (Eq. 2.15)
γ	Interfacial tension (Eq. 2.25)
π	Mathematical constant, $\pi = 3.141592654$ (Eq. 2.12)
θ	contact angle of the meniscus surface with the solid surface (Eq. 2.25)
Φ^1	porosity at atmospheric pressure (Eq. 3.1)
ρ	Density of the liquid (Eq. 2.3)
μ	Viscosity (Eq. 2.6)
ω	Angle measurement used in conical throats (Fig. 2.21)
Ω_i	Resistance to flow in a segment i (Eq. 2.30)
Ω_{cell}	Averaging operator over the whole unit cell (Eq. 6.16)
Π	Permeation (Eq. 6.12)

A.1. List of abbreviations

AP	Air permeance
Amazon	Amazon 90 SD
Clay	Kaolin
CMC	Carboxymethyl cellulose co-binder
DAT	Dynamic Absorption Tester

EHR	Effective hydraulic radius
ESD	Equivalent spherical diameter
GCC	Ground calcium carbonate
Gurley method	Gurley Air Resistance Method
ISD	Ink Stain Density
ISIT	Ink Surface Interaction Tester
ISAM	Ink Surface Absorption Method
PCC	Precipitated calcium carbonate
PPAM	Prufbau Printability Absorption Method
pph	Parts per hundred by weight
Pore-Cor	Pore-level properties Correlator
SB	Styrene Butadiene
SEM	Scanning electron microscope
Latex	SB latex binder
Number density	number of surface throat per unit area
Speswhite	Speswhite clay
-CL	Pigment samples containing CMC and SB latex binder
-SL	Pigment samples containing starch and SB latex binder

B. TABLES

B.1. Number density calculations

The total number of surface throats for each of the samples, along with the number density calculations, is shown in Table B.1 and B.2. An example of how the surface throats are identified is shown in Fig. B.1. The calculations are shown for the four primary samples and two complementary samples, OpacarbA60-CL and Amazon-SL. The number density results of the two complementary samples are discussed in the Section 7.5.2, 7.6.2 and 7.7.2.

Section	Number of surface throats					
	Speswhita-CL	Amazon-CL	OpacarbA40-CL	Albaglos-CL	Amazon-SL	OpacarbA60-CL
1	5	46	32	22	32	27
2	6	42	34	15	30	26
3	8	40	28	12	31	28
4	8	39	31	12	30	26
total	27	167	125	61	123	107

Table B. 1. The total number of surface throats in each of the samples.

Samples	mean number of surface throats in each section	Standard error	Mean x4	Standard error	Total area investigated (um ²)	Number Density- number of voids per surface area (um ⁻²)	Standard error
Speswhita-CL	6.75	0.75	27.00	3.00	40.66	0.66	0.07
Amazon-CL	41.75	1.55	167.00	6.19	40.86	4.09	0.15
OpacarbA40-CL	31.25	1.25	125.00	5.00	41.35	3.02	0.12
Albaglos-CL	15.25	2.36	61.00	9.43	43.70	1.40	0.22
Amazon-SL	30.75	0.48	123.00	1.91	38.98	3.16	0.05
OpacarbA60-CL	26.75	0.48	107.00	1.91	37.29	2.87	0.05

Table B. 2. The number density calculations for each of the samples

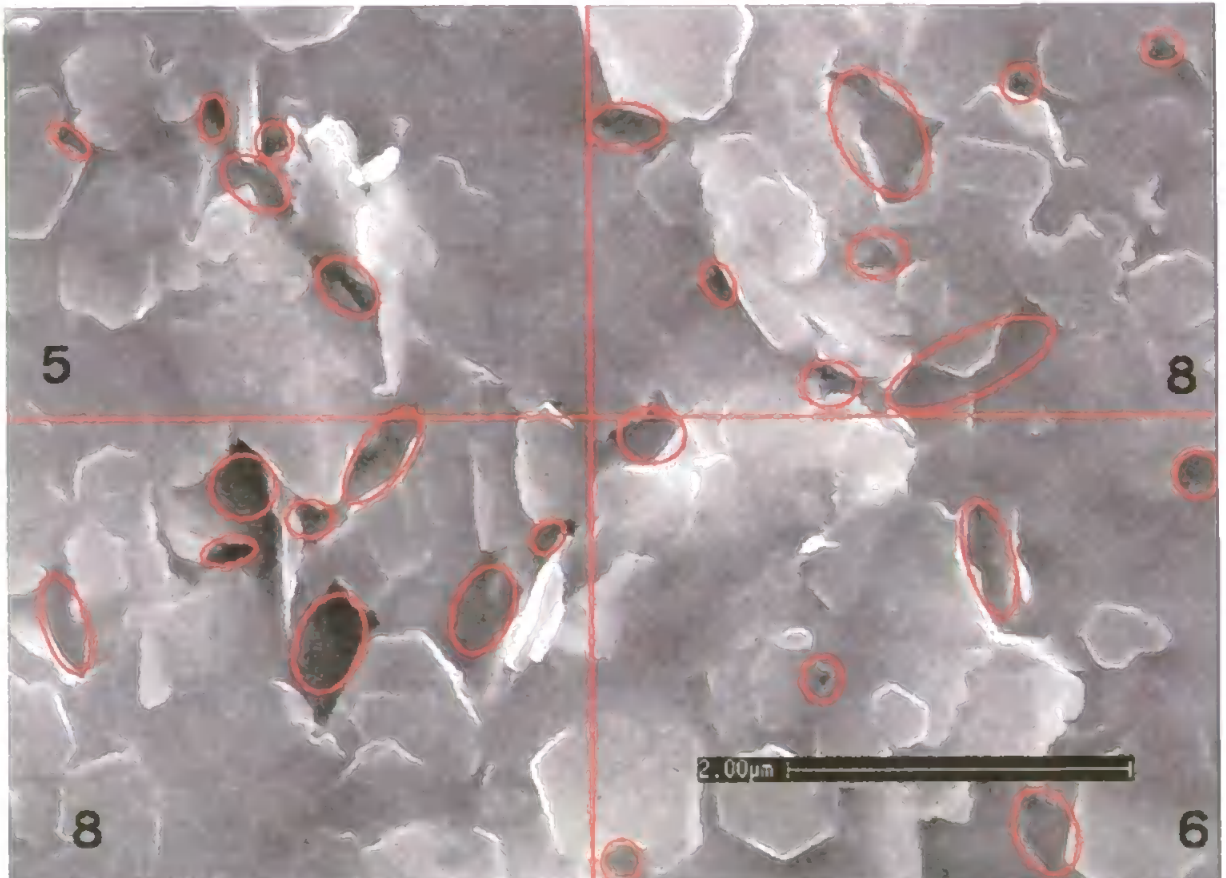


Fig. B. 1. An example of how the surface throats are identified from the SEM image of the surface of Speswhite-CL. The SEM image is shown to be divided into four sections, with the red circles indicating surface throats.

B.2. Calculated network permeabilities and optimised Pore-Cor parameters for complementary samples

The calculated network permeabilities and their optimised Pore-Cor parameters, for each stochastic generation, are shown for the two complementary samples, OpacarbA60-CL and Amazon-SL, in Table B.3 and B.4. The network permeability results of the two complementary samples are discussed in the Section 7.5.2, 7.6.2 and 7.7.2.

OpacarbA60-CL		Aspect factor = 2.0					
Stochastic generation	Liquid Permeability (mDarcy)	Methane Permeability (mDarcy)	Nitrogen Permeability (mDarcy)	Connectivity	Throat Skew	Pore-Row Spacing	Pore Skew
1	8.44E-04	5.59E-03	5.41E-03	4.30	1.01	1.83	1.50
2	4.45E-03	2.00E-02	1.94E-02	4.20	1.00	1.81	1.50
3	6.37E-04	3.36E-03	3.25E-03	4.60	1.17	1.78	1.50
4	1.03E-03	6.32E-03	6.12E-03	4.40	1.02	1.83	1.50
5	7.75E-04	4.31E-03	4.17E-03	4.80	1.20	1.77	1.50
6	6.62E-04	3.61E-03	3.49E-03	4.10	1.00	1.80	1.50
7	1.87E-03	1.13E-02	1.09E-02	4.70	1.10	1.80	1.50
8	4.29E-03	1.90E-02	1.84E-02	4.00	0.78	1.89	1.50
9	1.94E-03	8.25E-03	8.00E-03	3.90	0.86	1.84	1.50
10	7.73E-04	5.41E-03	5.23E-03	5.00	1.19	1.82	1.50
Mean	1.73E-03	9.08E-03	8.80E-03	4.40	1.03	1.82	1.50
Median	9.38E-04	6.32E-03	6.12E-03	4.30	1.01	1.81	1.50
Geometric mean	1.31E-03	7.22E-03	7.00E-03	4.38	1.02	1.82	1.50

Table B. 3. The optimised Pore-Cor parameters for OpacarbA60-CL, for a chosen aspect factor of $\alpha=2.0$, at each stochastic generation. The Calculated liquid permeabilities and its mean, median and geometric mean are also calculated.

Table B. 4. The optimised Pore-Cor parameters for Amazon-SL, for a chosen aspect factor of $\alpha=0.80$, at each stochastic generation. The Calculated liquid permeabilities and its mean, median and geometric mean are also calculated.

Amazon-SL		Aspect factor = 0.80					
Stochastic generation	Liquid Permeability (mDarcy)	Methane Permeability (mDarcy)	Nitrogen Permeability (mDarcy)	Connectivity	Throat Skew	Pore-Row Spacing	Pore Skew
1	1.14E-05	9.81E-05	1.02E-04	3.85	1.55	3.00	2.00
2	8.39E-06	1.07E-04	1.11E-04	3.97	1.65	3.06	2.49
3	5.43E-06	6.95E-05	7.21E-05	4.18	1.78	2.82	2.27
4	6.55E-06	8.52E-05	8.83E-05	3.98	1.60	3.09	2.36
6	4.99E-06	9.07E-05	9.42E-05	4.73	1.88	2.79	2.38
6	5.29E-07	1.31E-05	1.36E-05	3.84	1.66	2.83	2.01
7	3.61E-06	5.42E-05	5.62E-05	4.11	1.64	3.09	2.41
Mean	5.84E-06	7.39E-05	7.67E-05	4.09	1.68	2.96	2.27
Median	5.43E-06	8.52E-05	8.83E-05	3.98	1.65	3.00	2.36
Geometric mean	4.41E-06	6.64E-05	6.89E-05	4.08	1.67	2.96	2.28

C. PORE-COR PROGRAMMING

The Pore-Cor Fortran code was modified in several different subroutines such that the percolation characteristics of a sample were modelled for anisotropic structures. The secondary features of the structure, such as permeability and wetting, were also modified for anisotropic structures. As there are over 150 pages of Fortran code that were modified to some degree only the main subroutines for the permeability and the wetting algorithms are shown in the appendix²⁶.

C.1. Calculation for the flow capacity of an arc

The subroutine for calculating the flow capacity of all the arcs (F_{arcs}) in the network structure is shown below. This subroutine is part of a number of subroutines to calculate the network permeability of the structure (refer to Section 6.6).

```
!-----
! subroutine to calculate capacities for SAS routine
! subroutine capac(cus1,cus2,cus3,cusn1,cusn2,cusn3,rs1,rs2,hs,flowdir,ds)
!cus, cusn and rs refer to pore size and throat radii within subr.
!changed for anisotropic pores and ellipsoidal throats- PB- 28-03-00
! Calculates flow capacity from pore of size cus through throat of radius rs and length hs into pore of size cusn

REAL:: la,smallreal,as,bs,cs
! la refers to the mean free path of the gas in microns.
REAL:: cus1, cus2,cus3,cusn1,cusn2,cusn3,rs1,rs2,hs
REAL:: ds lds refers to the flow capacity from pore through throat
REAL:: CUEff, CUEfn, Reff,sumtan,calctan,aspec
REAL:: calctanN,sumtanN,sumconstant,sumconstantN
!effective Pore size radii, effective throat radius, and length of pore in flow direction and it neighbor
!permconst refers to the constant in the flow capacity equation, when aspec is 1 const=56.90
!aspec refers to aspect ratio
INTEGER::flowdir,m,totnum,i
common/type/la

smallreal=1e-20
aspec=1.5

sumtan=0
sumtanN=0

pi=4.0*ATAN(1.0)

m=flowdir
totnum=11

Reff=(2*rs1*rs2)/(rs1+rs2) !calculates the effective throat radius
```

```

pore_sides: select case (m)
!calculates the effective pore size for a specific flow direction
case (1)
CUeff=(2*cus2*cus3)/(cus2+cus3)
CUeffn=(2*cusn2*cusn3)/(cusn2+cusn3)

do i=1,totnum,2
calctan=TANH((i*pi*cus2)/(2*cus3))/i**5
calctanN=TANH((i*pi*cusn2)/(2*cusn3))/i**5
sumtan=calctan+sumtan
sumtanN=calctanN+sumtanN
END do

sumconstant=(192*cus3/pi**5*cus2)*sumtan
sumconstantN=(192*cusn3/pi**5*cusn2)*sumtanN

if (cus1.gt.smallreal)then
as=(cus2*cus3**3)/(12*cus1)*(1-(cus3*sumconstant/cus2))*(1+(8.8*la/CUeff))
as=1/as
else
as=0
end if

if (cusn1.gt.smallreal)then
bs=(cusn2*cusn3**3)/(12*cusn1)*(1-(cusn3*sumconstantN/cusn2))*(1+(8.8*la/CUeffn))
bs=1/bs
else
bs=0
end if

if (rs1.gt.smallreal)then
cs=((4*hs)*(rs1**2+rs2**2))/((pi*rs1**3*rs2**3)*(1+(4.4*la/Reff)))
ds=(8/pi)*(1/(as+bs+cs))
else
ds=0.00000000 ! no throat, so zero capacity
end if

case (2)
CUeff=(2*cus1*cus3)/(cus1+cus3)
CUeffn=(2*cusn1*cusn3)/(cusn1+cusn3)

do i=1,totnum,2
calctan=TANH((i*pi*cus1)/(2*cus3))/i**5

calctanN=TANH((i*pi*cusn1)/(2*cusn3))/i**5
sumtan=calctan+sumtan
sumtanN=calctanN+sumtanN
END do
sumconstant=(192*cus3/pi**5*cus1)*sumtan
sumconstantN=(192*cusn3/pi**5*cusn1)*sumtanN

if (cus1.gt.smallreal)then
as=(cus1*cus3**3)/(12*cus2)*(1-(cus3*sumconstant/cus1))*(1+(8.8*la/CUeff))
as=1/as
else
as=0
end if

if (cusn1.gt.smallreal)then
bs=(cusn1*cusn3**3)/(12*cusn2)*(1-(cusn3*sumconstantN/cusn1))*(1+(8.8*la/CUeffn))
bs=1/bs
else
bs=0
end if

if (rs1.gt.smallreal)then
cs=((4*hs)*(rs1**2+rs2**2))/((pi*rs1**3*rs2**3)*(1+(4.4*la/Reff)))
ds=(8/pi)*(1/(as+bs+cs))
else
ds=0.00000000 ! no throat, so zero capacity
end if

case (3)
CUeff=(2*cus1*cus2)/(cus1+cus2)
CUeffn=(2*cusn1*cusn2)/(cusn1+cusn2)

do i=1,totnum,2
calctan=TANH((i*pi*cus1)/(2*cus2))/i**5

calctanN=TANH((i*pi*cusn1)/(2*cusn2))/i**5

```

```

sumtan=calctan+sumtan
sumtanN=calctanN+sumtanN
  END do
  sumconstant=(192*cus2/pi**5*cus1)*sumtan
sumconstantN=(192*cusn2/pi**5*cusn1)*sumtanN

  if (cus1.gt.smallreal)then
as=(cus1*cus2**3)/(12*cus3)*(1-(cus2*sumconstant/cus1))*(1+(8.8*la/CUeff))
as=1/as
  else
      as=0
      end if

      if (cusn1.gt.smallreal)then
bs=(cusn1*cusn2**3)/(12*cusn3)*(1-(cusn2*sumconstantN/cusn1))*(1+(8.8*la/CUeffn))
bs=1/bn
  else
      bs=0
      end if

      if (rs1.gt.smallreal)then
cs=((4*hs)*(rs1**2+rs2**2))/((pi*rs1**3*rs2**3)*(1+(4.4*la/Reff)))
ds=(8/pi)*(1/(as+bs+cs))
  else
      ds=0.00000000 ! no throat, so zero capacity
      end if

      end select pore_sides
! print *,as,bs,cs,ds,as,bs,cs,ds
! PRINT *,sumtan
return
end
! .....
```

C.2. Modelling the permeation of a wetting fluid

The main subroutine which simulates the permeation of a wetting fluid into a network structure is shown below (refer to Section 6.5).

```

! *****
! subroutine WETPERC - percolation simulation for wetting fluid

! GPM & CJR 22/5/98 & PB 05-11-01

! pv and hgdiam arrays have been increased to 1000 terms
! calls to graph may not work but these are commented anyway

subroutine wetperc(iact,s,nn,ne,h,pi,r,cu,rl,vol,&
&dmin,dmax,nanswer,nplug,manswer,ianswer,aca,rca,snap)

dimension s(100),nn(1000,3),ne(1000,3),h(1000,3)
dimension hgrad(100),r(1000,3,2),cu(1000,3),pc(100)
dimension rl(1000,3,2),a(3),conediam(1000,3,2),ractual(1000,3,2),coneangle(1000,3,2)
dimension wet_advance(1000,3),wet_readvance(1000,3),wet_massbal(1000)

dimension wet_volrate(1000,3), avar(1000,3), bvar(1000,3)
REAL custatep(1000,4),rstatep(1000,3,4) ! degree of partial filling with the four different fluids, 1.000=full
real,dimension (1000,6) :: wet_cufillrate! rate at which fluid fills pore from x,y,z,-x,-y,-z throats,
! um**3/s and seconds

! real,dimension (1000) :: wet_cutfillrate ! total pore fill rate for fluids 1 to 4 (4 = wetting fluid)
real wet_flowin,wet_flowout ! total fill rate of a pore
real wet_gamma,wet_theta,wet_rho,wet_massbal ! defined below
real wet_param1,wet_param2,wet_param3,wet_eta,pressure,avar,bvar
real totwet,fracwet,wet_readvancemax ! defined below
INTEGER custate(1000,4),rstate(1000,3,4),rstated(1000,3,4)! rstated is direction of filling of fluid - +1 = positive direction
integer wet_nstep,wet_mbaldone(1000) ! time step number, wet mass balance done for this pore
INTEGER notfullflag ! flag to show that a throat exists but is not full
real rca,aca,snap,cuthresh
integer lanswer
character*80 samplename
real xstore(1000),ystore(1000),factor
integer sizestore
logical usebuffer
integer,dimension (10) :: vbo_generalint , vbi_generalint
real,dimension (10) :: vbo_generalreal , vbi_generalreal
real smallreal ! real numbers below this are assumed to be zero
REAL pic_size ! Size of diagram in um
INTEGER pic_celtype ! =0 for whole unit cell, =1 if only half cell required for viewing, =2 for multiple
INTEGER pic_drawinside ! =1 if inside of cell to be drawn
DOUBLE PRECISION wet_time, wet_tstep, wet_endtime, wet_tentry(1000,3)

COMMON/percdata/hgradmin,hgrad,vnwp,pore,size,pvol,press,pc,istart,tvol
COMMON/percstate/custate,rstate
COMMON/wetpercstate/custatep,rstatep,rstated
common/namesample/samplename
common/rambuffer/usebuffer,xstore,ystore,sizestore
common/unitcelldata/a
common/throat/conediam,ibulge,factor
common/wetperctest/pic_size,pic_celtype,pic_drawinside
common/generals/vbi_generalint,vbi_generalreal,vbo_generalint,vbo_generalreal
common/wetangle/wet_theta
COMMON/coneang/coneangle

REAL :: a1ep,a2ep,Ex,Yep,b1ep,b2ep !Variables and constants to calculate perimeter of an Ellipse
! REAL :: perimthroat(1000,3)
real :: perimpore(1000,6) !perimeter of throats, and perim of pores for all 6 sides

REAL :: aspec,wet_advance_um(1000,3) !wet advance in um

! REAL :: accelerate(1000,6) !term that defines the acceleration of fluid rate into pore. Defined as the ratio of
! of the perimeter of the pore over the perimeter of the filling throat (all 6 sides)
REAL :: volthroat,volpore,totvoidvol,fracporevol,fracfillvoids,fracfillpores
REAL :: conerad(1000,3,2),timepic(5),lucwash(1000,3)
integer :: cttimepic(5),bosan
!bosan tells whether one is using the Bosanquet equation or the Lucas-Washburn eqn.
CHARACTER(LEN=40) :: string1
CHARACTER(LEN=1) :: string2
CHARACTER(LEN=4) :: string3

```

CHARACTER(LEN=45) :: string4

a1ep=0.4630151 !constants to calculate perimeter for an ellipse
a2ep=0.1077812
b1ep=0.2452727
b2ep=0.0412496

bosan=0 !zero is for Lucas-washburn and 1 is for Bosanquet Eqn.

wet_tstep=1e-9 ! arbitrarily set

aspec=1.5

fracwetoldw=0.0

smallreal = 1e-20

vbi_generalreal(5)=1e-9 !this tells us the user defined times to plot graphic pictures from the wetting runs

vbi_generalreal(6)=1e-7

vbi_generalreal(7)=1e-5

vbi_generalreal(8)=1e-4

vbi_generalreal(9)=1e-3

do i=1,5

timepic(i)=vbi_generalreal(i+4) !this tells us the user defined times to plot graphic pictures from the wetting runs

ctimepic(i)=floor(timepic(i)/wet_tstep)

if (ctimepic(i)<1) then

ctimepic(i)=1

end if

END do

```
! open(21,file='c:\program files\pore-cor\datafiles\wetperc.csv,status='unknown')
! write (21,*) 'totwet'
! write (21,*) 'cu(991),r(1),r(2),r(3),r(nn1),r(nn2),r(nn3),cu(911),cu(901)'
! write (21,*) cu(881),',',r(991,1),',',r(991,2),',',r(991,3),',',r(1000,1),',',r(981,2),',',r(891,3),&
! &',',cu(911),',',cu(901)
! write (21,*) 'nstep,custatep(901),rstatep(2),cufillrate(2),rstatep(3),cufillrate(3),rstatep(nn1),cufillrate(4),&
! &rstatep(nn2),cufillrate(5),custatep(911),custatep(991),massbal(901),massbal(911),massbal(991)'
! write (21,*) 'nstep,wet_time,custatep(981),rstatep(1),cufillrate(1),rstatep(2),cufillrate(2),rstatep(3),cufillrate(3),&
! &rstatep(nn1),cufillrate(4),&
! &rstatep(nn2),cufillrate(5),rstatep(nn3),cufillrate(6),massbal(991),&
! &mbaldone(991)'
! open(22,file='c:\Program Files\Pore-Cor\datafiles\wetting.csv,status='unknown')
! write (22,*) 'timestep num,timestep,wet-time,%complete,totwet,sqrt(wet_time),wet-time,fracwet'

topthroats=0.0
toppores=0.0
```

!.....
!the below code was needed for calculating the acceleration term of the wetting fluid
!entering the pores, however we are no longer using the acceleration term in the in Lucas-Washburn (bosanquet) eq.
!however the below code is still left as it still calculates the circumference of the throats and pores which is useful.

```
do L=1,1000
do M=1,3
MM=M+3
if (r(L,M,1)>smallreal) then
if (aspec>=1) then
yep=(R(L,M,1)/R(L,M,2))**2
Ex=(1+a1ep*yep+a2ep*yep**2)+(b1ep*yep+b2ep*yep**2)*(LOG(1/yep))
! perimthroat(L,M)=4*R(L,M,2)*Ex
else
yep=(R(L,M,2)/R(L,M,1))**2
Ex=(1+a1ep*yep+a2ep*yep**2)+(b1ep*yep+b2ep*yep**2)*(LOG(1/yep))
! perimthroat(L,M)=4*R(L,M,1)*Ex
END if
else
! perimthroat(L,M)=0
END if

if (Cu(L,1)>smallreal) then
if (M==1) then
perimpore(L,M)=(Cu(L,2)*2)+(Cu(L,3)*2)
perimpore(L,MM)=perimpore(L,M)
else if (M==2) then
perimpore(L,M)=(Cu(L,1)*2)+(Cu(L,3)*2)
perimpore(L,MM)=perimpore(L,M)
else
perimpore(L,M)=(Cu(L,1)*2)+(Cu(L,2)*2)
perimpore(L,MM)=perimpore(L,M)
end if
else
```

```

        perimpore(L,M)=0
        perimpore(L,MM)=0
    END if
!
!   accelerate(L,M)=1
!   accelerate(L,MM)=1
end do
end do

do l = 1,1000
do m = 1,3
conerad(l,m,1) = conediam(l,m,1)/2 ! convert diameter to radius
conerad(l,m,2) = conediam(l,m,2)/2
enddo
enddo

do l=901,1000
if (cu(l,1).gt.smallreal) then
toppores=toppores+cu(l,1)*cu(l,2)*cu(l,3)
END if

do m=1,3

if (r(l,m,1).gt.smallreal) then
topthroats=topthroats+(pi*r(l,m,1)*r(l,m,2)*h(l,m))
end if

end do
end do

!-----
! PRINT*,cu(ne(993,3),3),' ',h(993,3),' ',cu(993,3),' ',a(3),' ',cu(093,3),r(993,3,1)
! general approximations:
! 1. wetting is inertial - no fluid viscosity (equations for visc flow are known - insert later)
! 2. wetting in pore is entirely controlled by rate of supply of fluid from adjacent filled throats
! 3. throat fills with wetting fluid from one direction only - from the direction of the first
! filled adjacent pore (or from the top surface)
! 4. pores can be filled simultaneously by more than one throat
! 5. rate of wetting in throats is independent of rate of supply of fluid from pores
! - this needs to be changed at some point so that flow is restricted when appropriate

! set wetting conditions

fracfillvoids=1 !fraction of voids filled in unit cell

wet_eta = 0.00334 ! kg.m-1.s-1 =0.001 for water, 0.0571 for 1,3-propandiol, 0.00334 for hexadecane
! PRINT *,'what is the viscosity value '
! read *,wet_eta
! wet_eta = 0.071
pressure = 0.0 ! Pa
wet_gamma = vbi_generalreal(1) ! N.m-1
wet_theta=vbi_generalReal(2) ! degrees
wet_rho= vbi_generalReal(3) ! kg.m-3
wet_endtime = vbi_generalReal(4)*1e-6 ! Visual basic endtime is in microseconds, wet_endtime in seconds

wet_param2=wet_gamma*cos(wet_theta*pi/180.0) !

if (wet_tstep.gt.wet_endtime/10.0) wet_tstep = wet_endtime/10.0
! always carry out at least ten steps, however short the endtime

! calculate volume of pores and volume of throats and then calculate percentage of pores in unit cell
! then calculate the percentage of pores unfilled (cuthresh) from percentage of voids unfilled. PB-07-06-01

volthroat=0
volpore=0

do L=1,1000
!volume of pores
volpore=volpore+CU(L,1)*CU(L,2)*CU(L,3)
do m=1,3
!volume of throats
volthroat=volthroat+(PI*H(L,1)*R(L,m,1)*R(L,m,2))
END do
END do

totvoidvol=volpore+volthroat
fracporevol=volpore/totvoidvol

if (fracfillvoids<1) then
fracfillpores=(fracfillvoids*totvoidvol-volthroat)/volpore
cuthresh=fracfillpores ! fractional pore fill when next throats start filling

```

```

else
cuthresh=1.0
end if

PRINT*, 'fill fraction of pores ', fracfillpores, ' total pore fraction ', fracporevol
! (ibulge.eq.7) then ! conical throats ! taken out because only looking at cylindrical throats PB 02-14-00
! do l=1,1000
! do m=1,3
!   ractual(l,m,1)=r(l,m,1) ! storing the actual radii values
!   ractual(l,m,2)=r(l,m,2)
!   if (ractual(l,m,1).lt.1e-10) then
!     r(l,m,1)=0.0
!     r(l,m,2)=0.0
!   else
!     r(l,m,1)=-(cos(wet_theta*pi/180.0)*r(l,m,1))/& ! equation for hold-up due to change in angle at entry to conical throat
&(cos(atan((conediam(l,m,1)-2.0*r(l,m,1))/h(l,m))+((wet_theta-180.0)*pi/180.0)))
!   endif
!   IF(coneangle(l,m)+wet_theta.gt.90)then
!     r(l,m)=0
!   END if
! end do
! end do
! else ! cylindrical throats

do l=1,1000 !cylindrical throats
do m=1,3
ractual(l,m,1)=r(l,m,1) ! storing the actual radii values
ractual(l,m,2)=r(l,m,2)
enddo
enddo
! end if

! RESET THE FEATURES OF THE PORES AND THROATS to use this
! subroutine after polymer pore-plug simulation or porosimetry curve
do l=1,1000
wet_massbal(l)=1.0 ! no mass balance correction initially
custate(l,1)=0 ! ensure no mercury in pore
custatep(l,1)=0.0 ! ensure no mercury in pore
custate(l,4)=0 ! no wetting fluid in pore to start with
custatep(l,4)=0.000 ! no wetting fluid in pore to start with
wet_mbaldone = 0 ! no mass balance done yet
do m=1,3
mm=m+3
rstate(l,m,1)=0 ! ensure no mercury in throat
rstatep(l,m,1)=0.000 ! ensure no mercury in throat
rstate(l,m,1)=0
rstate(l,m,4)=0 ! ensure no wetting fluid in throat
rstatep(l,m,4)=0.0 ! partial degree of filling of throat by wetting fluid = 0.0 at start
rstate(l,m,4)=0 ! setting direction of fill of wetting fluid to zero
wet_cufiltrate(l,m)=0 ! zero fill rate initially from x,y,z throats
wet_cufiltrate(l,mm)=0 ! zero fill rate initially from -x, -y, -z throats
wet_advance(l,m)=0.0
wet_cutentry(l,m)=0.0
! wet_cutentry(l,mm)=0.0
if (l.gt.900.and.m.eq.3) THEN ! topsurface, so starts to fill at time 0
wet_tentry(l,m)= 0.0
else
wet_tentry(l,m)= -1.0 ! dummy value of time of entry to feature to show that this time has not been calculated yet
endif
wet_volrate(l,m)=0.0

if (r(l,m,1).gt.smallreal) then
if (aspec>=1) then
yep=(R(L,M,1)/R(L,M,2))**2
Ex=(1+a1ep*yep+a2ep*yep**2)+(b1ep*yep+b2ep*yep**2)*(LOG(1/yep))
avar(l,m)=(8.0*wet_eta)/((r(l,m,1)*1e-6)*(r(l,m,2)*1e-6)*wet_rho) !calculation needs diameter in m (converts from um
to m)
bvar(l,m)=((pressure*pi*r(l,m,1)*1e-6)+4*Ex*wet_param2)/(pi*r(l,m,1)*1e-6*wet_rho)
lucwash(l,m)=(8*R(l,m,2)*1e-6*Ex*wet_param2)/(2*pi*wet_eta)
! add line above for just using the Lucas Washburn equation -pb 06-12-01
! PRINT *, 'ex ', ex, ' bvar ', bvar(l,m), ' avar ', avar(l,m)
else
yep=(R(L,M,2)/R(L,M,1))**2
Ex=(1+a1ep*yep+a2ep*yep**2)+(b1ep*yep+b2ep*yep**2)*(LOG(1/yep))
avar(l,m)=(8.0*wet_eta)/((r(l,m,1)*1e-6)*(r(l,m,2)*1e-6)*wet_rho) !calculation needs diameter in m (converts from um
to m)
bvar(l,m)=((pressure*pi*r(l,m,2)*1e-6)+4*Ex*wet_param2)/(pi*r(l,m,2)*1e-6*wet_rho)
lucwash(l,m)=(8*R(l,m,1)*1e-6*Ex*wet_param2)/(pi*wet_eta)
END if
END IF
end do

```



```

end do

! Sign convention: filling and movement in throats is positive if increasing in
! +x, +y +z direction. Fill of pores is positive if filling, negative if emptying.
! Therefore negative rstatep less than -1, e.g. -1.2 for throat 997,3 would cause
! positive filling of adjacent pore 997.
! wet_flowin is positive if fluid flowing into pore
! wet_flowout is positive for fluid flowing out of pore
! (keeping both these terms positive makes ratio simpler for mass balance)

wet_nstep = 0 ! time step number
! fracwetoldw= 0.0 ! fractional degree of wetting when fracwet was last written to file
wet_time=0.0

! Calculate advance of wetting fluid relative to pore row spacing (wet_reladvance) for all throats
! to obtain value of wet_reladvancemax, then zero the individual advance values again
wet_reladvancemax = 0.0
do l=1,1000
do m=1,3
if (r(l,m,1).gt.smallreal) then
! avar=(8.0*wet_eta)/(((r(l,m)*1e-6)**2)*wet_rho) ! calculation needs diameter in m
! bvar=((pressure*(r(l,m)*1e-6))+2*wet_param2)/((r(l,m)*1e-6)*wet_rho)
wet_param3=(1/avar(l,m))*(1-exp(-avar(l,m)*wet_tstep))
! wet_advance(l,m)=sqrt((2*bvar(l,m)/avar(l,m))*(wet_tstep-wet_param3)) ! units: metres

if (bosan==1) THEN !for using Bosanquet instead of lucas-washburn
wet_advance(l,m)=sqrt((2*bvar(l,m)/avar(l,m))*(wet_tstep-wet_param3)) ! units: metres
else
wet_advance(l,m)=SQRT(lucwash(l,m)*wet_tstep)
end if

wet_reladvance(l,m)=(wet_advance(l,m)*1e6)/h(l,m) ! wet_advance(l,m) units back in um for unit cell distance
advancement
end if
if (wet_reladvancemax.lt.wet_reladvance(l,m)) then
wet_reladvancemax = wet_reladvance(l,m)
end if
wet_advance(l,m)=0.0
wet_reladvance(l,m)=0.0
end do
end do
print *,wet_reladvancemax ,wet_reladvancemax

100 wet_time = wet_time+wet_tstep ! timestep loop ++++++

wet_nstep = wet_nstep+1

if (mod(wet_nstep,1000).eq.0) then
print *,'calcn ',int(wet_time/wet_endtime*100), '% complete, timestep no.', wet_nstep,'totwet',totwet&
&,'wet_time ',wet_time,'wet_tstep ',wet_tstep
endif

IF(wet_tstep.eq.0.0)then
wet_tstep=0.0
END if

! first, begin to fill throats on top surface of unit cell with wetting fluid from a nominal wetting source
! which supplies them all with as much fluid as they can take in the timestep

do l=901,1000 ! top surface

if(r(l,3,1).gt.smallreal.& ! throat exists
&and.rstate(l,3,1)+rstate(l,3,2)+rstate(l,3,3).eq.0& ! throat not filled with mercury, colloid or polymer
&.and.ABS(rstatep(l,3,4)).lt.1.0) then ! throat not already full of wetting fluid

wet_param1=(1-exp(-avar(l,3)*(wet_time-wet_tentry(l,3))))
wet_param3=(1/avar(l,3))*wet_param1
! wet_advance(l,3)=sqrt((2*bvar(l,3)/avar(l,3))*((wet_time-wet_tentry(l,3))-wet_param3))! in m

if (bosan==1) THEN !for using Bosanquet instead of lucas-washburn
wet_advance(l,3)=sqrt((2*bvar(l,3)/avar(l,3))*((wet_time-wet_tentry(l,3))-wet_param3))! in m
else
wet_advance(l,3)=SQRT(lucwash(l,3)*(wet_time-wet_tentry(l,3)))
end if

rstatep(l,3,4)=(wet_advance(l,3)*1e6)/h(l,3) ! wet_advance units back in um for unit cell distance advancement
! rstatep is rel degree of wetting intrusion, e.g. -0.33 = 1/3rd intruded in negative direction

! if (ibulge.eq.7) then ! conical throats, so instantly fill 2nd half of feature !not doing conical throats
! if(rstatep(l,3,4).ge.0.5) rstatep(l,3,4)=1.0
! if(rstatep(l,3,4).lt.-0.5) rstatep(l,3,4)=-1.0 ! instant fill in negative direction

```

```

!      end if

rstate(l,3,4)=1 ! all initial throats flow into pore in negative z direction

if (abs(rstate(l,3,4)).ge.1.000) then ! throat is full of wetting fluid so calculate filling rate of connected pore
  if (wet_cufillrate(l,3).lt.smallreal) then ! fill rate not calculated already

    if (bosan==1) then
      wet_volrate(l,3)=sqrt((bvar(l,3)*wet_param1**2)/(2*avar(l,3)*(wet_time-wet_tentry(l,3)-wet_param3)))
      !Cathy's derivation of the fluid rate
    ! wet_volrate(l,3)=(SQRT(bvar(l,3))*(1-EXP(-avar(l,3)*(wet_time-wet_tentry(l,3)))))/&
    ! &(SQRT(2*(avar(l,3)*(wet_time-wet_tentry(l,3))-1+EXP(-avar(l,3)*(wet_time-wet_tentry(l,3)))))
    !Ian Roy and Pau's derivation of the fluid rate for elliptical and cylindrical throats m/s -PB 05-12-01
    else
      wet_volrate(l,3)=0.5*((lucwash(l,3)/(wet_time-wet_tentry(l,3)))**0.5)
    endif

    wet_cufillrate(l,3)=wet_volrate(l,3)*1e6*pi*ractual(l,3,1)*ractual(l,3,2)
    ! volume rate of wetting fluid um3.s-1 which enters pore
    endif ! end of fill rate not calculated already
  endif ! end of throat is full of wetting fluid
end if ! end of throat exists
end do ! end of top surface

! now go through the rest of the throats, and fill them if they have adjacent filled pores.
! (Obviously nothing will happen in this loop for the first few time steps.)
! at the moment, this rate of filling is independent of the amount of fluid in the pore, so there will be
! mass conservation errors - need to change this later

do l=1,1000 ! temporary 1 -> 901 for debug
  do m=1,3
    mm=m+3

    if (l.lt.901.or.m.ne.3) then ! not already calculated in block above

      if(r(l,m,1).gt.smallreal.& ! throat exists
      &and.(rstate(l,m,1)+rstate(l,m,2)+rstate(l,m,3)).eq.0) then ! throat not filled with mercury, colloid or polymer

        IF(wet_mbaldone(l).lt.2) then

          if (custatep(l,4).ge.cuthresh.and.rstate(l,m,4).ge.0) then ! pore connected to this throat is
            ! sufficiently full, and throat is empty or filling in positive direction
          IF(wet_tentry(l,m).LT.smallreal) THEN ! entry time not already calculated, so set now
            wet_tentry(l,m)=wet_time
          ENDIF

          wet_param1=(1-exp(-avar(l,m)*(wet_time-wet_tentry(l,m))))
          wet_param3=(1/avar(l,m))*wet_param1

          IF(ABS(rstatep(l,m,4)).lt.1.000) THEN ! throat is not yet full, so need to calculate its varying fill rate

            if (wet_time-wet_tentry(l,m).le.0.0) then
              wet_advance(l,m)=0.0
              wet_volrate(l,m)=0.0
            else

              if (bosan==1) THEN !for using Bosanquet instead of lucas-washburn
                wet_advance(l,m)=sqrt((2*bvar(l,m)/avar(l,m))*((wet_time-wet_tentry(l,m))-wet_param3))! in m
              else
                wet_advance(l,m)=SQRT(lucwash(l,m)*(wet_time-wet_tentry(l,m)))
              end if

              rstatep(l,m,4)=(wet_advance(l,m)*1e6)/h(l,m) ! wet_advance units back in um for unit cell distance advancement
              ! rstatep is rel degree of wetting intrusion, e.g. -0.33 = 1/3rd intruded in negative direction

              if (ibulge.eq.7) then ! instant fill of second half of cones
                if (rstatep(l,m,4).ge.0.5) rstatep(l,m,4)=1.0
                if (rstatep(l,m,4).lt.-0.5) rstatep(l,m,4)=-1.0
              end if

              if (abs(rstatep(l,m,4)).ge.1.000) then ! throat is full of wetting fluid so calculate filling rate of connected pore
                !
                IF(wet_cutentry(ne(l,m),mm).lt.smallreal) then
                  wet_cutentry(ne(l,m),mm)=wet_time
                END if
              !

              if (bosan==1) then
                wet_volrate(l,m)=sqrt((bvar(l,m)*wet_param1**2)/(2*avar(l,m)*(wet_time-wet_tentry(l,m)-wet_param3)))
                !wet_volrate(l,m)=(SQRT(bvar(l,m))*(1-EXP(-avar(l,m)*(wet_time-wet_tentry(l,m)))))&
                !&(SQRT(2*(avar(l,m)*(wet_time-wet_tentry(l,m))-1+EXP(-avar(l,m)*(wet_time-wet_tentry(l,m)))))
              else
                wet_volrate(l,m)=0.5*((lucwash(l,m)/(wet_time-wet_tentry(l,m)))**0.5)
              end if
            end if
          end if
        end if
      end do
    end do
  end do

```

```

endif

wet_cufillrate(ne(l,m),mm)=wet_volrate(l,m)*1e6*pi*ractual(l,m,1)*ractual(l,m,2)
! volume of wetting fluid um3 which enters positive neighbour pore per second
wet_cufillrate(l,m) = -wet_cufillrate(ne(l,m),mm) ! volume of fluid leaving pore itself
end if
endif
END if

if (rstated(l,m,4).eq.0) rstated(l,m,4) = 1 ! throat has started filling in positive direction - so indicate this

! throats filling in a positive Cartesian direction are emptying their own pore
! They do this at a variable rate, as they fill, due to viscous forces building
! up. Once they are full, the cufillrate becomes constant.

else if(abs(custatep(ne(l,m),4)).ge.cuthresh.and.rstated(l,m,4).le.0)then ! adjacent pore sufficiently
! full, and throat is empty or filling in negative direction
IF(wet_tentry(l,m).LT.smallreal) THEN ! entry time not already calculated, so set now
wet_tentry(l,m)=wet_time
ENDIF

wet_param1=(1-exp(-avar(l,m)*(wet_time-wet_tentry(l,m))))
wet_param3=(1/avar(l,m))*wet_param1

IF(ABS(rstatep(l,m,4)).lt.1.000) THEN

IF(wet_time-wet_tentry(l,m).eq.0.0)then
wet_advance(l,m)=0.0
wet_volrate(l,m)=0.0
else

if (bosan==1) THEN !for using Bosanquet instead of lucas-washburn
wet_advance(l,m)=sqrt((2*bvar(l,m)/avar(l,m))*((wet_time-wet_tentry(l,m))-wet_param3))! in m
else
wet_advance(l,m)=SQRT(lucwash(l,m)*(wet_time-wet_tentry(l,m)))
end if

rstatep(l,m,4)=(wet_advance(l,m)*1e6)/h(l,m) ! wet_advance units back in um for unit cell distance advancement
! rstatep is rel degree of wetting intrusion, e.g. -0.33 = 1/3rd intruded in negative direction
! unmassbalanced pore vol fillrate

! if (ibulge.eq.7) then !not doing conical throats 17-02-01 pb
! if(rstatep(l,m,4).ge.0.5) rstatep(l,m,4)=1.0
! if(rstatep(l,m,4).lt.-0.5) rstatep(l,m,4)=-1.0
! END if

if (abs(rstatep(l,m,4)).ge.1.000) then ! throat is full of wetting fluid so calculate filling rate of connected pore
! IF(wet_cutentry(l,m).lt.smallreal) then
! wet_cutentry(l,m)=wet_time
! END if

if (bosan==1) then
wet_volrate(l,m)=sqrt((bvar(l,m)*wet_param1**2)/(2*avar(l,m)*(wet_time-wet_tentry(l,m)-wet_param3)))
!wet_volrate(l,m)=(SQRT(bvar(l,m))*(1-EXP(-avar(l,m)*(wet_time-wet_tentry(l,m)))))/&
!&(SQRT(2*(avar(l,m)*(wet_time-wet_tentry(l,m))-1+EXP(-avar(l,m)*(wet_time-wet_tentry(l,m))))))
else
wet_volrate(l,m)=0.5*((lucwash(l,m)/(wet_time-wet_tentry(l,m)))**(0.5))
endif
! unmassbalanced pore vol fillrate
wet_cufillrate(l,m)=wet_volrate(l,m)*1e6*pi*ractual(l,m,1)*ractual(l,m,2)
! volume of wetting fluid um3 which enters pore during wet_tstep
wet_cufillrate(ne(l,m),mm) = - wet_cufillrate(l,m) ! volume of fluid leaving neighbouring pore
endif
END if
END if

if (rstated(l,m,4).eq.0) rstated(l,m,4) = -1 ! throat has started filling in negative direction - so indicate this

end if
END if ! massbalance =2
endif
enddo
enddo

! now fill pores with wetting fluid, at a rate determined by the
! total supply from all the adjacent throats, as already calculated
do l=1,1000

if(cu(l,1).gt.1e-10) then ! pore exists, so calculate its overall fill rate

```

```

if (custatep(l,4).lt.cuthresh.and.custatep(l,4).ge.0.0.or.wet_mbaldone(l).eq.2) goto 444 ! if pore not sufficiently full,
! or already skipped, miss mass balance calculation

```

```

! skip mass balance calcn if done once when all adjacent existing throats are full
notfullflag=0 ! 0 if full, 1 if partially full
do m=1,3
if (ABS(rstatep(l,m,4)).lt.1.0.and.r(l,m,1).gt.smallreal) then ! throat exists but not full
notfullflag=1
end if
if (ABS(rstatep(nn(l,m),m,4)).lt.1.0.and.r(nn(l,m),m,1).gt.smallreal) then ! throat exists but not full
notfullflag=1
end if
enddo
if (wet_mbaldone(l).eq.1.and.notfullflag.eq.0) then ! mass balance previously calculated, and all existing throats full
wet_mbaldone(l)=2 ! to show it has been checked, and should be skipped next time
end if
! end of skip mass balance calcn

```

```

wet_flowin=0.0
wet_flowout=0.0

```

```

! calculate total flow in and total flow out, if more flows out than in then massbalance
do m=1,6
if (wet_cufillrate(l,m).gt.0.0) then
wet_flowin=wet_flowin+wet_cufillrate(l,m)
else
wet_flowout=wet_flowout-wet_cufillrate(l,m) ! negative here keeps flowout positive
endif
enddo

```

```

if (wet_mbaldone(l).lt.2) then
wet_mbaldone(l)=1 ! mass balance for this pore has been checked at least once
end if

```

```

! if wet_massbal > 1, then more flowing into pore than out - cannot correct for this at the moment
! if wet_massbal < 1, multiply outflowing wet_cufillrates, wet_advances and wet_reladvances by wetmassbal
! if wet_bassbal=0 then no outflow although pore could be filling up

```

```

if (wet_flowout.gt.wet_flowin) then
wet_massbal(l) = wet_flowin/wet_flowout

```

```

do m=1,3
mm=m+3

```

```

IF(ABS(rstatep(l,m,4)).gt.smallreal.and.ABS(rstatep(l,m,4)).lt.1.0)then ! partially filled
IF(wet_advance(l,m).gt.0.0)then ! partially filled throat flowing out
wet_advance(l,m)=wet_massbal(l)*wet_advance(l,m)
rstatep(l,m,4)=(wet_advance(l,m)*1e6)/h(l,m)
wet_cufillrate(l,m)=wet_massbal(l)*wet_cufillrate(l,m)
END if
else if (ABS(rstatep(l,m,4)).gt.1.0) then ! full throat
IF(wet_cufillrate(l,m).lt.0.0)then ! full throat flowing out
wet_cufillrate(l,m)=wet_massbal(l)*wet_cufillrate(l,m)
wet_cufillrate(ne(l,m),mm)=-wet_cufillrate(l,m)
END if
END if
IF(ABS(rstatep(nn(l,m),m,4)).gt.smallreal.and.ABS(rstatep(nn(l,m),m,4)).lt.1.0)then ! partially filled
IF(wet_advance(nn(l,m),m).lt.0.0)then ! partially filled throat flowing out
wet_advance(nn(l,m),m)=wet_massbal(l)*wet_advance(nn(l,m),m)
rstatep(nn(l,m),m,4)=(wet_advance(nn(l,m),m)*1e6)/h(nn(l,m),m)
wet_cufillrate(l,mm)=wet_massbal(l)*wet_cufillrate(l,mm)
END if
else if (ABS(rstatep(nn(l,m),m,4)).gt.1.0) then ! full throat
IF(wet_cufillrate(l,mm).lt.0.0)then ! full throat flowing out
wet_cufillrate(l,mm)=wet_massbal(l)*wet_cufillrate(l,mm)
wet_cufillrate(nn(l,m),m)=-wet_cufillrate(l,mm)
END if
END if
end do
END if

```

```

444 continue ! miss mass balance calculation

```

```

do m=1,3
mm=m+3
if (rstatep(l,m,4).LE.-1.0)then
custatep(l,4) = custatep(l,4)+((wet_tstep)*wet_cufillrate(l,m))/(cu(l,1)*cu(l,2)*cu(l,3)) ! flow in
endif
if (rstatep(nn(l,m),m,4).ge.1.0)then

```

```

    custatep(l,4)= custatep(l,4)+((wet_tstep)*wet_cufillrate(l,mm))/(cu(l,1)*cu(l,2)*cu(l,3)) ! flow in
  endif
  if (wet_cufillrate(l,m).lt.0)then
    custatep(l,4)=custatep(l,4)+((wet_tstep)*wet_cufillrate(l,m))/(cu(l,1)*cu(l,2)*cu(l,3)) ! flow out
  endif
  if (wet_cufillrate(l,mm).lt.0)then
    custatep(l,4)=custatep(l,4)+((wet_tstep)*wet_cufillrate(l,mm))/(cu(l,1)*cu(l,2)*cu(l,3)) ! flow out
  endif
END do

! debug printout
! IF(l.eq.981) then
! IF(MOD(wet_nstep,100).eq.0.or.wet_nstep.lt.100.or.wet_nstep.gt.2300.and.wet_nstep.lt.2400) THEN
! write (21,609) wet_nstep,wet_time,custatep(l,4),rstatep(l,1,4),wet_cufillrate(l,1),rstatep(l,2,4),wet_cufillrate(l,2),&
! &rstatep(l,3,4),wet_cufillrate(l,3),&
! &rstatep(nn(l,1),1,4),wet_cufillrate(l,4),rstatep(nn(l,2),2,4),wet_cufillrate(l,5),&
! &rstatep(nn(l,3),3,4),wet_cufillrate(l,6)&
! &,wet_massbal(991),wet_mbaldone(991)
! 609 format (i5,',',15(g13.5,','))
! END if
! END if
! end of debug printout

END if
enddo

if (wet_time.lt.wet_tstep*1000.OR.mod(wet_nstep,100).eq.0.or.wet_time.ge.wet_endtime) then ! Interim totwet calcn
*****
! if (fracwet-fracwetoldw.gt.0.001.or.wet_time.ge.wet_endtime) then ! interim totwet calcn *****
totwet=0.0

! pores
do l=1,1000
if(cu(l,1).gt.smallreal)then
if (abs(custatep(l,4)).gt.smallreal)then

if (abs(custatep(l,4)).gt.1.000) then ! pore is full
totwet=totwet+(cu(l,1)*cu(l,2)*cu(l,3))
else ! pore is partially full
totwet=totwet+abs(custatep(l,4))*(cu(l,1)*cu(l,2)*cu(l,3))
endif

end if
end if

! throats
do m=1,3
if(r(l,m,1).gt.smallreal) then ! throat exists
if (ibulge.eq.0) then ! cylindrical throat

if (abs(rstatep(l,m,4)).gt.smallreal.and.abs(rstatep(l,m,4)).lt.1.00) then ! throat is partially full
totwet=totwet+abs(rstatep(l,m,4))*pi*r(l,m,1)*r(l,m,2)*h(l,m)
else if (abs(rstatep(l,m,4)).ge.1.0) then ! throat is full
totwet=totwet+pi*r(l,m,1)*r(l,m,2)*h(l,m)
endif

! else if (ibulge.eq.7) then ! double conical throat
! if (abs(rstatep(l,m,4)).gt.smallreal.and.abs(rstatep(l,m,4)).lt.1.00) then ! throat is partially full
! totwet=totwet+((pi*H(l,M)*(conediam(l,M)**3-&
! &8.0*Ractual(l,M)**3))/(12.0*(conediam(l,M)-2.0*Ractual(l,M))))*abs(rstatep(l,m,4))

! else if (abs(rstatep(l,m,4)).ge.1.0) then ! throat is full
! totwet=totwet+(pi*H(l,M)*(conediam(l,M)**3-&
! &8.0*Ractual(l,M)**3))/(12.0*(conediam(l,M)-2.0*Ractual(l,M)))

! end if
end if ! end of cylindrical throat
end if ! end of throat exists
enddo ! end do m=1,3
enddo ! end of do 1,1000

fracwet=totwet/vol ! fraction of total pore and throat vol in um3 (=vol) which is wetted

! if (wet_time.lt.wet_tstep*20.or.fracwet-fracwetoldw.gt.0.001.or.wet_time.ge.wet_endtime) then ! print to file
if (wet_time.lt.wet_tstep*100.or.fracwet-fracwetoldw.gt.0.001.or.wet_time.ge.wet_endtime) then ! print to file

fracwetoldw=fracwet

write (22,608) wet_nstep, wet_tstep,wet_time,&
&int(wet_time/wet_endtime*100), totwet, SQRT(wet_time), wet_time, fracwet

```

```
608 format (i3,1,2(g13.5,1),i3,1,4(g13.5,1))
```

```
end if ! end of print results loop
```

!—set values of integers custate and rstate for wetting fluid based on real values of custatep and rstatep

```
do i=1,1000
  if (ABS(custatep(i,4)).gt.smallreal) then ! pore has some wetting fluid in it
    custate(i,4) = 1
  end if
  do m = 1,3
    if (ABS(rstatep(i,m,4)).gt.smallreal) then ! throat has some wetting fluid in it
      rstate(i,m,4) = 1
    end if
  end do
end do
```

!—this is the code for creating the csv file for the VRML picture—

```
do i=1,5
  if (ctimepic(i)==wet_nstep) then

    string1='c:\Program Files\Pore-Cor\datafiles\cell'
    !
    ! if (i==1) then
    ! string2 = '1'
    ! ELSEIF (i==2) then
    ! string2 = '2'
    ! ELSEIF (i==3) then
    ! string2 = '3'
    ! ELSEIF (i==4) then
    ! string2 = '4'
    ! ELSEIF (i==5) then
    ! string2 = '5'
    ! end if

    string2=ACHAR(i+48)
    string3='.csv'
    string4=string1//string2//string3

    open (unit=296,file=string4,status='replace')
    write(296,421)
    do i=1,1000
      write(296,422) ibulge,L,CU(L,1),CU(L,2),CU(L,3),r(L,1,1),r(L,2,1),r(L,3,1),&
&r(L,1,2),r(L,2,2),r(L,3,2),h(L,1),h(L,2),h(L,3),& ! throat lengths
&conerad(L,1,1),conerad(L,2,1),conerad(L,3,1),& ! cone throats max diameter,
&conerad(L,1,2),conerad(L,2,2),conerad(L,3,2),&
&custate(L,1),custate(L,2),custate(L,3),custate(L,4),&
! pores full of mercury, colloid, polymer, wetting fluid (empty=0, full or partially full =1)
&rstate(L,1,1),rstate(L,1,2),rstate(L,1,3),rstate(L,1,4),&
! throats in x direction full of mercury, colloid, polymer, wetting fluid
&rstate(L,2,1),rstate(L,2,2),rstate(L,2,3),rstate(L,2,4),&
! throats in y direction full of mercury, colloid, polymer, wetting fluid
&rstate(L,3,1),rstate(L,3,2),rstate(L,3,3),rstate(L,3,4),&
! throats in z direction full of mercury, colloid, polymer, wetting fluid
&custatep(L,1),custatep(L,2),custatep(L,3),custatep(L,4),&
! fraction of pores full of mercury, colloid, polymer, wetting fluid
&rstatep(L,1,1),rstatep(L,1,2),rstatep(L,1,3),rstatep(L,1,4),&
! fraction of throats in x direction full of mercury, colloid, polymer, wetting fluid
&rstatep(L,2,1),rstatep(L,2,2),rstatep(L,2,3),rstatep(L,2,4),&
! fraction of throats in y direction full of mercury, colloid, polymer, wetting fluid
&rstatep(L,3,1),rstatep(L,3,2),rstatep(L,3,3),rstatep(L,3,4),&
! fraction of throats in z direction full of mercury, colloid, polymer, wetting fluid
!(continuation...(if corresponding integer = 1, then e.g. 0.5 = half full)
&a(1),a(2),a(3),wet_tstep,wet_time,totwet,fracwet
END do
END if
END do
close (296)

421 format ('cylinders or cones?','pore number','pore_length-x-axis','pore length-y-axis','&
&'pore_length-z-axis','x thr rad 1','y thr rad 1','z thr rad 1','x thr rad 2','y thr rad 2','&
&'z thr rad 2','x thr length','y thr length','z thr length','x thr concl rad 1','&
&'y thr concl rad 1','z thr concl rad 1','x thr concl rad 2','y thr concl rad 2','&
&'z thr concl rad 2','pore full of Hg?','pore full of cld?','pore full of polymr?','&
&'pore full of wetting fluid?','x thr full of Hg?','x thr full of cld?','x thr full of polymr?','&
&'x thr full of wetting fluid?','y thr full of Hg?','y thr full of cld?','y thr full of polymr?','&
&'y thr full of wetting fluid?','z thr full of Hg?','z thr full of cld?','&
&'z thr full of polymr?','z thr full of wetting fluid?','pore frac fill Hg/wet-fluid','&
&'pore frac fill cld','pore frac fill polymr','pore frac fill wetting fluid','&
&'x thr frac fill Hg','x thr frac fill cld','x thr frac fill polymr','&
```

```

&x thr frac fill wetting fluid,'y thr frac fill Hg','y thr frac fill cld','y thr frac fill polymr','&
&y thr frac fill wetting fluid','z thr frac fill Hg','z thr frac fill cld','z thr frac fill polymr','&
&z thr frac fill wetting fluid','x-p-row-spacing','y-p-row-spacing','z-p-row-spacing','&
&wet_tstep,'wet_time','totwet','fracwet')

```

422 FORMAT (2(i5,''),18(f24.16,''),16(i5,''),19(f24.16,''),4(f24.16,''))

-----used for Pau's research-----

```

select case (wet_nstep)

```

```

case (1)

```

```

open (unit=66,file='c:\Program Files\Pore-Cor\datafiles\wetpara1.csv,status='replace')
write(66,755)
do I=1,1000
write(66,760) ibulge,L,CU(L,1),CU(L,2),CU(L,3),r(L,1,1),r(L,2,1),r(L,3,1),&
&r(L,1,2),r(L,2,2),r(L,3,2),h(L,1),h(L,2),h(L,3),& ! throat lengths
&conerad(L,1,1),conerad(L,2,1),conerad(L,3,1),& ! cone throats max diameter,
&conerad(L,1,2),conerad(L,2,2),conerad(L,3,2),&
&custate(L,1),custate(L,2),custate(L,3),custate(L,4),&
! pores full of mercury, colloid, polymer, wetting fluid (empty=0, full or partially full =1)
&rstate(L,1,1),rstate(L,1,2),rstate(L,1,3),rstate(L,1,4),&
! throats in x direction full of mercury, colloid, polymer, wetting fluid
&rstate(L,2,1),rstate(L,2,2),rstate(L,2,3),rstate(L,2,4),&
! throats in y direction full of mercury, colloid, polymer, wetting fluid
&rstate(L,3,1),rstate(L,3,2),rstate(L,3,3),rstate(L,3,4),&
! throats in z direction full of mercury, colloid, polymer, wetting fluid
&custatep(L,1),custatep(L,2),custatep(L,3),custatep(L,4),&
! fraction of pores full of mercury, colloid, polymer, wetting fluid
&rstatep(L,1,1),rstatep(L,1,2),rstatep(L,1,3),rstatep(L,1,4),&
! fraction of throats in x direction full of mercury, colloid, polymer, wetting fluid
&rstatep(L,2,1),rstatep(L,2,2),rstatep(L,2,3),rstatep(L,2,4),&
! fraction of throats in y direction full of mercury, colloid, polymer, wetting fluid
&rstatep(L,3,1),rstatep(L,3,2),rstatep(L,3,3),rstatep(L,3,4),&
! fraction of throats in z direction full of mercury, colloid, polymer, wetting fluid
!(continuation...(if corresponding integer = 1, then e.g. 0.5 = half full)
&a(1),a(2),a(3),wet_tstep,wet_time,totwet,fracwet
end do

```

```

CASE (10)

```

```

open (unit=66,file='c:\Program Files\Pore-Cor\datafiles\wetpara2.csv,status='replace')
write(66,755)
do I=1,1000
write(66,760) ibulge,L,CU(L,1),CU(L,2),CU(L,3),r(L,1,1),r(L,2,1),r(L,3,1),&
&r(L,1,2),r(L,2,2),r(L,3,2),h(L,1),h(L,2),h(L,3),& ! throat lengths
&conerad(L,1,1),conerad(L,2,1),conerad(L,3,1),& ! cone throats max diameter,
&conerad(L,1,2),conerad(L,2,2),conerad(L,3,2),&
&custate(L,1),custate(L,2),custate(L,3),custate(L,4),&
! pores full of mercury, colloid, polymer, wetting fluid (empty=0, full or partially full =1)
&rstate(L,1,1),rstate(L,1,2),rstate(L,1,3),rstate(L,1,4),&
! throats in x direction full of mercury, colloid, polymer, wetting fluid
&rstate(L,2,1),rstate(L,2,2),rstate(L,2,3),rstate(L,2,4),&
! throats in y direction full of mercury, colloid, polymer, wetting fluid
&rstate(L,3,1),rstate(L,3,2),rstate(L,3,3),rstate(L,3,4),&
! throats in z direction full of mercury, colloid, polymer, wetting fluid
&custatep(L,1),custatep(L,2),custatep(L,3),custatep(L,4),&
! fraction of pores full of mercury, colloid, polymer, wetting fluid
&rstatep(L,1,1),rstatep(L,1,2),rstatep(L,1,3),rstatep(L,1,4),&
! fraction of throats in x direction full of mercury, colloid, polymer, wetting fluid
&rstatep(L,2,1),rstatep(L,2,2),rstatep(L,2,3),rstatep(L,2,4),&
! fraction of throats in y direction full of mercury, colloid, polymer, wetting fluid
&rstatep(L,3,1),rstatep(L,3,2),rstatep(L,3,3),rstatep(L,3,4),&
! fraction of throats in z direction full of mercury, colloid, polymer, wetting fluid
!(continuation...(if corresponding integer = 1, then e.g. 0.5 = half full)
&a(1),a(2),a(3),wet_tstep,wet_time,totwet,fracwet
END do

```

```

CASE (100)

```

```

open (unit=66,file='c:\Program Files\Pore-Cor\datafiles\wetpara3.csv,status='replace')
write(66,755)
do I=1,1000
write(66,760) ibulge,L,CU(L,1),CU(L,2),CU(L,3),r(L,1,1),r(L,2,1),r(L,3,1),&
&r(L,1,2),r(L,2,2),r(L,3,2),h(L,1),h(L,2),h(L,3),& ! throat lengths
&conerad(L,1,1),conerad(L,2,1),conerad(L,3,1),& ! cone throats max diameter,
&conerad(L,1,2),conerad(L,2,2),conerad(L,3,2),&
&custate(L,1),custate(L,2),custate(L,3),custate(L,4),&
! pores full of mercury, colloid, polymer, wetting fluid (empty=0, full or partially full =1)
&rstate(L,1,1),rstate(L,1,2),rstate(L,1,3),rstate(L,1,4),&
! throats in x direction full of mercury, colloid, polymer, wetting fluid

```

```

&rstate(L,2,1),rstate(L,2,2),rstate(L,2,3),rstate(L,2,4),&
! throats in y direction full of mercury, colloid, polymer, wetting fluid
&rstate(L,3,1),rstate(L,3,2),rstate(L,3,3),rstate(L,3,4),&
! throats in z direction full of mercury, colloid, polymer, wetting fluid
&custate(L,1),custate(L,2),custate(L,3),custate(L,4),&
! fraction of pores full of mercury, colloid, polymer, wetting fluid
&rstate(L,1,1),rstate(L,1,2),rstate(L,1,3),rstate(L,1,4),&
! fraction of throats in x direction full of mercury, colloid, polymer, wetting fluid
&rstate(L,2,1),rstate(L,2,2),rstate(L,2,3),rstate(L,2,4),&
! fraction of throats in y direction full of mercury, colloid, polymer, wetting fluid
&rstate(L,3,1),rstate(L,3,2),rstate(L,3,3),rstate(L,3,4),&
! fraction of throats in z direction full of mercury, colloid, polymer, wetting fluid
!(continuation...(if corresponding integer = 1, then e.g. 0.5 = half full)
&a(1),a(2),a(3),wet_tstep,wet_time,totwet,fracwet
END do

```

CASE (1000)

```

open (unit=66,file='c:\Program Files\Pore-Co\datafiles\wetpara4.csv',status='replace')
write(66,755)
do I=1,1000
write(66,760) ibulge,L,CU(L,1),CU(L,2),CU(L,3),r(L,1,1),r(L,2,1),r(L,3,1),&
&r(L,1,2),r(L,2,2),r(L,3,2),h(L,1),h(L,2),h(L,3),& ! throat lengths
&conerad(L,1,1),conerad(L,2,1),conerad(L,3,1),& ! cone throats max diameter,
&conerad(L,1,2),conerad(L,2,2),conerad(L,3,2),&
&custate(L,1),custate(L,2),custate(L,3),custate(L,4),&
! pores full of mercury, colloid, polymer, wetting fluid (empty=0, full or partially full =1)
&rstate(L,1,1),rstate(L,1,2),rstate(L,1,3),rstate(L,1,4),&
! throats in x direction full of mercury, colloid, polymer, wetting fluid
&rstate(L,2,1),rstate(L,2,2),rstate(L,2,3),rstate(L,2,4),&
! throats in y direction full of mercury, colloid, polymer, wetting fluid
&rstate(L,3,1),rstate(L,3,2),rstate(L,3,3),rstate(L,3,4),&
! throats in z direction full of mercury, colloid, polymer, wetting fluid
&custate(L,1),custate(L,2),custate(L,3),custate(L,4),&
! fraction of pores full of mercury, colloid, polymer, wetting fluid
&rstate(L,1,1),rstate(L,1,2),rstate(L,1,3),rstate(L,1,4),&
! fraction of throats in x direction full of mercury, colloid, polymer, wetting fluid
&rstate(L,2,1),rstate(L,2,2),rstate(L,2,3),rstate(L,2,4),&
! fraction of throats in y direction full of mercury, colloid, polymer, wetting fluid
&rstate(L,3,1),rstate(L,3,2),rstate(L,3,3),rstate(L,3,4),&
! fraction of throats in z direction full of mercury, colloid, polymer, wetting fluid
!(continuation...(if corresponding integer = 1, then e.g. 0.5 = half full)
&a(1),a(2),a(3),wet_tstep,wet_time,totwet,fracwet
END do

```

CASE (10000)

```

open (unit=66,file='c:\Program Files\Pore-Co\datafiles\wetpara5.csv',status='replace')
write(66,755)
do I=1,1000
write(66,760) ibulge,L,CU(L,1),CU(L,2),CU(L,3),r(L,1,1),r(L,2,1),r(L,3,1),&
&r(L,1,2),r(L,2,2),r(L,3,2),h(L,1),h(L,2),h(L,3),& ! throat lengths
&conerad(L,1,1),conerad(L,2,1),conerad(L,3,1),& ! cone throats max diameter,
&conerad(L,1,2),conerad(L,2,2),conerad(L,3,2),&
&custate(L,1),custate(L,2),custate(L,3),custate(L,4),&
! pores full of mercury, colloid, polymer, wetting fluid (empty=0, full or partially full =1)
&rstate(L,1,1),rstate(L,1,2),rstate(L,1,3),rstate(L,1,4),&
! throats in x direction full of mercury, colloid, polymer, wetting fluid
&rstate(L,2,1),rstate(L,2,2),rstate(L,2,3),rstate(L,2,4),&
! throats in y direction full of mercury, colloid, polymer, wetting fluid
&rstate(L,3,1),rstate(L,3,2),rstate(L,3,3),rstate(L,3,4),&
! throats in z direction full of mercury, colloid, polymer, wetting fluid
&custate(L,1),custate(L,2),custate(L,3),custate(L,4),&
! fraction of pores full of mercury, colloid, polymer, wetting fluid
&rstate(L,1,1),rstate(L,1,2),rstate(L,1,3),rstate(L,1,4),&
! fraction of throats in x direction full of mercury, colloid, polymer, wetting fluid
&rstate(L,2,1),rstate(L,2,2),rstate(L,2,3),rstate(L,2,4),&
! fraction of throats in y direction full of mercury, colloid, polymer, wetting fluid
&rstate(L,3,1),rstate(L,3,2),rstate(L,3,3),rstate(L,3,4),&
! fraction of throats in z direction full of mercury, colloid, polymer, wetting fluid
!(continuation...(if corresponding integer = 1, then e.g. 0.5 = half full)
&a(1),a(2),a(3),wet_tstep,wet_time,totwet,fracwet
END do

```

CASE (100000)

```

open (unit=66,file='c:\Program Files\Pore-Co\datafiles\wetpara6.csv',status='replace')
write(66,755)
do I=1,1000
write(66,760) ibulge,L,CU(L,1),CU(L,2),CU(L,3),r(L,1,1),r(L,2,1),r(L,3,1),&
&r(L,1,2),r(L,2,2),r(L,3,2),h(L,1),h(L,2),h(L,3),& ! throat lengths
&conerad(L,1,1),conerad(L,2,1),conerad(L,3,1),& ! cone throats max diameter,

```



```

&conerad(L,1,2),conerad(L,2,2),conerad(L,3,2),&
&custate(L,1),custate(L,2),custate(L,3),custate(L,4),&
! pores full of mercury, colloid, polymer, wetting fluid (empty=0, full or partially full =1)
&rstate(L,1,1),rstate(L,1,2),rstate(L,1,3),rstate(L,1,4),&
! throats in x direction full of mercury, colloid, polymer, wetting fluid
&rstate(L,2,1),rstate(L,2,2),rstate(L,2,3),rstate(L,2,4),&
! throats in y direction full of mercury, colloid, polymer, wetting fluid
&rstate(L,3,1),rstate(L,3,2),rstate(L,3,3),rstate(L,3,4),&
! throats in z direction full of mercury, colloid, polymer, wetting fluid
&custate(L,1),custate(L,2),custate(L,3),custate(L,4),&
! fraction of pores full of mercury, colloid, polymer, wetting fluid
&rstate(L,1,1),rstate(L,1,2),rstate(L,1,3),rstate(L,1,4),&
! fraction of throats in x direction full of mercury, colloid, polymer, wetting fluid
&rstate(L,2,1),rstate(L,2,2),rstate(L,2,3),rstate(L,2,4),&
! fraction of throats in y direction full of mercury, colloid, polymer, wetting fluid
&rstate(L,3,1),rstate(L,3,2),rstate(L,3,3),rstate(L,3,4),&
! fraction of throats in z direction full of mercury, colloid, polymer, wetting fluid
!(continuation...(if corresponding integer = 1, then e.g. 0.5 = half full)
&a(1),a(2),a(3),wet_tstep,wet_time,totwet,fracwet
END do

CASE (1000000)
open (unit=66,file='c:\Program Files\Pore-Cor\datafiles\wetpara7.csv,status='replace')
write(66,755)
do I=1,1000
write(66,760) ibulge,L,CU(L,1),CU(L,2),CU(L,3),r(L,1,1),r(L,2,1),r(L,3,1),&
&r(L,1,2),r(L,2,2),r(L,3,2),h(L,1),h(L,2),h(L,3),& ! throat lengths
&conerad(L,1,1),conerad(L,2,1),conerad(L,3,1),& ! cone throats max diameter,
&conerad(L,1,2),conerad(L,2,2),conerad(L,3,2),&
&custate(L,1),custate(L,2),custate(L,3),custate(L,4),&
! pores full of mercury, colloid, polymer, wetting fluid (empty=0, full or partially full =1)
&rstate(L,1,1),rstate(L,1,2),rstate(L,1,3),rstate(L,1,4),&
! throats in x direction full of mercury, colloid, polymer, wetting fluid
&rstate(L,2,1),rstate(L,2,2),rstate(L,2,3),rstate(L,2,4),&
! throats in y direction full of mercury, colloid, polymer, wetting fluid
&rstate(L,3,1),rstate(L,3,2),rstate(L,3,3),rstate(L,3,4),&
! throats in z direction full of mercury, colloid, polymer, wetting fluid
&custate(L,1),custate(L,2),custate(L,3),custate(L,4),&
! fraction of pores full of mercury, colloid, polymer, wetting fluid
&rstate(L,1,1),rstate(L,1,2),rstate(L,1,3),rstate(L,1,4),&
! fraction of throats in x direction full of mercury, colloid, polymer, wetting fluid
&rstate(L,2,1),rstate(L,2,2),rstate(L,2,3),rstate(L,2,4),&
! fraction of throats in y direction full of mercury, colloid, polymer, wetting fluid
&rstate(L,3,1),rstate(L,3,2),rstate(L,3,3),rstate(L,3,4),&
! fraction of throats in z direction full of mercury, colloid, polymer, wetting fluid
!(continuation...(if corresponding integer = 1, then e.g. 0.5 = half full)
&a(1),a(2),a(3),wet_tstep,wet_time,totwet,fracwet
END do

CASE (5000000)
open (unit=66,file='c:\Program Files\Pore-Cor\datafiles\wetpara8.csv,status='replace')
write(66,755)
do I=1,1000
write(66,760) ibulge,L,CU(L,1),CU(L,2),CU(L,3),r(L,1,1),r(L,2,1),r(L,3,1),&
&r(L,1,2),r(L,2,2),r(L,3,2),h(L,1),h(L,2),h(L,3),& ! throat lengths
&conerad(L,1,1),conerad(L,2,1),conerad(L,3,1),& ! cone throats max diameter,
&conerad(L,1,2),conerad(L,2,2),conerad(L,3,2),&
&custate(L,1),custate(L,2),custate(L,3),custate(L,4),&
! pores full of mercury, colloid, polymer, wetting fluid (empty=0, full or partially full =1)
&rstate(L,1,1),rstate(L,1,2),rstate(L,1,3),rstate(L,1,4),&
! throats in x direction full of mercury, colloid, polymer, wetting fluid
&rstate(L,2,1),rstate(L,2,2),rstate(L,2,3),rstate(L,2,4),&
! throats in y direction full of mercury, colloid, polymer, wetting fluid
&rstate(L,3,1),rstate(L,3,2),rstate(L,3,3),rstate(L,3,4),&
! throats in z direction full of mercury, colloid, polymer, wetting fluid
&custate(L,1),custate(L,2),custate(L,3),custate(L,4),&
! fraction of pores full of mercury, colloid, polymer, wetting fluid
&rstate(L,1,1),rstate(L,1,2),rstate(L,1,3),rstate(L,1,4),&
! fraction of throats in x direction full of mercury, colloid, polymer, wetting fluid
&rstate(L,2,1),rstate(L,2,2),rstate(L,2,3),rstate(L,2,4),&
! fraction of throats in y direction full of mercury, colloid, polymer, wetting fluid
&rstate(L,3,1),rstate(L,3,2),rstate(L,3,3),rstate(L,3,4),&
! fraction of throats in z direction full of mercury, colloid, polymer, wetting fluid
!(continuation...(if corresponding integer = 1, then e.g. 0.5 = half full)
&a(1),a(2),a(3),wet_tstep,wet_time,totwet,fracwet
END do

CASE (10000000)
open (unit=66,file='c:\Program Files\Pore-Cor\datafiles\wetpara9.csv,status='replace')
write(66,755)

```

```

do I=1,1000
write(66,760) ibulge,L,CU(L,1),CU(L,2),CU(L,3),r(L,1,1),r(L,2,1),r(L,3,1),&
&r(L,1,2),r(L,2,2),r(L,3,2),h(L,1),h(L,2),h(L,3),& ! throat lengths
&conerad(L,1,1),conerad(L,2,1),conerad(L,3,1),& ! cone throats max diameter,
&conerad(L,1,2),conerad(L,2,2),conerad(L,3,2),&
&custate(L,1),custate(L,2),custate(L,3),custate(L,4),&
! pores full of mercury, colloid, polymer, wetting fluid (empty=0, full or partially full =1)
&rstate(L,1,1),rstate(L,1,2),rstate(L,1,3),rstate(L,1,4),&
! throats in x direction full of mercury, colloid, polymer, wetting fluid
&rstate(L,2,1),rstate(L,2,2),rstate(L,2,3),rstate(L,2,4),&
! throats in y direction full of mercury, colloid, polymer, wetting fluid
&rstate(L,3,1),rstate(L,3,2),rstate(L,3,3),rstate(L,3,4),&
! throats in z direction full of mercury, colloid, polymer, wetting fluid
&custatep(L,1),custatep(L,2),custatep(L,3),custatep(L,4),&
! fraction of pores full of mercury, colloid, polymer, wetting fluid
&rstatep(L,1,1),rstatep(L,1,2),rstatep(L,1,3),rstatep(L,1,4),&
! fraction of throats in x direction full of mercury, colloid, polymer, wetting fluid
&rstatep(L,2,1),rstatep(L,2,2),rstatep(L,2,3),rstatep(L,2,4),&
! fraction of throats in y direction full of mercury, colloid, polymer, wetting fluid
&rstatep(L,3,1),rstatep(L,3,2),rstatep(L,3,3),rstatep(L,3,4),&
! fraction of throats in z direction full of mercury, colloid, polymer, wetting fluid
!(continuation...(if corresponding integer = 1, then e.g. 0.5 = half full)
&a(1),a(2),a(3),wet_tstep,wet_time,totwet,fracwet
END do

CASE (30000000)
open (unit=66,file='c:\Program Files\Pore-Cor\datafiles\wetpara10.csv,status='replace')
write(66,755)
do I=1,1000
write(66,760) ibulge,L,CU(L,1),CU(L,2),CU(L,3),r(L,1,1),r(L,2,1),r(L,3,1),&
&r(L,1,2),r(L,2,2),r(L,3,2),h(L,1),h(L,2),h(L,3),& ! throat lengths
&conerad(L,1,1),conerad(L,2,1),conerad(L,3,1),& ! cone throats max diameter,
&conerad(L,1,2),conerad(L,2,2),conerad(L,3,2),&
&custate(L,1),custate(L,2),custate(L,3),custate(L,4),&
! pores full of mercury, colloid, polymer, wetting fluid (empty=0, full or partially full =1)
&rstate(L,1,1),rstate(L,1,2),rstate(L,1,3),rstate(L,1,4),&
! throats in x direction full of mercury, colloid, polymer, wetting fluid
&rstate(L,2,1),rstate(L,2,2),rstate(L,2,3),rstate(L,2,4),&
! throats in y direction full of mercury, colloid, polymer, wetting fluid
&rstate(L,3,1),rstate(L,3,2),rstate(L,3,3),rstate(L,3,4),&
! throats in z direction full of mercury, colloid, polymer, wetting fluid
&custatep(L,1),custatep(L,2),custatep(L,3),custatep(L,4),&
! fraction of pores full of mercury, colloid, polymer, wetting fluid
&rstatep(L,1,1),rstatep(L,1,2),rstatep(L,1,3),rstatep(L,1,4),&
! fraction of throats in x direction full of mercury, colloid, polymer, wetting fluid
&rstatep(L,2,1),rstatep(L,2,2),rstatep(L,2,3),rstatep(L,2,4),&
! fraction of throats in y direction full of mercury, colloid, polymer, wetting fluid
&rstatep(L,3,1),rstatep(L,3,2),rstatep(L,3,3),rstatep(L,3,4),&
! fraction of throats in z direction full of mercury, colloid, polymer, wetting fluid
!(continuation...(if corresponding integer = 1, then e.g. 0.5 = half full)
&a(1),a(2),a(3),wet_tstep,wet_time,totwet,fracwet
END do

CASE (50000000)
open (unit=66,file='c:\Program Files\Pore-Cor\datafiles\wetpara11.csv,status='replace')
write(66,755)
do I=1,1000
write(66,760) ibulge,L,CU(L,1),CU(L,2),CU(L,3),r(L,1,1),r(L,2,1),r(L,3,1),&
&r(L,1,2),r(L,2,2),r(L,3,2),h(L,1),h(L,2),h(L,3),& ! throat lengths
&conerad(L,1,1),conerad(L,2,1),conerad(L,3,1),& ! cone throats max diameter,
&conerad(L,1,2),conerad(L,2,2),conerad(L,3,2),&
&custate(L,1),custate(L,2),custate(L,3),custate(L,4),&
! pores full of mercury, colloid, polymer, wetting fluid (empty=0, full or partially full =1)
&rstate(L,1,1),rstate(L,1,2),rstate(L,1,3),rstate(L,1,4),&
! throats in x direction full of mercury, colloid, polymer, wetting fluid
&rstate(L,2,1),rstate(L,2,2),rstate(L,2,3),rstate(L,2,4),&
! throats in y direction full of mercury, colloid, polymer, wetting fluid
&rstate(L,3,1),rstate(L,3,2),rstate(L,3,3),rstate(L,3,4),&
! throats in z direction full of mercury, colloid, polymer, wetting fluid
&custatep(L,1),custatep(L,2),custatep(L,3),custatep(L,4),&
! fraction of pores full of mercury, colloid, polymer, wetting fluid
&rstatep(L,1,1),rstatep(L,1,2),rstatep(L,1,3),rstatep(L,1,4),&
! fraction of throats in x direction full of mercury, colloid, polymer, wetting fluid
&rstatep(L,2,1),rstatep(L,2,2),rstatep(L,2,3),rstatep(L,2,4),&
! fraction of throats in y direction full of mercury, colloid, polymer, wetting fluid
&rstatep(L,3,1),rstatep(L,3,2),rstatep(L,3,3),rstatep(L,3,4),&
! fraction of throats in z direction full of mercury, colloid, polymer, wetting fluid
!(continuation...(if corresponding integer = 1, then e.g. 0.5 = half full)
&a(1),a(2),a(3),wet_tstep,wet_time,totwet,fracwet
END do

```

```

CASE (10000000)
open (unit=68,file='c:\Program Files\Pore-Cor\datafiles\wetpara12.csv,status='replace')
write(66,755)
do I=1,1000
write(66,760) ibulge,L,CU(L,1),CU(L,2),CU(L,3),r(L,1,1),r(L,2,1),r(L,3,1),&
&r(L,1,2),r(L,2,2),r(L,3,2),h(L,1),h(L,2),h(L,3),& ! throat lengths
&conerad(L,1,1),conerad(L,2,1),conerad(L,3,1),& ! cone throats max diameter,
&conerad(L,1,2),conerad(L,2,2),conerad(L,3,2),&
&custate(L,1),custate(L,2),custate(L,3),custate(L,4),&
! pores full of mercury, colloid, polymer, wetting fluid (empty=0, full or partially full =1)
&rstate(L,1,1),rstate(L,1,2),rstate(L,1,3),rstate(L,1,4),&
! throats in x direction full of mercury, colloid, polymer, wetting fluid
&rstate(L,2,1),rstate(L,2,2),rstate(L,2,3),rstate(L,2,4),&
! throats in y direction full of mercury, colloid, polymer, wetting fluid

&rstate(L,3,1),rstate(L,3,2),rstate(L,3,3),rstate(L,3,4),&
! throats in z direction full of mercury, colloid, polymer, wetting fluid
&custatep(L,1),custatep(L,2),custatep(L,3),custatep(L,4),&
! fraction of pores full of mercury, colloid, polymer, wetting fluid
&rstatep(L,1,1),rstatep(L,1,2),rstatep(L,1,3),rstatep(L,1,4),&
! fraction of throats in x direction full of mercury, colloid, polymer, wetting fluid
&rstatep(L,2,1),rstatep(L,2,2),rstatep(L,2,3),rstatep(L,2,4),&
! fraction of throats in y direction full of mercury, colloid, polymer, wetting fluid
&rstatep(L,3,1),rstatep(L,3,2),rstatep(L,3,3),rstatep(L,3,4),&
! fraction of throats in z direction full of mercury, colloid, polymer, wetting fluid

!(continuation...(if corresponding integer = 1, then e.g. 0.5 = half full)
&a(1),a(2),a(3),wet_tstep,wet_time,totwet,fracwet
END do
end select

755 format ('cylinders or cones?', 'pore number', 'pore length-x-axis', 'pore length-y-axis', &
&'pore length-z-axis', 'x thr rad 1', 'y thr rad 1', 'z thr rad 1', 'x thr rad 2', 'y thr rad 2', &
&'z thr rad 2', 'x thr length', 'y thr length', 'z thr length', 'x thr concl rad 1', &
&'y thr concl rad 1', 'z thr concl rad 1', 'x thr concl rad 2', 'y thr concl rad 2', &
&'z thr concl rad 2', 'pore full of Hg?', 'pore full of cld?', 'pore full of polymr?', &
&'pore full of wetting fluid?', 'x thr full of Hg?', 'x thr full of cld?', 'x thr full of polymr?', &
&'x thr full of wetting fluid?', 'y thr full of Hg?', 'y thr full of cld?', 'y thr full of polymr?', &
&'y thr full of wetting fluid?', 'z thr full of Hg?', 'z thr full of cld?', &
&'z thr full of polymr?', 'z thr full of wetting fluid?', 'pore frac fill Hg/wet-fluid', &
&'pore frac fill cld', 'pore frac fill polymr', 'pore frac fill wetting fluid', &
&'x thr frac fill Hg', 'x thr frac fill cld', 'x thr frac fill polymr', &
&'x thr frac fill wetting fluid', 'y thr frac fill Hg', 'y thr frac fill cld', 'y thr frac fill polymr', &
&'y thr frac fill wetting fluid', 'z thr frac fill Hg', 'z thr frac fill cld', 'z thr frac fill polymr', &
&'z thr frac fill wetting fluid', 'x-p-row-spacing', 'y-p-row-spacing', 'z-p-row-spacing', &
&'wet_tstep', 'wet_time', 'totwet', 'fracwet,')

760 FORMAT (2(i5,' '),18(f24.16,' '),16(i5,' '),19(f24.16,' '),4(f24.16,' '))

CLOSE(66)

!-----end of fortran used for Pau's research-----

endif ! end of interim totwet calcn *****

! write (21,*) 'nstep,custatep(1,901),rstatep(2),cufillrate(2),rstatep(3),cufillrate(3),rstatep(nn1),cufillrate(4),&
! &rstatep(nn2),cufillrate(5),custatep(911),custatep(991),massbal(901),massbal(911),massbal(991)'
! write (21,*) 'nstep,wet_time,custatep(981),rstatep(1),cufillrate(1),rstatep(2),cufillrate(2),rstatep(3),cufillrate(3),&
! &rstatep(nn1),cufillrate(4),&
! &rstatep(nn2),cufillrate(5),rstatep(nn3),cufillrate(6),massbal(991),&
! &mbaldone(991)'

if (wet_time.lt.wet_endtime) goto 100 ! $$$ end of timestep loop ++++++

fracwet=totwet/vol ! fraction of total pore and throat vol in um3 (=vol) which is wetted
print *, 'wet_endtime = ',wet_endtime,' totwet = ',totwet
print *, 'fracwet = ',fracwet

open (unit=297,file='c:\Program Files\Pore-Cor\datafiles\endcell.csv,status='replace')
write(297,421)
do I=1,1000
write(297,422) ibulge,L,CU(L,1),CU(L,2),CU(L,3),r(L,1,1),r(L,2,1),r(L,3,1),&
&r(L,1,2),r(L,2,2),r(L,3,2),h(L,1),h(L,2),h(L,3),& ! throat lengths
&conerad(L,1,1),conerad(L,2,1),conerad(L,3,1),& ! cone throats max diameter,
&conerad(L,1,2),conerad(L,2,2),conerad(L,3,2),&
&custate(L,1),custate(L,2),custate(L,3),custate(L,4),&
! pores full of mercury, colloid, polymer, wetting fluid (empty=0, full or partially full =1)
&rstate(L,1,1),rstate(L,1,2),rstate(L,1,3),rstate(L,1,4),&
! throats in x direction full of mercury, colloid, polymer, wetting fluid
&rstate(L,2,1),rstate(L,2,2),rstate(L,2,3),rstate(L,2,4),&
! throats in y direction full of mercury, colloid, polymer, wetting fluid

```

```

&rstate(L,3,1),rstate(L,3,2),rstate(L,3,3),rstate(L,3,4),&
! throats in z direction full of mercury, colloid, polymer, wetting fluid
&cstatep(L,1),cstatep(L,2),cstatep(L,3),cstatep(L,4),&
! fraction of pores full of mercury, colloid, polymer, wetting fluid
&rstatep(L,1,1),rstatep(L,1,2),rstatep(L,1,3),rstatep(L,1,4),&
! fraction of throats in x direction full of mercury, colloid, polymer, wetting fluid
&rstatep(L,2,1),rstatep(L,2,2),rstatep(L,2,3),rstatep(L,2,4),&
! fraction of throats in y direction full of mercury, colloid, polymer, wetting fluid
&rstatep(L,3,1),rstatep(L,3,2),rstatep(L,3,3),rstatep(L,3,4),&
! fraction of throats in z direction full of mercury, colloid, polymer, wetting fluid
!(continuation...(if corresponding integer = 1, then e.g. 0.5 = half full))
&a(1),a(2),a(3),wet_tstep,wet_time,totwet,fracwet
END do
close (297)

! if (ibulge.eq.7) then !conical throats so put back to original radii
!taken out only looking at cylindrical throats 17-02-01 PB
! do l=1,1000
! do m=1,3
! r(l,m)=ractual(l,m)
! end do
! end do
! end if

close (unit=21)
close (unit=22)
return
end

```

END NOTES

¹ Ink Surface Interaction Tester (ISIT) is a product name of SeGan Ltd., Perrose, Lostwithiel, Cornwall PL22 0JJ, U.K.

² Fibro System AB (www.fibro.se) is the supplier of the DAT instrument.

³ Lorentzen & Wettres is the supplier of the Gurley permeameter.

⁴ The supplier of the Prubau Printability Tester is Prüfbau, Aich 17-23, D-82380, Peissenberg, München, Dr-ing H. Dürner GmbH D 8123 Peissenberg, Tschermanny. (www.prufbau.de)

⁵ Pore-Cor is a software package developed by the Environmental and Fluid Modelling Group of the University of Plymouth, Plymouth, Devon, UK, PL4 8AA. (www.pore-cor.com).

⁶ The picture in the figure is uncopyrighted and obtained from an internet site for educational purposes.

⁷ Refer to endnote number 6.

⁸ Refer to endnote number 6.

⁹ Refer to endnote number 6.

¹⁰ Refer to endnote number 6.

¹¹ Refer to endnote number 6

¹² Refer to endnote number 6.

¹³ Speswhite clay was supplied from Imerys Inc., UK.; Amazon 90 SD was supplied from Caulim da Amazônia S.A., Brazil; Hydrocarb60 and Hydrocarb90 were supplied from Omya AG, Switzerland; OpacarbA60, OpacarbA40 and Albaglos were supplied from Specialty Minerals Nordic Oy, Finland.

¹⁴ SB Latex binder (trade name: DPL 935) and the starch co-binder (product number: *07312) were both supplied from Dow Rheinmünster GmbH, Germany; CMC co-binder (product number: FF5) was supplied from Noviant, Finland.

¹⁵ Sodium polyacrylate (trade name: Dispex N 40) was supplied from Colloids Ltd., UK.

¹⁶ Synteape was supplied from Arjo Wiggins Ltd.

¹⁷ The bench coater (product name: K-coater) was supplied by RK Print-Coat Instruments Ltd., Royston, UK.

¹⁸ Micromeritics Sedigraph was supplied by the Micromeritics Instrument Corporation (www.micromeritics.com).

¹⁹ The SEM was supplied from Leica Cambridge, a Stereoscan 360, and is fully integrated with an Oxford Instruments (Link) eXL-II energy dispersive x-ray microanalyser.

²⁰ Gemini 2360 BET surface analyzer was supplied from the Micromeritics Instrument Corporation (www.micromeritics.com).

²¹ Autopore III Mercury Porosimeter was supplied from the Micromeritics Instrument Corporation (www.micromeritics.com).

²² The supplier of the Gretag densitometer (product name: Gretag D186) is Colour Data Systems Ltd.

²³ The gravure roller was supplied from IGT Testing Systems, Amsterdam.

²⁴ The non-setting test oil was supplied from Haltermann Products, a division of Ascot Speciality Chemicals.

²⁵ Control Stress Rheometer was supplied from TA Instruments (product name: AR1000).

²⁶ Further enquiries pertaining to the Pore-Cor Fortran code can be directed to the Environmental and Fluids Modelling Group, University of Plymouth, Plymouth, UK, PL4 8AA. (www.pore-cor.com).

REFERENCES

- Abramowitz, M. and Stegun, I.A. (Eds.), *Handbook of Mathematical functions with formulas and mathematical tables*, 1965.
- Adler, P.M., Jacquin, C.G. and Quiblier, J.A., *International Journal of Multiphase Flow*, 1990, **16**, 691.
- Ahuja, R.K., Kodialam, M., Mishra, A.K. and Orlin, J.B., *European Journal Of Operational Research*, 1997, **97**, 509.
- Allen, T., *Particle Size Measurement*, Chapman and Hall Ltd., London, England, 1981.
- Baudet, G., Bizi, M. and Rona, J.P., *particulate Sci. Technol.*, 1993, **11**, 73.
- Bear, J., *Dynamics of Fluids in Porous Media*, New York: Dover, New York. 1988.
- Bloss, F. D., *Crystallography and Crystal Chemistry*, Washington, D.C.: Mineralogical Society of America, 1994. 545 pages.
- Borhan, A. and Rungta, K.K., *J. Colloid Interface Sci.*, 1993, **155**, 438.
- Bosanquet, C.H., *Phil. Mag. Series 6*, 1923, **45**, 525.
- Bousfield, D.E. and Toivakka M., *Tappi Journal*, in Prep., 2000.
- Bristow, J.A. and Bergenblad, H., *Advances in Printing Science and Technology*, 1982, **16**, 373.
- Brooks, C.S. and Purcell W.R., *Transaction of the American Institute of Mining Engineers (AIME)*, 1952, **195**, 289.
- Bryant, S.L., King, P.R. and Mellor, D.W., *Trans. Por. Med.*, 1993, **11**, 53.
- Cadle, R.D., *Particle Size*, Reinhold Publishing Corporation, London, England, 1965.
- Carman, P.C., *J. Agri. Sci*, 1939, **29**, 262.
- Carman, P.C., *Soil Sci*, 1941, **52**, 1.

- Chibowski, E. and Holysz, L., *Journal of Adhesion Science Technology*, 1997, **11**, 1289.
- Childs, E.C. and Collis-George, N., *Proceedings Of The Royal Society Of London Series A -Mathematical Physical And Engineering Sciences*, 1950, **A20**, 392.
- Choi, P.K. and Staszczuk, P., *Clays and Clay Minerals*, 1988, **36**, 455.
- Cloud, W.F., *oil weekly*, 1941, **103**, 26.
- Coulliette, C. and Pozrikidis, C., *J. Fluid. Mech.*, 1998, **358**, 1.
- Coulson, J.M., *Trans. Inst. Chem. Engrs.*, 1949, **27**, 237.
- Cumberland, D.J. and Crawford, R.J.. *The Packing of Particles*, Elsevier, Amsterdam, Netherlands, 1987.
- Dawe, R.A., *Rev. Sci. Instrum.*, 1973, **44**,1271.
- Dong, M. and Chatzis, I., *J. Colloid Interface Sci.*, 1995, **172**, 278.
- Donigian, D.W., Ishley, J.N. and Wise, K.J., *Tappi Journal*, 1997, **80**, 5.
- Dullien, F.A.L., *Porous Media. Fluid transport and pore structure*, 2 ed., Academic Press, 1992.
- Eastman, J.E. and Carlson, A.J., *Transaction Proceedings of the American Institute of Mining, Metallurgical, and Petroleum Engineers AIME T.P.*, 1940, p. 1196.
- Fair G.M. and Hatch L.P., *Journal of American Water Works Association*, 1933, **25**, 1551.
- Gane, P.A.C., *Wochenblatt für Papierfabrikation*, 2001, 110.
- Gane, P.A.C., Kettle, J.P., Matthews, G.P. and Ridgway, C.J., *Ind. Eng. Chem. Res.*, 1995, **35**, 1753.
- Gane, P.A.C., Schoelkopf, J., Spielmann, D.C., Matthews, G.P. and Ridgway, C.J., *Tappi Advanced Coating Fundamentals Symposium proceedings*, Tappi Press, Atlanta, 1999, p. 213.
- Gane, P.A.C., Schoelkopf, J., Spielmann, D.C., Matthews, G.P. and Ridgway, C.J., *Tappi Journal*, 2000, **83**, 77.
- Gane, P.A.C. and Seyler, E.N., *Tappi Coating Conference Proceedings*, 1994.

- Ginzbourg, I. and Adler, P.M., *Trans. Por. Med.*, **20** (1995) 37.
- Graton, L.C. and Fraser, H.J, *The Journal of Geology*, **43** (1935) 785.
- Haines, W.B., *J. Agri. Sci*, **17** (1927) 264.
- Hutta, J.H. and Griffiths, J.C., *Producers Monthly*, **19** (1955) 24.
- Hwang, K.-J., Wu, Y.-S. and Lu, W.M., *Powder Tech.*, 1997, **91**, 105.
- Ichikawa, N. and Satoda, Y., *J. Colloid Interface Sci.*, 1994, **162**, 350.
- Institute of Paper Science & Technology, *Paper Trade Journal*, 1940, **110**, 27.
- Ioannidis, M.A., Chatzis, I., *J. Coll. Int. Sci.*, 1993 **161**, 278.
- Ishigami, Y., Gama, Y., Sano, Y., Lang, S. and Wagner, F., *Biotechnol. Lett.*, 1994, **16**, 593.
- Jennings B.R. and Parslow, K., *Proc. R. Soc. Lond. A*, 1988, **A419**, 137.
- Jerauld, G.R. and Salter, S.J., *Trans. Por. Med.*, 1990, **5**, 103.
- Johnson, W.E., Breston, J.N., *Producers Monthly*, 1951, **15**, 10.
- Kent, H.J., *Nordic Pulp and Paper Research Journal*, 1991, **6**, 191.
- Kent, H.J. and Lyne, M.B., *Nordic Pulp and Paper Research Journal*, 1989, **2**, 141.
- Klein, C., and Hurlbut, C., *Manual of Mineralogy*, 20 ed., John Wiley & Sons, New York, 1985.
- Knackstedt, M. A., Sheppard, A., Pinczewski, W. V. *et al.*: *Meso-scale Physics - disordered Materials*, 2000. University web site: <http://www.rspphysse.anu.edu.au/appmaths/disord.html>. Department of Applied Mathematics, The Australian National University.
- Kozeny, J., *S.-Ber.Wiener Akad.*, 1927, **Abt. Ila**, 271.
- Kozeny, J. and Wasserkr, U., *Wasserw*, 1927, **22**, 86.
- Lee, L.-H., *Journal of Adhesion Science Technology*, 1993, **7**, 583.
- Lepoutre, P., *Prog. Org. Coatings*, 1989, **17**, 89.

- Li, T.Q., Haggkvist, M. and Odberg, L., *Colloids And Surfaces A-Physicochemical And Engineering Aspects*, 1999, **159**, 57.
- Liu, H.L., Zhang, L. and Seaton, N.A., *Chem. Eng. Sci.*, 1992, **47**, 4393.
- Lohmander, S., *Nordic Pulp and Paper Research Journal*, 2000a, **15**, 221.
- Lohmander, S., *Nordic Pulp and Paper Research Journal*, 2000b, **15**, 300.
- Lohmander, S. *The influence of particle shape of coating pigments on their packing ability and on the flow properties of coating colours*, (Ph.D. Thesis). Royal Institute of Technology, Department of Pulp and Paper Chemistry and Technology, Division of Paper Technology; 2000c; 72 p.
- Lohmander, S. and Rigdahl, M., *Nordic Pulp & Paper Research Journal*, 2000, **15**, 231.
- Lu, T.X., Nielsen, D.R. and Biggar, J.W., *Wat. Resour. Res.*, 1995, **31**, 11.
- Lucas, R., *Kolloid Z.*, 1918, **23**, 15.
- Lundqvist, A. and Odberg, L., *Journal of Pulp and Paper Science*, 1997, **23**, J298-J303.
- Ma, S.X., Mason, G. and Morrow, N.R., *Colloids And Surfaces A-Physicochemical And Engineering Aspects*, 1996, **117**, 273.
- Maasland, M. and Kirkham, D., *Soil Sci. Soc. Am. J.*, 1955, **19**, 395.
- MacDonald, L.A., *Subsurface migration of an oil pollutant into aquifers*. (Ph.D. Thesis). School of Environmental Sciences, University of Plymouth, Plymouth, UK. 2000.
- Macey, H.H., *Proceedings of the Royal Physical Society (Proc. Phys. Soc.)*, 1940, **52**, 625.
- Maitland, G.C, Rigby, M., Smith, E.B. et al., *Intermolecular Forces-their Origin and Determination*, Clarendon Press, Oxford, 1981.
- Marmur, A., *J. Colloid Interface Sci.*, 1988, **122**, 209.
- Marmur, A., *Advances in Colloid and Interface Science*, 1992, **39**, 13.
- Mason, G. and Morrow, N.R., *J. Coll. Int. Sci.*, 1991, **141**, 262.

- Matthews, G.P., Moss, A.K. and Ridgway, C.J., *Powder Tech.*, 1995 **83**, 61.
- Matthews, G.P., Moss, A.K., Spearing, M.C. and Volland, F., *Powder Tech.*, 1993, **76**, 95.
- Matthews, G.P., Ridgway, C.J. and Spearing, M.C., *J. Coll. Int. Sci.*, 1995, **171**, 8.
- Mathews, T.J., Matthews, G.P., Ridgway, C.J. and Moss, A.K., *Trans. Por. Med.*, 1997, **28**, 135.
- McCoy, J.W., *Tappi Proceedings-1998 Coating/Papermakers Conference*, 1998, p. 121.
- Melrose, J.C., Unger, K.K. et al. (Eds.), *Characterization of Porous Solids*, Elsevier Science Publishers B.V., Amsterdam, 1988, p. 253.
- Morris, H.H., Sennett, P. and Drexel, R.J., *Tappi Journal*, 1965, **48**, 92A.
- Moshinskii, A.I., *Colloid Journal*, 1997, **59**, 62.
- Niskanen, K.J., Rasi, M., Aaltosalmi, U., Timonen, J. and Jataja, M., *TAPPI International Paper Physics Conference*, 1999, p. 297.
- O'Neill, M.E. and Chorlton, F., *Viscous and compressible fluid dynamics*. Edited by Horwood, E., Chichester, 1989.
- O'Shea, J.E., *Pigments for Paper*, 2nd edition. Edited by Hagemeyer, R.W., Tappi Press, Atlanta, 1997.
- Pan, S.X., Davis, H.T. and Scriven, L.E., *Tappi Journal*, 1995, **78**, 127.
- Paterson, L., Painter, S., Knackstedt, M.A. and Pinczewski, W.V., *Physica A*, 1996, **233**, 619.
- Patwardhan, V.S. and Tien, C., *Chem. Eng. Sci.*, 1985, **40**, 1051.
- Patwardhan, V.S. and Tien, C., *AIChE Journal*, 1986, **32**, 321.
- Peat, D.M.W., Matthews, G.P., Worsfold, P.J. and Jarvis, S.C., *European J. Soil Sci.*, 2000, **51**, 65.
- Physical Committee of the Process and Product Quality Division, editor. , *Tappi Test Methods: 2000-2001*, TAPPI Press. 1996, T 460 om-96.
- Portsmouth, R.L. and Gladden, L.F., *Chem. Eng. Sci.*, 1991, **46**, 3023.

- Portsmouth, R.L. and Gladden L.F., *Trans. Inst. Chem. Engrs.*, 1992, **70**, 63.
- Powell, M.J., *Powder Tech.*, 1980, **25**, 45.
- Preston, J.S., Elton, N.J., Husband, J.C., Dalton, J., Heard, P.J. and Allen, G.C., *Colloids And Surfaces A-Physicochemical And Engineering Aspects*, 2002, **205**, 183.
- Preston, J.S., Elton, N.J., Legrix, A. and Nutbeem, C., *TAPPI Proceedings: Advanced Coating Fundamentals Symposium*, TAPPI, 2001.
- Purcell, W.R., *Transaction of the American Institute of Mining Engineers (AIME)*, 1949, **186**, 39.
- Ransohoff, T.C. and Radke, C.J., *J. Colloid Interface Sci.*, 1988, **121**, 392.
- Reyes, S.C. and Iglesia, E., *Chem. Eng. Sci.*, 1991, **46**, 1089.
- Ridgway, C.J., Gane, P.A.C. and Schoelkopf, J., *J. Colloid Interface Sci.*, 2002, **252**, 373.
- Ridgway, C.J., Ridgway, K. and Matthews, G.P., *J. Pharm. Pharmacol.*, 1997, **49**, 377.
- Ridgway, C.J., Schoelkopf, J., Matthews, G.P., Gane, P.A.C. and James, P.W., *J. Colloid Interface Sci.*, 2001, **239**, 417.
- Scheidegger, A.E., *Petroleum engineering*, 1953a, **25**, B121.
- Scheidegger, A.E., *Producers Monthly*, 1953b, **17**, 17.
- Scheidegger, A.E., *The physics of flow through porous media*, University of Toronto Press, Toronto, 1974.
- Schoelkopf, J., Gane, P.A.C., Ridgway, C.J. and Matthews, G.P., *Nordic Pulp and Paper Research Journal*, 2001, **15**, 422.
- Schoelkopf, J., Ridgway, C.J., Gane, P.A.C., Matthews, G.P. and Spielmann, D.C., *J. Colloid Interface Sci.*, 2000, **227**, 119.
- Sell, P.-J., Maisch, E. and Siekmann, J., *Acta Astronautica*, 1986, **13**, 87.
- Sherwood, D.J., *Proceedings of the Royal Society: Mathematical and Physical Sciences*, 1994, **445**, 679.

- Slepety, R.A. and Cleland, A.J., *Clay Minerals*, 1993, **28**, 495.
- Soppe, W., *Powder Tech.*, 1990, **62**, 189.
- Starov, V.M., Kalinin, V.V. and Ivanov, V.I., *Colloids And Surfaces A-Physicochemical And Engineering Aspects*, 1994, **91**, 149.
- Suzuki, M. and Oshima, T., *Powder Tech.*, 1985, **44**, 213.
- Szekely, J., Neumann, A.W. and Chuang, Y.K., *J. Colloid Interface Sci.*, 1971, **35**, 273.
- Technical Association of the Pulp and Paper Industry. *2000-2001 TAPPI test methods*. Atlanta: TAPPI Press, 2002, T 558 om-97.
- Tiller, F.M., Yeh, C.S. and Leu, W.F., *Separation Science And Technology*, 1987, **22**, 1037.
- Toivakka, M. and Nyfors, K., *Tappi Coating Conference*, Washington DC, 2000.
- Tsakiroglou, C.D., Payatakes, A.C., *J. Coll. Int. Sci.*, 1990, **137**, 315.
- Van Brakel, J., Modry, S. and Svata, M., *Powder Tech.*, 1981, **29**, 1.
- Wang, H., Zinchenko, A.Z. and Davis, R.H., *J. Fluid. Mech.*, 1994, **265**, 161.
- Wardlaw, N.C., Li, Y. and Forbes, D., *Trans. Por. Med.*, 1987, **2**, 597.
- Washburn, E.W., *Physical Review*, 1921, **17**, 273.
- Weast, R.C. and Astle, M.J. (Eds.), *CRC Handbook of Chemistry and Physics*, 60 ed., CRC Press, Inc., Florida, USA, 1979.
- Webb, P.A. and Orr, C., *Analytical Methods in Fine Particle Technology*, 1 ed., Micromeritics, Norcross, GA, 1997.
- Weislogel, M.M. and Lichter, S., *J. Fluid. Mech.*, 1998, **373**, 349.
- Woodward, J.T., Ulman, A. and Schwartz, D.K., *Langmuir*, 1996, **12**, 3626.
- Yamazaki, H. and Munakata, Y., *Oxford Fundamental Research Symposium Proceedings*, 1993, p. 913.